

RESERVOIR MODELING
WITH MULTIPLE GEOLOGICAL SCENARIOS
FOR DEFORMATION OF RESERVOIR STRUCTURE
AND EVOLUTION OF RESERVOIR PROPERTIES

A DISSERTATION
SUBMITTED TO THE DEPARTMENT OF
ENERGY RESOURCES ENGINEERING
AND THE COMMITTEE ON GRADUATE STUDIES
OF STANFORD UNIVERSITY
IN PARTIAL FULFILLMENT OF THE REQUIREMENTS
FOR THE DEGREE OF
DOCTOR OF PHILOSOPHY

Yongduk Shin

March 2016

© 2016 by Yongduk Shin. All Rights Reserved.

Re-distributed by Stanford University under license with the author.



This work is licensed under a Creative Commons Attribution-Noncommercial 3.0 United States License.

<http://creativecommons.org/licenses/by-nc/3.0/us/>

This dissertation is online at: <http://purl.stanford.edu/mm845vs3519>

I certify that I have read this dissertation and that, in my opinion, it is fully adequate in scope and quality as a dissertation for the degree of Doctor of Philosophy.

Tapan Mukerji, Primary Adviser

I certify that I have read this dissertation and that, in my opinion, it is fully adequate in scope and quality as a dissertation for the degree of Doctor of Philosophy.

Jef Caers

I certify that I have read this dissertation and that, in my opinion, it is fully adequate in scope and quality as a dissertation for the degree of Doctor of Philosophy.

David Pollard

Approved for the Stanford University Committee on Graduate Studies.

Patricia J. Gumport, Vice Provost for Graduate Education

This signature page was generated electronically upon submission of this dissertation in electronic format. An original signed hard copy of the signature page is on file in University Archives.

Abstract

Deformational uncertainty about subsurface structures and accommodational uncertainty about rocks are not only closely linked to each other, but also significantly impact reservoir responses. The main objective of this dissertation is to investigate the effects of these two geological uncertainties on reservoir responses. To achieve this goal, we aim to develop and test a reservoir modeling and evaluation workflow that accounts for the mode of deformation of a reservoir and the mode of accommodation of reservoir properties for a given deformation, by utilizing structural attributes and rock physics models.

First, we investigate the sources of geological uncertainty in structural deformation and rock accommodation. We employ different combinations of structural geometry and deformation models to represent multiple scenarios for structural deformation. Distributed and localized accommodation styles and their subsets can represent scenarios for rock accommodation.

Second, we develop a new geomodeling workflow accounting for the mode of structural deformation and rock accommodation. The new workflow links the forward deformation and restoration of the reservoir structure to the same processes on the rock. An application on a synthetic field demonstrates that realizations and dynamic responses from different scenarios can be distinguished from one another by comparing seismic responses.

Next, we propose a new rock physics method, Reconstruction of Equivalent Isotropic Medium (REIM), which allows us to compute the angular variation of seismic responses of arbitrarily oriented fracture inclusions in an anisotropic medium, and to apply our new workflow to unconventional shale resources. Specifically, we apply these tools to an unconventional Marcellus gas field in which structural complexity and sparse data cause substantial difficulties in evaluation. We identify the sources of geological uncertainties and define multiple scenarios based on basin-wide and field-specific

observations. By using rock physics models as vehicles to link geological scenarios with reservoir properties, we propagate geological assumptions to reservoir responses. We then select combinations of structural deformation and rock accommodation scenarios by comparing the actual and synthetic seismic responses. The selected scenario and models successfully explain the field-specific anomalies.

Acknowledgements

I would like to express the deepest appreciation to my principal advisor, Professor Tapan Mukerji, not only for his great knowledge and genius but also for his great personality. He continually and convincingly encouraged a spirit of adventure in regard to research. His wide and in-depth range of research has been an endless source of great motivation and guidance in my own work. When I had difficulties finding field data, he reached out to his numerous industry contacts to help, and never gave up after some of them turned him down. Tapan, thank you so much for giving the most concrete support just when I needed it. Without your guidance and persistent help, this dissertation would not have been possible. I am truly grateful to have you as my advisor.

I would also like to thank Professor Jef Caers for inspiring me intellectually with his great research. I was amazed by his vigorous explorations and the new ideas and questions he proposed to Earth Science communities. Many technical parts of my work started when Jef put me in the benchmark project, aiming to create a synthetic fractured reservoir. Jef, I am in debt to you for your support and kindness throughout the journey.

I feel truly honored to have Professor David D. Pollard on my committee. To encourage me to come to Stanford, one of my former colleagues, a structural geologist, told me, “David Pollard is at Stanford.” Yes. We have David Pollard at Stanford! His lecture on structural geology and rock mechanics inspired much of my work, including my goal to integrate geologists’ excellent insights into the reservoir evaluation processes. Not only did he inspire me, but he also helped keep my self-esteem higher than safety margins by giving me good feedback and warm words. Thank you so much, David!

Likewise, I also thank Dr. Celine Scheidt and Professor Stephan Graham for being my committee member and committee chair. Celine is one of the most helpful and influential researchers in my research group, Stanford Center for Reservoir Forecasting (SCRF), and shared her invaluable ideas and source codes, the bread and

butter of every SCRF project. Steve's lecture on sedimentary basins was an eye-opener for me, and made me start to understand how geologists progress from observations to geological ideas, and how important imagination is to be a good earth scientist (Steve picked my final report as the best report among the class, one of my proudest accomplishments). The field trip with his vivid explanations are one of my favorite experiences at Stanford. I am truly thankful to them both.

I also want to thank my master's program advisor, Professor Jongguen Choe. He introduced me to earth science and guided me throughout the master program. Like many others, I have greatly benefited from his academic excellence, his love for teaching, and his care for his students.

My research was also made possible by the SCRF sponsors and their financial support. Generous donations of academic licenses from Schlumberger, Paradigm, and Middle Valley Exploration were a great help to advance my research. The data donor of the Marcellus data set wants to remain anonymous. I deeply appreciate the donor's help and support on my research. I also thank Professor Mark Zoback for introducing me to the donor, and Gader Alalli for sharing his idea and expertise on Marcellus play. I am thankful to Anadarko providing me a summer internship opportunity and a full-time job offer.

It was a great joy having such great SCRF friends and colleagues. Their wide range of different research topics but with enormous depth always make me intrigued and amused. I want to thank Kwangwon, Andre, Siyao, Ognen, Orhun, Cheolkyun, Hyucksoo and Jaehoon, among many others, not only for helping me overcome research obstacles but also for making my campus life more vivid and energetic.

My ERE friends and colleagues are awesome not only because they are smart, but also because they are super-friendly and easy to get along with. Many thanks to Mehrdad, Wenyue, Boxiao, Lin, Hangyu, Peipei, Sumeet, and Manish for being such good friends. The ERE administrative staff always provided timely and excellent help. I especially thank Thuy Nguyen, Eiko Rutherford, and Joanna Sun for their extraordinary support.

My officemates in room 137, Jincong, Da, Ruslan, Motonao, and Yifan, made my life at Stanford more colorful. Playing tennis with Da and Jincong became one of my favorite ways to refresh my brain, and they gave me a full understanding of the crucial differences between northern Chinese and Cantonese foods. I took my first short bike trip with Ruslan (Do not cry Ruslan! I will keep in touch). I took my first Tahoe ski trip with Motonao (and he saved me by providing his apartment when I had nowhere to go). Yifan gave me a chance to have hand-made authentic dumplings by using his own Chinese cookware (and he is a great philosopher). Their friendship makes me wonder how I ever got along without them.

I am also greatly thankful to my ERE Korean friends. Hyunki helped me prepare my SOP when I first applied to Stanford. Jieun and Kyungjin, good luck on your defense. Wonjin always made me laugh; thank you for providing me a place to live for a month (I moved 10 times over the last 4.5 years. What a great journey). I am thankful to Timothy for his and his wife Yesul's wonderful cooking and endless emotional support. Good luck on your research.

I was lucky to have two great editors, Jody Bileu and John Acker. Jody helped me with my SOP and in the early parts of my doctoral program, and John helped with the later part of my program, including this dissertation. Tapan once said when he got an edited version, "Now we can talk about science." David also mentioned, "the dissertation is well written and Tapan and you must put a huge effort on it." Thank you Jody and John!

My family and family-in-law in Korea have been constant sources of emotional and financial support. Mom always believed in me, even when I felt too down to believe in myself, while my mother-in-law always gave me more practical advice - eat good food and get some massages (she also sent quite a few wire transfers to help me follow her advice). I am likewise in great debt to my two lovely sisters, Jiwon and Jihae. Whenever something important happened in my families in Korea, Jiwon told me "how it feels" and Jihae told me "what actually happened." Oh! How miserable it would be if I only had one sister! I miss and love my lovely nephew and niece, Siwon and Yejin.

My sister-in-law, Jookyung, gave me great amusement by her endless chitchat, and I love her semi-professional cuisine.

Pursuing a Ph.D. in Stanford was one of the most fantastic experiences of my life, though a Ph.D. was the last thing that I ever imagined doing when I was a child – I wanted to be a carpenter or a cook. This sometimes made my parents embarrassed when I said it in front of their friends. I still think that I could be a decent carpenter or a cook. All the possible misery of a Ph.D. just evaporated whenever I stepped out from my office into the beautiful sunshine and fresh air of Stanford. The dish and Lake Lagunita were the most powerful meditation gurus to help me unload my stress.

Finally, I want to acknowledge the two human beings that I have loved the most: my grandma, Guisoon Gooh, and my better half, Yookyung Lee. According to my grandma, love is binary, not comparative. It is either do or don't, is or isn't. For her, love is somewhat similar to a scientific discovery which only holds true in one's own universe. She loved me in that way. I love Yookyung in the same way that my grandma loved me. Yookyung, I love you and I am sorry because I cannot love you more or less. Because I just cannot. But I will do what I want to do: live a long and healthy life with you, appreciating the most amazing discovery that only you and I can see - the love between us. I love you as I always do – no more, no less.

Contents

- Abstract iv**
- 1 Introduction 25**
 - 1.1 Problems and Motivations 26
 - 1.1.1 Origins of weak connections between subsurface geometry and petrophysical properties in subsurface modeling..... 26
 - 1.1.2 Scale and resolution dependency on subsurface evaluation..... 30
 - 1.1.3 Endeavors to see beyond seismic resolution 31
 - 1.2 Objectives and Scope..... 35
 - 1.3 Dissertation Outline 37
- 2 Linking Geological Uncertainty in Modes of Structural Deformation and Rock Accommodation..... 39**
 - 2.1 Uncertainty about structural deformation 39
 - 2.1.1 Relationships among geometrical, kinematic, and dynamic models..... 40
 - 2.1.2 Sources of uncertainty in structural deformation 47
 - 2.1.3 Why does this matter for reservoir modeling and evaluation?..... 50
 - 2.2 Uncertainty in the mode of rock accommodation..... 52
 - 2.2.1 Distributed versus localized rock accommodation..... 55
 - 2.2.2 Localized accommodation..... 57
 - 2.2.3 Distributed accommodation 58
 - 2.2.4 Vague areas for classification: microcracks in shale, and pervasive cleavage. 60
 - 2.2.5 Factors affecting modes of accommodation..... 61
 - 2.2.6 Factors affecting on distribution pattern and characteristics of crack 66
 - 2.3 Endeavors to link structural deformation and rock properties to forecast reservoir responses..... 70
 - 2.3.1 Geometrical approaches 71
 - 2.3.2 Kinematic and dynamic approaches..... 71
 - 2.3.3 Linkage between structural deformation and rock accommodation..... 72
 - 2.4 Summary 76

3 Reservoir Modeling with Multiple Geological Scenarios on Modes of Structural Deformation, and Accommodation..... 77

3.1	Motivation.....	77
3.1.1	To assess the impact of a parameter, we have to vary it.	79
3.1.2	Deformation changes not only the geometry, but also the internal properties .	80
3.1.3	Well data is precious, but it is one-dimensional.....	83
3.2	Methodology.....	84
3.2.1	Proposed workflow.....	84
3.2.2	Defining scenarios for mode of structural deformation and mode of rock accommodation	87
3.2.3	Structural deformation attributes and a proxy restoration	89
3.2.4	Restoring the hard data and forward deformation of reservoir properties.....	95
3.2.5	In defense of using an inaccurate and simplified pseudo restoration of properties.....	99
3.2.6	Comparing the likelihood of scenarios.....	100
3.3	Application on a 3D synthetic reservoir	102
3.3.1	Synthetic model description	102
3.3.2	Multiple geological scenarios in structural deformation	103
3.3.3	Multiple geological scenarios in rock accommodation	104
3.3.4	Creating reservoir models for each scenario	109
3.3.5	Comparisons.....	112
3.3.6	Discussion	117
3.4	Summary.....	119

4 Modeling Seismic Anisotropy while Honoring Vertical Velocities and Bulk Density with Multiple Sets of Inclusions..... 121

4.1	Rock physics models for multiple geological scenarios.....	121
4.1.1	Rock physics models for isotropic and anisotropic medium without cracks..	122
4.1.2	Rock physics models for isotropic and anisotropic mediums with cracks	125
4.1.3	Comparing Hudson’s and Kachanov’s models with Rathore’s experimental data: the importance of proper model choice with proper implementation.....	134
4.1.4	Problem statement.....	143
4.2	A new rock physics workflow to determine effective stiffness tensors of crack inclusions in an anisotropic medium.....	146
4.2.1	Background idea and requirements of a new model.....	146

4.2.2	A two-step optimization to find equivalent isotropic hosts and crack-like inclusion	148
4.2.3	Different host medium properties for different geological assumptions	156
4.2.4	Cone search method	160
4.3	Summary	163
5	Unconventional Shale Reservoir Modeling with Multiple Geological Scenarios for Deformation of Reservoir Structure and Evolution of Rock Properties: Application on a Marcellus shale gas field	165
5.1	Introduction and Motivations	165
5.1.1	Marcellus shale with unconventional resources	165
5.2	Field and data description	171
5.2.1	Available data	171
5.2.2	General characteristics of the data area	172
5.3	Factors affecting gas productivity in Marcellus play	173
5.3.1	Basin scale factors: Lithofacies of shale and their thickness	173
5.3.2	Field scale factor: Joint sets and their importance in Marcellus play	175
5.4	Problem statements of the field	178
5.4.1	Higher well connectivity on a structurally gentle area	179
5.4.2	Water influx without water injection	180
5.4.3	Existence of pre-existing sub-seismic geological features and their orientation	181
5.4.4	Uncertainty on geometrical interpretation	184
5.4.5	Consequences for further appraisal and developments	185
5.5	Defining sources of geological uncertainty	186
5.5.1	Defining sources of structural deformation uncertainty	186
5.5.2	Defining sources of rock accommodation uncertainty	193
5.5.3	Effects of hydrocarbon generation	200
5.5.4	Non-deformational factors affecting the accommodation style of shale: saturation and burial history	201
5.6	The effect of interaction among different formations	202
5.6.1	Structural deformation and rock accommodation for adjacent formations: the necessity of expanding the boundary of investigation	203
5.6.2	Contrasting flexural rigidity among adjacent stiff formations	208

5.6.3	Differences between interactions among adjacent formations: joints from shale vs. joints from non-shale formations.....	209
5.7	Applying the proposed framework to the Marcellus data.....	211
5.7.1	Facies and rock property interpretation along well-A.....	212
5.7.2	Variogram modeling for property generation.....	215
5.7.3	Modeling alternative structural models with different structural deformation modes	216
5.7.4	Defining rock accommodation styles	217
5.7.5	Modeling background shale anisotropy.....	219
5.7.6	Reconstruction of equivalent isotropic medium along the well under different rock accommodation scenario.....	222
5.7.7	Petrophysical property modeling for each scenario	227
5.7.8	Comparisons and discussion.....	228
5.8	Expansion to 3D model.....	234
5.8.1	3D structural model of Tully duplex scenario	234
5.8.2	Discussion	239
5.9	Summary	243
6	Conclusions and Future Works.....	245
7	Bibliography	251

List of Tables

Table 2-1: Rutter's classification of modes of rock failure (Rutter, 1986).....	57
Table 2-2: Factors affecting mode of accommodation - distributed versus localized. We can categorize the effect as promoting the role of pores as internal flaws versus cracks and mineral phase. References marked with “*” compiled relations from previous experiments. Other references are independent experiments.	62
Table 2-3: Failure criteria. (Jaeger et al., 2007, Pollard and Fletcher, 2005, Mogi, 1971).....	65
Table 4-1: Properties of the host sandstone and geometry of the artificial cracks. The velocity measurement on crack-free host sandstone for both the dry and water-filled case are in the right column.	135
Table 4-2: Measurements and results of Sarout’s experiment on wet shale	150
Table 4-3: Properties and measurements of Sarout's wet shale with vertical cracks .	156
Table 4-4: Assumptions about subsurface and corresponding optimization results of the host rock properties, and Thomsen's parameters on a final effective medium..	157
Table 5-1: Lithofacies and average properties of each formation (CMS – calcareous mudstone, POM – pyritic organic mudstone, MS – mudstone, COM – calcareous organic mudstone).	213
Table 5-2: Variogram ranges for lithofacies and properties.....	215
Table 5-3: coefficient of 2 nd order polynomial linking porosity to aspect ratio, crack-like pores, and the elastic moduli of equivalent isotropic media. Three numbers correspond to a,b, and c of $ax^2 + bx + c$	221
Table 5-4: Comparison by Rpp0.	228
Table 5-5: Comparison by dVfVs.	228
Table 5-6: Comparison by AzimVfast.	229
Table 5-7: Comparison by multiple of Rpp0 – dVfVs - AzimVfast.	229
Table 5-8: Comparison by multiple of Rpp0 – dVfVs – AzimVfast (likelihood).....	229
Table 5-9: Comparison volume-weighted SSE by structural deformation scenarios. SSEs from 14 accommodation scenarios sharing the same structural deformation	

scenario are averaged and normalized by the minimum value among four deformational scenarios..... 231

Table 5-10: Comparison of likelihood by structural deformation scenarios. Likelihood probabilities from 14 accommodation scenarios sharing the same structural deformation scenario are averaged and normalized by the minimum value among four deformational scenarios. 231

Table 5-11: Comparison of volume-weighted SSE by accommodation scenarios. Results from different assumptions on shale anisotropy are combined for comparison focusing on the effects of accommodational style only. 231

Table 5-12: Comparison of likelihood probability by accommodation scenarios. Results from different assumptions on shale anisotropy are combined for comparison focusing on the effects of accommodational style only. Likelihood probability is normalized by the maximum value. 231

Table 5-13: comparison of SSE of near-offset seismic reflectivity (R_{pp0}), differences between fastest and slowest P-wave velocity (dV_fVs), and azimuth of fastest P-wave velocity ($AzimV_{fast}$) by different accommodation scenarios. 239

Table 5-14: comparison of likelihood probability of near-offset seismic reflectivity (R_{pp0}), differences between fastest and slowest P-wave velocity (dV_fVs), and azimuth of fastest P-wave velocity ($AzimV_{fast}$) by different accommodation scenarios. 239

List of Figures

Figure 1.1: Advances on static and dynamic reservoir evaluations from 1930' to present	27
Figure 1.2: Developments and improvements in reservoir modeling accuracy	29
Figure 1.3: Example of an MPS algorithm.....	32
Figure 1.4: Example of the usefulness of a rock physics model	33
Figure 1.5: Developments in structural interpretations and visualizations	34
Figure 2-1: A picture from outcrop (a) and geometrical model (b)	41
Figure 2-2: Suppe's (1983) fault-bend folding interpretation using his kink band model explains thickness variations of Chinshui shale between two adjacent wells.	42
Figure 2-3: Schematic explanation of the principal of balanced restoration by Dahlstrom (1969).....	43
Figure 2-4: Maerten and Maerten's (2006) geomechanically based restoration applied to McClay's sandbox experiments (1990) to mimic an extensional fault syste	44
Figure 2-5: Drawing by Cloos (1936), reprinted in Blandes and Tanner (2014). Cartoon 4 is a simplified geological sketch containing geological features such as reverse faults, folds, horizons, lobes, and canyons (a geometrical model of present conditions).....	46
Figure 2-6: Alternative modes of kinematic models from the identical initial geometry	48
Figure 2-7: Dahstrom's (1969) example of equally plausible interpretations from the same observation.....	49
Figure 2-8: An example of the usefulness of restoration analysis (Novoa et al., 2000).	51
Figure 2-9: Comparison between a folded horizon in a geometrical model and internal features on a fold from a lab experiment	52
Figure 2-10: Mode of rock failure by mode of localized deformation, and form of deformation localization (Aydin et al., 2006)......	58
Figure 2-11: Ductile deformation of rock under Paterson and Wong's (2005) classification.	59
Figure 2-12: Fabric developments in vertical cleavage (left) and shale (right). Vertical fabric in cleavage was developed while the maximum compressional direction was horizontal. In shale, horizontal fabric is most common because the vertical stress is	

usually significant. The left figure is from Powell (1979), and the right figure is from Vernik and Landis (1996). 60

Figure 2-13: Effect of velocity exponents on crack propagation 68

Figure 2-14: Inferring paleostress from natural fracture observation..... 69

Figure 2-15: Geological observation from outcrops of folds and fractures (Hanks et al., 2004) 73

Figure 2-16: Shear deformation on shale develops permeability anisotropy in a way to promote horizontal flow..... 75

Figure 3.1: A typical geomodeling process 78

Figure 3.2: Schematic cartoons of a thought experiment to test the “copy & paste” convention..... 81

Figure 3.3: Comparison of a well trajectory across a normal fault in a vertical section 82

Figure 3.4: A schematic diagram of the three proposed components. 86

Figure 3.5: Examples of geological explanations for having different fracture sets on a fold structure. Paths A and B go through different burial histories, and thus have different stress history and generate different fracture sets (Hanks et al., 2004)..... 88

Figure 3.6: Displacement vectors between a present structural grid and a past depositional grid..... 89

Figure 3.7: Typical geometrical distortions caused by not considering the structural deformation of the reservoir..... 93

Figure 3.8: Pictorial demonstration of “flexural slip” forward deformation and UVT coordinate transformation by Mallet (2004). 94

Figure 3.9: Schematic explanation of porosity changes by dilatation..... 96

Figure 3.10: Example of comparison between fracture densities and deformation strain magnitude..... 98

Figure 3.11: 2D projection of 3D models using MDS 101

Figure 3.12: Structural geometry of the synthetic reservoir. 103

Figure 3.13: Reservoir structures colored by dilation from deformational strain. Left – deformation scenario A. Right – deformation scenario B 104

Figure 3.14: Geological scenarios for reservoir property evolution. In the synthetic case, a sequence of a diagenesis event and geological deformation are considered. 105

Figure 3.15: Petrophysical property generation under the localized accommodation scenario	106
Figure 3.16: Workflow for generating petrophysical properties under the distributed accommodation scenarios.	107
Figure 3.17: Reservoir property evolution of the true case. Syn-depositional porosity is populated by unconditional SGSim. As diagenesis occurred, porosity reduction by cementation was applied. As deformation took place, fractures were generated by following fracture intensity from the principal stress and fracture normals, from the most tensile principal strain direction. An explicit discrete fracture network was only populated in the initial production area. Flow-related reservoir properties are modeled as a single medium with a summation of matrix and fracture properties, since the matrix permeability is relatively high compared to the fracture permeability.	108
Figure 3.18: Calculating the effective medium with fractures and cementing, using the effective medium model. Hudson’s model is used for effective stiffness tensor calculation	109
Figure 3.19: Multiple scenarios of structural deformation and reservoir property evolution	110
Figure 3.20: Porosity modeling using the proposed framework under scenario 2. Porosity along the wells have larger values by un-cementing and un-deforming.	111
Figure 3.21: Porosity modeling from the conventional workflow.	111
Figure 3.22: One realization and its reservoir responses, out of 20 realizations from each scenario.	113
Figure 3.23: MDS plot by distance of porosity (left) and distance of seismic attribute (right)	114
Figure 3.24: Flow responses of all realizations from different scenarios in the proposed and conventional workflows. Left – Cumulative oil production, Right – Cumulative water production.	115
Figure 3.25: MDS plot using distance of the total oil production curve and the water cut curve.	116
Figure 3.26: Situations when the proposed framework would be beneficial vs. less beneficial.	118
Figure 4.1: Configuration of the experiment of Rathore et al., 1994. A series of disc planes of sandstone were assembled after the crack-voids were carved out. The crack density of the artificial crack was controlled to be 0.1.....	134
Figure 4.2: Rathore and colleagues’ experiments on dry sample.	136

Figure 4.3: Rathore and colleagues’ experiments on a wet sample 137

Figure 4.4: Comparison of implementation A and implementation B with the experiment data. 138

Figure 4.5: Comparisons of computation results from other options. Red solid – Hudson’s model with 2nd order correction adding wet inclusion in wet matrix; blue solid – Hudson’s model with 2nd order correction adding dry crack in dry matrix, then fluid substitution applied; Blue dash - 2nd order correction by Cheng; green cross - Kachanov model; cyan star - dry Kachanov model with fluid substitution. 139

Figure 4.6: Schematic comparison between Hudson's and Kachanov's models. Both models make the adjustment linearly proportional to the crack abundance, which is expressed by crack density. In a way, Hudson’s model subtracts stiffness while Kachanov’s adds compliance. 140

Figure 4.7: Comparison among Hudson, Kachanov, and Hudson by Cheng 142

Figure 4.8: Schematic figure of an example when data from the well can miss abundant subsurface features. 144

Figure 4.9: Schematic figure of the proposed model. 147

Figure 4.10: Flow charts of the inner and outer optimization loops. The inner loop aims to find the optimal isotropic host medium, while the outer loop aims to find the optimal shape of the crack-like pores. 149

Figure 4.11: A decomposed isotropic medium and crack-like pores. Equivalent stiffness tensors are preserving the C11, C33, and C44 components. 151

Figure 4.12: Comparison of true vs. calculated velocity using the proposed model.. 152

Figure 4.13: Effective stiffness tensors: left - when the background medium was modeled as VTI; right - when the background medium was modeled as isotropic medium. 154

Figure 4.14: P-wave velocity with angle of incidence from vertical to dipping toward axis-1. Red solid-crack on anisotropic medium; blue dash-crack on isotropic medium. 155

Figure 4.15: Thought experiments on extrapolation of surface properties. By having sandstone over the Sarout shale with vertical cracks, we have negative reflectivity on the right-hand region. The left-hand region has no drilling has nearly zero reflectivity. 159

Figure 4.16: Stiffness tensor after rotation gives faster vertical velocity. 159

Figure 4-17: Cartoon example of a cone searching method to find the azimuth of fastest velocity.. 162

Figure 5.1: Natural gas production in the U.S. by region, from 2012 to 2015. Color-coded regions are marked on the U.S. map	166
Figure 5.2: Generalized stratigraphy of Middle Devonian formations in the Appalachian Basin	167
Figure 5.3: Cartoon depicting the paleogeography of the Middle Devonian Acadian foreland basin.....	168
Figure 5.4: Iron fertilization by dust storms near the Sahara desert.....	169
Figure 5.5: Trend map of Marcellus shale play. The blue solid lines are defined folds, with black dashes for faults. The basin-wide trends of folds and faults are striking NE-SW.....	170
Figure 5.6: 3D PSDM seismic data and the two main exploration well locations. Well-A is located toward the basin while Well-B is located toward the Appalachian thrust belt. Thus, the Well-A region is seismically gentle, while the Well-B region has more complex seismic responses.....	172
Figure 5.7: Volume comparison of the required amount of source rock to produce one barrel of oil.....	174
Figure 5.8: Orientations of J1 and J2 sets of joints in Marcellus shale (Engelder et al., 2009). The strike of J1 is parallel with the current maximum compressional stress, NE-SW (SHmax), and the strike of J2 is perpendicular with the current maximum compressional stress.....	177
Figure 5.9: Photo of outcrop of J1 and J2 joint sets (Engelder et al., 2009). Both sets are vertical and have nearly perfect planarity.	178
Figure 5.10: Horizon tops of a formation above Marcellus shale (left) and a formation below Marcellus shale (right). The Well-A region is seismically gentle, while the Well-B region has geometrical complexity from seismic data.....	179
Figure 5.11: Micro-seismicity during hydraulic fracturing (left) and a vertical section of the seismic inline along Well-A.	180
Figure 5.12: Seismic crossline along Well-B. Unlike Well-A, the Well-B region has more complex geometry around the target formation from seismic responses.	181
Figure 5.13: Core sections selected from cores from Well-A	182
Figure 5.14: Section slides of cores from Mahantango and Lower Marcellus.....	183
Figure 5.15: Stereonet (a) and Rossette plot of the strikes of drilling-induced cracks	183

Figure 5.16: Repeated sections near the target horizons along a seismic crossline including Well-A. The type and origin of the feature is unclear and it leads to uncertainty in structural interpretation. 185

Figure 5.17: Duplex models as a branch of the thrust system. a) Imbricate fans and duplexes (Boyer and Elliott, 1982). b) Conceptual cartoon of duplex system (from data donor). c) Cartoon of fault-bend fold (FBF) (2001, Thomas). An FBF can be understood as the smallest component to compose a duplex that may have a series of FBFs inside. 187

Figure 5.18: Alternative interpretation of abrupt thickening by a band of reef carbonate 188

Figure 5.19: Seismic pull-up below reef platform..... 189

Figure 5.20: Wells with localized thickness anomalies. Section AA’ and BB’ are wells from Philadelphia and CC’ is from West Virginia 190

Figure 5.21: Satellite image of well sections with thickness anomalies 191

Figure 5.22: Duplex of Silurian-Ordovician formation observed from an outcrop section in West Virginia (Ferrill and Dunne, 1987) 192

Figure 5.23: Joint sets in Marcellus shale and trends of their orientation 196

Figure 5.24: Aydin’s (2014) model to explain J1 to J3 as consequences of tectonic loadings. Tectonic loading is parallel to these vertical sections. J2 was generated from compressional loading by having joint surfaces with surface normals perpendicular to the loading. J1 (2nd-a) was generated when structural deformation occurred, with J3 (2nd-b) as a splay set. 197

Figure 5.25: A kinematic model of the sub-seismic features of the Marcellus shale play in Wilkins et al. (2014). The model focuses on detachment faults near stiffer carbonate formations as the main drivers of forming joints and stylolite..... 198

Figure 5.26: Subcritical crack index of U.S. onshore unconventional shale play (Gale et al., 2014). 199

Figure 5.27: Blind duplex and cover deformation observed in an Ordovician formation in the Appalachian Basin (Ferrill and Dunne, 1989), with a seismic section of cross line along Well-A of the given data set. 204

Figure 5.28: Cleavage duplexes accommodate up to 40% of LPS by forming vertical cleavage and inter-layer cleavage (figure modified from Nickelsen, 1986). Vertical lines with orange colors represent vertical cleavage development during LPS. The red tilted line is a reverse fault component of interlayer cleavage. 205

Figure 5.29: Sketches of cleavage and cleavage duplex development under LPS (Nickelsen, 1986). Left (a): vertical cleavage development from LPS. Horizontal

foliation prior to LPS is masked out, as cleavage is development during LPS. Right (b): Excessive LPS on top of pre-developed cleavage deformation ignites to develop thrusting by forming an interlayer blind duplex.....	206
Figure 5.30: A combination of structural deformations and rock accommodations considering adjacent formations to Marcellus shale. In these specific combinations, a duplex of stiff formation above the Marcellus formation in the central part absorbs LPS.	207
Figure 5.31: Young's modulus along Well-A. Red boxes are carbonate formations and blue boxes are shale formations. The figure on the right side shows the relative thickness and Young's modulus of the Onondaga and Tully carbonate formations.	209
Figure 5.32: Vertical fracture connectivity to overlaying shale formations (Ink et al., 2015).	211
Figure 5.33: Defined lithofacies along the well from well log interpretation, core analysis, and mud log interpretation (left), up-scaled lithofacies in property grids (right).	213
Figure 5.34: Modeling grids color coded by populated lithofacies (left) and formation (right). Only the Marcellus formations are shown.	216
Figure 5.35: Structural models of four different scenarios on modes of structural deformation.	216
Figure 5.36: Vertical cleavage development during the LPS resulting in both a perpendicular and stiffer orientation.	219
Figure 5.37: Relations among equivalent bulk and shear modulus, and the aspect ratio, crack density to porosity of crack-like pores color-coded by formations. ...	220
Figure 5.38: Reproduction of velocity and P-wave anisotropy (Thomsen's epsilon). Left figure shows calculated P-wave anisotropy by combining crack-like pores with the equivalent isotropic solid phase using Hudson's model and Cheng's second order correction terms.	221
Figure 5.39: Left – comparison of assumptions on background shale. By having stiffer solid isotropic media, resultant vertical stiffness will be preserved with one more crack inclusion – crack-like pores. Right – different accommodation styles yield different bulk modulus profiles.....	224
Figure 5.40: Trend among porosity and equivalent bulk and shear moduli of isotropic background media.	226

Figure 5.41: Seismic amplitude from true seismic survey (top). Synthesized amplitude in field scale from a realization on the scenario of Tully duplex with blind duplex (bottom)..... 233

Figure 5.42: Indication of blind duplex from thickness variation and weakness of seismic responses on Onondaga formation..... 234

Figure 5.43: Seismic section with Mahantango horizon of localized thickening..... 235

Figure 5.44: Horizon picks of Rhinestreet shale formation 236

Figure 5.45: Optimized surfaces and partial manual picks for Tully limestone horizons..... 236

Figure 5.46: Structural model of Tully duplex model with surface horizons. 237

Figure 5.47: Duplex features captured in the structural model. The left figure is the surface top of a Mahantango formation and the right figure is the repeating horizon by duplex..... 238

Figure 5.48: Property grid colored by formation index..... 238

Figure 5.49: Blind duplex indication from normalized Onondaga thickness and normalized weakness of seismic amplitude. All of them are scaled from zero to one. 241

Figure 5.50: Azimuthal variation of fastest P-wave velocity visualized on Onondaga formation..... 241

Figure 5.51: Comparison of blind duplex indication and azimuth of fastest P-wave velocity in the Well-A and Well-B regions. 242

Chapter 1

1 Introduction

Understanding and assessing the heterogeneity and anisotropy of reservoir properties is one of the most important tasks in reservoir evaluation. As the oil and gas industry explores and develops deeper targets and unconventional resources, difficulties in assessing reservoirs are giving rise to greater uncertainty as to reservoir response and reservoir value. The scarcity and limited resolution of subsurface data make it challenging to define three critical components: the structural geometry of target subsurface formations, the spatial distributions of petrophysical properties of rocks and sub-resolution geological features such as fractures and deformation bands, and the underlying geological models explaining the relation between the first two items.

Spatial uncertainty and structural uncertainty are two of the most important aspects for modeling uncertainty in subsurface problems (Caers, 2011). The uncertainty of depositional conditions, the spatial distribution of lithofacies, and their impact on reservoir responses have been studied by applying multiple scenarios that feature multiple training images (Park et al., 2013; Jeong, 2014; Strebelle and Journel, 2001). By using different training images, these studies attempted to capture different geological scenarios in the depositional environments. For the structural uncertainty, there are many studies of structural uncertainty to utilize structural attributes on property estimations. However, previous research used a single structural interpretation and single realization of the abundance and orientations of fracture sets, without considering alternative models for both the mechanism of structural deformation and the linkage among structural attributes and rock properties (Lohr et al., 2008; Paul et al., 2009). Thus, the geological uncertainty by having alternative structural interpretations and their effects on reservoir properties have not been investigated in a reservoir modeling context. As previous works on scenario uncertainties for depositional conditions

revealed, reservoir uncertainty can be largely underestimated if bounded by a single geological interpretation when alternatives are exist.

To fill this gap, the goal of this dissertation is to investigate geological uncertainties on structural geometry, their deformational mechanisms, and their interaction with reservoir properties in the subsurface evaluation process. Specific research problems and motivations are described below.

1.1 Problems and Motivations

1.1.1 Origins of weak connections between subsurface geometry and petrophysical properties in subsurface modeling

Attempts to correlate sub-seismic fractures and joints with structural deformation of reservoir geometry utilizing restoration/forward deformation analysis started recently (Paul et al., 2009; Lohr et al., 2008). Before that, many research studies linking reservoir structures to fractures and joints were limited to purely geometrical approaches (Picou and Utzmann, 1962; Bergbauer et al., 2003).

Conventionally, we conduct a geomodeling process in the following sequence: (1) seismic and geological interpretation of reservoir structure, (2) creating reservoir geometry, (3) lithofacies modeling, (4) petrophysical modeling, (5) seismic or dynamic forward simulation, and (6) comparison with observation (Castro et al., 2005). It is intriguing that we conduct the geometrical modeling and petrophysical modeling independently, without considering any plausible correlations. If the structure is bent, it is a very natural consequence to anticipate perturbation on the curved geometry, such as compaction, stress concentration, or mechanical failure of the rocks. By treating the geometrical modeling and property modeling independently, we implicitly assume either no geological correlations among them or a homogeneity of the correlations between structural geometry and reservoir properties within the modeling boundary. It is worthwhile to consider geomodeling practice retrospectively, from the 1930s to the present time, to see how and why it has developed.

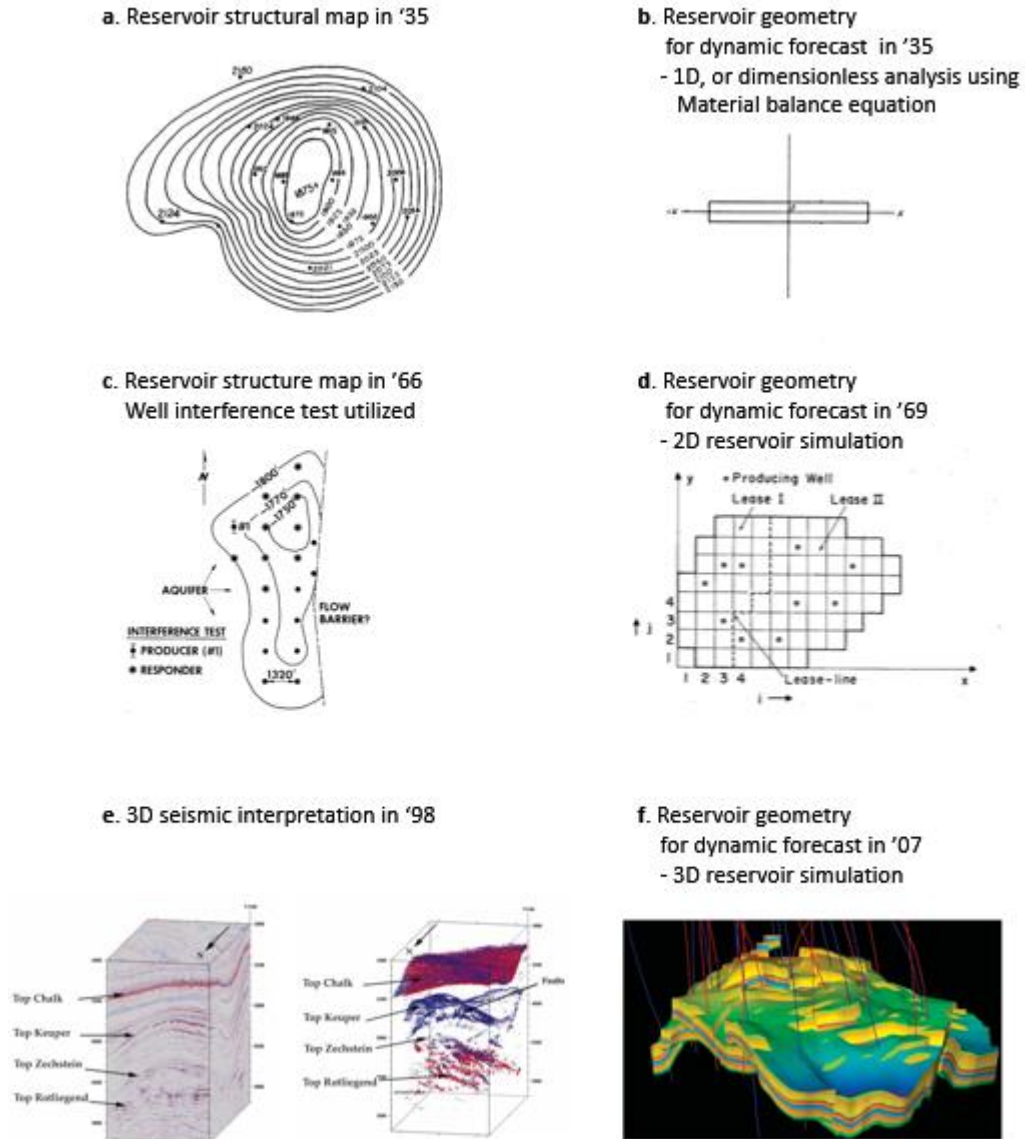


Figure 1.1: Advances on static and dynamic reservoir evaluations from 1930' to present. Left column – a, c, and e, correspond to static evaluation – defining subsurface geometry of reservoir structure. Right column – b, d, and f depicts geometrical representations of reservoir structures for dynamic forecast (flow simulation). Figure **a** – Reservoir structures were constructed from well picks. A seismic survey was not standard at that time (Smiser and Wintermann., 1935). Figure **b** – In 1935, this material balance equation was introduced, and reservoir engineers started to provide time-dependent reservoir responses in analytic form while ignoring any spatial heterogeneity (Schilthuis and Hurst, 1935). Figure **c** – a well interference test was used to infer reservoir boundaries (Jahns, 1966). Figure **d** – the availability of computers allowed discretizing the material balance equation into higher resolution and physical dimensions. Modern reservoir simulation was applied to predict spatially varying reservoir production by including heterogeneous reservoir properties (Coats, 1969). Figure **e** – structural interpretation conducted in 3D

seismic cubes (Dorn, 1998). Figure *f* – a complex reservoir model that has tens of faults and compartmentalization (Jolley et al., 2007).

Figure 1.1 depicts the resolutions and levels of detail in reservoir evaluation in from the mid-30s to present. Since digital seismic imaging had not been invented, subsurface structures were constructed based on the contours of well picks and surface geometries in 30's (Figure **a**; (Smiser and Wintermann., 1935)). Mathematical modeling of dynamic responses was conducted in a dimensionless manner (Figure **b**), only focusing on overall time-dependent behavior, and using a material balance equation due to the lack of ability for modeling complex geometry—on top of the computational limitations before computers were available (Schilthuis and Hurst, 1935). Figure 1.1c and **d** show developments in reservoir modeling thanks to the development of well testing analysis (Figure **c**; (Jahns, 1966)) and numerical reservoir flow simulation (Figure **d**; (Coats, 1969)). Reservoir flow simulation became available due to advances in computer science. Since digital seismic image processing was not available until the late 60s, resolution of seismic data was limited to defining major horizons and structural shapes. Refining sub-resolution boundary of a reservoir were heavily relying on well testing analysis. For reservoir flow simulation, the objectives were to find the best lease block to acquire or the best candidates to drill, considering the sweep from pre-existing producer and injector wells. Defining exact reservoir geometry in the simulation grid was irrelevant at that point because we did not have relatively detailed geometry to match from the beginning. Indeed, exact geometry was far less important than having proper methods to assign spatially varying properties across simulation grids – geostatistics – at that time.

Modern geostatistics were not born until 1962 (Matheron, 1962). In Coat's (1969) example of the usage of numerical flow simulation to find the best new lease acreage, the block-by-block transmissibility, *kh*, was “estimated” from 41 wells – without explaining how – and Coat claimed that the *kh* distribution is “fairly well known” (p. 1393). This makes sense because, in Coat's example, each grid block represents a lease acreage. The resolution of the structural model was more or less similar with that in the 30s, and the simulation grid block was as coarse as the lease acreage. This

demonstrates that modern geostatistics had not widely penetrated the field, even within geoscience communities, in the late 60s. Figure 1.1e and f depict reservoir modeling practices after 3D seismic images became industry standards. Compared to the structural geometry resolution of reservoir models from the 30s and 60s, contemporary resolutions are incomparably detailed. Indeed, the structural shapes from contours were almost irrelevant to production forecasting from either dimensionless material balance approaches, or from 2D numerical reservoir simulations with simplifications of the reservoir into almost flat disk plates. The necessity to consider any plausible relations between structural geometry and reservoir properties in the subsurface structure can be meaningful only when a certain degree of resolution on structural geometry and detailed modeling becomes available.

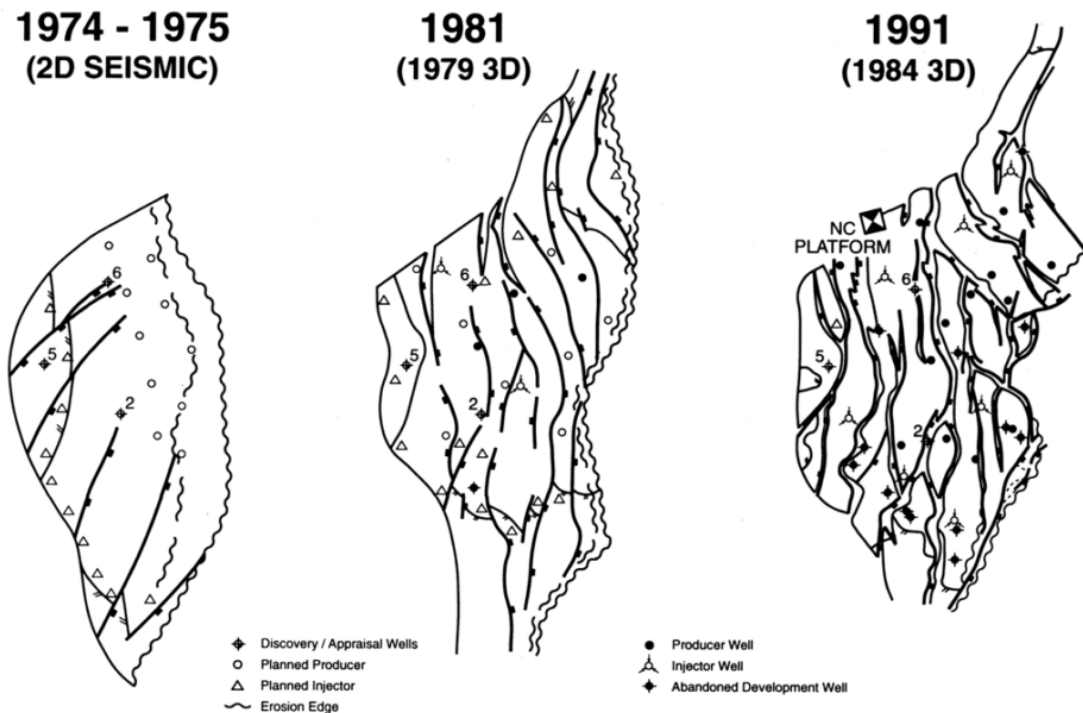


Figure 1.2: Developments and improvements in reservoir modeling accuracy (Demyttenaere et al., 1993). The same reservoir was re-evaluated using different vintages of seismic data. With a 3D seismic image, the fault interpretations became much finer than the interpretation of the 2D image. With a finer and more advanced 3D image, structural interpretation became even finer. For reservoir modeling in the 30s and 60s, when even 2D images were not available, the structural interpretation would not be that meaningful, except to give the general contours of the simplified geometry of the simulation grids.

Figure 1.2 depicts structural interpretations on the same reservoir using seismic images from different vintages (Demyttenaere et al., 1993). With 2D data, the interpretation of faults underestimated the number of faults and the complexity of the reservoir structure. With more advanced 3D seismic images, interpretation of faults and horizons with the reservoir boundary are even become finer than the older 3D vintage. Numerical reservoir simulations in the 60s and 70s were based on interpretations like the leftmost image, or even simpler versions. Thus, it is more logical to consider these two parts – geological structural interpretation and numerical reservoir flow simulation – almost as two independent evaluation tasks. This example offers a good way to explain why reservoir evaluation processes are so disjointed among the modeling steps. Indeed, the research question of this dissertation would be pointless in the 1960s, when the purpose of geometrical subsurface models was merely to capture relative horizontal distances and vertical depths as input parameters for flow simulations. However, now we can conduct geometrical interpretations with a higher resolution that captures the details of structural shapes in greater detail, and the resolution of flow simulations is not constrained by numerical capability but by the resolutions of the property we can define.

1.1.2 Scale and resolution dependency on subsurface evaluation

As computational capacity increased, there is a tendency to make the simulation boundary larger, and the grid size finer. Before we move on, it is meaningful to ask ourselves why we want a geomodel at a finer and even finer scale. This can be explained as a typical change of support problem (COSP) (Isaaks and Srivastava, 1989). A COSP involves a discrepancy between the observation and estimation we made, based on specific observation resolution and the actual scale/resolution when it occurs (Gelfand et al., 2001).

Let us assume that current technology requires having a minimum concentration of x percent of mineral A in a feeder volume of bulk soil in a concentration process to make mineral A marketable. If the feeder soils are excavated and tested for quality by a dump truck capacity, evaluating a mining site by measuring the concentrations in a smaller volume than the capacity of a dump truck will lead to an overestimation of the

valuation. If we have a sorting technology finer than the conventional volume of evolution, we can make a profit by the differences of underestimated values of the mining sites and the value we can get from a finer sorting. Here the conventional COSP includes human-controlled, or more specifically process-controlled, factors. On top of that, it is a static problem.

However, a COSP in subsurface responses is different in that we can only control the resolution of the evaluation, not the natural process. Moreover, it is a dynamic process. If we set a resolution for discretization, we always miss the sub-resolution heterogeneity of dynamic responses. This was one of the biggest motivations to discretize a dimensionless material balance equation into the physical and multi-dimensional domains, to estimate leftover oil-bearing regions among producing wells (Aziz and Settari, 1979). Thus, it is legitimate to question the endeavors to model at a finer and finer scale, as it might be a false precision: the global constraints such as aquifer strength and compartmentalization would still be more impacting parameters on the overall valuation of the reservoirs.

However, with modern developments in secondary and tertiary enhanced recovery, together with hydrofracturing technology, we can actually perturb the global parameters of the subsets of reservoirs. If we can model and simulate a finer scale in a realistic way, we can increase the value of the reservoir. From the COSP perspective, finer is better in geomodeling. But here's the catch: do we know the fine scale properties?

1.1.3 Endeavors to see beyond seismic resolution

Digital 3D seismic image provides geoscientists with a geological “Hubble” telescope to see the subsurface (Cartwright and Huuse, 2005). With increased computational powers, geomodeling with finer gridblock resolution becomes available. Thus, modeling subsurface properties beyond seismic resolution becomes one of the utmost challenges in E&P projects.

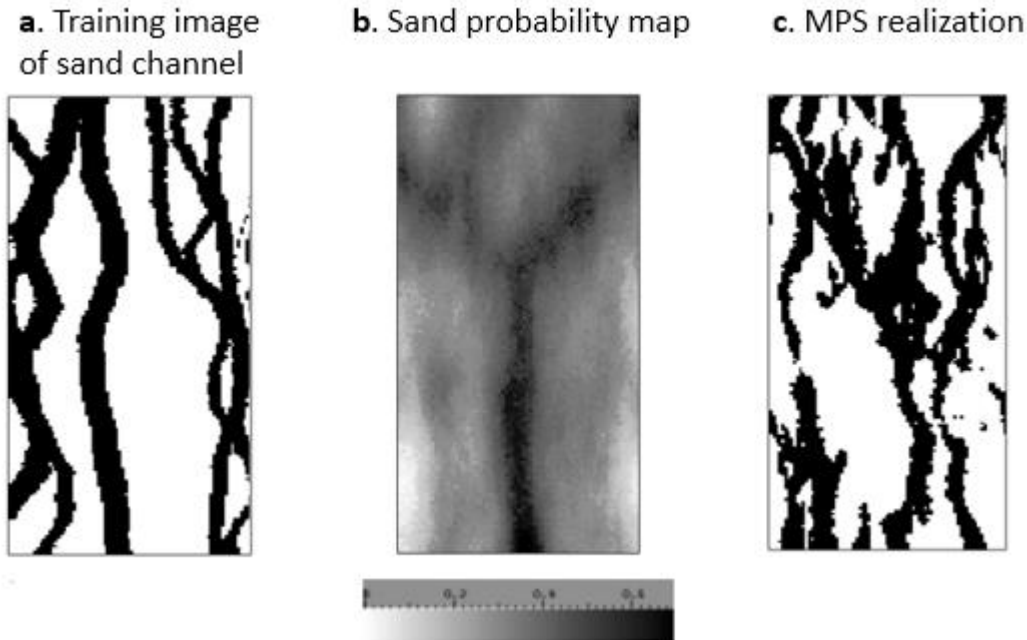


Figure 1.3: Example of an MPS algorithm (Strebelle and Journel, 2001). Figure *a* – training image that represents a spatial pattern of a categorical geobody. In this case, it is channelized sand. Figure *b* – sand probability map. Figure *c* – MPS simulation result. The realization has sand channels on a high sand probability location. It also tries to reproduce the shape of the training image.

Multiple-point simulation algorithms (MPS) provided a breakthrough in geostatistics by allowing users to reproduce the “shapes” of geological features – sand channel bodies, lobes, and coral reefs – while honoring conditioning data along the wells (Strebelle and Journel, 2001). A “training image” – a conceptual visual representation of spatial patterns in the geometry of a depositional geobody or lithofacies – provides a vehicle to quantitatively transfer geological knowledge of depositional environments and the geometrical characteristics of lithofacies into geostatistical modeling (Figure 1.3a). Figure 1.3c is a realization using the MPS algorithm. It honors the target proportion, Figure 1.6b, while trying to reproduce the spatial patterns from the training image.

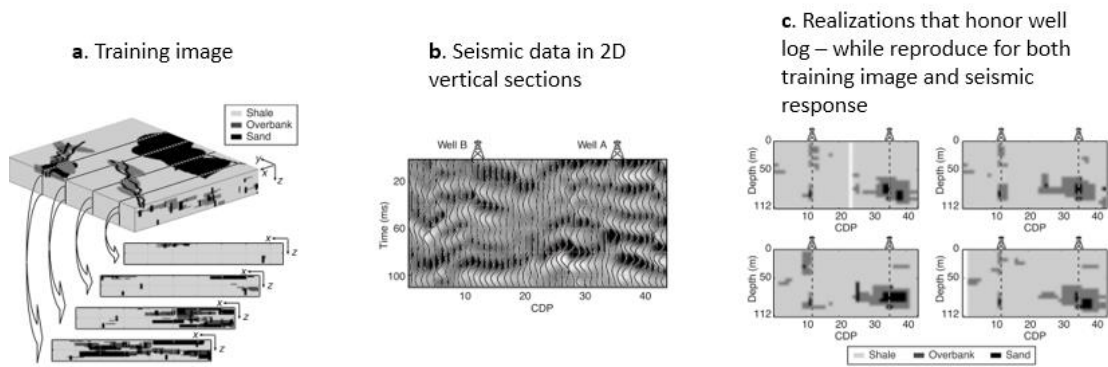


Figure 1.4: Example of the usefulness of a rock physics model (González et al., 2008). Rock physics models allow us to estimate elastic properties once lithology and petrophysical properties are populated. With using the MPS algorithm (1.7a), we can compare the synthetic seismic response with the actual data (1.7b). The results (1.7c) honor the underlying assumptions on the spatial distribution of facies – from the training image – and are also compatible with actual seismic data.

Rock physics models have been recognized since the late 60s as powerful tools to link geophysical observations and components of rock – pore, mineral, cements, fluid, the way they are arranged, pore pressure, and confining stress (Nur and Simmons, 1969). With their capability to synthesize “what-if” seismic responses, rock physics models were used as guiding tools to infer subsurface heterogeneity in quantitative ways for example, (González et al., 2008; Mukerji et al., 2001; Mukerji et al., 1995), amongst others. By comparing the what-if seismic response with the actual seismic data, we can select more likely realizations. (Figure 1.4).

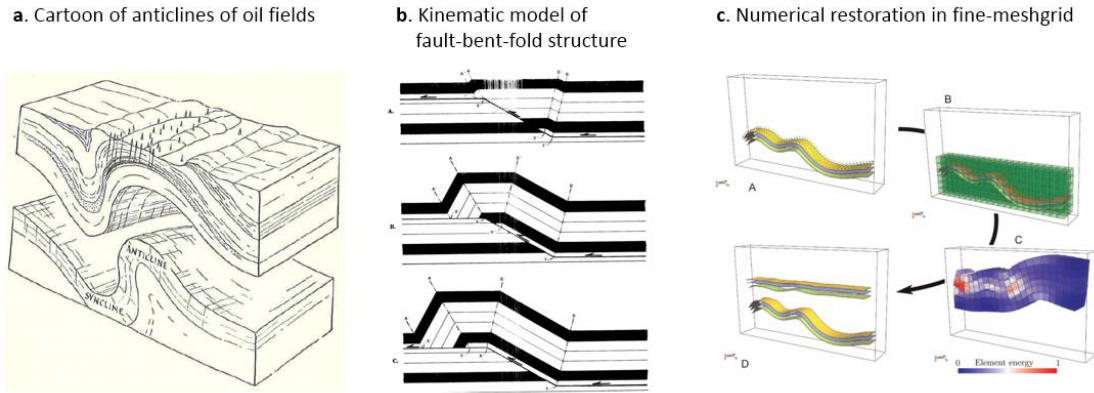


Figure 1.5: Developments in structural interpretations and visualizations. Figure *a* - H. Cloos' sketch of an oil bearing anticline drawn before 1914 (Cloos, 1947). Figure *b* – a kinematic model of fault-bent-fold structure (Suppe, 1983). Figure *c* – numerical computation and visualization allow geologists to conduct restoration of more complex or finely defined geometry (Laurent et al., 2015).

The emergence of quantitative descriptions of geometrical deformation of subsurface structures also hugely advanced between the late 1960s and the 2000s (Dahlstrom, 1969; Maerten et al., 2014; Brandes and Tanner, 2014). Figure 1.5a is a geologist's sketch of an oil field in Java, Indonesia before 1914 (Cloos, 1953). The subsurface geometry was reconstructed purely by the observer's educated imagination. However, like in Figure 1.1a, when conditioning the subsurface geometry quantitatively with limited observations, the structural map ironically became less informative. This could originate from the lack of a transfer algorithm to convert geologists' qualitative models into quantitative forms, on top of the limited data from which to infer the subsurface geometry. Starting in the late 60s, kinematic restoration algorithms were introduced to link the current structural geometry to more appropriate stratigraphy (Figure 1.5b) (Dahlstrom, 1969; Suppe, 1983). With seismic images and computational aids on restoration/deformation analysis, geologists can conduct structural analysis in finer resolution, not only for the present geometry but also for the kinematic or mechanical analysis involved during structural evolution (Figure 1.5c) (Laurent et al., 2015).

Indeed, very recent geoscientific developments and achievements provide relatively enough data for geologists to reconstruct the present subsurface geometry,

reconstruct the likely depositional geometry at a fine scale, populate facies while honoring spatial distribution on depositional conditions, and create petrophysical properties under different geological conditions. Now, the resolution of the data, developments for converting qualitative geological knowledge into quantitative models, and developments in geostatistics and rock physics have narrowed the huge gaps among the geometry of the subsurface structure, geometry for flow responses, and reservoir properties in the models.

Besides the existence of hydrocarbon, lithofacies and the existence of flow hindering/enhancing features are two of the most important pieces of information that we want to know about sub-resolution features. For lithofacies modeling, MPS allows us to honor and reproduce geometrical realism of facies distribution beyond the statistically random process. However, endeavors to infer the flow hindering/enhancing features are mostly limited to statistical approaches. As lithofacies cannot be free from depositional environments, flow hindering/enhancing features, such as fractures or compaction bands, cannot be free from deformational evolutions. As lithofacies modeling uses training images to make the realizations more geologically realistic, we need to investigate how we can enhance reservoir property modeling by utilizing the attributes of structural deformation.

1.2 Objectives and Scope

The intent of this work is to develop and apply a new workflow for the geomodeling process that allows the honoring of geological assumptions on 1) structural deformation of reservoirs and 2) how the deformation is affecting the evolution of the rock. We use the term “mode of structural deformation” to denote a set of structural interpretations and a model that consists of the present geometry of the subsurface structure and the underlying deformational mechanism explaining the present geometry. We use the term “mode of rock accommodation” to denote geological assumptions of how the structural attributes affect the spatial abundances and orientations of geological features existing in sub-scale to the modeling grid size.

We conduct the reservoir evaluation and reservoir simulation on geomodels created from the current geometry. When geologists observe the earth, an outcrop, or subsurface, they observe and process them as phenomena, which involves the idealization of observed geometry and a possible processes to create the observed geometry. Implicit models give qualitative explanations, while we may have the geometry of past subsurface conditions if we have explicit models. Whether implicitly or explicitly, we see the geoscience objects with models. As we discussed in Section 1.1.3, thanks to advances in 3D seismic technology, discrepancies between reservoir geometry from seismic and well data and reservoir geometry from numerical simulations have been reduced. From Section 1.1.3, we see that quantitative analysis of structural deformation is available. Thus, we want to attempt to link reservoir structure, especially how the structure has been deformed, to rock accommodation – how the rock accommodates the applied deformation – and propagate the assumptions on structural deformation and rock accommodation to petrophysical properties and subsurface responses.

Using this new workflow, we want to test and select more likely geological scenarios of structural deformation and rock accommodation. Under each combination of scenarios on structural deformation and rock accommodation, the new workflow generates multiple subsurface realizations, following each assumption made in the early stages of the subsurface evaluation process. If realizations from different scenarios give different responses, defining the more likely scenario will give a better understanding of subsurface evaluation, and corresponding realizations may serve as better starting points for any reservoir evaluation processes such as uncertainty quantification and history matching.

The key research objectives for this work are:

- Define the sources of geological uncertainty on structural deformation and rock accommodation.
- Develop a new workflow for subsurface modeling, to capture the effects of multiple scenarios of structural deformation and rock accommodation.

- Develop a new rock physics model to calculate the stiffness tensors of rock having multiple sets of sub-resolution geological features such as deformation bands, fractures, and cleavages in anisotropic media.
- Test the new workflow and effects of geological uncertainty from structural deformation and rock accommodation on subsurface responses to an unconventional Marcellus Shale gas field.

1.3 Dissertation Outline

This research entails the development and implementation of a geomodeling workflow for subsurface evaluation when there are uncertainties on structural deformation and on how the rock has accommodated the deformation. In Chapter 2, we investigate sources of uncertainty in geological interpretation for structural deformation and rock accommodation. We cover the sources of uncertainty in two ways: discrepancy between geological models and true earth, and coverage and resolution of observations. Accommodation styles describe how the rock absorbs the applied deformation through sub-resolution processes such as faulting, pore arrangements, or developing deformation bands. We attempt to provide qualitative explanations of key factors affecting the modes of accommodation.

In Chapter 3, we propose a new geomodeling workflow to capture the geological assumptions about structural deformation of reservoirs – how the structural geometry changed from the past to the present condition – and rock accommodation – how the rock responded to the applied deformation – from structural modeling to property modeling. Multiple interpretations of structural restoration and assumptions about sub-resolution accommodation processes gives rise to multiple sets of geological scenarios. Multiple realizations of geomodels under each scenario have different sub-resolution geological features and petrophysical properties that honor individual scenarios. We apply the workflow to a synthetic sandstone reservoir, and compare the effects of different assumptions on structural deformation and rock accommodation to reservoir response for both flow and seismic responses.

In Chapter 4, we propose a new rock physics model to compute the seismic attributes of having multiple sets of inclusions in an anisotropic background media. This new model decomposes the background anisotropic medium into an equivalent isotropic medium that gives identical density and velocity profiles with the measurements. By having equivalent isotropic media, we can calculate any combinations of “what-if” seismic attributes under different geological assumptions about rock accommodation. The new rock physics model can be used to compute seismic attributes on unconventional shale reservoirs that have background anisotropy that cannot be ignored, with the possible presence of multiple sets of inclusions.

Chapter 5 presents the application of the new geomodeling workflow and the new rock physics model to an unconventional Marcellus shale gas field in the Appalachian basin in the United States. The field has uncertainty related to structural interpretations and uncertainty related to the existence of sub-resolution faults and fractures. By using the rock physics model from Chapter 4, we can compute seismic attributes from effective stiffness tensors representing multiple sets of inclusions in anisotropic background medium, for different scenarios. After developing multiple geological scenarios on structural deformation and rock accommodation from field data and analogy data, we can compute the seismic attributes under each scenario. Compared with actual seismic attributes from the 3D seismic survey, realizations from different scenarios have different levels of similarity with the true seismic attributes. Comparing spatial distributions – abundances and orientations – of sub-resolution features such as fractures from the scenarios with higher similarity with true seismic data gives a better qualitative explanation of field observations of the given field.

Chapter 6 concludes this dissertation and provide recommendations for future work. Recommendations include developing alternative tools for conducting deformation/restoration analysis on top of the ones used in this dissertation, applying the ideas here to conventional reservoirs, the need for a tailored proxy of seismic forward simulations, and recommendations for applying the proposed workflow to basin and petroleum system modeling.

Chapter 2

2 Linking Geological Uncertainty in Modes of Structural Deformation and Rock Accommodation

This chapter reviews two sources of subsurface uncertainty: deformational uncertainty about reservoir structure, and accommodational uncertainty about how the rock absorbed the applied deformation. The first source creates uncertainty by not knowing the exact geometry of the present and past subsurface structures, or how the past geometry deformed to the current geometry. We also do not know whether a certain portion of a reservoir has been going through porosity reduction by mineral rearrangement, or developed a series of fractures when it compressed during the structural deformation. To evaluate surface responses effectively, we have to be aware of the sources of uncertainty on structural deformation, and of rock accommodation on given deformation.

2.1 Uncertainty about structural deformation

We do the reservoir evaluation and reservoir simulation on geomodels created from the current geometry. When geologists observe earth, an outcrop, or the subsurface, they observe and process them as phenomena, which involve idealization of the observed geometry and a possible process that shaped the earth into the observed geometry. If it is implicit, we can give a qualitative explanation, while we may have geometry of past subsurface conditions if we have explicit models.

2.1.1 Relationships among geometrical, kinematic, and dynamic models

When we observe geological features, either from an outcrop or through seismic images of the subsurface, we always use a set of prior knowledge and try to fit the observations with our conceptual understandings. For some observers, a vertical section can be merely full of wiggles in pretty patterns, while for others it can be full of information that can help reconstruct how it looks and how it ended up in that shape during geological timeframes. If we turn these interpretations into a set of explicit quantifications and explanations to help them make sense, they become explicit models.

Brandes and Tanner (2014) provide the following classification and definitions of geological models:

- *Geometrical models* contain a primary data set, 2D or 3D, of stratigraphic units, faults, and other geological information.
- *Kinematic models* determine the evolution of a geometrical structural model.
- *Dynamic models* study the forces and stresses required to produce the geometrical structural model.

Brandes and Tanner (2014) likewise suggest that every model must be based on a guiding conceptual model, have a theoretically-based submodel, have predictive capability, and have the ability to deliver testable predictions.

The following figure (Nenna and Aydin, 2011) is a perfect example of how observations are turned into a geometrical model. Figure 2-1a is a picture which contains pixels. Geologists observe it and conduct interpretations – run implicit models – based on their prior knowledge and conceptual models of geological features, and simplify the picture into a simplified data set of lines and figures. In terms of Brandes and Tanner’s (2014) criteria, Nenna and Aydin’s sketch presents conceptual models of deformation bands. They define the observations into pressure solution seams and veins that have their own definitions. By comparing this information with adjacent faults, they can

estimate that the geological setting was compressional, and from lab measurements and experiments, they can confirm whether their interpretation is correct or incorrect. Now it becomes a geometrical model.

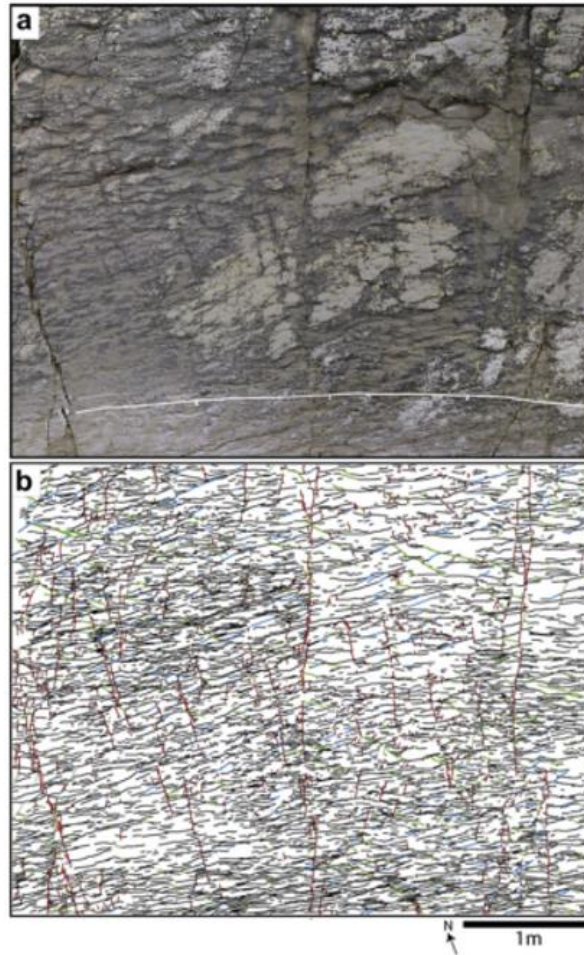


Figure 2-1: A picture from outcrop (a) and geometrical model (b) (Nenna and Aydin, 2011). A picture (an observation) is simplified and idealized into a geometrical model by geological interpretation - implicit models that contain geological information. Pixels of different colors are turned into simplified geological features.

Kinematic models attempt to explain the evolution of geometrical structural models. Thus, kinematic models require more than two geometrical models that represent different time points – one for the present, and others for any past time. By having multiple geometries, kinematic models involve kinematic vectors linking different geometries and representing different geological times. An example of a

kinematic model is the well-known kink band migration model for fault-bend folds from Suppe (1983). Figure 2-2 shows Suppe's interpretations of locally thickened shale layers by using his kink-band migration model.

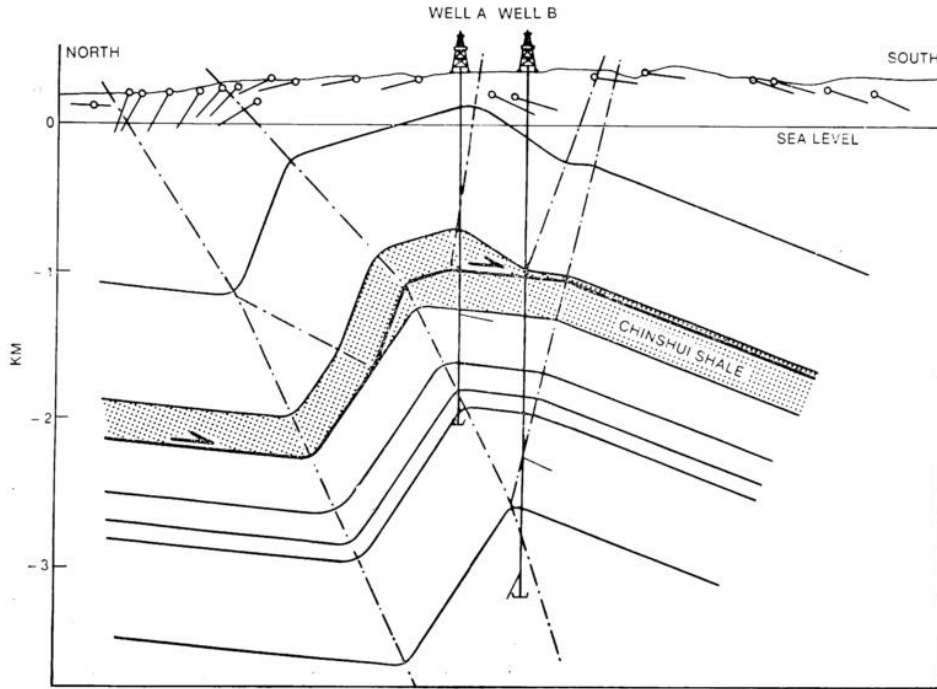


Figure 2-2: Suppe's (1983) fault-bend folding interpretation using his kink band model explains thickness variations of Chinshui shale between two adjacent wells.

Dynamic models involve kinematic models, and thus automatically geometrical models, and require rheological information such as density, elastic modulus, and Poisson's ratio to simplify the equations of motion so they can be solved to capture forces and stress, and constraints of the deformation of geometrical shapes of the geomodel.

The process of creating past geometrical models from current geometrical models is called restoration, or retro-deformation analysis. If we use any kinematic model as a governing model during restoration analysis, the restoration is called kinematic restoration or section restoration. Dahlstrom's balanced cross section (1969) is one of the earliest example of kinematic restoration (Dahlstrom, 1969). The following figure is a schematic explanation of Dahlstrom's cross section restoration using two

surfaces. His kinematic model preserves the surface length during the restoration process.

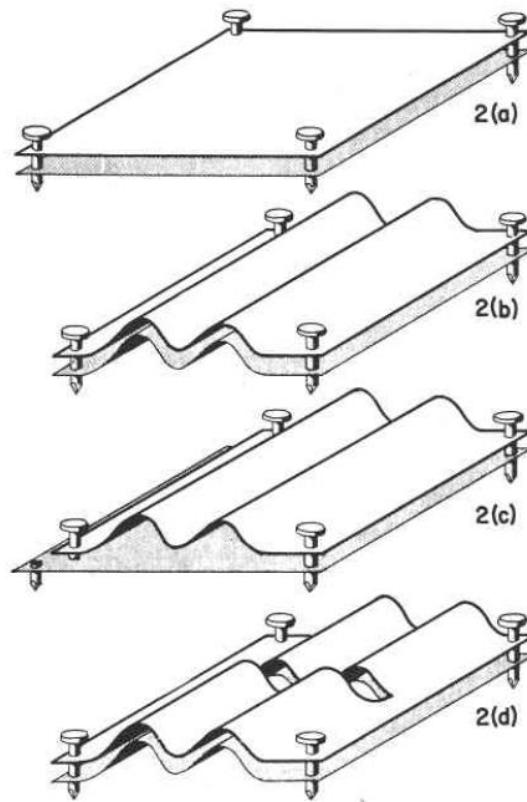


Figure 2-3: Schematic explanation of the principal of balanced restoration by Dahlstrom (1969). He used nails as visual cues for boundary conditions. In (c), a nail on the left bottom corner is broken, and the lower surface was flattened. In (d), the lower surface was re-compacted horizontally, while the center of the upper surface was cut and dropped on top of the bottom surface. In both cases, the length and area of the two surfaces are preserved.

If we use dynamic models to reconstruct past geometrical models, they become mechanics-based restorations (Maerten et al., 2006; Maerten et al., 2001). This offers restored geometrical models with a certain amount of force and stress applied to make the deformation conform to the governing equations of motion, assuming the constitutive law of stress-strain relations. The following figures depict Maerten and Maerten's (2006) claims about the merits of mechanics-based restorations for estimating sub-seismic resolution faults via stress distribution from restoration and forward deformation analysis. Figure 2-4a shows a result of the sandbox experiment of

McClay (1990) to mimic an extensional fault system. Figure 2-4b shows digitized geometrical models of the McClay experiments by Maerten and Maerten (2006). Figure 2-4c and 1.4d are the computed shear stress distribution, magnitudes, and direction of the principal strain components from a restoration analysis.

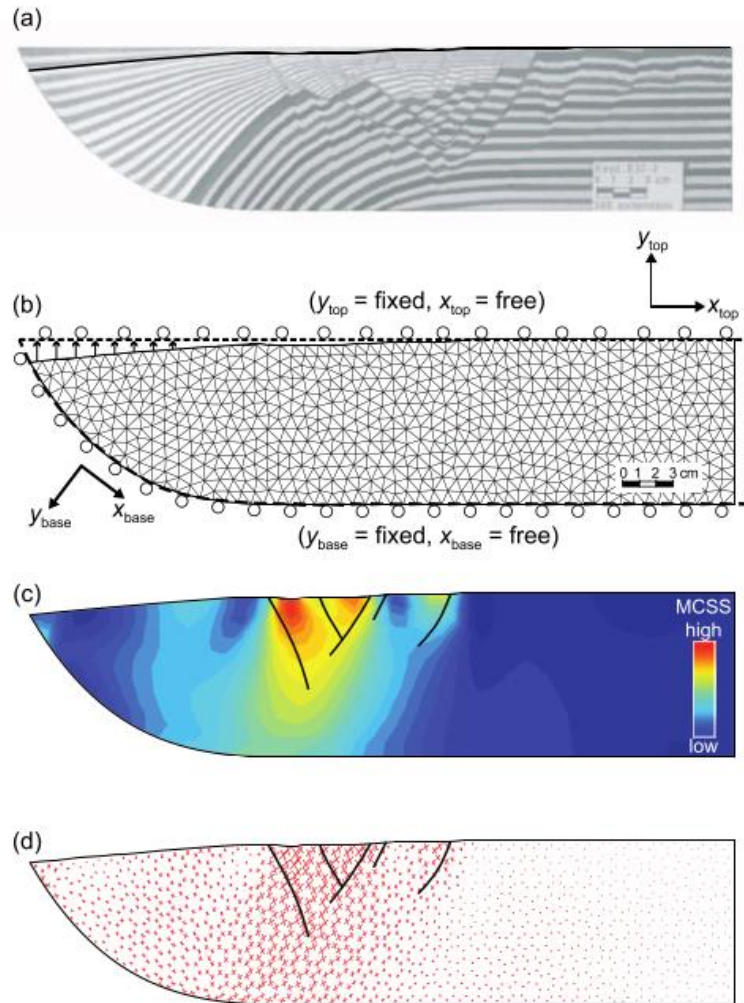


Figure 2-4: Maerten and Maerten's (2006) geomechanically based restoration applied to McClay's sandbox experiments (1990) to mimic an extensional fault system. Maerten and Maerten's restorations use linear elasticity as a constitutive law to reproduce the distributions of maximum shear stress around the densely faulted area from McClay's experiment. (a) The sandbox experiment, (b) geometry of the deformed (current) and restored (past) conditions, (c) shear stress distribution from the dynamic model used, and (d) direction and magnitudes of restoration vectors.

Above all, models are reversible. They give the same kinematic displacement vectors, or deformational stress, regardless of the direction of the restoration – from present to past (forward deformation) or past to present– except for the direction of the restoration and the forward deformation vectors. For example, if the restoration displacement of an arbitrary point A is 10 meters north, the forward deformation displacement of the point A is 10 meters south. However, if we use nonlinear elasticity assumptions, the restoration and forward deformation cannot be the same. Analysis in these terms is called retro-deformational analysis (Lovely et al., 2012). It focuses on irreversible deformation, and it may require a recursive process to optimize the restored geometrical models to the current geometry, in order to make the geometrical models consistent under the assumed constitutive laws of nonlinear behaviors (Lovely et al., 2012). Since dynamic models, whether assuming linear elasticity or nonlinear elasticity, also involve kinematics, we are going to call all of the qualitative and quantitative models explaining the evolution of geometrical models kinematic models when we do not attempt to differentiate them from dynamic models.

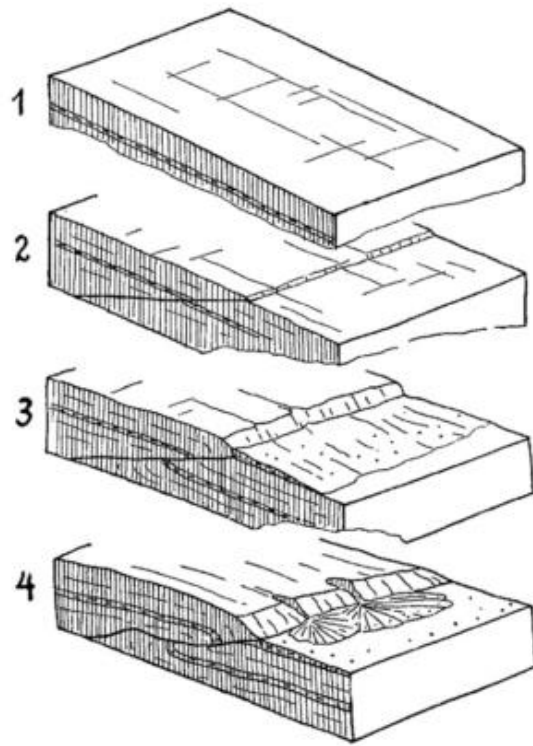


Figure 2-5: Drawing by Cloos (1936), reprinted in Brandes and Tanner (2014). Cartoon 4 is a simplified geological sketch containing geological features such as reverse faults, folds, horizons, lobes, and canyons (a geometrical model of present conditions). Cloos drew sketches of unseen shapes of geometries at past times (geometric models in the past). He processed them using his own mental model, without an explicit form of equations. Thus, the model of the relations among the sketches is Cloos' conceptual model on fault-related folds. But it is not a "kinematic" model because it does not involve any kinematic principles, and not a "dynamic" model because it does not give any explicit number and orientations of forces from one figure to another.

Figure 2-5 gives a good summary of these models and their relations (Cloos, 1936; Brandes and Tanner, 2014). Cartoon 4 is a geometrical model including geological features such as reverse faults, folds, horizons, lobes, and canyons. Cartoons 3, 2, and 1 are geometrical models representing past geological time. Cloos linked one cartoon to another using his own mental model of geological processes, without an explicit form of governing laws or equations. Thus, the model showing the relations among cartoons is "Cloos' qualitative model" on fault-related folds. If any kinematic principles were used to reconstruct cartoons of past time, we could call this process a

kinematic restoration analysis. The mathematical expression of the kinematic principle and the sets of assumptions used form a kinematic model. Note that the above models and explanations only cover very limited components of the geological modeling processes that are relevant to this research.

Notice that when we use the term “model,” it is not referring to any actual observation, but to an idealized concept of either geometry, kinematics or dynamics, or their evolutions. When we use “application” or “experiment,” it involves interpretations used to convert an observation of current geometry into a geometrical model, and applies kinematic or dynamic models to attempt to explain the evolution of the geometrical models. The part in which we investigate how well the models work, and try to explain why, is called “analysis.”

2.1.2 Sources of uncertainty in structural deformation

Truly, the present is the key to the past. The first source of uncertainty in structural deformation comes from that key, the present geometrical model. We have the key that has been produced from data with poor resolution, or limited coverage. In E&P projects, seismic images are one of the primary sources to extract current geometrical models. Due to the uncertainty of not knowing the exact velocity model together with the seismic resolution, seismic data itself has huge uncertainty when providing geometrical models (Li et al., 2015). Thus, we idealize and conceptualize data into geological features to build a geometrical structure model. The current geometry of the subsurface is certain. Only our geometrical subsurface models of the present are uncertain and imperfect. Not knowing the exact current geometry is the first source of structural uncertainty.

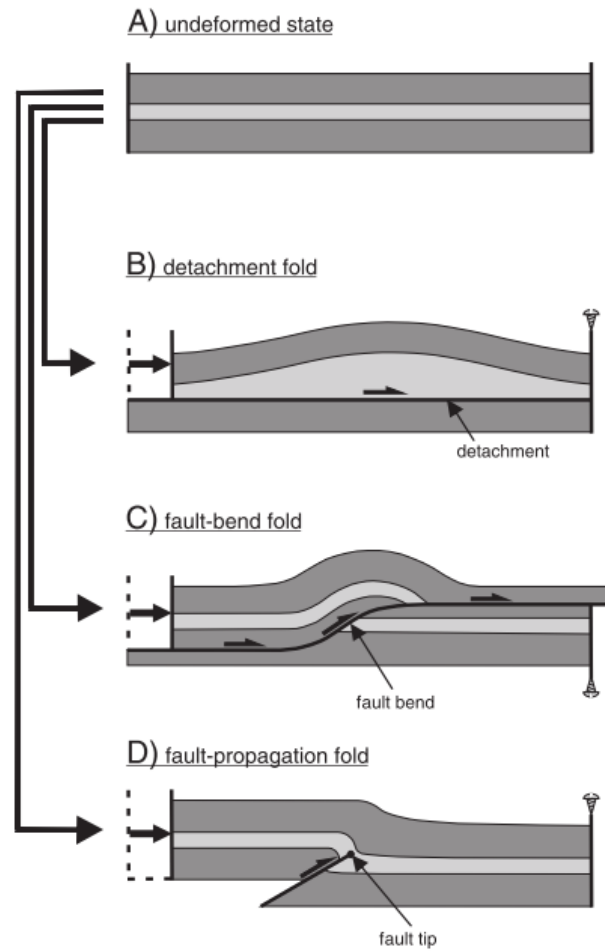


Figure 2-6: Alternative modes of kinematic models from the identical initial geometry - cartoon A. By having slightly different boundary conditions, structural geometry can evolve in different shapes. (Brandes and Tanner, 2014)

The second source of uncertainty comes from not knowing the past geometry and its boundary conditions. Figure 2-6 depicts how an identical flat formation can be deformed into different geometrical models by having slightly different boundary conditions under the applied lateral shortening (Brandes and Tanner, 2014). Even in the case when we know the region of the subsurface has been laterally compressed, it is highly possible that the seismic data we have will not give enough resolution to distinguish cartoon B from cartoon C.

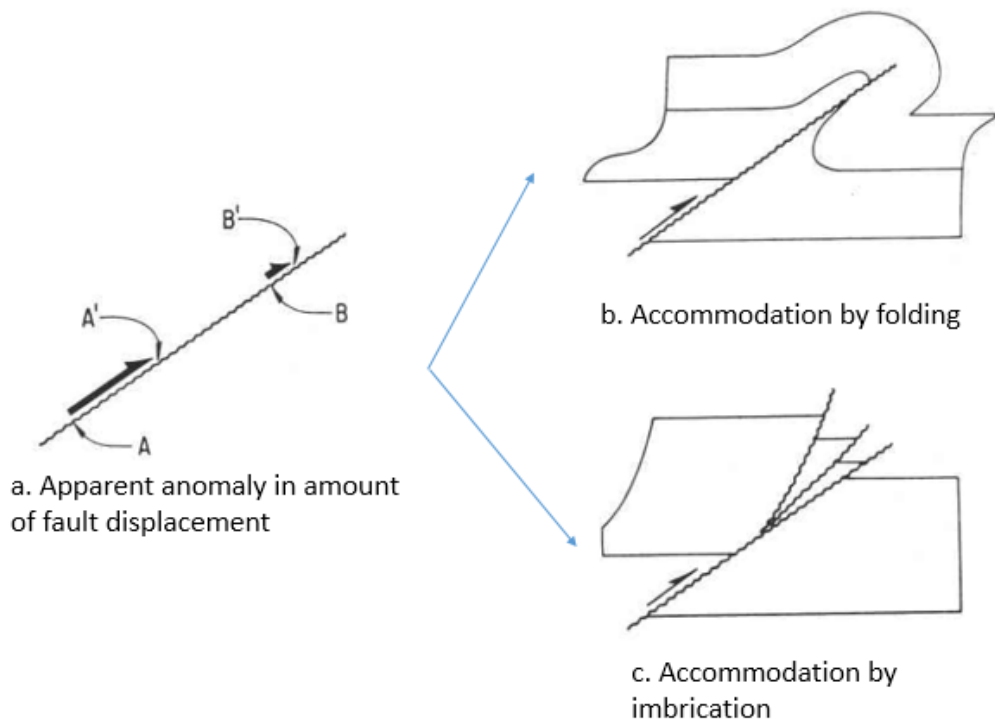


Figure 2-7: Dahstrom's (1969) example of equally plausible interpretations from the same observation. An apparent anomaly in the amount of fault displacement (a) can be explained by both folding (b) and imbrication (c). By choosing one model over another, the geometrical models for both present and past conditions will be distinct from those made by other kinematic models.

In Figure 2-7, Dahstrom (1969) depicts cases when an observation along a fault surface can be explained by two different geological mechanisms. Both folding and imbrication make localized formations shorter and thicker than the original. As Dahstrom (1969) depicted, we can have multiple geological features that explain our observations. Even when we choose one geological feature or mechanism that makes the most sense, we still have many kinematic models that lead us to different combinations of present and past geometrical models. Likewise, even in a case when kinematic displacement is identical, different boundary loading conditions may lead to different geomechanical history (Lewis et al., 2007). With the same boundary conditions, if we assume different constitutive laws, the stress and strain distributions and orientations cannot be the same (Lovely, 2011).

Not knowing 1) the correct current geometry, 2) the geometry of past time, and 3) the processes or governing laws during the deformation yields geological uncertainty and thereby a number of alternative geological explanations for a given subsurface condition. Indeed, subsurface uncertainty is not from the subsurface itself, but from our lack of knowledge and understanding.

2.1.3 Why does this matter for reservoir modeling and evaluation?

Some might ask why we need to care about the past geometrical shape or how the structure has been deformed for engineering purposes, considering the fact that all the reservoir volume calculations and flow simulations are conducted on models using the present geometrical models. First, knowing the past conditions gives more geologically consistent interpretations of current geometry (Novoa et al., 2000). Figure 2-8 depicts the usefulness of kinematic models and restoration analysis. Figure 2-8a is the original interpretation with three major horizon tops picked. The restored section from a kink-band-migration model of Suppe (1983) has a thickness anomaly in a restored section (Figure 2-8b). By updating the interpretation of the current geometry by adding a fault and re-picked horizons for deeper formations (Figure 2-8c), the thickness anomaly in the restored section was resolved (Figure 2-8d). Now the depth interpretations for each horizon on the right side have been changed. Estimation of the drilling cost should likewise be changed. The thickness of the formations on the right side also changed; now it even has a reverse fault. Results of flow simulations will thus also change.

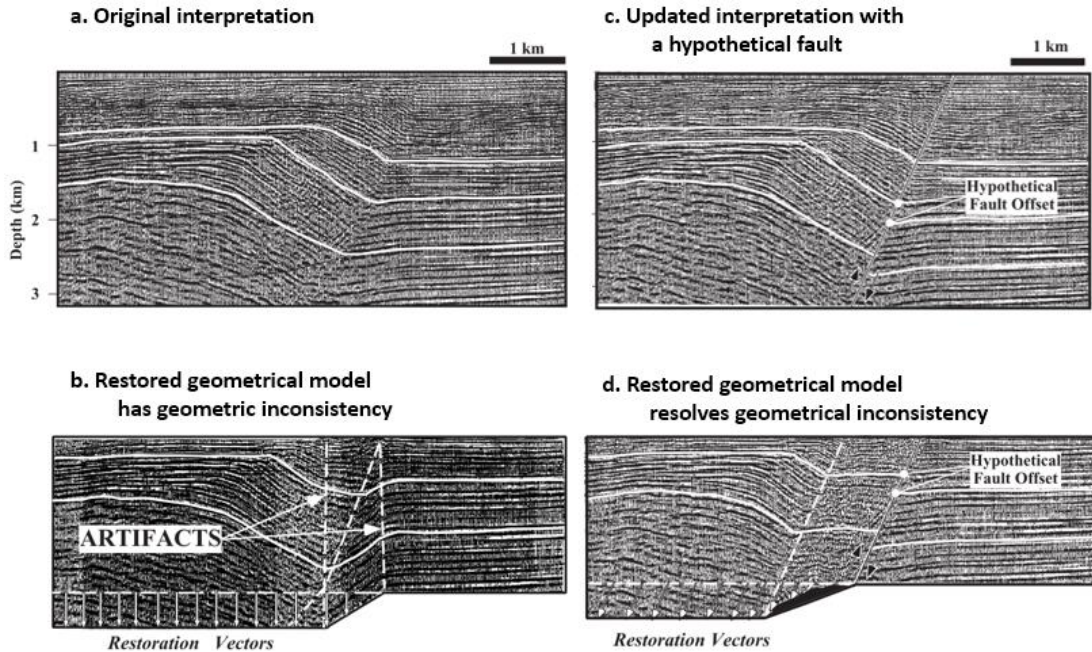


Figure 2-8: An example of the usefulness of restoration analysis (Novoa et al., 2000). *a* is the original interpretation of the horizons. *b* is a restored section using a kink-band-migration kinematic model. *b* has an area that does not have even thickness in the restored section. In *c*, a fault is added. The restored section resolved the thickness issue by including a fault in the model (*d*).

Second, past geometry directly affects lithofacies modeling. We can run flow simulations based on current geometry. However, we should not model reservoir properties based on the current geometry, because deposition of the lithofacies happened when the formation was horizontal. By knowing the kinematic relations between the current geometry and the restored geometry, we can use geological distances on property modeling, not the current spatial distance (Mallet, 2004; Caers, 2005). If we use Figure 2-8 again, under the original interpretation, the lithofacies around the hypothetical fault will not have a vertical throw since it does not assume a fault. Lithofacies distribution under the updated interpretation will have a vertical throw from the reserve fault. With the combined amount of fault displacement, conductivity across the fault will be different. The original interpretation will fail to forecast possible flow barriers across the fault.

Third, geometrical models with kinematic/dynamic models can give useful information on the spatial distribution of reservoir properties. We will cover this advantage in the following section.

2.2 Uncertainty in the mode of rock accommodation

In the previous section, we roughly simplified the process and characteristics of geological interpretations on subsurface structures, by using observations, geometrical models, kinematic and dynamic models, and restoration/forward deformation analysis. These models implicitly or explicitly assume how the subsurface accommodated structural deformation by adding geological features – such as faults, folds, imbrications, and so on – with kinematical and dynamical considerations. Like any model, by the nature of its simplification, these approaches do not explicitly model how the materials among the horizons, faults, and folds accommodated the applied geometrical evolutions.

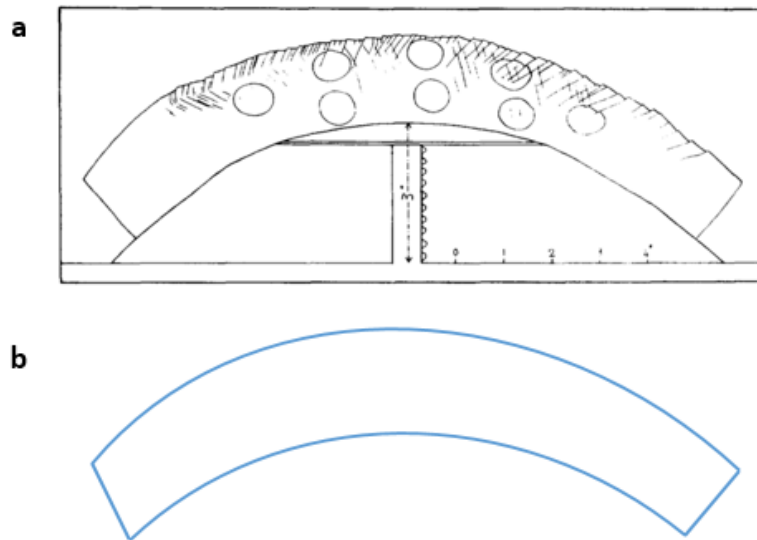


Figure 2-9: comparison between a folded horizon in a geometrical model and internal features on a fold from a lab experiment. **a** - Cloos' experiment to investigated fold-related features (Cloos, 1968). **b** - Schematic diagram of a folded horizon.

Figure 2-9 depicts differences between an idealized horizon in a geometrical model of a fold, **b**, and the evolution of geological features within a layer from a lab experiment, **a** (Cloos, 1968). Figure 2-9a shows the results of a metal beam folding to

mimic an extensional fold. The outer parts of the beam have many mechanical failures, which can be considered analogies of joints and fractures. The ellipses were circles before the beam bent. They represent how the material deformed during the bending. Imagine that Figure 2-9b is the shape of our reservoir model and we do not know the geological features within the formation. If the formation was stiff when bent, like the steel beam used in the figure, we can have joints and fractures. If the formation was soft and ductile, like clay, it may have some fabric development but no joints or fractures. Both of them are compatible with the geometrical model we have. However, for the subsurface responses we are interested in, such as production forecasting, the estimated recovery factors will be different for different geological features.

Note that the differentiation between the geological deformation on a typical geomodel resolution, such as basin modeling or reservoir modeling, and the deformation on a subscale, such as voxels of modeling grid/mesh, is not from the natural characteristics of the earth, but from the characteristics of the way we see the natural phenomenon through models. If we recall Nenna and Aydin's (2011) interpretations on the pressure solution seams in Figure 2-1, the geometrical modeling (geological interpretation) boundary is around 5 meters by 5 meters, and the resolution of the geological features of investigation, pressure solution seams (PSS), is in centimeters to tens of centimeters. It still involves a conceptualized geometry of PSS, which is a geometrical model. Nenna and Aydin interpret the observation, meaning they find geometries that fit the PSS model from the observation. They have kinematic and dynamic models explaining how PSS forms. From the governing laws they have, they can link the geometry before forming PSS to the geometry of PSS (Nenna and Aydin, 2011).

Now, we call the second source of structural uncertainty the uncertainty from the mode of rock accommodation. Like the first source of uncertainty, there is no uncertainty in the subsurface. Uncertainty comes from the way we understand the subsurface phenomenon (by the model) with our observations (under limited coverage and resolution). For the first source, the major uncertainty is rooted in kinematic-dynamic models of observable features. At least we can extract the horizon tops and

some major faults – whether they are slightly bigger or deeper or not is secondary to knowing of their existence. However, the second source comes from the sparseness and resolution of the observation. Unless we have well data such as image logs and cores, the only available observations are outcrops. In a 2D or 3D model, we cannot see features finer than the seismic resolution. Thus, the main issue is not the location, and not the size, but the existence.

Another noticeable difference between the two sources of uncertainty is the typical way of reproducing and observing the geological processes we want to investigate. For a basin, or a reservoir scale structural deformation, we cannot conduct deformation experiments with the actual scale. Thus, we either have to conduct scaled analogue experiments or numerical simulations. Scaled analogue experiments and scaled laboratory models have been used extensively in geological research (Hubbert, 1937; Hubbert, 1951; Pollard and Fletcher, 2005). However, the fundamental difficulty of the scaled models is that it is extremely difficult to select proper materials that are weak enough to meet the strength ratio to be scaled as the length ratio. Earth breaks by its own weight. To be scalable, if we make a scaled model with a 1:100,000 scale, we should find or invent a material we can use to represent the subsurface formation, which has 1/100,000 of the formation strength.

Numerical simulations are free from all the issues related to scaled models. However, their main challenges are the fact that we have very limited knowledge on the governing laws of kinematics and dynamics, and the boundary conditions of simulations (Lovely et al., 2012). For sub-seismic scale reservoir deformation, we do not have scale related problems because we can conduct the rock failures and deformation under the same scale, with the same pressure and temperature conditions of the subsurface. Due to the fact that we achieve favorable conditions in lab experiments for core or sub-core resolution phenomena with lots of experimental data, mathematical and numerical models tend to be more complex and reproduce the experiment data well (Borja and Aydin, 2004). However, two challenges in geomodeling perspectives are first, that experiments and numerical models of deformation and failures are events within a geologically instantaneous time. Second, even if we want to use these perspectives, we

do not have enough input data. They are sub-resolution phenomena. A rough and simple comparison would be at a coarse scale, where we are not sure about our model, while at a finer scale, we do not have the necessary measurements.

We still can infer the existence of fractures with higher confidence from seismic attribute analysis (Grechka and Tsvankin, 2004; Chopra and Marfurt, 2007). However, it is different in that seismic attribute analysis gives the statistical likelihood of having sub-resolution features, not geometrical models of them.

2.2.1 Distributed versus localized rock accommodation

When rock is deformed, there must be a discontinuous displacement in one or more different scales. Thus, any description of deformed rock, whether it has discontinuous features such as fractures or not, is a scale-dependent description. For instance, if flat parallel formations are compressed laterally, they may deform in a way to create a gentle anticline. When we describe this deformation with a scale of a fold model, we can say the deformation was ductile, or continuous. However, if we focus on rocks inside the horizon, rocks may develop joints and shear fractures like in Figure 2-9a. If we still cannot see any visible fracture or joint with the naked eye, the contact or cement among grains should be broken or detached, to rearrange the mineral and pore structure to be deformed. Mineral grains can also be broken by micro-cracking, or even on the scale of dislocating an atom (Marder and Fineberg, 1996).

Dahstrom (1969) used the term “accommodation” to link the kinematic evolution of the structure and the geological features that absorb the structural deformation (Figure 2-7a and b). Walsh et al. (1996) used the term “accommodation” to distinguish sub-resolution deformation into ductile versus non-ductile strains: “The limited vertical resolution of reflection seismic data results in sub-resolution structures accommodating appreciable ductile strains which should be taken into structural restoration and balancing and in analysis of fault displacements” (Walsh et al., 1996, p. 27).

In above quote, Walsh et al. define accommodation as deformation resolved by sub-resolution structure, either continuously or discontinuously. The claim is simple: we should have more “break-out” to make the structure make sense kinematically or dynamically. Note that they use “ductile strains” for accommodation by deformation not definable as discontinuous deformation in a given resolution, while they use “non-ductile strains” for accommodation via discontinuous features such as fault displacement. If we go back to Lovely et al.’s claims (2012) that retro-deformation using nonlinear elasticity is superior to kinematic, or forward deformation by linear elasticity, we can re-phrase it in a simpler way: “we need to add more faults, fractures, or even microfractures to make sense of the structural shape.” However, the question is “at which resolution?”

Following these usages, we use “mode of accommodation” or “accommodation style” to refer to any geometrical or kinematic model of sub-resolution rock deformation, and more specifically, to the resolution of a grid mesh or grid voxel on geomodels. If the accommodation style involves discontinuous features like joints, fractures, or veins, we will call it a “localized” accommodation style. If the rock accommodates the voxel/mesh resolution deformation without adding discontinuous features like fractures and joints, we will call it “distributed” accommodation. Note that the categorization of distributed and localized accommodations are soft or pseudo classifications, to avoid unnecessary distraction from the fact that different disciplines have slightly different definitions and purposes when they use descriptions such as brittle and ductile. Rutter also commented on the ambiguity by using “ductility” to explain the mode of rock failure, because many “ductile” rock deformations also involve microcracking on a finer scale (Rutter, 1986). If we zoom out the scale of observation to the global scale, rocks are ductile and there is no need to prove it, because Earth remains a globe through the geological time span. However, on a smaller scale, rocks are brittle because they eventually break out at some scale. Nevertheless, the bigger scale ductility is rooted in the brittleness at a finer scale.

Table 2-1: Rutter's classification of modes of rock failure (Rutter, 1986).

		Localization	
		Yes	No
Deformation mechanism	Cataclastic	Cataclastic faulting	Cataclastic flow
	Crystal-plastic	Plastic shear zone	Plastic flow

In the following three subsections, 2.2.2, 2.2.3, and 2.2.5, we cover some classifications of localized and distributed rock accommodations, give short descriptions of some important models of these accommodations, and identify some key factors to distinguish the mode of specific accommodation style from others, based on Rutter's classification, shown in Table 2-1 (1986), with slight modifications. Note that we are not going to cover detailed kinematic/dynamic laws of each accommodation model. We focus more on geometrical models of them, and analyze assumptions of their kinematic or dynamic models. The reasons are simple; our main interest here is in the existence and the impact of accommodations on subsurface responses, and we are not going to model their geometrical or kinematic/dynamic models because they are sub-resolution features.

2.2.2 Localized accommodation

In Table 2-1, localized accommodation can be divided into cataclastic and crystal-plastic mechanism. Aydin et al. (2006) classify localized accommodation into deformation bands and sharp discontinuities, which corresponds to the crystal-plastic and cataclastic mechanisms in Rutter (Aydin et al., 2006; Rutter, 1986). Figure 2-10 shows the classification of localized modes of rock deformation by mode of localized deformation – shortening/shear/extension – and form of deformation localization – sharp surface/tabular band– given by Aydin et al. (2006). If we use a typical classification of fractures – mode I, II, and III, (Pollard and Fletcher, 2005)—the joint

in the following figure is a mode I fracture, while slip surface can be mode II or III depending on the direction of the shearing of fracture surfaces. The anticrack model from Fletcher and Pollard (1981) can be understood as a geometrical and dynamic model of solution surface (Sternlof et al., 2005). If the void of a joint is filled and cemented by a mineral, we call it a vein.

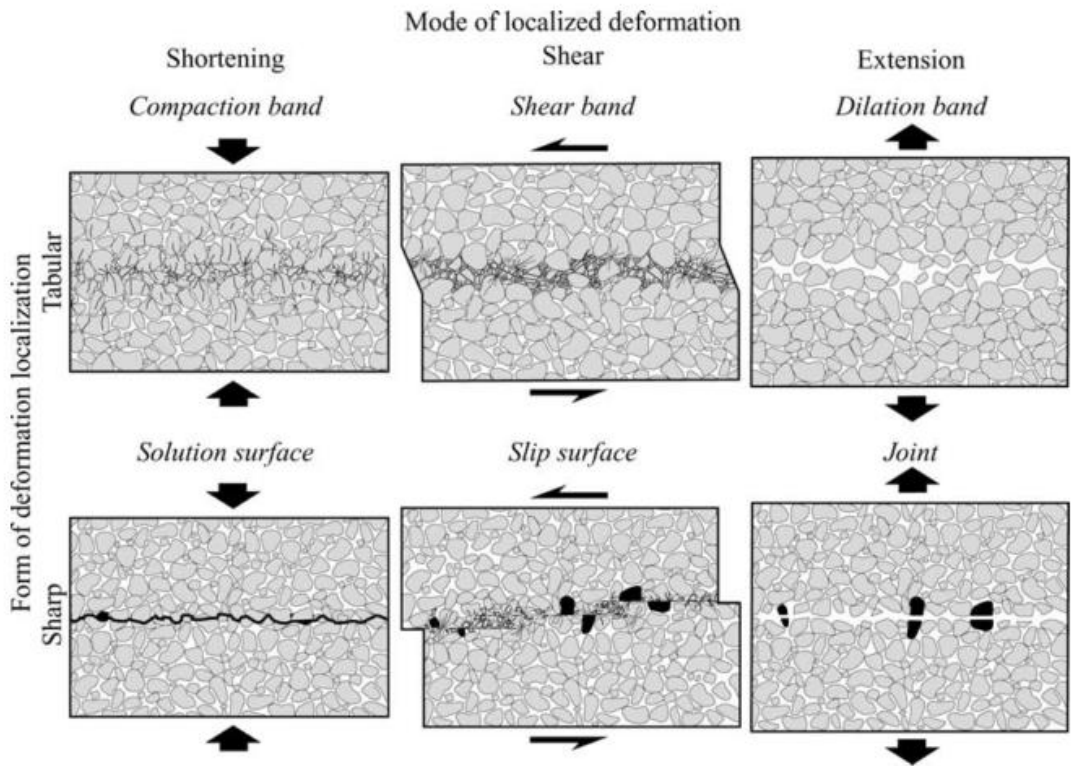


Figure 2-10: Mode of rock failure by mode of localized deformation, and form of deformation localization (Aydin et al., 2006).

2.2.3 Distributed accommodation

Distributed accommodation involves either plastic deformation or cataclastic flow (Rutter, 1986; Owen, 1987; Paterson and Wong, 2005). Paterson and Wong classified ductile deformation as follows:

- a) Deformation of the individual grain is same as the macroscopic deformation (grain neighbors remain the same)

- a. Crystal plasticity (dislocation flow): volume-constant deformation and independent of confining pressure
- b. Diffusion flow (diffusion creep): change in the shape of the grain
- b) Reconfiguration of grain positions (grain neighbors change)
 - a. Cataclastic flow (microbrittle granular flow):
 - Distributed fracturing makes the materials into fragments (“brittle” aspect)
 - The relative movement of the fragment (“granular flow” aspect)
 - Strongly pressure-sensitive
 - b. Microplastic granular flow:
 - No fracture and disruption of the grain boundary

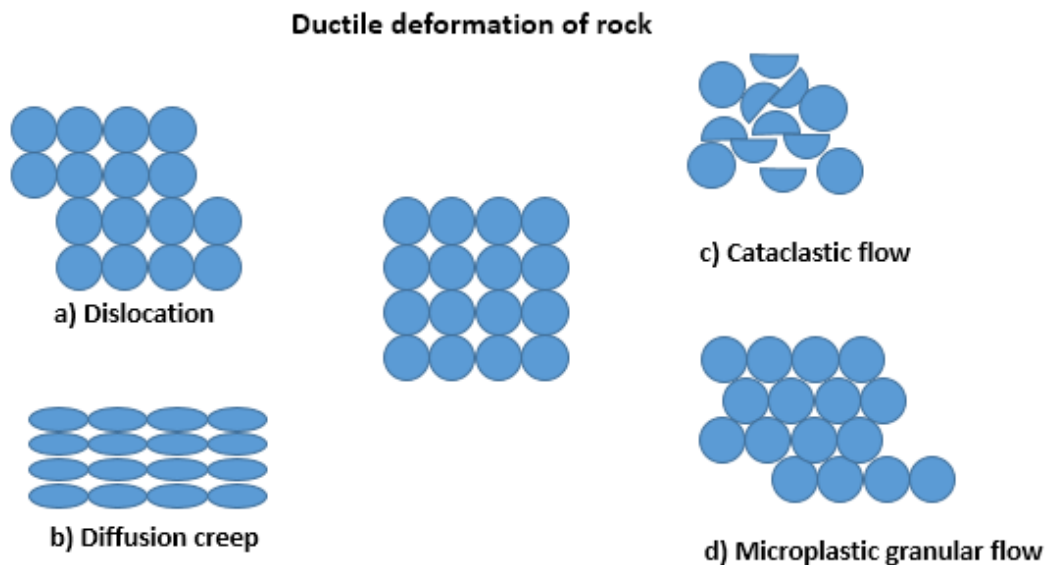


Figure 2-11: Ductile deformation of rock under Paterson and Wong’s (2005) classification.

Figure 2-11 depicts Paterson and Wong's (2005) classification. Dislocation involves instantaneous detachment and reattachment among either minerals or atoms to accommodate lateral slip displacement. Diffusion creep involves geometrical changes of the grains to accommodate deformation. Cataclastic flow has both mineral breakout and rearrangement of pores and mineral components. Microplastic granular flow accommodates deformation by rearrangement of pore and mineral arrangements, without mineral shape changes or breakouts.

2.2.4 Vague areas for classification: microcracks in shale, and pervasive cleavage

Shale tends to be considered a ductile subsurface material because it is relatively compliant, soft, and is less likely to contain fractures and joints than stiffer rocks such as sandstone and carbonate. However, due to the horizontal fabrics by platy minerals and alignments from compaction, the geometry of pores are similar to cracks (Vernik and Nur, 1992; Bandyopadhyay, 2009). Together with the anisotropy from horizontal alignments of platy mineral, crack-like pores make shale anisotropic. The effect of these crack-like pores are equivalent to horizontal fractures with respect to their effect on seismic responses. Figure 2-12b shows the horizontal alignments of platy minerals in shale from vertical compaction (Vernik and Landis, 1996).

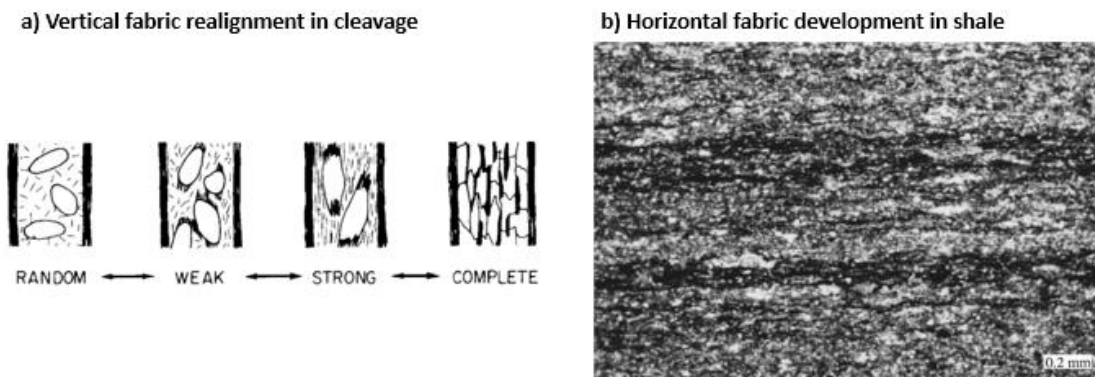


Figure 2-12: Fabric developments in vertical cleavage (left) and shale (right). Vertical fabric in cleavage was developed while the maximum compressional direction was horizontal. In shale, horizontal fabric is

most common because the vertical stress is usually significant. The left figure is from Powell (1979), and the right figure is from Vernik and Landis (1996).

Cleavage is a fine scaled structure which features 1) a strong planar alignment, 2) mineral alignments with a perpendicular orientation to the most compressed direction, and 3) a tendency to break out to form a joint or fractures along the cleavage (Pollard and Fletcher, 2005). It forms in a place that compressed, and once formed it is pervasive (Powell, 1979). Because rock is easy to be broken along the cleavage, cleavages can be understood as potential surfaces for fractures or joints. Once a rock with cleavage experiences de-compaction, or stress perturbations, some of the fabrics in the cleavage will be converted to joints and fractures. In shale, when it is uplifted or deformed, creating a horizontal crack is relatively easy due to the pre-existing fabric (Vernik and Nur, 1992; Bandyopadhyay, 2009). Note that if we flip the completed fabric development in Figure 2-12a by 90° , it is more or less identical in a geometrical sense to Figure 2-12b. The two most significant differences between them are that first, cleavages are only pervasive within a certain structural area, while fabric in shale will be pervasive across the formation, except in a certain area where we expect the existence of cleavage. Second, one is usually horizontal, while the other is non-horizontal. We leave the classification of cleavage and crack-like pores of shale as choices of usefulness from the engineering prospective on subsurface modeling.

2.2.5 Factors affecting modes of accommodation

We divided modes of accommodation – modes of deformation in the sub-horizon, modeling grid voxel/mesh resolution – into “distributed” and “localized.” Thus, we first need to go through the factors affecting whether rock deforms under the distributed or localized mode. One useful viewpoint for clarifying the differences between these two modes of accommodation is classifying rock deformation into two classes of internal flaws – cracks or pores – and seeing the deformation as competition between cracking and porosity changes (Hamiel et al., 2004).

Before we discuss this distinction further, by just seeing the deformation of rock as either development of cracks or porosity changes, it intuitively makes sense that if internal flaws are cracks, and they propagate with deformation, it would be localized rather than distributed. However, pores are connected to some degree, and linked pores can communicate by fluid and pressure. Thus, any deformation processed by changes in and re-distribution of pores is aptly called a distributed accommodation. If cracks in a rock play the roles of internal flaws, the deformation process involves stress concentration around cracks and promotes brittle failure. When pores act as internal flaws, they easily dissipate stress or energy concentration across the rock, leading to distributed deformation. Thus, if a factor is more promoting roles of pores and pore-filled fluid, distributed accommodation becomes more likely.

Other two key factors are temperature and time span of deformation. With higher temperature, rocks become less brittle (Rutter, 1986; Mogi and Publishing, 1972; Nevitt et al., 2014). However, this temperature oriented brittle-ductile transition is more dominant factors for much deeper formations than typical target depths of hydrocarbon bearing formations (Bürgmann and Pollard, 1994). If deformations occur over a long period of time, it is more likely to have distributed accommodation (Owen, 1987).

Table 2-2: Factors affecting mode of accommodation - distributed versus localized. We can categorize the effect as promoting the role of pores as internal flaws versus cracks and mineral phase. References marked with “*” compiled relations from previous experiments. Other references are independent experiments.

	Distributed accommodation	Localized accommodation	References
Low porosity	De-promote	Promote	Hamiel et al. ('04), Wong et al. ('97)*
Coarse grain size	Promote	De-promote	Wong et al. ('97)*
Increasing confining pressure	Promote	De-promote	Hamiel et al. ('04), Tobin and Donath ('71), Mogi ('71), Peterson and Wong ('05)*

Increasing differential stress	De-promote	Promote	Hamiel et al. ('04), Mogi ('71), Buseti et al. ('12)
Increasing intermediate compressional stress	De-promote	Promote	Mogi ('71)
Increasing temperature	Promote	De-promote	Rutter ('85), Mogi ('71), Peterson and Wong ('05)*
Increasing pore pressure	Promote	De-promote	Rutter ('85), Mogi ('71), Owen ('87), Buseti et al. ('12)
Increasing strain	De-promote	Promote	Rutter ('85), Tobin and Donath ('71), Mogi ('71), Peterson and Wong ('05)*
Longer time span of deformation	Promote	De-promote	Owen ('87)
Increasing cementation among grains	De-promote	Promote	Rutter ('85)
Increasing fluid saturation	Promote	De-promote	Owen ('87), Peterson and Wong ('05)*

Table 2-2 lists the factors affecting modes of accommodation, with references. If conditions were promoting the role of pores as internal flaws, it would be more likely to have distributed accommodation. Factors promoting pores as internal flaws are increasing relative importance of pore fluids while de-promoting the role of solid phases. It is convenient to examine whether the factors increase the role or proportion of pores to accommodate stress-strain loading. With higher porosity, pore volumes increase. Thus, the role of pores as flaws become more dominant. As grain size becomes coarser, the area of mineral contacts among minerals becomes smaller and de-promotes the role of solid phase. When confining pressure is decreased and differential stress increased,

the role of pores is reduced since pore fluid or gas cannot handle the shear stress. Thus, the role of solid phase on accommodation increases. Increasing intermediate compressional stress increases the rock strength and reduces the influence of pores. Increasing temperature makes solids more ductile. Increasing pore pressure makes liquid-like flaws dominant. As strain increases, fluid cannot resist shear, thus solid-like flaws become more dominant. In a longer time-span with less cementing among minerals, rock can deform in a less brittle way. Wet rocks are more compliant than dry rocks.

Note that the researchers in the above references conducted experiments within relatively short periods. Compared with a geological time scale, this can be considered as instantaneous. Thus, we should not estimate which modes of accommodation are more or less likely based on the present observations. We need to reconstruct geological conditions when the major structural deformation happened, either qualitatively or, if possible, quantitatively.

The second classification from Table 1-1 – cataclastic versus plastic accommodation – is less impactful than the localized versus distributed classification. Once we correctly estimate one mode between localized and distributed, assuming localized features as a set of shear fractures or the swam of shear compaction bands is not that significantly different for modeling purposes than modeling them into a single porous medium. As Rutter (1986) classified in Table 2-1, cataclastic versus plastic accommodation comes from the dominance of elastoplastic or plastic behavior of rocks. Roughly, mineral components, temperature, and the timespan of overall deformations act as criteria to determine more or less plastic behavior (Table 2-1).

Here, however, we are not going to cover the cataclastic vs. plastic criteria, for several reasons. First, the structural models we use for the basin-reservoir scale are either geometrical, kinematically constrained, or dynamically constrained under linear elasticity. Thus, attempting to model the guiding factors within the modeling frameworks can yield unnecessary complexity to pursue false accuracy. Second, we can have information on the existence of deformation bands, fractures, or joints from outcrops and analogies from adjacent fields. For the case of distributed accommodation,

the evidence is more pervasive and widespread than localized accommodation. The features we can see from the well log and cores are good indicators of accommodation style within distributed accommodation. Third, for the distributed accommodation, whether the grains have deformed by cataclastic flow, granular flow, or by creeping, does not matter practically for both flow simulations and seismic responses.

In Rutter’s diagram, a subset of localized and cataclastic accommodation style is the fracture and joint (Table 2-1). Though kinematic strain from restoration analysis, or stress from retro-deformation analysis, is not the same as instantaneous stress-strain when the fracture occurred, comparing restoration-deformation stress-strain with fracture criteria can be meaningful to conduct qualitative comparisons. In Table 2-3, the first three failure criteria are more suitable for discrete failures such as joints and fractures. Mogi (1971) found the Von Mises criteria useful to capture the yield strength of sedimentary rock to start ductile behavior. S_o is cohesion strength, μ is the coefficient of internal friction, τ is shear stress, σ is effective normal stress, T_u is uniaxial tensile strength, and P is pore pressure.

Table 2-3: Failure criteria. (Jaeger et al., 2007, Pollard and Fletcher, 2005, Mogi, 1971)

Coulomb’s	$\tau = S_o + \mu\sigma$
Mohr’s	$\tau = f(\sigma)$
Griffith’s	$(\sigma_1 - \sigma_3)^2 + 8T_u(\sigma_1 + \sigma_3 + 2P) = 0$
Von Mises	$\{(\sigma_1 - \sigma_3)^2 + (\sigma_2 - \sigma_3)^2 + (\sigma_3 - \sigma_1)^2\}^{\frac{1}{2}} = const.$

For the case when we have a geometrical subsurface model that has linked nonlinear dynamic models, we can start to attempt to classify sub-categories of rock accommodation mode numerically. In that case, the following criteria can be used to classify sub-accommodation modes within deformation bands (Aydin et al., 2006; Borja and Aydin, 2004).

$$\mathbf{m} \cdot \mathbf{n} = 1 \quad \text{pure dilation band;}$$

$0 < \mathbf{m} \cdot \mathbf{n} < 1$	dilatant shear band;
$\mathbf{m} \cdot \mathbf{n} = 0$	simple shear band;
$-1 < \mathbf{m} \cdot \mathbf{n} < 0$	compactive shear band;
$\mathbf{m} \cdot \mathbf{n} = -1$	pure compaction band.

where

\mathbf{m} is a normalized unit eigen vector of A

$$A_{ij} = n_k c_{ikjl}^{ep} n_l \quad (2-1)$$

In equation (2-1), \mathbf{n} is the unit normal vector of the band, c_{ikjl}^{ep} is the elastoplastic constitutive tensor, and A is the elastoplastic acoustic tensor. Note that the classifications in equation (2-1) correspond with Figure 2-10.

2.2.6 Factors affecting on distribution pattern and characteristics of crack

In previous sections, we covered sources of geological uncertainty on structural deformation and rock accommodation. Even after we define proper sets of joints and fractures when localized accommodation is the case, we still have another uncertainty regarding distribution patterns of joints and fractures. They can be randomly grouped and form so called, “fracture swam”, or they can be evenly distributed across a certain area (Atkinson, 1984). Having same number of cracks with same geometry and orientation in a same volume in a evenly distributed way versus grouped together in sparse locations will lead hugely different impact on not only level of confidence on estimation but also on uncertainty on development and production. We are going to

cover two different types of approaches to link geological conditions on affecting characteristics of crack distribution.

First, understandings from a subcritical crack growth model can be useful to estimate pattern of crack distribution (Atkinson, 1984; Gale et al., 2014; Olson, 2004; Holder et al., 2001; Renshaw and Pollard, 1994). Subcritical crack growth is a fracture or joint generations at stress intensity significantly below the critical stress intensity factor (Holder et al., 2001; Renshaw and Pollard, 1994). This model is considered as an important mechanism to understand the generations of natural fractures (Holder et al., 2001).

$$V = A \cdot K_I^n \quad (2-2)$$

In Equation (2-2), V is crack propagation velocity, K_I is mode I stress intensity, A is a case specific constant, and n is subcritical crack index. When N is larger, fracture propagations depends more on pre-existing cracks and propagate around them. When N is smaller, fracture propagation becomes more wide-spread and less dependent on pre-existing cracks (Holder et al., 2001).

$$l_{adv} = 2a_0 \left(\frac{G}{G_{max}} \right)^\alpha \quad (2-3)$$

Equation (2-3) is a crack tip advance of individual crack in simulation time step when subcritical crack is modeled numerically (Renshaw and Pollard, 1994). In the equation, a_0 is crack length, G is elastic energy release rate for the fracture tip, G_{max} is maximum of G among every crack set, and α is velocity exponent that explain how strongly the propagation velocity of fracture is related to the degree of stress concentration. When α is small, every crack propagate relatively evenly while with α larger, crack propagation

depend more on tip stress concentration. Thus, α is acting similar with subcritical crack index, n , in equation (2-2).

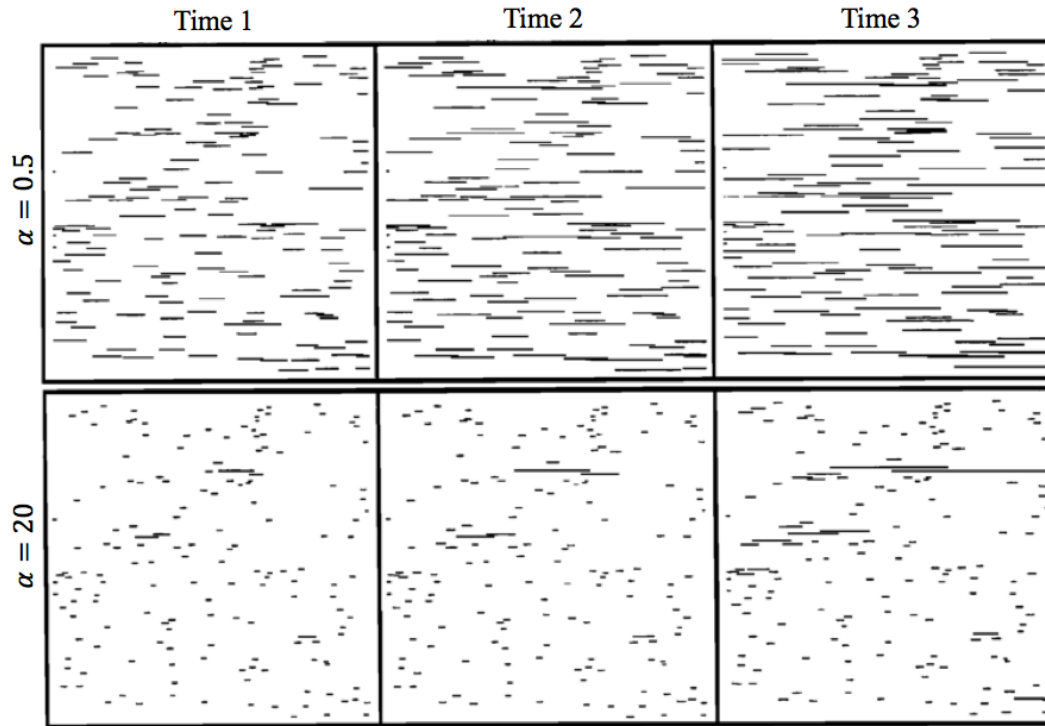


Figure 2-13: Effect of velocity exponents on crack propagation (Renshaw and Pollard, 2001). Time 1,2, and 3 is simulation results in different time steps that can be understood as different geological time. With higher velocity exponent, cracks having relatively bigger lengths tend to become even bigger while results from smaller velocity exponent tend to develop propagate other cracks evenly.

Figure 2-13 shows simulation results of subcritical crack development with different effect velocity exponent values (Renshaw and Pollard, 1994). When subcritical crack mechanism is dominant (having larger velocity exponent), crack propagation is focused on some dominant cracks and dependency on flaw distribution become negligible. However, when subcritical crack mechanism becomes less dominant (smaller velocity exponent), crack propagations spread more evenly and distribution of flaws are become more critical. Note that both of numerical simulations in Figure 2-13 share same flaw distribution for initial condition.

The second factor is interplay of differential tectonic stress and fluid pressure. From numerical sensitivity study of plastic deformation and damage of rock with

calibrations from experimental data, following observations were found (Busetti et al., 2012b; Busetti et al., 2012a). 1) When post-failure softening is considered, fractures are extremely localized; 2) When the difference between maximum and minimum principal stress, fractures are more easily generated, but localized with low connectivity; 3) Small difference between principal tectonic stress is require higher pore pressure to generate fracture. However, the abundance of fracture will be high with better connectivity; 4) When pore fluid is less viscous, fracture distribution is more uniform and both of tensile and shear fractures observed; When pore fluid is viscous, fractures are more localized and tensile failure becomes dominant.

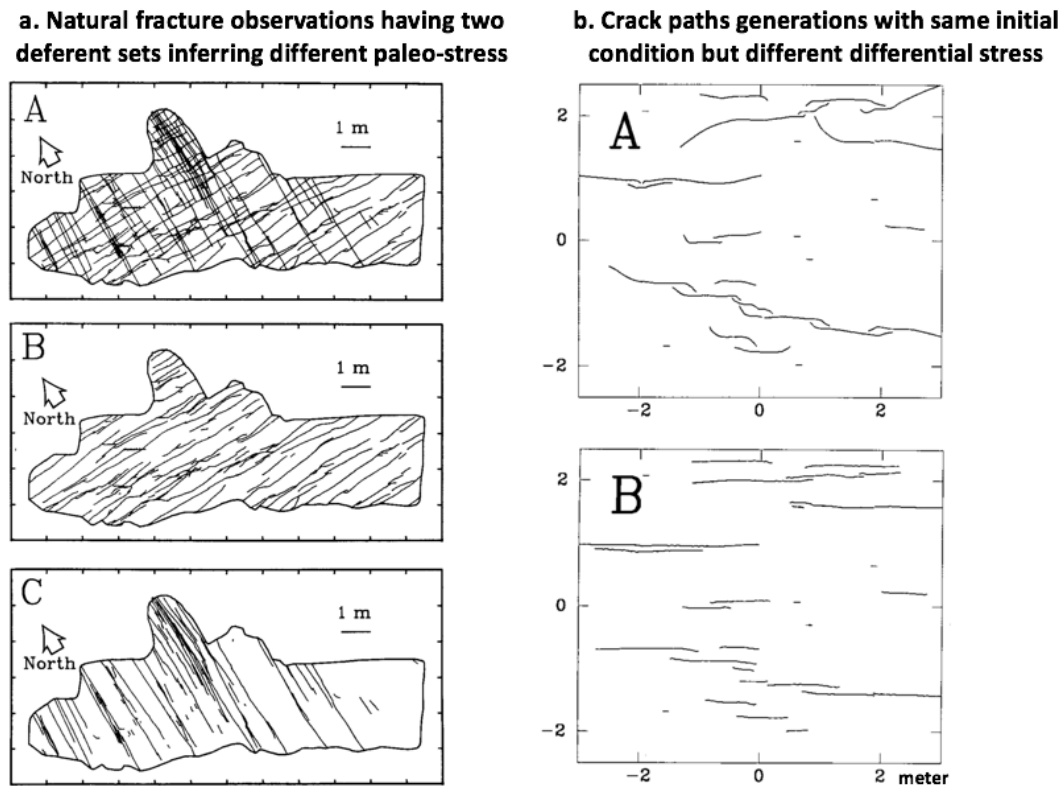


Figure 2-14: Inferring paleostress from natural fracture observation (Olson and Pollard, 1989). a) natural fractures observed from outcrops (a-A). First set is more evenly distributed and infer less differential paleostress (a-B). Second set infer paleostress when generating cracks had more differential stress than the first set (a-C). b) Numerical simulation of crack propagation under nearly isotropic stress condition (b-A) and significant differential stress (b-B) to reproduce field observations on figure a.

Figure 2-14 shows a study on inferring paleostress by patterns from natural fractures (Olson and Pollard, 1989). Left column of the figure is a field observation of natural fractures in outcrops of Rico Formation, Utah. Olson and Pollard categorized cracks into two groups and link the first SW-NE striking set with a paleo stress having smaller differential horizontal stress than the paleo stress for the time when the second NW-SE striking cracks generated. They reproduce consistent results from numerical simulations – when larger differential stress applied, cracks propagate along the major cracks and crack abundance becomes more heterogeneous.

This results are actually a repeat of factors affecting rock accommodation modes in Table 2-2. As we discussed in Section 2.1 and 2.2, discrete failure in a finer resolution can be a ductile deformation in a coarse resolution. The previous categorization was the factors to infer accommodation modes on each individual grid, or node. If we zoom out to the whole boundary of interest, the same factors we discussed to distinguish localized and distributed can be reused. The effect of viscosity of pore fluid can be useful to distinguish the geological timing of joints and shear fractures when both of them are encountered from observations.

2.3 Endeavors to link structural deformation and rock properties to forecast reservoir responses

As we discussed throughout Chapter 2.1, for larger-scale geological features, e.g. formation tops, faults, folds, and reservoir boundaries, we can extract geometrical models with uncertainty – due to data resolution and coverage – with high levels of uncertainty on kinematics/dynamics of structural deformation. By having geometrical models only, we can estimate static values such as total pore volume, or original volume of hydrocarbons in place.

To estimate dynamic responses, we need to populate the sub-resolution property that we covered in Chapter 2.2. Unlike estimating static volumes, forecasting reservoir responses is highly dependent on spatial distributions and values. However, we do not know the existence, abundance, and spatial distribution of sub-resolution features. Thus,

reservoir property modeling involves some level of statistical approaches (Caers, 2005; Mukerji et al., 2001). However, we know sub-resolution features such as fractures, deformation bands, and low porosity zones are geometrically, kinematically, and dynamically linked with reservoir structure. Obviously, there have been many approaches to try to link sub-resolution reservoir features and properties with larger scale reservoir structures.

2.3.1 Geometrical approaches

Curvature analysis is a typical example of a geometrical approach using subsurface geometrical models or seismic data to estimate reservoir properties, especially sub-resolution faults and fractures (Al-Dossary and Marfurt, 2006; Hakami et al., 2004; Bergbauer et al., 2003). These approaches rely on geological knowledge that certain sub-resolution features are linked with certain geometry of larger scale structural geometry, or geophysical knowledge on how seismic anomalies relate to certain geological features (Sava, 2004; Avseth et al., 2001; Teng, 1998). Since they do not have kinematic or dynamic models on their estimations, they are statistical approaches from the beginning. As we discussed in Chapter 2.1, different kinematic and dynamic models can give identical geometrical models in the present time.

2.3.2 Kinematic and dynamic approaches

Kinematic information from restoration analysis has been used for sub-resolution fracture estimation (Paul et al., 2009; Hennings et al., 2012; Lohr et al., 2008; Suzuki et al., 2005). The basic idea of these studies is linking restoration strain tensors to estimate spatial distributions of fracture abundance and their orientations. If the principal strain is tensile, we can attempt to link it with a mode-I fracture, or joint. If the strain is compressional with a differential strain component, we can link it with mode-II, a shear fracture. In Lohr and colleagues' case (2008), observations from wells and estimation based on using restoration strain worked well for open mode fractures, but less well for shear mode fractures. Hennings et al. used restoration strain to calculate deformational

stress by using linear elasticity (Hennings et al., 2000). Then, using the Mohr-Coulomb failure criteria, they estimated fractures in 3D models. They also used well data on one region as hard data for calibrating restoration stress and fracture abundance. Their results reproduced good matches around the calibrated area, but less similar results for other regions, which was the other side of a major fault on the modeling area. Dynamic models with linear elasticity were used to model secondary fault development from local stress perturbation by major faults, and compared with fault interpretation of an oil field in the North Sea (Maerten et al., 2002). Secondary fault estimation from the dynamic model regenerated major trends and orientations, but failed to reproduce the local heterogeneity of directions.

Lovely et al. (2012) pointed out that dynamic restorations heavily depend on the boundary conditions, including the assumptions on the restored geometrical model. They also demonstrated that dynamic models under linear elasticity and nonlinear elasticity give similar principal strain-stress orientations overall, but hugely different magnitude of stress distributions.

2.3.3 Linkage between structural deformation and rock accommodation

Larger-scale structural deformation is accommodated by smaller-scale deformation. We covered endeavors to link structural deformation with reservoir property estimation in Chapter 2.3. It was more focused on practical applications, i.e. how to utilize the spatial distribution of structural attributes for property modeling and theoretical models already formalized into mathematical formulations. It is worth briefly covering how geoscientists extract the relationship between structural deformation and rock accommodation.

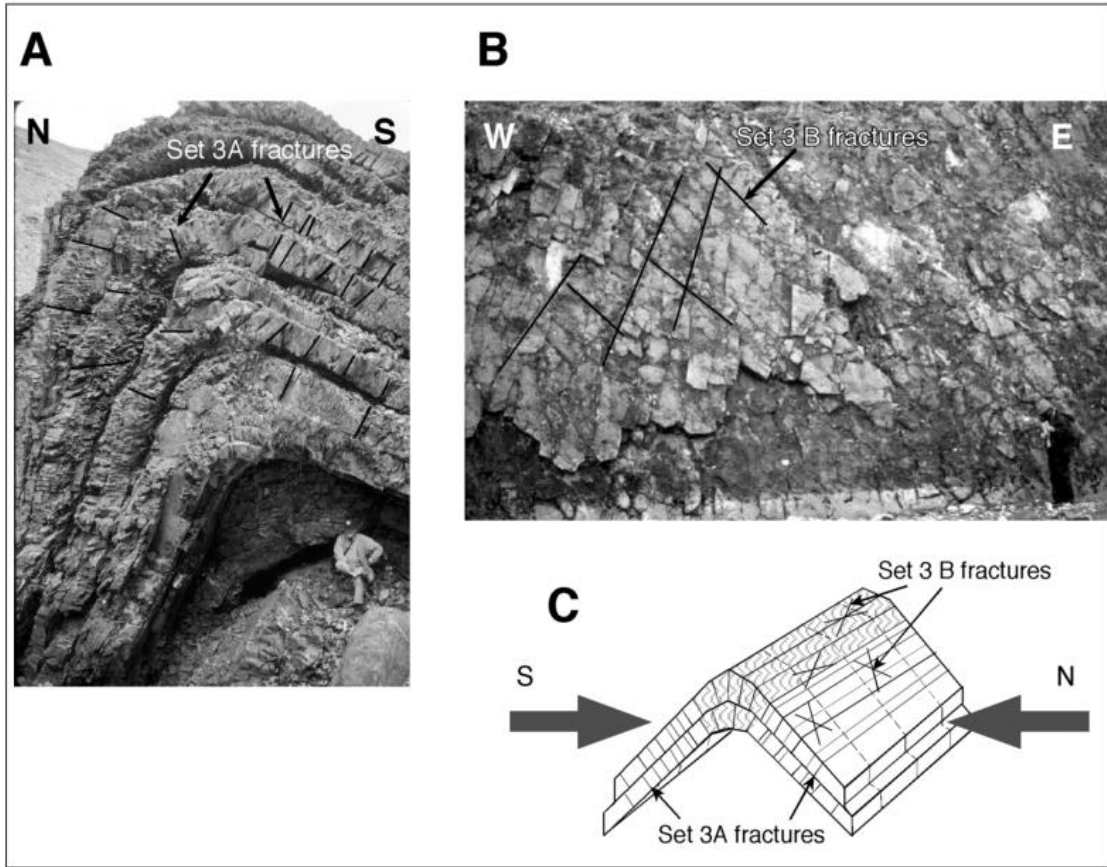


Figure 2-15: Geological observation from outcrops of folds and fractures (Hanks et al., 2004). The observed fracture set from pictures A and B is conceptualized as a geometrical model in picture C.

The first typical tool is a field survey. Figure 2-13 shows a typical geological survey and interpretation process to develop a model to link macro deformation with sub-resolution accommodation (Hanks and Wallace, 2004). Geoscientists observe and conceptualize the geometry of large-scale and small-scale features. Then, they analyze whether the features kinematically and dynamically make sense.

A second common tool is lab experiments. Since many instances of sub-seismic scale accommodation, such as fractures and ductile deformation, can be reproduced under lab conditions while preserving the scale, many lab experiments have been conducted to investigate the relationship among stress-strain loading, temperature, and pore pressure conditions to develop geological features and change rock properties. Peterson and Wong (2005) compiled many of the key lab experiments regarding these different subsurface conditions. Mathematical formulations of the kinematics and

mechanics of the geological features are obtained from, or compared with, the experimental results. In Chapter 2.2.5, we did not cover distributed accommodation, noting that cores can capture those features more easily than localized accommodation. Since geoscientists observed distributed accommodation from field surveys and cores, they also conducted many lab experiments to investigate how deformational loadings change rock properties.

Many researchers investigated how stress-strain loading on rocks develop permeability anisotropy (David et al. 1994; Gray and Fatt 1963; Zoback and Byerlee 1976). Gray and Fatt (1963) conducted a uniaxial load test on a sandstone core to investigate the horizontal and vertical permeability anisotropy induced by stress anisotropy. Zoback and Byerlee (1976) expanded the investigation to pore volume strain induced by differential stress, and measured relations among differential stress, stress anisotropy, and pore volume changes. David et al. (1994) focused on compaction-induced permeability changes and their hysteresis over typical sandstones, but did not consider the anisotropy of permeability. Unlike previous studies focusing mainly on stress-induced changes to permeability, Arch and Maltman (1990) studied shear deformation in clay samples, conducting comparative Darcy flow experiments by rotating the sheared clay to change the fluid flow direction and sheared zone angle, and assessing measured permeability and tortuosity using a scanning electron microscope. Dewhurst et al. investigated how shear with compaction develops anisotropy in shale (Dewhurst et al., 1996).

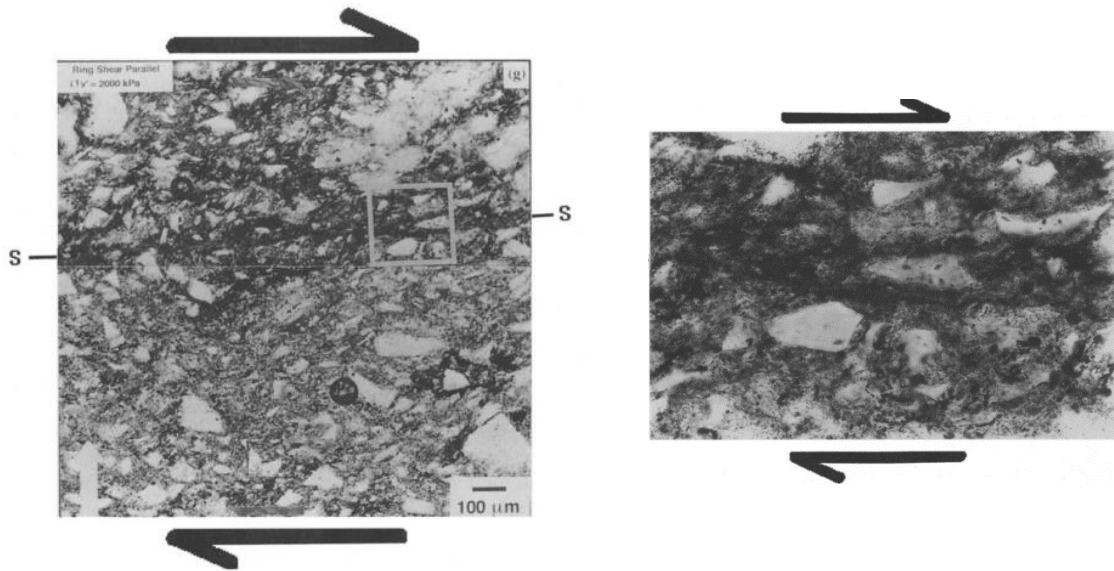


Figure 2-16: Shear deformation on shale develops permeability anisotropy in a way to promote horizontal flow (Dewhurst et al., 1996)

Figure 2-16 shows the results of Dewhurst et al. (1996). From shear deformation, shale develops horizontal connectivity by pore and mineral arrangement. It increases horizontal permeability at least two orders of magnitude bigger than vertical permeability. This depicts why shale can be a good sealing formation but still promote hydrocarbon migrations over a geological time span.

The third tool is numerical simulation. Numerical simulation has benefits over lab experiments by allowing more freedom on boundary conditions, allowing sensitivity analysis that are limited in lab experiments by the type of available materials, and including the capability to calculate point by point strain-stress evolutions. Finite Element Method (FEM) and Distinct Element Method (DEM) are typical examples in earth science and rock mechanics contexts (Antonellini and Pollard, 1995; Borja and Aydin, 2004; Bruno, 1994). Comparing Antonellini and Pollard's experiments with Bruno's is a good example of the usefulness of numerical simulations. Both of them used DEM, which uses spheres or circular cylinders as representations of mineral grains, to simulate how the synthetic rock behaves under vertical compression. They produced significantly different results, which represent different geological process. One experiment that did not consider cementing among grains in the DEM simulation gave

a rearrangement of grains and pores to accommodate vertical loading (Antonellini and Pollard, 1995). The other study, which does consider cementing – merely using a cut-off tensile stress to let two grains fall apart – produced vertical fracture developments as vertical loading increased (Bruno, 1994). The first result may be a representation of the deformation of soft rock or development of compaction bands, while the latter one may be a representation of stiff rock. In Table 2-2, the amount of cementing was one important factor to promote localized accommodation. These two numerical simulations depict the effect of cementing among grains.

2.4 Summary

In this chapter, we discussed two sources of geological structural uncertainties: structural deformation, and rock accommodation. Uncertainty about structural deformation comes from not knowing the exact current geometry, and not knowing the kinematical and dynamic evolution of the structure from the past to the present status. Uncertainty on rock accommodation mainly comes from limited observations under subsurface conditions, and a lack of geometries of geological features due to the resolution of our observations.

In the end, we want to evaluate a given area of subsurface for a given purpose – pollution mitigation, or hydrocarbon exploration and development. To do that, we have to fill the area and volumes within geometrical models of horizons and faults with reservoir properties. As we discussed, bigger scale structural deformation and smaller scale rock accommodation are closely linked. Indeed, it is a categorization introduced by the way we investigate subsurface problems and the way we do the geomodeling process, not from the inherent natural characteristics of the Earth.

In the next chapter, we will propose a new reservoir modeling workflow that models reservoir properties while considering multiple geological scenarios in different mode of structural deformation, and different rock accommodation scenarios.

Chapter 3

3 Reservoir Modeling with Multiple Geological Scenarios on Modes of Structural Deformation, and Accommodation

In this chapter, we propose a reservoir modeling workflow to capture the effects of both sources of geological uncertainty we discussed in Chapter 2: mode of structural deformation, and mode of rock accommodation. Whether we have an explicit form of geological explanations for structural evolution or not, interpretations of current structural geometry always involve the interpreters' assumptions on how the earth kinematically or dynamically evolved. Thus, if we only focus on the *geometry* of faults and folds and their *geometrical* uncertainty, we lose some of the valuable geological information and interpretations implicitly or explicitly used during the structural interpretation process. We want to make a subsurface model from structural interpretations to allow petrophysical modeling in a way that is relevant with our implicit or explicit underlying geological assumptions. If the interpretations are uncertain, we should have the capability to propagate the influence of different assumptions through the modeling process. The proposed workflow in this chapter aims to capture the higher-level uncertainty of not knowing the exact reservoir structure and the relation between reservoir structure and the sub-resolution reservoir properties.

3.1 Motivation

For reservoirs with relatively large structural and deformational complexity, reservoir forecasting, and uncertainty quantification becomes more difficult, as the governing

conditions of reservoir characteristics vary within the reservoirs. For example, the Suban gas field case in Indonesia shows fracture orientations, and its flow characteristics in one region are very different from those in another region within the same formation but at a different structural location (Hennings et al., 2012). Other similar approaches also showed partially successful results by showing good agreements with observations from wells within a region close to the calibration wells (but not from other well observations), or agreement with only certain modes of fractures (Lohr et al., 2008; Paul et al., 2009). Before we abandon these approaches that attempted to utilize attributes from restoration analysis, it is worthwhile to compare a typical geomodeling process, depicted in Figure 3.1 (modified from Caers, 2005), with the geological uncertainties we discussed in Chapter 2.

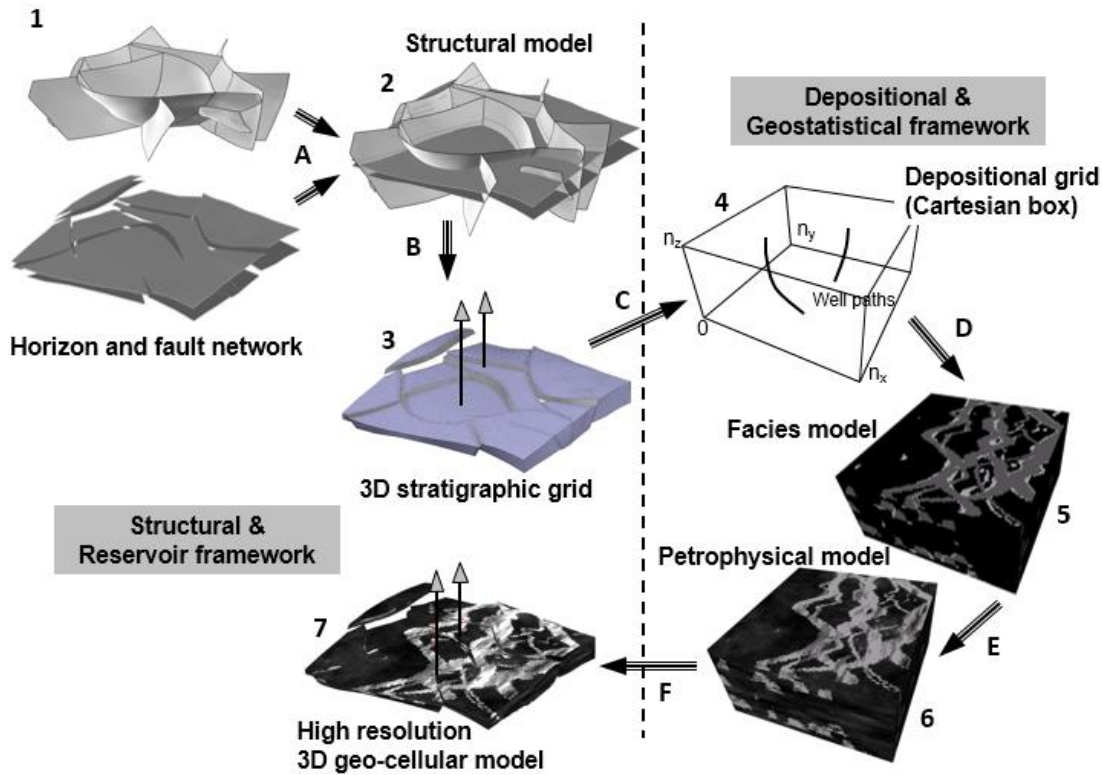


Figure 3.1: A typical geomodeling process (figures modified based on Caers, 2005). 1 - horizon and fault interpretation, 2 - geometrical structural model, 3 - gridding in current geometry, 4 - depositional grid for property modeling, 5 - facies modeling, 6 – petrophysical property modeling, and 7 – final model in current geometry. The processes along these steps are marked by the capital letters. In each step, some

level of simplification and approximation is made. Thus, during the process, we lose certain levels of qualitative and quantitative information.

Cartoon 1 in Figure 3.1 depicts the interpreted faults and horizons. As Walsh (1996) commented, structural features from seismic interpretations usually have too few faults for the structure to make sense kinematically. Due to the seismic uncertainty (Li et al., 2015) and structural modeling uncertainties (Aydin and Caers, 2015), the geometrical model from interpreters are already uncertain. Cartoon 2 is a manually or numerically optimized structural model of the current geometry. When we convert faults and surface interpretations into a set of optimized surfaces that are ready to be discretized for further processes, they are again simplified. Cartoon 3 is a stratigraphic grid for property modeling. Cartoon 4 is a depositional grid that represents the paleo depositional condition. The C between Cartoons 3 and 4 marks a coordinate transformation between current geometry and paleo geometry.

In Cartoon 4, using the hard data along the well and the chosen geostatistical algorithm, we populate the spatial distribution of the lithology (Cartoon 5) and petrophysical properties (Cartoon 6). Thus, D represents a geostatistical simulation for the categorical properties, and E represents the geostatistical simulations for actual physical properties. Finally, we “copy and paste” the populated lithofacies and petrophysical properties into a geometrical structure model in Cartoon 7. The processes of B, C, and F involve coordinate transformation between two different geometrical domains – the physical domain representing the present, and the depositional domain representing the past. In each step the layers are discretized and we transfer the data to the next step. In this transferring process, we lose qualitative information that is not explicitly quantified, or the information that is excluded from models in the subsequent processes.

3.1.1 To assess the impact of a parameter, we have to vary it.

Without having any detailed geomodeling knowledge, we can say without providing any references that the modeling activities on Cartoon 1 to 3 are more influential sources

of uncertainty than the uncertainty captured by having different geostatistical realizations in cartoon 5 and 6. If we go back to previous endeavors to link structural information with property estimations, they all fixed the part to the left of the dashed vertical line and only tried to estimate fractures using the fixed structural attributes (Lohr et al., 2008; Paul et al., 2009; Hennings et al., 2012; Maerten et al., 2001). To investigate uncertainty without knowing the proportions among different lithofacies, we need to compare subsurface responses from subsurface models generated with different target proportions of lithofacies, or with different training images for the Multiple-Points-Geostatistics (MPS) algorithm (Jeong, 2015). If we want to estimate geological features that we believe have a strong relationship with reservoir structures, we should have more than one structural model to properly investigate the influence of structural aspects on subsurface responses. This is the first theme motivating the new workflow: if we want to assess the influence of a parameter on responses, we have to vary the parameter.

3.1.2 Deformation changes not only the geometry, but also the internal properties

The second motivation involves restoration and forward deformation among the present and past geometries. We can notice that the vertical wells in Cartoon 3 become curvilinear wells in Cartoon 4. Since the present geometry of the subsurface features are faulted and folded, they cannot remain vertical if we rewind the geological time to the past condition. If the stratigraphic grid is made from proper comparisons between present and past geometry (Mallet, 2004), the present spatial distance will be distorted in the property modeling grid, just as the vertical wells are distorted in Cartoon 5. Recall from Chapter 2 that we have uncertainty from not knowing the mode of structural deformation. Thus, it is uncertain how the curvilinear shapes of well trajectories would be in the depositional grid. A second question originated from this point: “How about the measured property along the well?” From Cartoons 3 to 4, we just copy and paste, so to speak. From Cartoon 6 to Cartoon 7, we again copy and paste them back. Rocks along the imaginary curvilinear path are aligned in a vertical line from the deformation.

But we do not care about the possible influence of the deformation on the petrophysical properties.

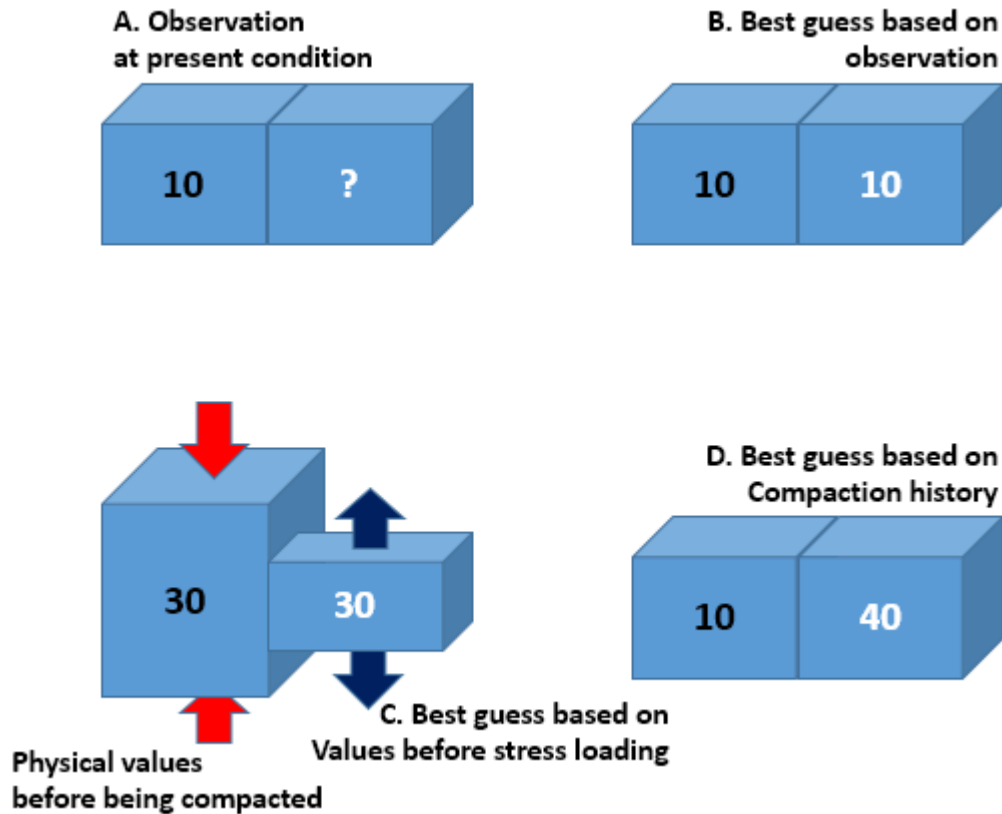


Figure 3.2: Schematic cartoons of a thought experiment to test the “copy & paste” convention.

Figure 3.2 is a schematic cartoon of a thought experiment, depicting how the current practice of “copy and paste” can go wrong. Let assume we have an observation of any physical value of 10 at a grid block, and we want to estimate the physical property of a block on the right (Cartoon A). Estimating a value of 10 would be a safe choice if we can assume the environments of the left block and right block are similar. However, if the left block has been exposed to compression and it originally had a value of 30, while the right block has been exposed to tensile loadings (Cartoon C), then in this case, the best guess would be a value of 30 before loading was applied. Then, the value of the right block would be increased to a value bigger than 30 (Cartoon D). Copying and pasting A to B, and B to A, would give the wrong answer.

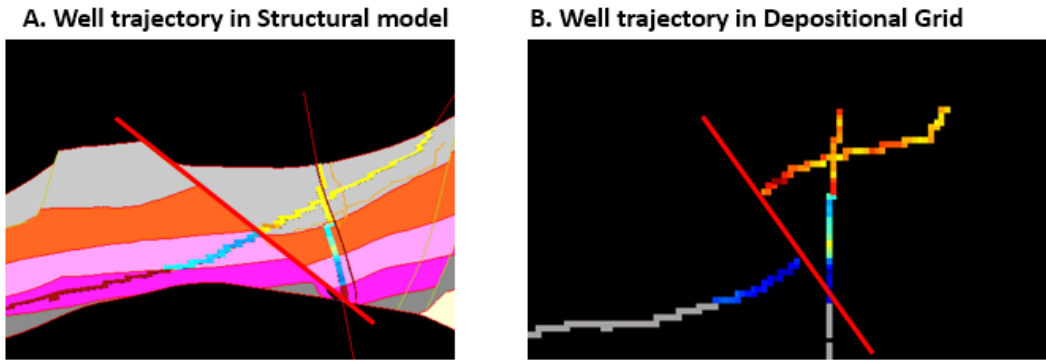


Figure 3.3: Comparison of a well trajectory across a normal fault in a vertical section. A - in a present structural model (visualized using geomodeling software Paradigm SKUA[®]). B - in a depositional grid (visualized using Stanford Geostatistical Modeling Software, SGeMS). The scale is intentionally omitted.

Figure 3.3 depicts geometrical differences of a well trajectory in the present structural model and a well trajectory in a depositional grid. A horizontal well drilled from the right to the left in inset A becomes discontinuous in inset B when plotted in a depositional grid. We can anticipate that kinematic and dynamic evolutions of the deformation of reservoir rocks across the hanging wall and the footwall may not be the same. Probably the formation penetrated by the horizontal well on the left footwall side has been compacted during normal faulting, while the formation on the hanging wall side exposed dilation from dragging forces during normal faulting. Using the thought experiment we conducted in Figure 3.2, “copying and pasting” the measured physical values along the well into the depositional grid, and “copying and pasting” them back after property modeling makes the results less useful. As we geometrically “restore” and “forward deform” the geometrical spatial location via coordinate transformation we also have to restore the petrophysical values across the wells when the values are used as hard data in the depositional grid. When we copy and paste the populated petrophysical properties into the present structural model, we have to forward deform the values. We do not want to make and use petrophysical properties that are inconsistent with the geological assumptions we have – structural deformation and rock accommodation.

3.1.3 Well data is precious, but it is one-dimensional

From the beginning, well data is a biased representation of a reservoir description. We drill a bright spot that looks to be the most promising after considering all of our knowledge. Thus, extrapolations from the well data can lead us to certain levels of over- and underestimation on property extrapolation. On top of that, as we discussed in Chapter 2, there are many alternative evolution paths by which sub-resolution volumes of formation and rocks accommodate the applied structural deformation. Wells are curvilinear lines in a vast three-dimensional space. We have possibilities of having unseen geological features from well interpretations in the subsurface away from the wells. We also need to include sub-resolution geological features that were not observed from the well, but are geologically possible to exist. This is the third motivation for creating a new modeling workflow. We should not stick with only the features observed along the well paths.

With these ideas from the three motivations, we can see previous attempts to link structural information with fracture estimation differently (Lohr et al., 2008; Paul et al., 2009; Hennings et al., 2012; Maerten et al., 2001). First, all of the previous studies used single geometrical structure models for present geometries with single restoration models. Structural uncertainty is a higher order uncertainty than spatial distributions of sub-resolution geological features. To investigate the effects or correlations of structural deformation attributes with the spatial distribution of reservoir properties, we should use multiple structural or deformational models. If we want to assess the impact of a parameter, we should vary it.

Second, previous studies only focused on fractures, typically emphasizing specific types of fracture sets. Hennings et al. (2012) used restoration strain with rock properties to calculate the Mohr-Coulomb failure criteria. Other failure criteria could be tested, or even other accommodation modes could be considered. For instance, a study on a CS field in Indonesia shows that even in a naturally fractured reservoir, areas with no fractures give the highest productivity within the field (Paul et al., 2009). That region could have been deformed by a distributed accommodation in a way that preserved high

permeability, or the region might have too many fracture sets that fragmented the fracture surfaces, and made the flow and seismic responses similar to typical highly porous and permeable rocks.

We can reuse Figure 3.2 to depict the previous studies with some other possibilities. Hennings et al. used present petrophysical values when computing Mohr-Coulomb failure criteria with strain from restoration analysis. This can be mapped by applying compaction and extension in Figure 3.2-B, which has underestimated values for the right block. Even if we have exact values like in Cartoon D, applying failure criteria on Cartoon D is wrong because the spatial distribution of values were for Cartoon C. However, we also have the possibility that the two blocks accommodate the compaction and extension with a distributed accommodation style.

3.2 Methodology

We propose a reservoir property modeling workflow to capture the effects of both sources of geological uncertainties: how the reservoir has been deformed, and how the rock has accommodated the deformation. The new framework requires the following capabilities to capture uncertainty on structural deformation and rock accommodation:

- Use structural deformation attributes from restoration/forward deformation analysis.
- Restore the hard data using structural deformation attributes under the mode of rock accommodation.
- Use the restored hard data, not the measured hard data to condition geostatistical simulation.
- When transferring populated reservoir properties into the present structural model, copy, forward-deform, and paste, rather than just copying and pasting.

3.2.1 Proposed workflow

The new geomodeling framework consists of three processes different from the typical geomodeling process (Figure 3.1):

- A. Restoration of hard conditioning data by using the structural deformation attributes and rock accommodation mode
- B. Geostatistical modeling using restored hard data
- C. Forward-deformation of populated data

Equations (3-1), (3-2), and (3-3) correspond with these three components. Equation (3-1) express the restoration of the measured hard data along the well to a restored condition. In equation (3-1), f is the functional expression of the evolution of a reservoir property from past condition to present condition. Thus, f^{-1} is the inverse function of f , a restoration of reservoir properties. O stands for the observations in the present condition, while O^* is the restored value of O to a past condition. r is the structural deformation attributes that contain spatial variables containing deformational information, such as displacement vectors or restoration strains and stress. Subscript n is an index for a specific mode of structural deformation scenario out of N alternatives. Subscripts m and M correspond to an index for a specific mode of rock accommodation scenario out of M alternatives. If we have N different scenarios for structural deformation, which are a combination of a geometrical structural model with certain kinematic/dynamic models, and M different scenarios for rock accommodation, an identical set of observed values along the wells will be converted into N by M number of sets of different values. Note that the curvilinear well trajectory of Cartoon 4 in Figure 3.1 and the disconnected well trajectory in Figure 3.3 are slightly different in the depositional grids because they have different scenarios for the mode of structural deformation.

$$O_{nm}^* = f^{-1}(O, r_n, A_m), \quad n = 1:N, \quad m = 1:M \quad (3-1)$$

$$S_{nm}^* = \text{geostat.}(O_{nm}^*) \quad (3-2)$$

$$S_{nm} = f(S_{nm}^*, r_n, A_m), \quad n = 1:N, \quad m = 1:M \quad (3-3)$$

Equation (3-2) is a geostatistical simulation to populate and fill the depositional grid with petrophysical values. Note that we use O_{nm}^* , not O . Thus, the values we use as conditioning hard data are restored values based on a combination of structural deformation mode n and rock accommodation mode m . Equation (3-3) is the forward-deformation of the populated petrophysical properties, S_{nm}^* , into the values of the present status.

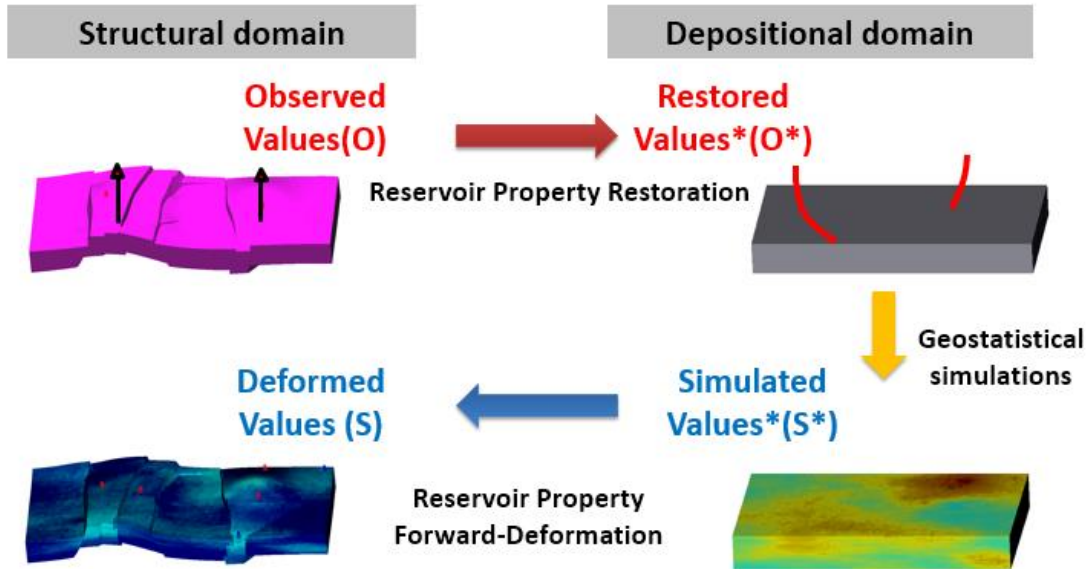


Figure 3.4: A schematic diagram of the three proposed components. The red arrow represents equation (3-1), the yellow arrow is for equation (3-2), and blue arrow is for equation (3-3). Explanations of the structural model used are covered in the following sections.

Figure 3.4 is a pictorial explanation of the proposed workflow under a specific combination of structural deformation and rock accommodation scenarios. We can notice that the spatial distribution of the simulated property, S^* , in the depositional domain looks like a typical realization using a two-point sequential geostatistical algorithm, such as Sequential Gaussian Simulation (SGSim) (Remy et al., 2009; Caers,

2005). However, the property values in present structural domain, S , deviate from the original results by considering compaction and extensional loading during structural deformation.

Equations (3-1) and (3-3) only contain two different time steps. By doing so, we implicitly assume that all the target reservoirs in the geomodels are deposited within a shared geological time span. However, if we have multiple geological episodes that affect structural deformation and the depositional environment, and we have multiple geometrical models to represent different episode times, we can discretize the forward deformation functions into multiple series of functions.

3.2.2 Defining scenarios for mode of structural deformation and mode of rock accommodation

In Chapter 2, we covered the sources of geological uncertainty from structural deformation, and from mode of rock accommodation in a general sense. When we have a specific subsurface area to model, first we can assess the geometrical uncertainty from seismic interpretation. If we are uncertain on a geometrical interpretation, we may have multiple present geometrical structure models. On top of that, we can select available kinematic/dynamic models that are compatible with the interpreted geometrical models. From this process, we can introduce multiple scenarios for the mode of structural deformation. Thus, a scenario of structural deformation is a combination of the present geometrical model and a kinematic or dynamic model explaining the link between the present and past structural geometry.

To develop multiple scenarios for rock accommodation modes, categories from Chapter 2 can be useful. For instance, say we have a core section from wells showing that grains are tightly bounded by cementing, and we are not sure of the relative timing of cementing over major extensional faulting. By changing the order of cementing and extensional deformation, we can double the number of scenarios of rock accommodation modes because if a major structural deformation happened prior to

cementing, it is apt to accommodate it by distributed accommodation, and localized accommodation for the order of cementing and structural deformation.

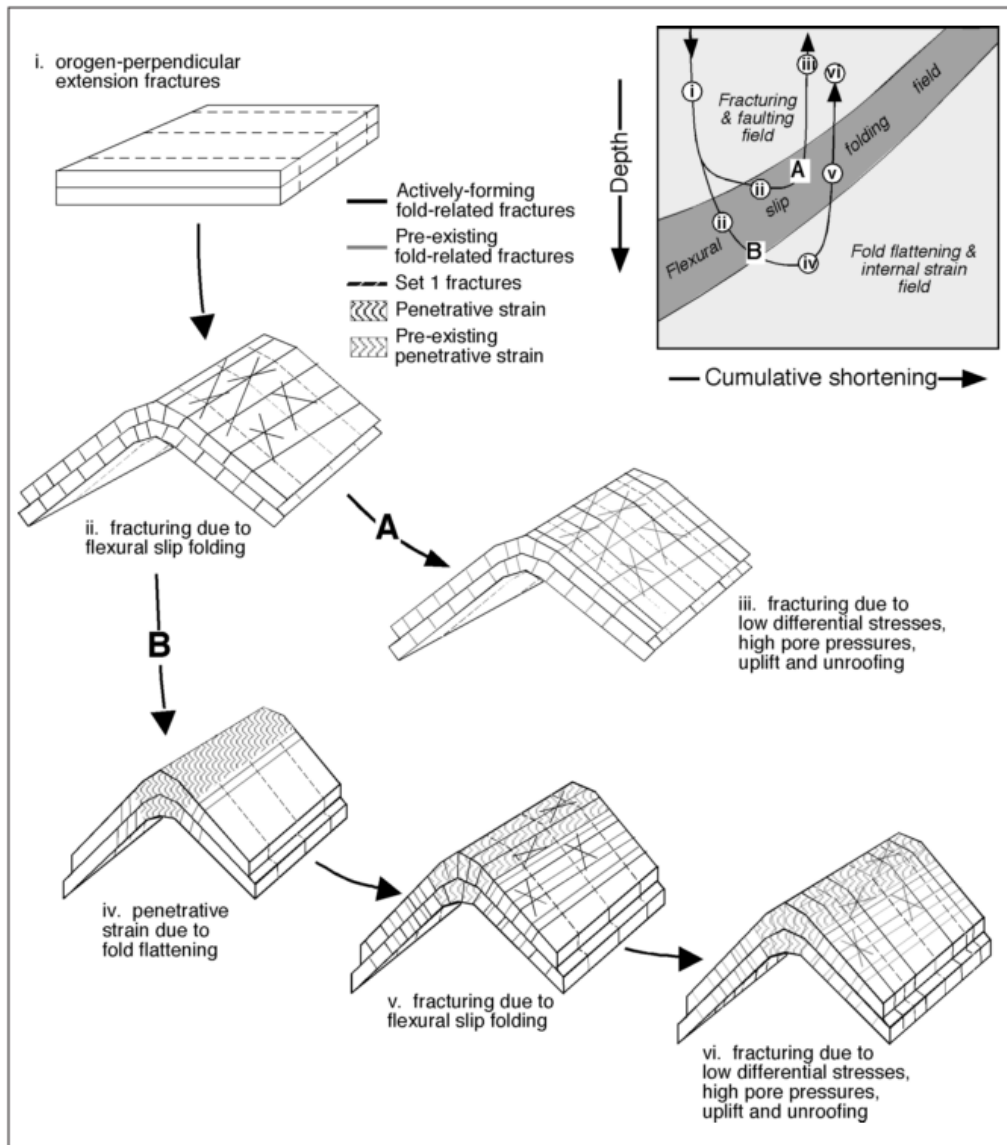


Figure 3.5: Examples of geological explanations for having different fracture sets on a fold structure. Paths A and B go through different burial histories, and thus have different stress history and generate different fracture sets (Hanks et al., 2004).

Figure 3.5 offers a good example of having multiple geological explanations, and thus multiple scenarios of different geometrical and kinematic models, for almost identical fold structures (Hanks and Wallace, 2004). The authors conducted field observations of many fold outcrops in Brooks Range, Alaska. Many of the folds have

different fracture sets. The above figures are multiple possible geological interpretations to make sense of the structure and observations.

3.2.3 Structural deformation attributes and a proxy restoration

Kinematic models and restoration under a certain kinematic model give restoration displacement vectors. Figure 3.6 depicts the relations between two different grids that are linked by displacement vectors. If dynamic models link the two grids, we have force and stress information in addition to the attributes we get from kinematic models.

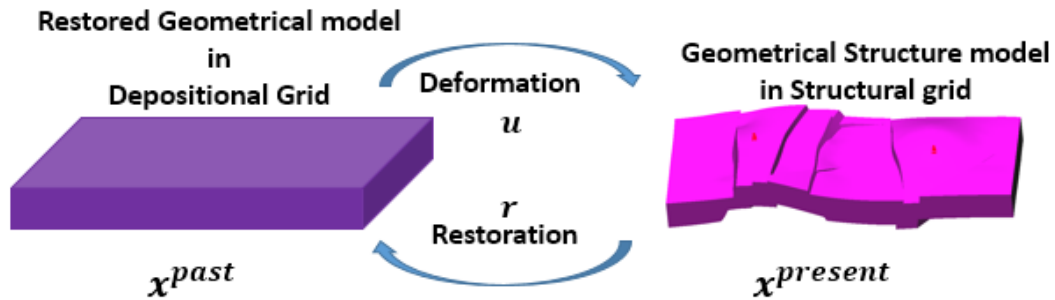


Figure 3.6: Displacement vectors between a present structural grid and a past depositional grid.

$$\mathbf{x}^{[past]} = \mathbf{x}^{[present]} + \mathbf{r}$$

$$\mathbf{r} \approx -\mathbf{u} \tag{3-4}$$

Equation (3-4) shows the relations between present and past geometry with a restoration displacement vector. The reason why we use “ \approx ” is because when using dynamic models for restoration, restoration displacement and deformation displacement are not symmetrical in some cases (Maerten et al., 2006; Lovely et al., 2012; Lewis et al., 2013). From the deformation displacement vector, the Lagrangian strain can be calculated using equation (3-5).

$$E_{ij} = \frac{1}{2} \left(\frac{\partial u_i}{\partial X_j} + \frac{\partial u_j}{\partial X_i} + \frac{\partial u_k}{\partial X_i} \frac{\partial u_k}{\partial X_j} \right) \quad (3-5)$$

$$\varepsilon_{ij} = \frac{1}{2} \left(\frac{\partial u_i}{\partial X_j} + \frac{\partial u_j}{\partial X_i} \right) \quad (3-6)$$

$$\begin{aligned} \begin{bmatrix} \frac{\partial u_i}{\partial X_i} & \frac{\partial u_i}{\partial X_j} \\ \frac{\partial u_j}{\partial X_i} & \frac{\partial u_j}{\partial X_j} \end{bmatrix} &= \begin{bmatrix} \frac{\partial u_i}{\partial X_i} & \frac{1}{2} \left(\frac{\partial u_i}{\partial X_j} + \frac{\partial u_j}{\partial X_i} \right) \\ \frac{1}{2} \left(\frac{\partial u_j}{\partial X_i} + \frac{\partial u_i}{\partial X_j} \right) & \frac{\partial u_j}{\partial X_j} \end{bmatrix} \\ &+ \begin{bmatrix} 0 & -\frac{1}{2} \left(\frac{\partial u_j}{\partial X_i} - \frac{\partial u_i}{\partial X_j} \right) \\ \frac{1}{2} \left(\frac{\partial u_j}{\partial X_i} - \frac{\partial u_i}{\partial X_j} \right) & 0 \end{bmatrix} \\ &= \begin{bmatrix} \varepsilon_{ii} & \varepsilon_{ij} \\ \varepsilon_{ji} & \varepsilon_{jj} \end{bmatrix} + \begin{bmatrix} 0 & -\omega \\ \omega & 0 \end{bmatrix} \end{aligned} \quad (3-7)$$

The infinitesimal components of strain (equation (3-6)) are defined using the first two parts of the right-handed part of equation (3-5). Deformation gradients can be divided into symmetric and asymmetric parts, as shown in equation (3-7). The left term of the right-handed part is for the infinitesimal strain, equation (3-5), and the right term is for pure rotation. Using infinitesimal strain over Lagrangian strain will introduce errors in the process. However, using infinitesimal strain over Lagrangian strain is more convenient since it contains deformation information alone by excluding infinitesimal rotation. Justification to use the infinitesimal strain can be made by comparing the magnitude of error introduced by using infinitesimal strain over the accuracy of the

collected data and considerations of the application of the analysis (Pollard and Fletcher, 2005). Since there is uncertainty about the exact geometry and underlying deformation process, we focus more on capturing in a relative sense the spatial distributions and magnitudes of deformation strain. Thus, we will use the infinitesimal expression for further applications.

By Eigen value decomposition of the strain tensor we can extract the principal strains and directions, equation (3-8). The trace of the strain tensor, equation (3-9) is dilatation that represents volume changes by deformation. If we use Hooke's law with pre-deformed elastic properties, we can calculate the elastic deformational stress.

$$\{\boldsymbol{\varepsilon}_I, \boldsymbol{\varepsilon}_{II}, \boldsymbol{\varepsilon}_{III}\}$$

$$\{\boldsymbol{W}_I, \boldsymbol{W}_{II}, \boldsymbol{W}_{III}\} \quad (3-8)$$

$$dilatation = \sum \varepsilon_i \quad (3-9)$$

Note that if we use dynamic models, for a model with multiple layers with different stiffness, the spatial distribution of the deformational strain will be different from those from kinematic models in that the stiffer layers will deform less. If we use a single stiffness values for all layers, the deformational strain will become identical with the results using the same kinematic laws.

Here, we are not aiming to propose a single way to utilize structural deformation attributes. We can use different attributes, or modify the attributes into different forms to serve a given research purpose better. For instance, the orientation of maximum tensile principal strain from deformation analysis can be used to estimate the direction of open mode joints when the area underwent tensile deformation. The magnitudes of principal stress can be used to infer possibility, or abundance of fractures.

Likewise, we are not attempting to test or compare which kinematic/dynamic models are superior over the others. In reality, we seldom conduct restoration analysis, especially for reservoir modeling practices. Kinematic restoration analysis is usually conducted at a basin level to reconstruct paleo depositional conditions in sedimentology or sequence stratigraphy related research (Burgreen and Graham, 2014). Dynamic restoration is usually used in research of structural geology contexts, to model relatively larger scale deformation such as deformation of crust with faults (Lovely, 2011; Nevitt et al., 2014). This is partially because the concepts and techniques of restoration, for both kinematic and dynamic models, are new enough that their industrial applications have been limited thus far. After Dahstrom (1969), many breakthroughs on kinematic restoration were made in the '90s and after the new millennium (Brandes and Tanner, 2014). Dynamic restoration was first introduced early in the 2000s (Maerten et al., 2002).

It has been only a couple of decades since we started to develop structurally complex reservoirs. Offshore, we develop reservoirs with a relatively smaller number of wells – which increases the probability that the differences among wells' structural deformation are not negligible. Onshore, we develop unconventional fields where the areas of interest are vast compared to the conventional reservoirs (Zagorski et al., 2012; Carter et al., 2011). By the magnitude of the size, we cannot always assume that the effect of structural deformation is homogeneous.

A proper coordinate transformation between the present structural grid and the depositional grid (arrows C and F in Figure 3.1) was neglected, or at least not conducted in a rigorous way, until Mallet introduced the Space-Time mathematical framework, known as UVT-transformation (Mallet, 2004). Figure 3.7 depicts typical problems of neglecting kinematics between the structural and depositional grids. Because numerical flow simulation is one of the end products of typical reservoir modeling practices, grid system within structural models – faults and horizons – are generated optimized to run flow simulations. The grid system in inset A that has fault parallel grids is called a pillar grid. Since coordinates of this grid do not correspond with geological spatial distance in the depositional condition, the geobody, a channel in this case, cannot preserve a realistic size and shape (Gringarten et al., 2008). Inset B shows the distortion created in

an opposite way from inset A. It started from facies modeling in a depositional grid system. Thus, the spatial distance and geological distance agreed with one another. However, when made into the present structural model, it just changes the elevations while preserving the horizontal location (Castro, 2007). The geometrical inconsistencies of these two cases originated by neglecting the kinematic models of the horst-graben system, for A, and the anticline, for B.

A. Distortion of geobody by using flow simulation grid for facies modeling



B. Distortion of geobody by using depositional grid for structural grid

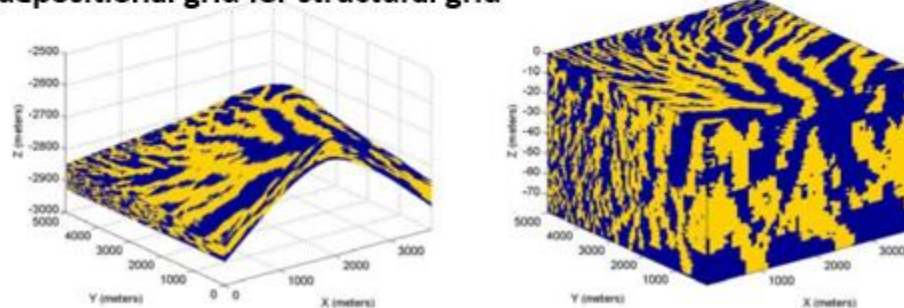


Figure 3.7: Typical geometrical distortions caused by not considering the structural deformation of the reservoir. A – A pillar grid is created for numerical flow simulation. Object based modeling of channel bodies using pillar grid systems create distortions of geobody shapes (Gringarten et al., 2008). B – Unlike inset A, facies realization of deltaic deposits are modeled in a depositional grid. However, due to not having kinematic/dynamic models to link it with present structural shape, this model only shifted the elevations of each grid block (Castro, 2007).

However, as we discussed, it is not common to conduct explicit forms of restoration/forward-deformation analysis. Mallet introduced UVT transformation to

give a coordinate transformation between present geometry and a time domain representation of restored geometry (Mallet, 2004).

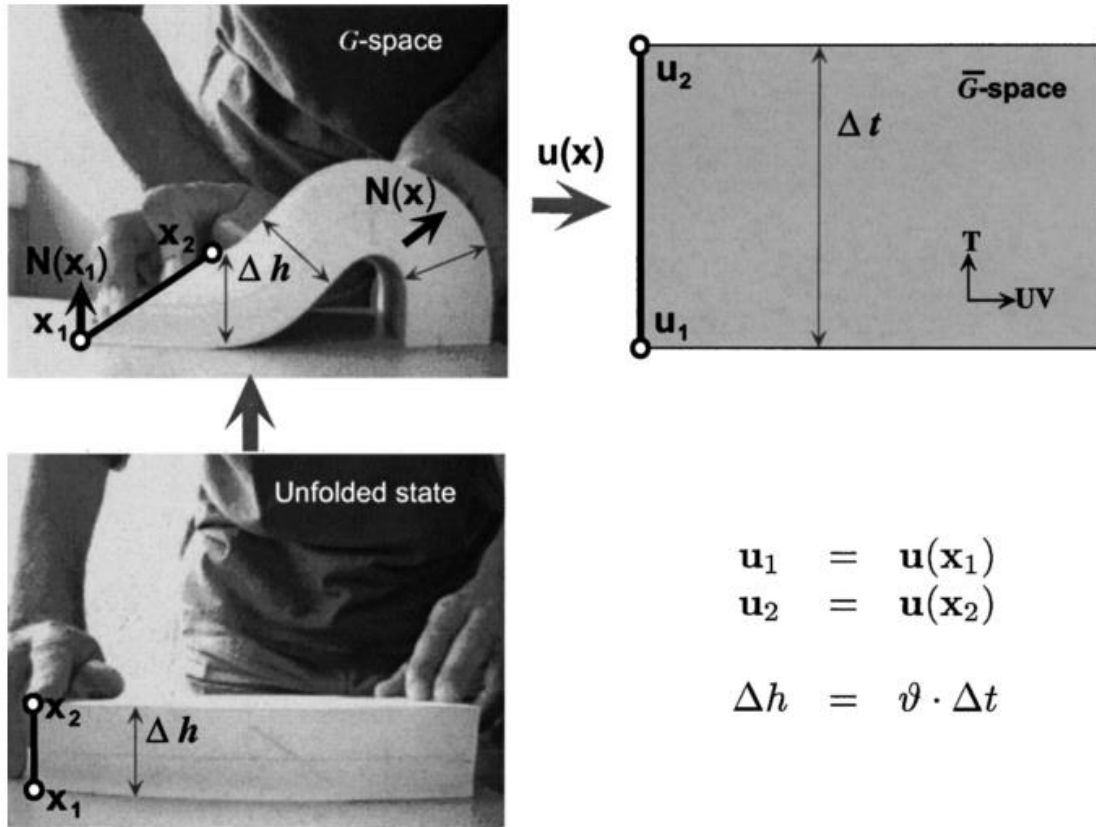


Figure 3.8: Pictorial demonstration of “flexural slip” forward deformation and UVT coordinate transformation by Mallet (2004).

Figure 3.8 depicts the idea of UVT transformation. \mathbf{G} -space means the present structural domain with present geometry. If we reconstruct the spatial geometry of an unfolded state, it is restoration, or retro-deformation. $\bar{\mathbf{G}}$ -space represents a parametric space where the present spatial coordinates of X and Y are parameterized into U and V, while the vertical axis of $\bar{\mathbf{G}}$ -space is a chronological time axis to represent the time-stratigraphy (Wheeler, 1958). While restoration analysis involves geometrical models, UVT transformation has a geochronological model, “Geochron model”, which has parameterized space coordinates of u and v, and a parameterized stratigraphic time coordinate, t. Thus, it does not have restored geometry.

By definition, this is not a restoration, or a kinematic model. However, it does try to assign the same geochronological time, t , after unfauling and unfolding structures into parametric (u, v) space from mathematical optimization. While kinematic restoration aims to secure the kinematic consistency of the current structural geometry, and dynamic restoration aims to investigate the evolution of a structure with the required force to generate the structure on top of kinematic consistency, the main purpose of UVT transformation focuses on reconstructing parametric space to secure stratigraphic modeling in the parametric space that is less distorted. While restoration is a reconstruction of past geometry in physical space, UVT transformation is a reconstruction of past stratigraphy in unitless parametric space. If both UVT transformation and kinematic models use flexural slip models with same boundary conditions, both of them will give identical restoration in a different space with the same deformational strain.

Since the parametric space is a hybrid space of space and time, displacement vectors among the two coordinates are physically meaningless. However, strain among the coordinates is still meaningful because strain itself is independent of the scale of the model. Thus, if we want to use strain from restoration-deformation, UVT transformation can be considered and used as a proxy of actual restoration analysis. To make a long story short, UVT transformation does not provide a physical deformation displacement vector, but it does give a physically meaningful deformation strain.

3.2.4 Restoring the hard data and forward deformation of reservoir properties

Once we extract structural deformation attributes from a specific structural deformation scenario, we can start hard data restoration with a certain rock accommodation scenario (the red arrow in Figure 3.4). Under a specific scenario of a structural deformation mode and a rock accommodation mode, equation (3-1) can be re-written as equation (3-10) because the accommodation style is fixed, and the structural deformation attributes and present observation values are the only spatially varying variables.

$$O^* = f^{-1}(O, r) \quad (3-10)$$

This result does not necessarily have to be the exact way that the reservoir properties have evolved. The important thing here is to capture the most important geological events that geoscientists are considering in the transfer relations, in a simple yet representative way. As long as the observed values are conserved from consecutive forward and backward transfers, and the forward and inverse of the relations are bounded within physically meaningful ranges, any transfer relations can be postulated. We may call the equation (3-10) a pseudo restoration, and the pseudo function, f , can be called a transfer function of the pseudo restoration.

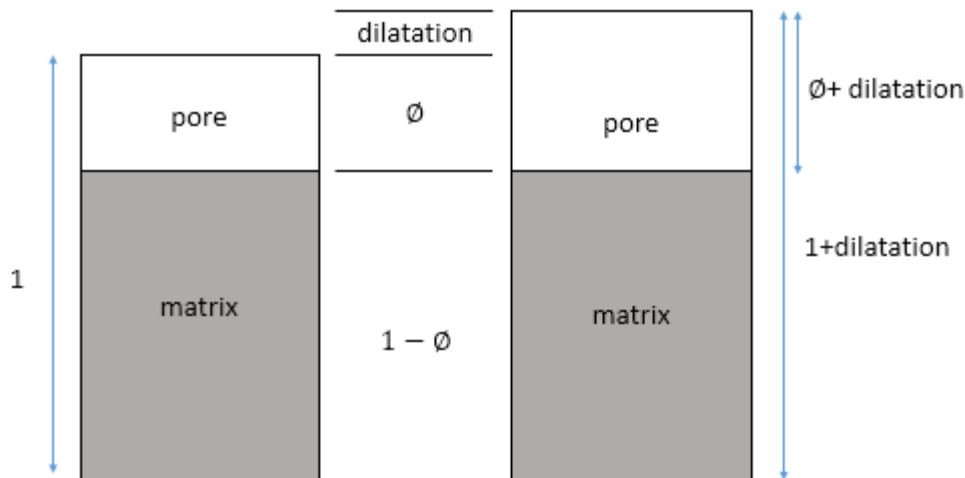


Figure 3.9: Schematic explanation of porosity changes by dilatation. Since all volume changes are accommodated by pore volume changes, the new numerator for deformed porosity is the summation of the original porosity and dilatation. The new denominator for deformed porosity is merely a sum of 1 and the dilatation.

For instance, use the dilatation in equation (3-10) to restore porosity. If we assume all the deformation strains are accommodated by pore volume changes – and thus, by distributed accommodation – the bulk volume change can be depicted by Figure 3.9. With dilatation, which represents proportional volume changes, the measured porosity can be restored by equation (3-11):

$$\phi_{restored} = (1 + dilatation)\phi_{measured} - dilatation \quad (3-11)$$

Again, equation (3-11) is one way of postulating a possible transfer function for porosity. Other possible options include using lab experiments. Using depth-porosity trends from many experiments, we can postulate compaction-porosity relations. The compaction-porosity curve can be used as a transfer function to restore and forward deform the porosity values.

When conducting geostatistical simulations using restored values, one thing we should be careful is that we should not use the probability density function (pdf) of current values when conducting a normal score transformation if Gaussian assumptions are needed. We should use “what-if” properties in depositional conditions. For instance, if porosity measured in a specific well is 10 percent and the restored porosity under a certain scenario is 20 percent, the percentile of 10 percent porosity in the present condition does not necessary to be same with percentile of 20 percent porosity in a past depositional condition. If the measured 10 percent porosity is a lower quartile, rank transformed value using present pdf of porosity would be -0.67449. However, if restored 10 percent porosity is around median of restored porosity distribution, the rank transformed value would be around 0. Figure 3.20 in Section 3.3.4 shows an example of how porosity distribution changes from the present values to restored values. This point offers a strong benefit, because in actual subsurface modeling we always have very limited data and information to infer the proper pdf of subsurface values. However, by using restored values in simulation, we can utilize the pdf of values from currently deposited conditions of the same lithology.

After we populate the properties in the depositional condition, we can “copy, forward-transform, and paste” back to the present structural model. For the case where we assume a localized accommodation mode, we can either use the magnitude of the Eigen strain or the elastic deformational stress, by using the Eigen strain with elastic properties in depositional conditions as an index for fracture abundance. In a rigorous

sense, we should use stress to infer the existence and abundance of fracture sets and their abundance. However, using field specific empirical relations between deformation strain and fracture abundance can be useful when kinematic restoration is conducted (Lohr et al., 2008). Figure 3.10 is comparison of the magnitude of the deformation strain in the wells and the fracture abundance measured at the well.

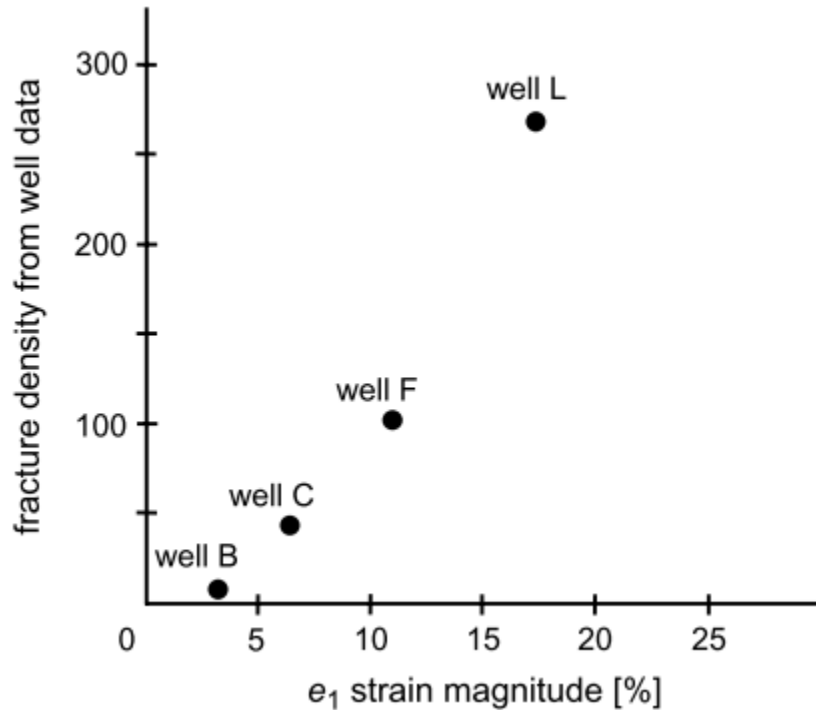


Figure 3.10: Example of comparison between fracture densities and deformation strain magnitude (Lohr, 2008).

Recall from Lovely et al. (2012) that when accommodation modes use a localized style, the relation between deformational strain and deformational stress is nonlinear, so the relationship between stress and an abundance of localized features is likewise nonlinear. In this case, we can make nonlinear transfer relations between the structural deformation attributes and an abundance of localized features from a curve between strain and abundance, either from detailed numerical simulation or from the empirical curves of lab experiments. By doing so, we can mimic nonlinear behavior related to structural deformation even as we do restore/forward by deforming the kinematic model or dynamic model with linear elasticity.

$$O^* = O \quad \& \quad S = S^* \quad (3-12)$$

If we revisit the conventional “copy and paste” process within the proposed process, restoration and forward deformation returns the same values as equation (3-12). The typical “copy and paste” convention can be understood as one of the accommodation modes that assume no influence of structural deformation on reservoir property evolution.

3.2.5 In defense of using an inaccurate and simplified pseudo restoration of properties

It is possible to challenge the above examples of linking deformational attributes in restoration and forward deformation of petrophysical properties. For instance, we would rather numerically simulate the elastoplastic behavior of rock with a finite element model, by creating a finer inner mesh within a depositional grid block to model localized deformation, assuming deformation strain as boundary conditions for each sub simulation block. This scenario is from an actual research paper, except the context is not a reservoir scale and the time is not geological time (Borja et al., 2000). It is true that there are many available advanced models that can reproduce many of the subsurface features that we are interested in.

However, using more detailed physics does not mean that a model is more useful for a given situation. Subsurface geomodeling, especially property modeling on sub-resolution grid blocks, demonstrates such a case. First, since it is subsurface and sub-resolution we do not have enough modeling input parameters, especially for the geometrical models of sub-resolution features. We do not even have the geometry of the sub-resolution features for the area away from the wells. From the beginning, this is a reason to use geostatistical algorithms to populate petrophysical properties. Second, the available detailed physical models capture the kinematic and dynamic evolution of rock deformation over geologically infinitesimal time. We can widen and deepen our knowledge on the behavior of rock deformation by those models, but cannot restore or enact forward deformation exactly over geological time. It would be beneficial to use

those models to develop transfer relations, like a curve of the volume proportion of compaction bands by an increased amount of compaction strain. Thus, they also can be considered as possible pseudo restoration models.

Third, even when assuming we have a reliable model to simulate rock deformation over a geological time span, with the capability to model different types of failures, we have a higher level of uncertainty on the current geometry of structural, kinematic, and dynamic models. Thus, it would be more beneficial to use the new model as a better version of a dynamic model to conduct structural restoration for a reservoir scale. Thus, under a sub-resolution accommodation style sub-resolution features would remain, even given an imaginary deformation model for the geological time span.

3.2.6 Comparing the likelihood of scenarios

By having N structural restoration modes with M accommodation modes, $N \times M$ number of geological scenarios become available. We can make any number of scenarios if we want to, and we can populate any number of realizations under each scenario. However, two questions arise:

- Do the realizations from different scenarios give meaningfully different subsurface responses?
- How can we rank more or less likely scenarios among $N \times M$?

One straightforward solution is cross validation by using well data. By dividing the available wells into two groups, we can use one group as conditioning data and the other group as validation data. If the number of wells is limited, we can compare seismic attributes between the seismic data we have and the synthesized attributes from realizations. We can use seismic attributes along a number of ghost wells – imaginary well trajectories we are interested or candidates for future drillings-- along a number of key vertical sections, or even along a full 3D survey volume.

To compare the realizations with either upscaled well data or seismic attributes from a seismic survey, we need to calculate the effective medium property of the grid

blocks in the present structural model, combined with the sub-resolution geological features that we assumed from different rock accommodation scenarios. Effective medium theories from rock physics give mathematical and empirical models to calculate the effects of changes in porosity and pore fluids, as well as the effective medium properties that have geological features such as crack-like pores, thin lamination in shale, and crack inclusions. We will cover some useful models and demonstrate their usage in Chapter 4.

To compare the similarity or dissimilarity among actual and synthetic observations from realizations in quantifiable manners, we can use distance-based multidimensional scaling (MDS) (Caers et al., 2010; Park et al., 2013; Jeong et al., 2014; Borg and Groenen, 2003). By using any metric of distance, we can capture pairwise dissimilarity among the actual and synthetic observations. We can then visualize the dissimilarity in a metric space using MDS.

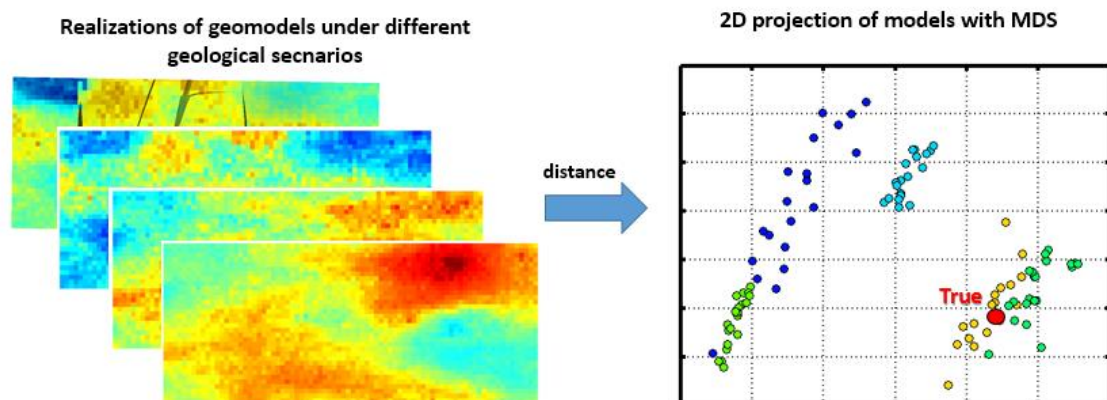


Figure 3.11: 2D projection of 3D models using MDS. We cannot plot the 3D volume in physical space (left). However, we can display dissimilarity among models by using pairwise distance in a metric space using MDS.

Figure 3.11 is the example of the usefulness of MDS. Using geostatistical simulations, we can have a number of geomodels under each specific geological scenario. We can visually compare the difference among models when there are several. However, it is less practical to visually compare hundreds, or even thousands of models. After choosing a problem-tailored distance metric, we can visualize the differences in a metric space like the plot on the right of Figure 3.11. Each dot corresponds with actual

models, and we can trace them back by indexing them. These plots are the results that we will cover in a later section.

Plots in metric space are color coded by different scenarios in the figure. If the color coded dots are segregated well from each other, that means different scenarios that we selected to model have sensitive factors in the results of numerical simulations. In the figure, the red dot, the true model, is placed closely with the scenarios of the yellow and green dots. From the plot, we can raise the likelihood or rank of these two scenarios while lowering the rank of the other three scenarios (Park et al., 2013). Alternatively, we can investigate whether the assumptions used in the yellow and green scenarios can be supported with other geological, geophysical, or engineering evidence.

3.3 Application on a 3D synthetic reservoir

To test the proposed framework and effects of different geological scenarios of structural deformation and rock accommodation modes, we created a synthetic reservoir that has a certain level of structural complexity and ambiguity in its dominant sub-resolution geological features.

3.3.1 Synthetic model description

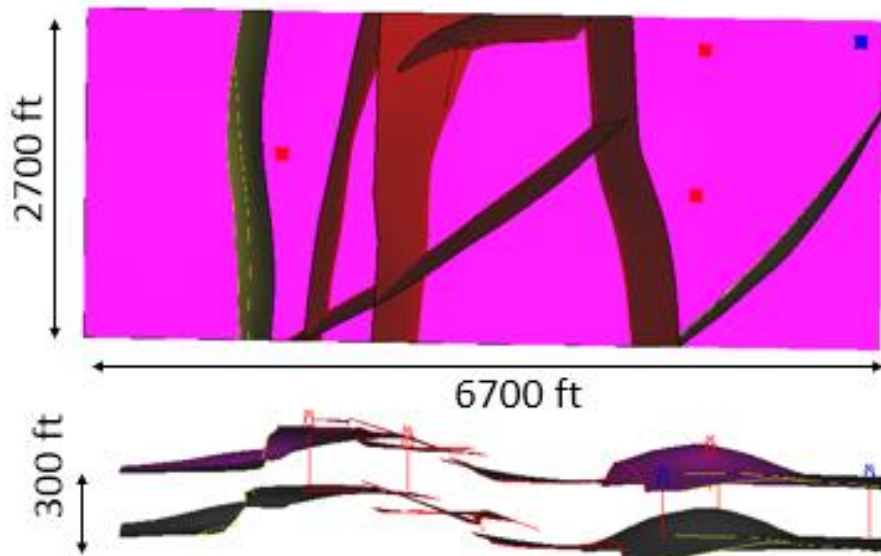


Figure 3.12: Structural geometry of the synthetic reservoir. Top – top view of geometry. Bottom – side view of geometry. Red dots – exploratory wells. Blue dots – exploratory wells converted to injectors. The synthetic subsurface reservoir structure has seven faults that make compartmentalized reservoir blocks, horst-graben in the central parts, and anticline dome in the right region.

Figure 3.12 shows the fault networks and top and bottom horizon of the synthetic reservoir (the present geometrical model). It has seven faults, a horst in the central region, and an anticline dome in the right region. Paradigm® SKUA-GOCAD™ subsurface modeling software was used for this example case.

3.3.2 Multiple geological scenarios in structural deformation

As discussed in Chapter 2, different kinematic/dynamic models will lead to different geometry in deformation or restoration analysis. In reservoir modeling with real field data, we can never know exactly how the structure has been deformed. However, for this example case, we are going to apply two different kinematic models to construct depositional grids, and choose one of them as the true deformation of the structure.

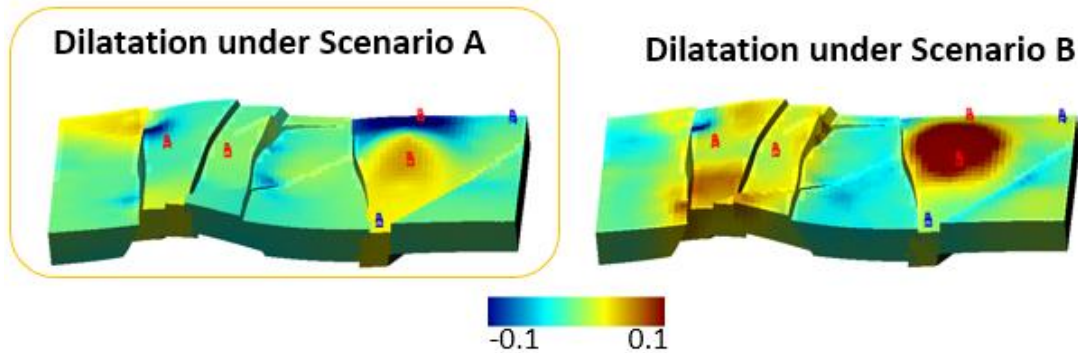


Figure 3.13: Reservoir structures colored by dilatation from deformational strain. Left – deformation scenario A. Right – deformation scenario B

Figure 3.13 shows dilatation distributions from two different deformation analyses using different kinematic models. Dilatation is the summation of the Eigen strain values that are obtained by equation (3-9). It can be understood as a representation of the fractional changes of the volumes by structural deformation.

Scenario A results from a flexural slip model that preserves area and line length, by allowing strain discontinuity across faults and horizons (Suppe, 1983; Mallet, 2004). Scenario B is conducted under a minimum-deformation principle, which minimizes strain discontinuity over the area (Mallet, 2002). We chose scenario A as the true deformation history of the synthetic reservoir. It is noteworthy that we arbitrarily chose one restoration principle to represent the true deformational history of the synthetic reservoir. This does not say anything about which scenario is more geologically realistic.

3.3.3 Multiple geological scenarios in rock accommodation

As we simplified the deformation history of the reservoir, we made rock accommodation styles by altering the sequence of two rock accommodation events. The two events are diagenesis and deformation. For further simplicity, diagenesis is modeled as a 10% porosity reduction by cementation. Deformation is modeled by using the deformational dilatation. Figure 4 depicts two geological scenarios of how the reservoir properties have evolved.

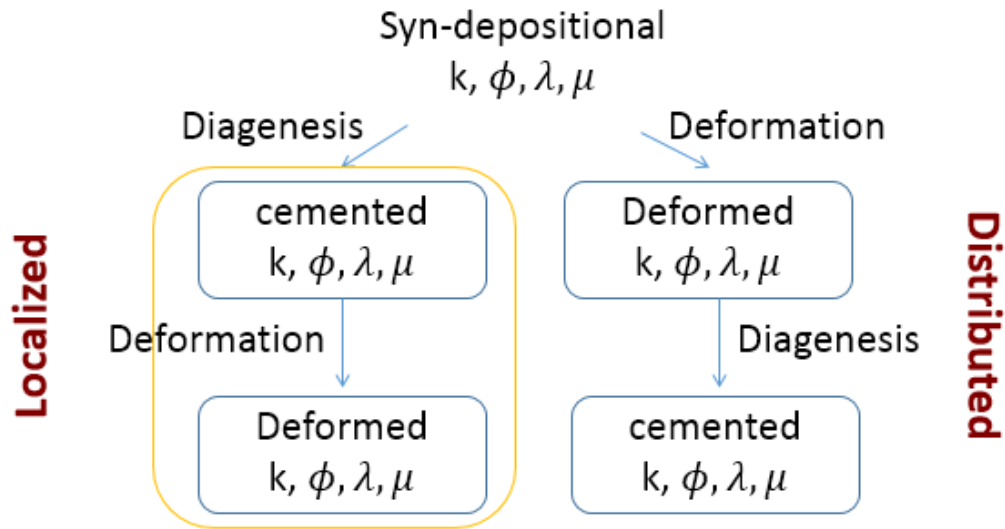


Figure 3.14: Geological scenarios for reservoir property evolution. In the synthetic case, a sequence of a diagenesis event and geological deformation are considered. The left column means the reservoir experienced diagenesis, and then deformation was applied. Since the deformation was applied after the rock became stiffer, the deformation is assumed to be accommodated by a localized feature – by generating fractures. The right column is the case where structural deformation was applied when the rocks were soft. On this route, cataclastic flow accommodates structural deformation. Then cementation occurs, resulting in porosity reduction. Overall, both accommodation routes will lead to nearly identical mean porosity values.

For the localized accommodation scenario, the true porosity in the depositional domain will be reduced by 10%. The elastic properties of the cemented rock are calculated by a rock physics model. In this example, we use the constant cement model (Avseth et al., 2001). Since we already have the principal strain components – their magnitudes and directions – from the structural deformation, we can calculate the stress components using Hooke’s law, by using a point by point elastic modulus from a constant cement model. We assume that the synthetic reservoir may have only open mode fractures. Fracture intensity is scaled from the principal stress where it is tensile. Fracture normal direction is decided by the most tensile principal strain direction. Figure 3.15 depicts the workflow for calculating petrophysical properties within the localized accommodation scenario. Details of the rock physics models used here will be covered in Chapter 4.

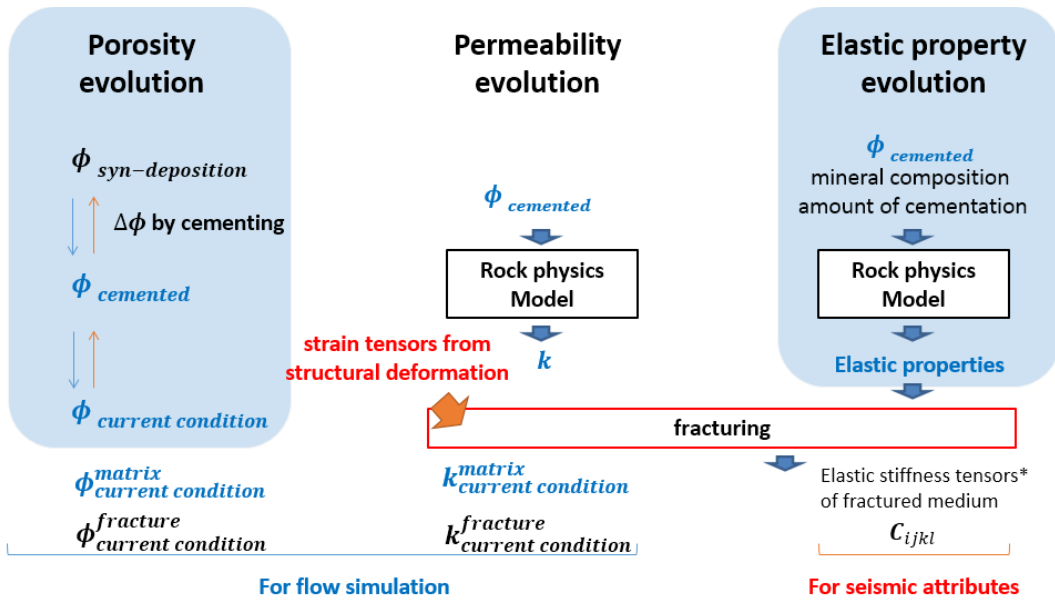


Figure 3.15: Petrophysical property generation under the localized accommodation scenario. "*" in the elastic stiffness tensor will be covered in Chapter 4.

For the distributed accommodation scenario, the true porosity is changed proportionally by the dilatation from the deformation. Fractional changes on a volume of interest need to be accommodated by pore volume changes, as depicted in Figure 3.9. After the porosity is updated by the dilatation, a uniform 10% reduction, by adding cement, is applied as a diagenesis event. In this scenario, there is no fracture generation. Figure 3.16 depicts the petrophysical property generation under the distributed accommodation style.

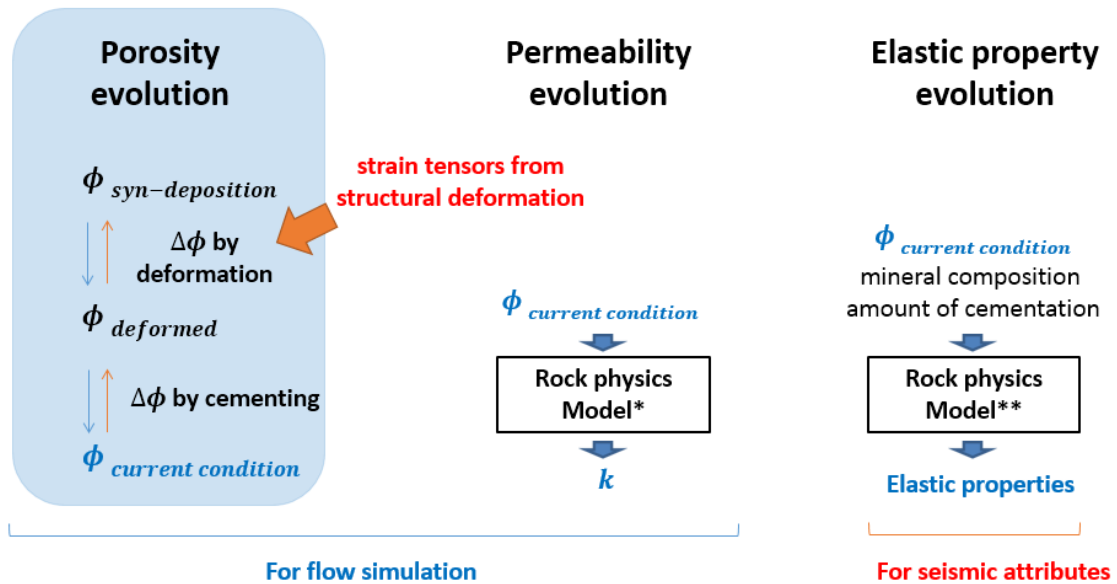


Figure 3.16: Workflow for generating petrophysical properties under the distributed accommodation scenarios.

For matrix permeability, the Kozeny-Carman relation is used (Mavko et al., 2003). Thus, we assume the matrix permeability is a function of matrix porosity. For the synthetic reservoir, we chose the localized accommodation scenario as the true scenario. Thus, we created a naturally fractured reservoir.

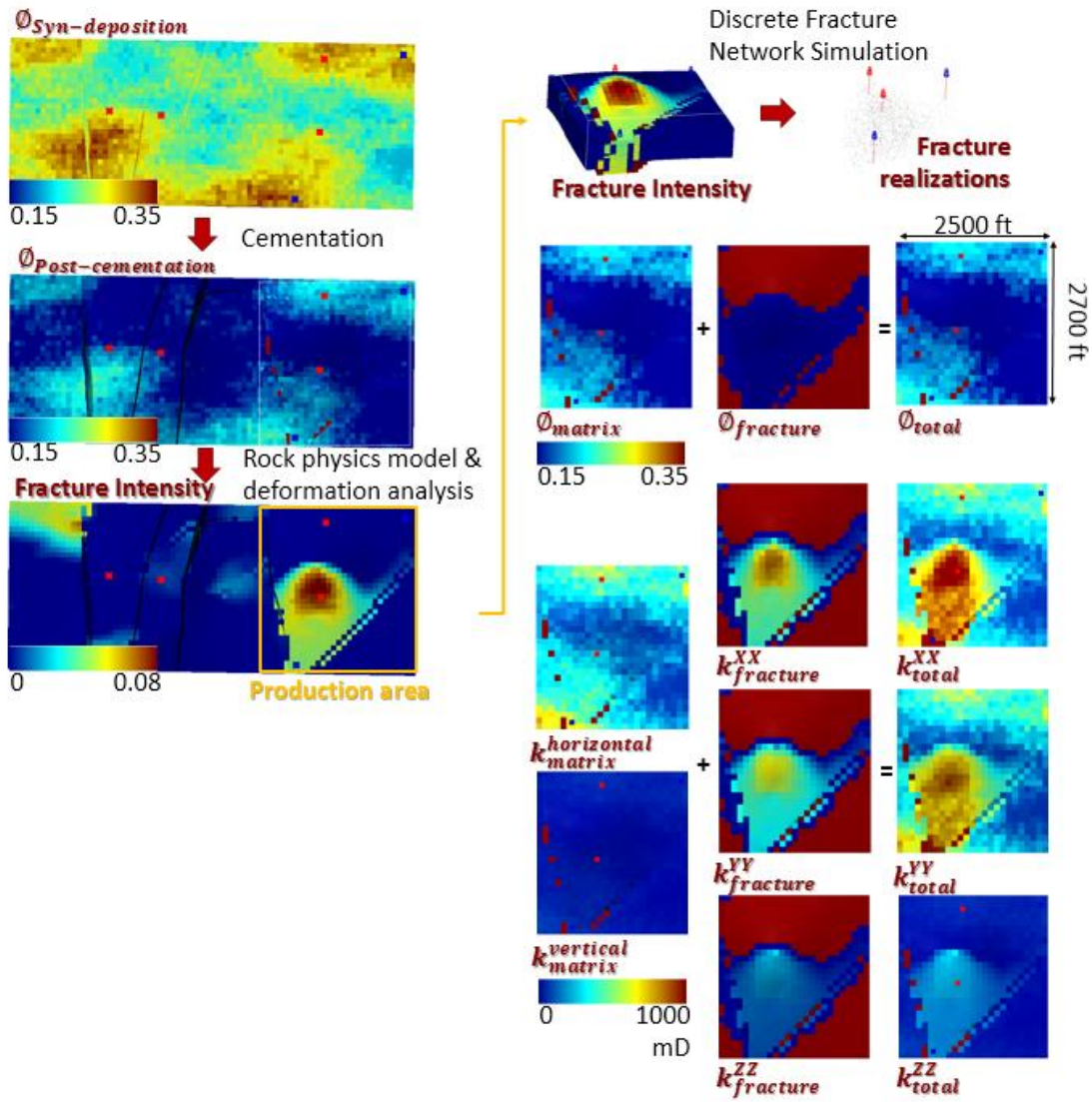


Figure 3.17: Reservoir property evolution of the true case. Syn-depositional porosity is populated by unconditional SGSim. As diagenesis occurred, porosity reduction by cementation was applied. As deformation took place, fractures were generated by following fracture intensity from the principal stress and fracture normals, from the most tensile principal strain direction. An explicit discrete fracture network was only populated in the initial production area. Flow-related reservoir properties are modeled as a single medium with a summation of matrix and fracture properties, since the matrix permeability is relatively high compared to the fracture permeability.

Figure 3.17 depicts how the true reservoir properties relating to flow behavior are generated for the synthetic reservoir. Porosity in the syn-deposition condition was cemented first. Then, the reservoir had been deformed under deformation scenario A.

While it deformed, open mode fractures were populated by following the most tensile direction as the normal direction of fracture surfaces with the fracture intensity, which is scaled proportionally to the tensile stress induced from deformation. Since we are going to run a flow simulation only on the development area, actual DFN realizations are populated only within the production area.

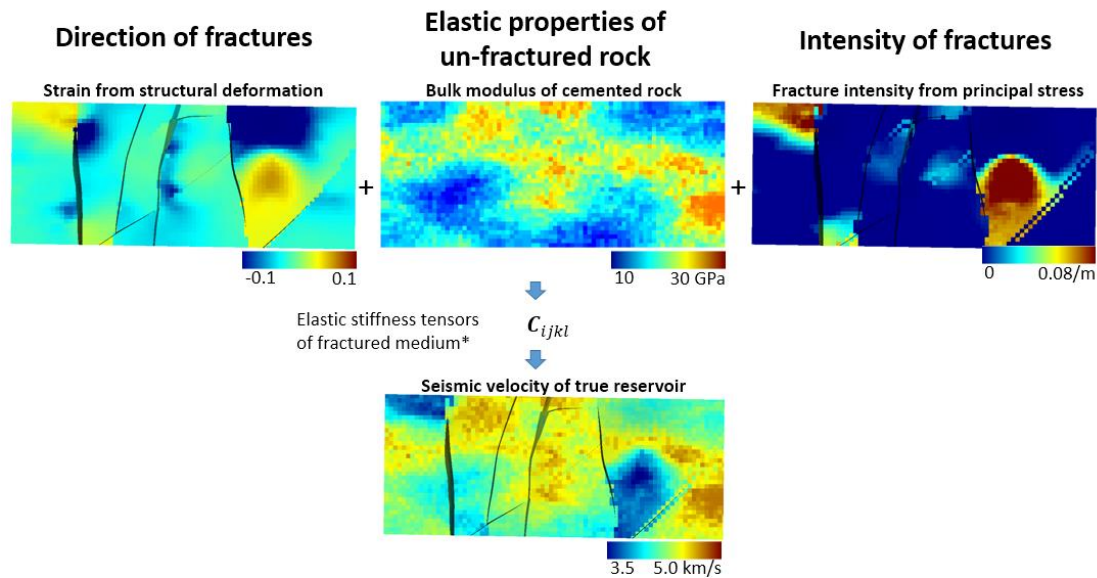


Figure 3.18: Calculating the effective medium with fractures and cementing, using the effective medium model. Hudson’s model is used for effective stiffness tensor calculation (see Chapter 4).

3.3.4 Creating reservoir models for each scenario

Now we can apply and test the proposed geomodeling workflow with the synthetic reservoir we have created. Let assume that we do not know the actual geological history of the reservoir, but that the true history is within our prior scenarios.

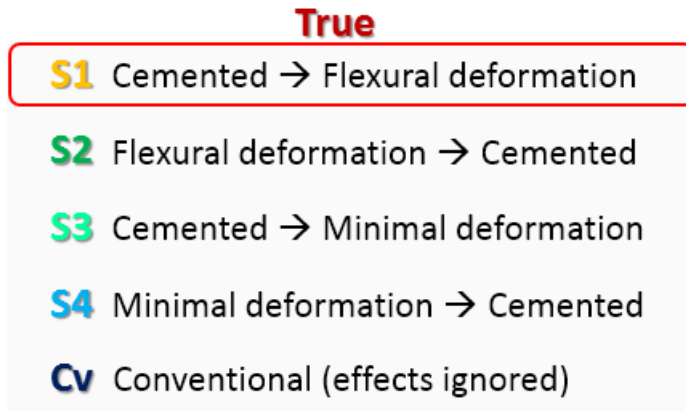


Figure 3.19: Multiple scenarios of structural deformation and reservoir property evolution. Two scenarios on structural deformation and two scenarios on rock accommodation mode give four different potential scenarios. By including the conventional approach as one scenario, we need to test five different scenarios.

Figure 3.19 compares all the scenarios by combining alternatives in our understanding of the mode of deformation and the mode of rock accommodation. Scenario S1 is the case when we chose the correct deformation interpretation and the correct timing of cementation. S1 and S3 will generate fractured reservoirs, while S2 and S4 will generate reservoirs without fractures. Again, we are assuming that we have not seen any fractures from the vertical wells. “Cv” is a conventional geomodeling case, in which we implicitly assume that the reservoir properties remain identical from one state to another. The color codes in Figure 3.19 will be used in the same order on the following plots of reservoir responses.

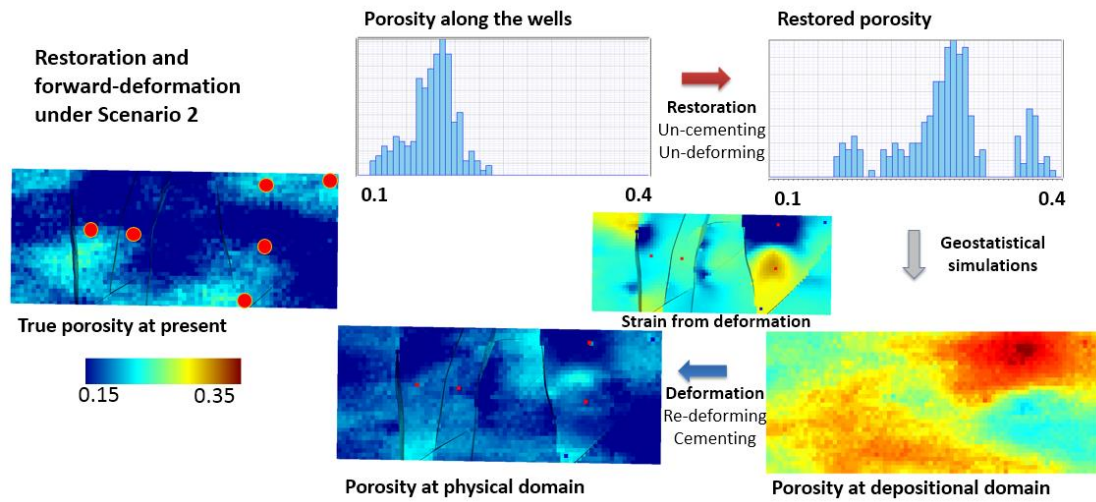


Figure 3.20: Porosity modeling using the proposed framework under scenario 2. Porosity along the wells have larger values by un-cementing and un-deforming. Since we use higher porosity values in the geostatistical simulation, the realization in the depositional domain has higher porosity values. By forward-deformation, the range of the porosity becomes smaller. Values along the wells are identical with the original values.

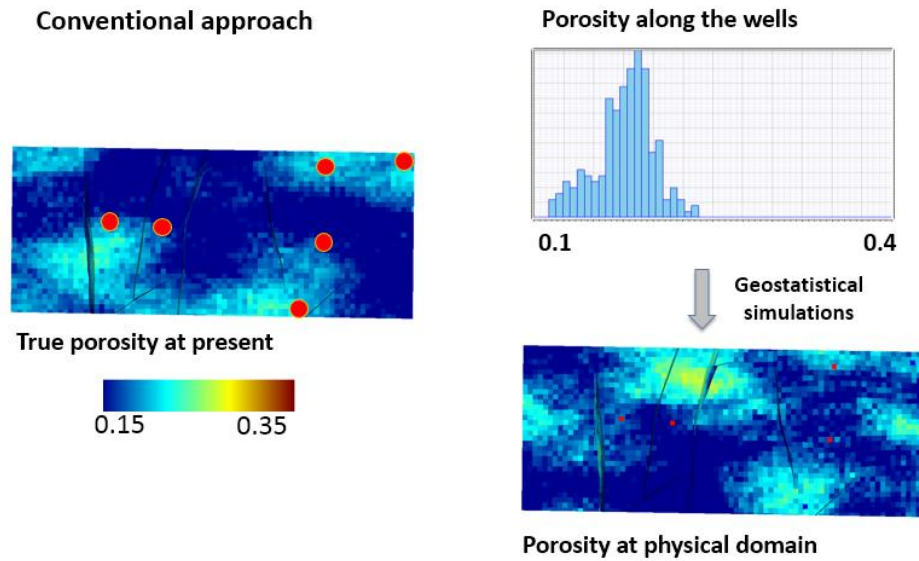


Figure 3.21: Porosity modeling from the conventional workflow. Deformational compaction and extension are neglected, or it is intrinsically assumed that those effects are negligible for reservoir modeling purposes.

Figure 3.20 and Figure 3.21 compare the conventional workflow and the proposed workflow under scenario S2, in terms of how the porosity values are treated. For both cases, the porosity along the wells in the current condition is identical. The conventional approach conducts a geostatistical simulation – a conditional SGSim in this case – using the observed porosity. The proposed workflow uses the “restored” porosity under the geological assumptions. Since scenario S2 assumed the right deformation with the wrong sequence order of cementation events, the restored values will deviate from the true porosity along the well location in the depositional domain.

For the fractured cases, i.e. scenarios S1 and S3, the fracture intensity is slightly different for each realization, since the elastic moduli for each realization are different by the populated porosity differences. Using the fracture intensity, one DFN simulation is conducted for individual realizations within the production area. Thus, each realization has a different fracture permeability & fracture porosity. Across the five scenarios, 20 realizations are simulated. Thus, we have 101 realizations including the true model.

3.3.5 Comparisons

Figure 3.22 depicts one realization from each scenario, with the corresponding reservoir responses. Flow simulations are conducted using the Schlumberger ECLIPSE reservoir simulator. Rock physics models are used to calculate seismic velocity while considering porosity, saturation, mineralogy, cementation, and fractures (Hudson, 1990; Mavko et al., 2003). Realizations from S2 and S4 do have all zero values on the fracture intensity maps, since S2 and S4 assume the deformation has been accommodated by the rocks via rearrangement of pore and matrix structures (distributed accommodation). The third column is the permeability tensor component on the X axis. The S2, S4, and Cv cases have different permeability tensor components for vertical direction, since they assume no fractures. Reference, S1, and S3 have different tensor components for each direction.

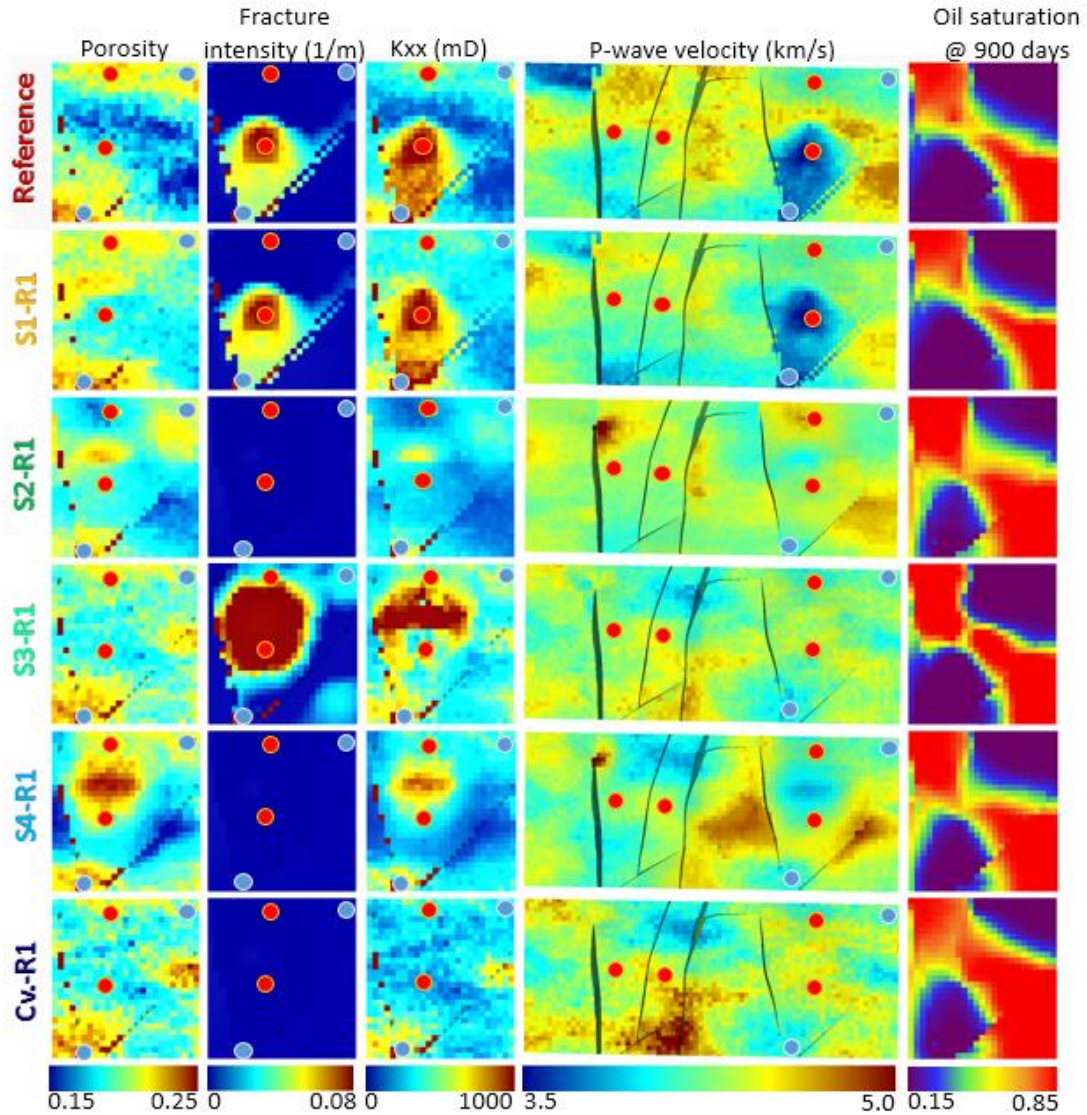


Figure 3.22: One realization and its reservoir responses, out of 20 realizations from each scenario. The circles are the locations of exploratory vertical wells. Blue circles are converted to injectors. Porosity along these locations is used as hard data for geostatistical simulations. Top row – Ref. means true case. S1~S4 and Cv correspond to each scenario, including the conventional approach. Colors correspond to Figure 3.19. 1st column – matrix porosity, 2nd – fracture intensity, 3rd – fracture permeability component on X axis, 4th – P-wave velocity distribution, 5th – oil saturation distribution after 900 days of production.

In reality, we cannot have access to the true flow responses until we drain the field. Even though the proposed workflow gives better production forecasts, it would be less interesting unless we could see which scenario is more suitable at an early stage. Since we have actual seismic data in the early stage and we can calculate synthetic

seismic attributes for each realization, we may choose a more suitable scenario over a less suitable one if seismic attributes from one scenario are more similar to the true data while realizations from other scenarios are less similar. Since it is practically impossible to manually quantify similarity using the naked eye, MDS plots using Euclidean distance are applied. For comparison purposes, we also applied an MDS plot on porosity for every realization.

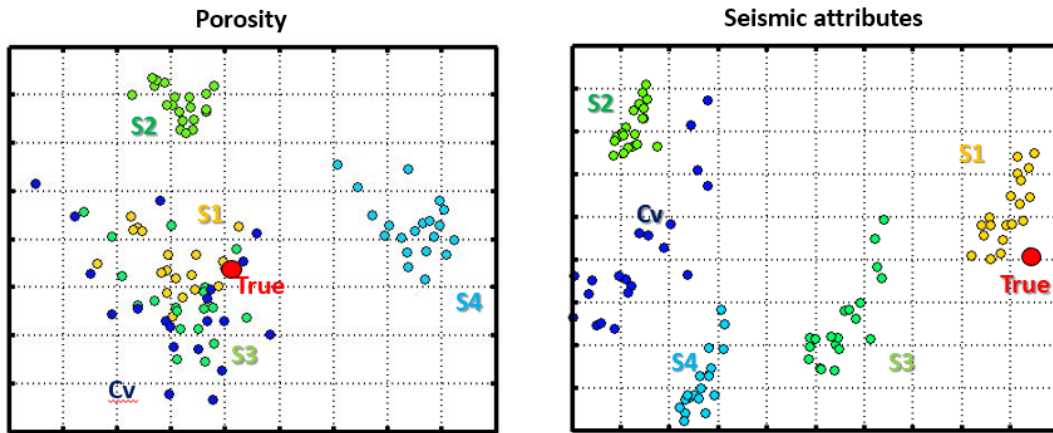


Figure 3.23: MDS plot by distance of porosity (left) and distance of seismic attribute (right). Since fracture porosity is negligible, realizations from S1, S3, and the conventional case have similar porosity distributions. Thus, all of them are grouped together. However, when MDS is done by using distance between seismic attributes, S1, S3, and Cv are all grouped separately because realizations from the Cv scenario does not have fractures while S1 and S3 have fractures but under different distribution characteristics. When plotted by seismic attributes, S2, S4, and Cv, which have distributed accommodation assumptions, are grouped relatively closely.

Figure 3.23 shows the MDS plots of the porosity and seismic attributes (MDS plots using production attributes are shown later). This figure depicts the usefulness of using seismic attributes when we are not sure about the existence of sub-resolution geological features. In the left figure, realizations under scenarios S1, S3, and the conventional approaches are clustered together. This is because realizations from S1 and S3 accommodated structural deformation by forming fractures, and fracture porosity is negligible compared to the matrix porosity, around 20 percent. Thus, all of them are grouped together. In the meantime, realizations from S2 and S4 are clustered separately. For S2 and S4, we assume the structural deformation is accommodated in a

distributed style by pore volume change. Since S2 and S4 assume different kinematic laws, their deformational attributes have different spatial distributions and the porosity realizations are deformed differently. Even using the point-by-point values of true porosity, we cannot distinguish what scenario would be more appropriate for the given reservoir.

Obviously, we do not have access to a true 3D porosity map for real field applications. However, when MDS is plotted by seismic attributes, realizations from scenario S1, S3, and Cv are all grouped separately because realizations from the Cv scenario do not have fractures, while S1 and S3 have fractures but under different distribution characteristics. When plotted by seismic attributes, realizations under scenarios S2, S4, and Cv that have distributed accommodation assumptions are grouped relatively closely. Due to the nonlinear relation between porosity, or density with seismic responses, especially when having fractures, using seismic attributes provides segregations among realizations compared to the case when we just use static values like porosity. This is because the changes in rock properties are nonlinear functions to the attributes that we use – porosity, fracture abundance, and deformation strain-stress. Now, let’s see whether the good segregations in the MDS plot with seismic attributes show good agreement with the reservoir flow responses.

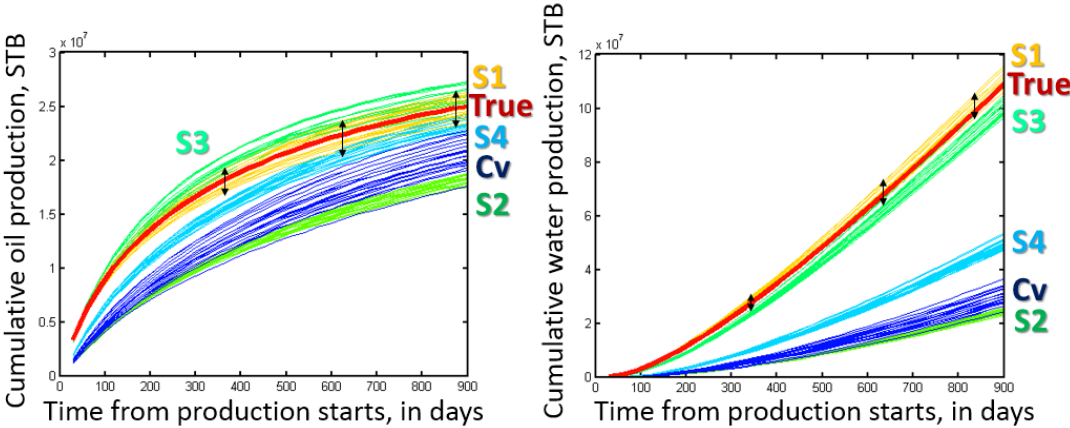


Figure 3.24: Flow responses of all realizations from different scenarios in the proposed and conventional workflows. Left – Cumulative oil production, Right – Cumulative water production.

Figure 3.24 plots the cumulative oil and water production of true reservoir responses and 100 realizations from different geological assumptions. As can be seen from the band of responses in each scenario, results from different geological assumptions are grouped together. Realizations from S1 and S3, which assume a fractured reservoir, show responses closer to the true responses than do the cases that do not assume a fractured reservoir. Specifically, S1, which shares a deformation history with the true case, produces bands of responses which scatter around the true oil production.

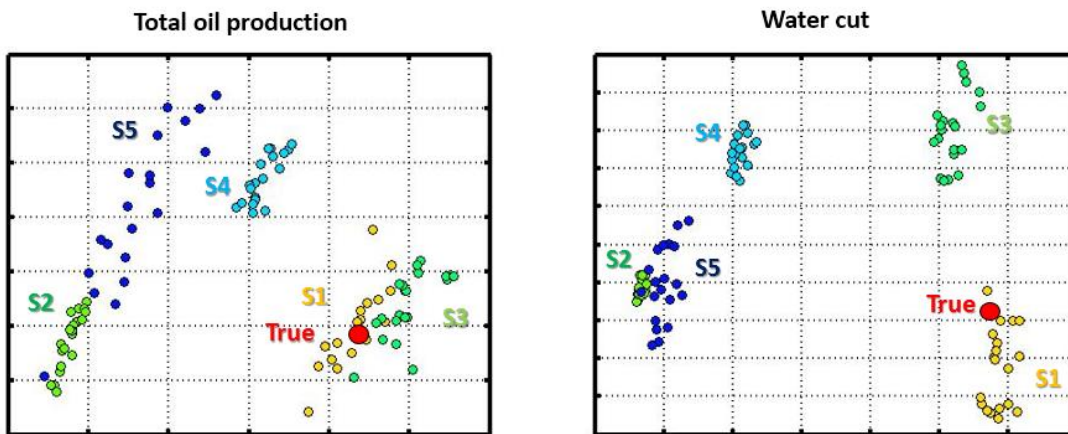


Figure 3.25: MDS plot using distance of the total oil production curve and the water cut curve.

Figure 3.25 shows MDS plots of total oil production and water cut curves. Normally, it is not necessary to use MDS to plot production curves since we can easily display many curves at the same time. However, an MDS plot still gives a visually more friendly display of the similarity and clustering of responses, because production curves tend to be overcrowded and it is hard to see if curves overlap. If we examine the water production, the effect of using the proposed workflow with a good geological assumption becomes more noticeable. Except for realizations from S1 and S3, none of the 60 realizations from S2, S4, or Cv achieve close forecasting of water production. The difference between oil and water production can be induced from the fact that the reservoir was initially oil filled. Therefore, in any case, the initial status of production will have enough influx of oil. However, the water breakthrough is hugely influenced by the permeability distribution. It is worth noting that realizations from conventional

approaches are far from the true cases. Even with similar oil production, which may impact revenue, giving a better prediction of water-cut, which is related to cost, would be important for reservoir evaluation.

3.3.6 Discussion

100 realizations from five different geological scenarios of structural deformation and reservoir property evolution were compared with true responses from a synthetic reservoir. Flow responses of the realizations using the correct scenario give good forecasts and uncertainty quantifications of flow responses. Realizations are grouped separately in an MDS plot, and the correct scenario gives closer segregation on the MDS plot when acoustic impedance is used.

If we assume the strain distribution from the deformation is uniform across the reservoir, and that any property evolution is also uniform around the reservoir, the proposed workflow becomes identical with the conventional workflow. For cases where any major geological event influences an area uniformly, or with minor variation over the area of interest, the advantages of the proposed workflow may be less noticeable. However, for cases where the effects of geological events vary spatially or are uncertain, the proposed workflow may become effective. For instance, in some cases, we know whether the reservoir is naturally fractured or not. However, there are many cases where we fail to see any significant evidence of fractures, not only from seismic responses, but also from the vertical exploratory wells. In S3 in Figure 3.22, for instance, even though the realization has fractures, the low matrix porosity in the fractured area compensates for the seismic velocity drop by the existence of fractures. This may present difficulties in distinguishing fracture swarms. The realization on S4, a case with no fractures, gives the opposite example. Localized high porosity returns low seismic velocity, so we may want to consider the possibility of having fractures in that area. The virtue of the proposed workflow is being able to test the scenario at an early stage of the project cycle. Moreover, if it does not produce any significant differences from the conventional one, we can always use the conventional process. In that case, we may conclude that the area of interest may share a more or less homogenous geological history and impact.

The proposed framework may not be required in every situation. Obviously, the E&P industry has successfully conducted subsurface modeling and production for decades. However, if the reservoir has relatively higher structural complexity within the modeling boundary, the proposed framework is expected to be beneficial.

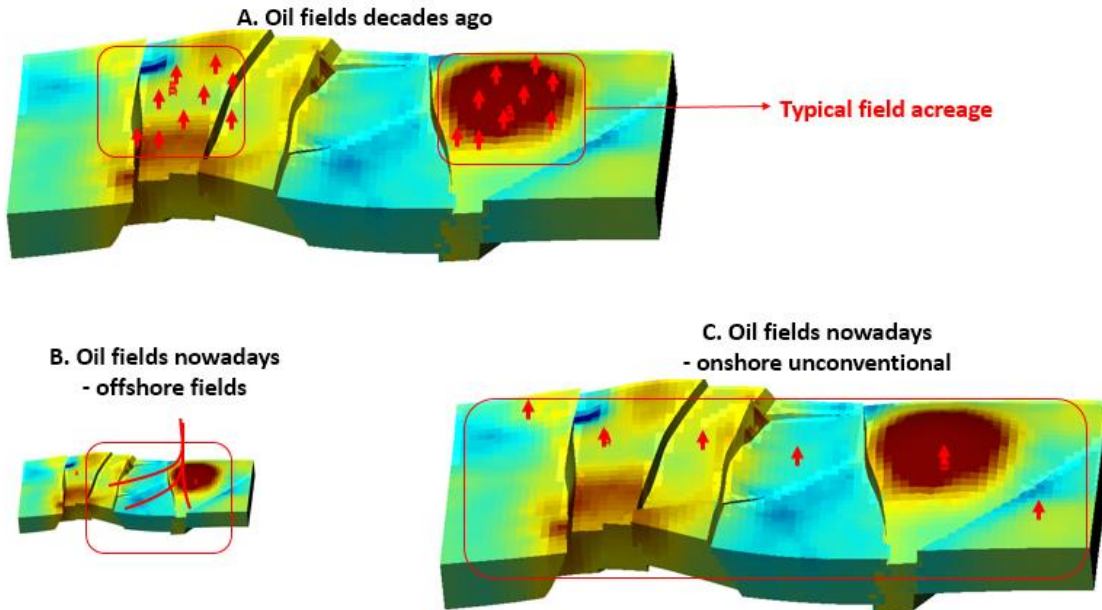


Figure 3.26: Situations when the proposed framework would be beneficial vs. less beneficial. Cartoon A – structural attributes are relatively homogeneous within the field boundary and the fields have densely drilled wells. B – fields have higher structural complexity within the area of interest. Deep-water conditions limit the number of wells and they need to share the same well pad, which limits the area we can investigate from wells. C – in unconventional fields, the areas of development are different orders of magnitude. Thus, even with a relatively gentle structure from the scale of conventional reservoirs, they can have relatively high structural complexity across the fields. In A and B, the red arrow and lines mean wells. In C, the red arrow may represent hundreds of intensive drilling layouts.

Figure 3.26 uses cartoons to explain the cases when the proposed workflow could be useful or not. In cartoon A, we found oil or gas fields with gigantic structure and have dense production wells. Thus, we have less spatial heterogeneity on structural deformation attributes. In addition, having data from enough wells resolved the property estimation as interpolation problems. In cartoon B, we have to develop compartmentalized reservoirs from the same one or two rigs. The number of wells is limited by the capacity of the well pads. Since all the wells from the same rigs are

sharing almost identical entry points, additional information from the wells is limited. In cartoon C, unconventional fields are explored across a relatively large surface area with intense drilling activities. Since unconventional resources are spread out in the basin level, though the area may have relatively less complex structure with the scale of a conventional reservoir, an unconventional reservoir may contain a higher level of complexity by having much wider areas of interest.

3.4 Summary

In this chapter, we proposed a framework for a geomodeling workflow to model geological uncertainty arising from structural deformation and rock accommodation. To test the proposed framework, we applied it on a 3-D synthetic reservoir made for testing purposes. We compared the effect of geological uncertainty on structural deformation of reservoir and reservoir property evolution in reservoir responses. Realizations of the reservoir from different geological scenarios generate distinctively different reservoir responses when applied to a synthetic reservoir. Realizations from the correct scenario give closer reservoir responses to the true reservoir, not only in the flow responses but also in the seismic attributes on an MDS plot. This approach is very promising because we can test our geological understanding at an early stage of the project cycle. For the given synthetic case, the conventional workflow fails to generate realizations that produce similar reservoir responses. Application to a real field case should be conducted as a future study.

Chapter 4

4 Modeling Seismic Anisotropy while Honoring Vertical Velocities and Bulk Density with Multiple Sets of Inclusions

As demonstrated in Chapter 2, proper rock physics models are essential for propagating geological assumptions on structural deformation and rock accommodation to "what-if" seismic responses. When implementing these ideas in a field application, the first challenge is how to honor the well log and velocity profiles, while still creating offset and angle-dependent seismic responses according to the specific geological assumptions we want to test. In this chapter, we first review currently available rock physics models to model elastic anisotropy arising from aligned inclusions. Then, we propose a new approach to model effective stiffness tensors with any number of crack sets with arbitrary crack orientations, within an anisotropic background matrix. This model is applied to Sarout's shale experiment data (Sarout and Guéguen, 2008; Sarout et al., 2008).

4.1 Rock physics models for multiple geological scenarios

Rock physics models have been successfully used to quantify subsurface heterogeneities, such as lithology estimations (Avseth et al., 2001), pore pressure effects (Mukerji and Mavko, 1994), linking seismic properties with flow properties in a coherent way (Castro et al., 2005), and investigating multiscale problems (Mukerji et al., 1995). By using rock physics models, we can predict the possible seismic signatures for different subsurface conditions, including degree of cementation (Avseth et al.,

2000), whether we have fractures or not (Sava and Mukerji, 2001), and how saturation changes from the productions may impact seismic responses (Lee and Mukerji, 2012).

To use rock physics models for differentiating rock properties for distributed accommodations (deformations absorbed by rearrangement of pores and minerals) or localized accommodations (deformations absorbed by creating discontinuous features such as cracks or fractures), we need to model the elastic properties of the host medium without crack inclusions, and the elastic properties of the medium with inclusions. This section first reviews the current rock physics models available for this modeling.

4.1.1 Rock physics models for isotropic and anisotropic medium without cracks

For isotropic medium

All natural rocks have a certain degree of anisotropy in the core or well log scale, due to various geological factors and processes such as layering, compactions, pore shapes, and mineral orientation (Bandyopadhyay, 2009). But in many cases, rock properties are modeled as isotropic at a given scale by default, unless the medium is clearly anisotropic or the anisotropy is the main focus of the investigation. For modeling elastic properties of isotropic mediums, we can use either empirical rock physics models, theoretical models, or both. Basically, if we know the bulk density, P-wave, and S-wave velocity, we know all the elastic properties for isotropic mediums. But we also need to know how P-wave velocity would change if porosity and bulk density were changed, and likewise how the S-wave would be changed. Empirical models are either derived from lithology or basin-specific measurements. They usually do not give elastic properties such as bulk or shear moduli directly, but rather give empirical relations between two or three key measurements, such as P-wave and S-wave velocity, so we can reconstruct the elastic properties of the rock using other measurement data (Greenberg and Castagna, 1992).

Theoretical models are based on simplified and idealized physical models such as the contact model of spheres (Mindlin, 1940), or cement models of contacts among spheres (Dvorkin and Nur, 1996) or ellipsoidal inclusions (Berryman, 1980). Even when

we use theoretical models, we still use observed data to find the optimal model parameters.

For anisotropic medium

To model the anisotropy of a rock, we need to assume a certain degree of symmetry. By following Voigt's notation, we can express stiffness tensors in a 6 by 6 matrix. For isotropic material, we have two independent constants in the stiffness tensor, so we need two velocity measurements, while a transversely isotropic medium has five independent constants and thus requires five different measurements (Mavko et al., 2003). For the typical sources of anisotropy, vertically transversely isotropy (VTI) symmetry serves as a good approximation for anisotropic rocks in many cases (Bandyopadhyay, 2009).

Modeling an effective elastic medium involves mixing problems. Theoretical bounds, such as the Voigt and Reuss bounds, give theoretical minimum and maximum elastic properties when different elastic materials are mixed. Rock anisotropy can be understood as having different stiffness in different directions within the theoretical bounds. When the shape of inclusion falls in specific shapes and the properties of inclusion are known, effective medium models for inclusions, such as self-consistent approximation (SCA) (Budiansky, 1965; Hill, 1965; Tai Te Wu, 1966; Berryman, 1980) or the differential effective medium model (DEM) (Cleary et al., 1980; Norris, 1985), can be used.

The five independent constants of a VTI medium are related to Thomsen's anisotropic parameters by equation (4-1): To model the anisotropy of a rock, we need to assume a certain degree of symmetry. By following Voigt's notation, we can express stiffness tensors in a 6 by 6 matrix. For isotropic material, we have two independent constants in the stiffness tensor, so we need two velocity measurements, while a transversely isotropic medium has five independent constants and thus requires five different measurements (Mavko et al., 2003). For the typical sources of anisotropy, vertically transversely isotropy (VTI) symmetry serves as a good approximation for anisotropic rocks in many cases (Bandyopadhyay, 2009).

Modeling an effective elastic medium involves mixing problems. Theoretical bounds, such as the Voigt and Reuss bounds, give theoretical minimum and maximum elastic properties when different elastic materials are mixed. Rock anisotropy can be understood as having different stiffness in different directions within the theoretical bounds. When the shape of inclusion falls in specific shapes and the properties of inclusion are known, effective medium models for inclusions, such as self-consistent approximation (SCA) (Budiansky, 1965; Hill, 1965; Tai Te Wu, 1966; Berryman, 1980) or the differential effective medium model (DEM) (Cleary et al., 1980; Norris, 1985), can be used.

The five independent constants of a VTI medium are related to Thomsen's anisotropic parameters by equation (4-1):

$$\begin{aligned}
 c_{33} &= \rho\alpha^2, \quad c_{44} = \rho\beta^2, \\
 c_{11} &= c_{33}(1 + 2\varepsilon), \quad c_{66} = c_{44}(1 + 2\gamma), \\
 c_{13} &= \pm\sqrt{2c_{33}(c_{33} - c_{44})\delta + (c_{33} - c_{44})^2} - c_{44}
 \end{aligned} \tag{4-1}$$

Thomsen's weak anisotropic parameters are expressed in equation (4-2):

$$\begin{aligned}
 \alpha &= \sqrt{c_{33}/\rho} & \beta &= \sqrt{c_{44}/\rho} & \varepsilon &= \frac{c_{11} - c_{33}}{2c_{33}} \\
 \gamma &= \frac{c_{66} - c_{44}}{2c_{44}} & \delta &= \frac{(c_{13} + c_{44})^2 - (c_{33} - c_{44})^2}{2c_{33}(c_{33} - c_{44})}
 \end{aligned} \tag{4-2}$$

Transversely, isotropic elastic material can be expressed in Voigt notation as equation (4-3):

$$\begin{bmatrix} c_{11} & c_{12} & c_{13} & 0 & 0 & 0 \\ c_{12} & c_{11} & c_{13} & 0 & 0 & 0 \\ c_{13} & c_{13} & c_{33} & 0 & 0 & 0 \\ 0 & 0 & 0 & c_{44} & 0 & 0 \\ 0 & 0 & 0 & 0 & c_{44} & 0 \\ 0 & 0 & 0 & 0 & 0 & c_{66} \end{bmatrix}, \text{ where } c_{66} = \frac{1}{2}(c_{11} - c_{12}) \quad (4-3)$$

4.1.2 Rock physics models for isotropic and anisotropic mediums with cracks

Theoretically, we can extract effective elastic properties from inclusions with complex geometry by using stress-strain analysis with finite discretization (Grechka et al., 2006). But in reality, we do not know the exact geometry, density, and orientation distribution of the inclusions. Moreover, our measurements and data are usually much coarser resolution than the expensive computation needed to honor exact geometry. Thus, computations from FEM or FVM methods are used to test and compare more easy-to-calculate effective medium models for materials with aligned cracks, such as Hudson's penny shape inclusion model (Hudson, 1990) or Kachanov's inclusion model (Kachanov, 1980). Both Hudson's and Kachanov's models assumes isotropic host medium and simplify the geometry of inclusion as penny-shaped ellipsoids, where the abundance of crack inclusions are expressed in a well-known definition of crack density as equation (4-4) (Bristow, 1960; Kachanov, 1980):

$$e = \frac{3\phi_{crack}}{4\pi\alpha} = \frac{N}{V}a^3 \quad (4-4)$$

where crack porosity is ϕ_{crack} , α is the aspect ratio of the crack ellipsoid, N is the number of cracks in measured volume V , and a is the crack radius.

Hudson's model, equation (4-5) calculates the elastic stiffness tensor using 1st and 2nd order correction terms expressed in terms of the crack density and aspect ratio.

$$\mathbf{C}_{ij}^{eff} = \mathbf{C}_{ij}^0 + \mathbf{C}_{ij}^1 + \mathbf{C}_{ij}^2, \quad (i, j = 1, 2, 3) \quad (4-5)$$

In the above equation (4-5), the superscript "0" indicates the background isotropic elastic stiffness without cracks. \mathbf{C}_{ij} is the stiffness tensor components which are expressed in Voigt notation. Superscripts "1" and "2" correspond to the 1st order and 2nd order correction terms. Hudson proposed his original 2nd order correction terms, but Cheng (1993) demonstrated that using only the 1st correction terms gives numerically stable results. Cheng also provided a modified 2nd order terms using a Pade approximation which does not have instability problems (Cheng, 1993). When the crack normals are aligned with axis-3, meaning the horizontal fractures are parallel with the axis-1 and axis-2 plain, the stiffness tensor, from Hudson's model with 1st order correction, can be expressed by equation (4-6). \mathbf{K} ' and μ ' are the bulk and shear moduli of the inclusion material, while λ and μ are the Lamé constants of the un-fractured rock.

$$\begin{aligned} c_{11}^1 &= -\frac{\lambda^2}{\mu} eU_{33} \\ c_{13}^1 &= -\frac{\lambda + 2\mu}{\mu} eU_{33} \\ c_{33}^1 &= -\frac{(\lambda + 2\mu)^2}{\mu} eU_{11} \\ c_{66}^1 &= 0 \end{aligned}$$

where

$$U_{11} = \frac{16(\lambda + 2\mu)}{3(3\lambda + 4\mu)} \frac{1}{1 + M} \quad U_{33} = \frac{4(\lambda + 2\mu)}{3(\lambda + \mu)} \frac{1}{1 + k}$$

and

$$M = \frac{4\mu'(\lambda + 2\mu)}{\pi\alpha\mu(\lambda + \mu)} \quad k = \frac{[K' + (\frac{4}{3})\mu'](\lambda + 2\mu)}{\pi\alpha\mu(\lambda + \mu)} \quad (4-6)$$

As can be seen from equation (4-6), Hudson's model adjusts the stiffness constants proportional to the crack density. The original 2nd order correction terms proposed by Hudson are in equation (4-7).

$$\begin{aligned} c_{11}^2 &= \frac{q}{15} \frac{\lambda^2}{(\lambda + 2\mu)} (eU_{33})^2 \\ c_{13}^2 &= \frac{q}{15} \lambda (eU_{33})^2 \\ c_{33}^2 &= \frac{q}{15} (\lambda + 2\mu) (eU_{33})^2 \\ c_{44}^2 &= \frac{2q}{15} \frac{\mu(3\lambda + 8\mu)}{(\lambda + 2\mu)} (eU_{11})^2 \\ c_{66}^2 &= 0 \end{aligned}$$

where

$$q = 15 \frac{\lambda^2}{\mu^2} + 28 \frac{\lambda}{\mu} + 28 \quad (4-7)$$

Cheng (1993) pointed out that using only first order correction terms gives more stable results than using second order terms. He also proposed a modified second order corrections, shown in equation (4-8), which solves the instability problem of using the original second order terms. C_{ij}^2 is the second order correction term from equation (4-7), and C_{ij}^1 is the first order correction term from equation (4-6).

$$c_{ij}^{eff} = c_{ij}^0 \frac{1 - a_{ij} \cdot e}{1 + b_{ij} \cdot e}$$

where

$$b_{ij} = -\frac{c_{ij}^2}{c_{ij}^1 \cdot e}$$

and

$$a_{ij} = -\frac{c_{ij}^1}{c_{ij}^0 \cdot e} - b_{ij} \quad (4-8)$$

On the other hand, Kachanov's model starts with a compliance tensor, which is the inverse of stiffness, and proportionally increases the compliance constant to crack density as expressed in equation (4-9). The superscript 0 denotes the background properties without inclusions.

$$\mathbf{s}_{ij}^{eff} = \mathbf{s}_{ij}^0 + \Delta \mathbf{s}_{ij} \quad (4-9)$$

For the case when one set of crack inclusions coincide with the normal to the axis-1 with crack density e_1 , the correction terms can be simply expressed as equation (4-10). K_{fl} is the bulk modulus of the inclusion material, ν_0 and E_0 are Poisson's ratio and Young's modulus of background material, respectively, and ζ is a fluid factor.

$$\Delta \mathbf{s}_{11} = \frac{16e_1(1 - \nu_0^2)}{3E_0} (1 - \zeta), \quad \Delta \mathbf{s}_{55} = \frac{32e_1(1 - \nu_0^2)}{3(1 - 2\nu_0)}$$

$$\Delta \mathbf{s}_{66} = \Delta \mathbf{s}_{55}$$

where

(4-10)

$$\zeta = \frac{1}{(1 + \alpha(\frac{E_0}{K_{fl}} - 3(1 - 2\nu_0)))}$$

Hudson's model was compared with clean sand having artificial penny-shaped inclusion, and showed good reproduction of P-wave velocity measurements in a dry condition (Rathore et al., 1995). Both Kachanov's and Hudson's models were also compared with FEM computations, and Kachanov's model gives slightly better results for inclusions on impermeable mediums (Grechka and Kachanov, 2006). Comparisons between these two models are covered in later sections.

Both Hudson's and Kachanov's models require an isotropic host medium. Models to calculate the effective elastic properties of inclusions in anisotropic mediums exist, but require certain conditions for implementation to have explicit forms for the calculations. Both SCA and DEM models can be used to calculate the effective medium of anisotropic inclusion within an anisotropic host medium, when the axis of symmetry of the host and the inclusion medium are aligned (Mura, 1983; Nishizawa, 1982; Bandyopadhyay, 2009; Sevostianov et al., 2005; Sevostianov and Kachanov, 2007). Available explicit forms would be useful when we want to model a crack-like pore and its effect on the effective medium with the intrinsic anisotropy from mineral fabrics of shale (Bandyopadhyay, 2009; Vernik and Nur, 1992).

Once the rocks have either background anisotropy or crack inclusions, the resultant medium is anisotropy. Thus, seismic propagation in the rock has angular dependency. Phase velocity calculations with explicit forms are only available when the type of symmetry is known, along with directional information on the symmetry axis (Mavko et al., 2003).

$$(C_{ijkl}n_jn_l - \delta_{ik}\rho V^2)p_k = 0 \quad (4-11)$$

Christoffel's equation (4-11) allows one to calculate the phase velocity of any angle of incidence once we construct stiffness tensors in Voigt notation and know the bulk

density (Auld, 1990; Sun, 2002). In equation (4-11), \mathbf{n}_i are the unit vector components in the direction of wave propagation, δ_{ik} is the Kronecker delta, \mathbf{p}_k are unit displacement polarization vectors, ρ is the density, C_{ijkl} are the effective elastic stiffness tensor components, and \mathbf{V} is the phase velocity. This equation can be rewritten in matrix form as follows:

$$\begin{bmatrix} \Gamma_{11} - \rho V^2 & \Gamma_{12} & \Gamma_{13} \\ \text{sym.} & \Gamma_{22} - \rho V^2 & \Gamma_{23} \\ & & \Gamma_{33} - \rho V^2 \end{bmatrix} \begin{Bmatrix} p_1 \\ p_2 \\ p_3 \end{Bmatrix} = 0$$

where,

$$\Gamma_{ik} = C_{ijkl} n_j n_l \quad (4-12)$$

Eigen values of the LHS of the matrix form of Christoffel's equation gives $\rho \mathbf{V}^2$ for a given angle of the wave propagation. To construct the matrix, the following relations can be used (Sun, 2002):

$$\Gamma_{11} = n_1^2 C_{11} + n_2^2 C_{66} + n_3^2 C_{55} + 2n_2 n_3 C_{56} + 2n_3 n_1 C_{15} + 2n_1 n_2 C_{16}$$

$$\Gamma_{22} = n_1^2 C_{66} + n_2^2 C_{22} + n_3^2 C_{44} + 2n_2 n_3 C_{24} + 2n_3 n_1 C_{46} + 2n_1 n_2 C_{26}$$

$$\Gamma_{33} = n_1^2 C_{55} + n_2^2 C_{44} + n_3^2 C_{33} + 2n_2 n_3 C_{34} + 2n_3 n_1 C_{35} + 2n_1 n_2 C_{45}$$

$$\begin{aligned} \Gamma_{12} = & n_1^2 C_{16} + n_2^2 C_{26} + n_3^2 C_{45} + n_2 n_3 (C_{25} + C_{46}) \\ & + n_3 n_1 (C_{14} + C_{56}) + n_1 n_2 (C_{12} + C_{66}) \end{aligned}$$

$$\begin{aligned}
\Gamma_{13} &= n_1^2 C_{15} + n_2^2 C_{46} + n_3^2 C_{35} + n_2 n_3 (C_{36} + C_{45}) \\
&\quad + n_3 n_1 (C_{13} + C_{55}) + n_1 n_2 (C_{14} + C_{56}) \\
\Gamma_{23} &= n_1^2 C_{56} + n_2^2 C_{24} + n_3^2 C_{34} + n_2 n_3 (C_{44} + C_{23}) \\
&\quad + n_3 n_1 (C_{36} + C_{45}) + n_1 n_2 (C_{25} + C_{46})
\end{aligned} \tag{4-13}$$

For example, let us assume that we have an isotropic medium with bulk and shear moduli of 25 GPa and 15 GPa, and bulk density of 3.5 g/cc. Because it is isotropic, there is no directional dependency on phase velocity. The stiffness tensor for this isotropic medium is given by

$$\mathbf{C} = \begin{bmatrix} 45 & 15 & 15 & 0 & 0 & 0 \\ 15 & 45 & 15 & 0 & 0 & 0 \\ 15 & 15 & 45 & 0 & 0 & 0 \\ 0 & 0 & 0 & 15 & 0 & 0 \\ 0 & 0 & 0 & 0 & 15 & 0 \\ 0 & 0 & 0 & 0 & 0 & 15 \end{bmatrix} \tag{4-14}$$

For a vertically propagating seismic wave, the normal \mathbf{n} would be $[0 \ 0 \ 1]$. We can construct Christoffel's matrix using equations (4-13) and (4-12), and they give the following 3 by 3 matrix \mathbf{G} .

$$\mathbf{G} = \begin{bmatrix} 15 & 0 & 0 \\ 0 & 15 & 0 \\ 0 & 0 & 45 \end{bmatrix} \tag{4-15}$$

If we conduct an eigen value decomposition on Christoffel's matrix \mathbf{G} , using equation (4-15), it is obvious that its Eigen values are (45, 15, 15). Together with the given density, now we have a P-wave velocity of 3.5857 km/s, and an S-wave velocity of 2.0702 km/s. This is identical with the P- and S-wave velocity of an isotropic medium calculated using the following equation (4-16).

$$V_p = \sqrt{(K + \frac{4}{3}G)/\rho}, \quad V_s = \sqrt{G/\rho} \quad (4-16)$$

Previous equations applying Hudson's and Kachanov's models demonstrated the case when the axes of symmetry is axis-3, which means horizontal fractures. For the case when we have multiple sets of inclusion with different orientations, we can, as an approximation, simply superimpose the correction terms of each inclusion set using the previous equations, after rotating the correction terms with respect to the orientation of specific fracture sets. Since the Voigt's stiffness tensor is a simplified notation of the 4th order tensors, we need to use special tensor rotation equation to re-orient the correction terms into the right direction. This can be done by using equation (4-17) and a Bond transformation (Auld, 1990). In the equation, matrix \mathbf{M} and \mathbf{N} are 6 by 6 Bond transformation matrices (Equation 3.18). β_{ij} is the cosine of the angle between new i -axis and the original j -axis.

$$\begin{aligned} [C'] &= [M][C][M]^T \\ [S'] &= [N][S][N]^T \end{aligned} \quad (4-17)$$

$$\mathbf{M} = \begin{bmatrix} \beta_{11}^2 & \beta_{12}^2 & \beta_{13}^2 & 2\beta_{12}\beta_{13} & 2\beta_{13}\beta_{11} & 2\beta_{11}\beta_{12} \\ \beta_{21}^2 & \beta_{22}^2 & \beta_{23}^2 & 2\beta_{22}\beta_{23} & 2\beta_{23}\beta_{21} & 2\beta_{21}\beta_{22} \\ \beta_{31}^2 & \beta_{32}^2 & \beta_{33}^2 & 2\beta_{32}\beta_{33} & 2\beta_{33}\beta_{31} & 2\beta_{31}\beta_{32} \\ \beta_{21}\beta_{31} & \beta_{22}\beta_{32} & \beta_{23}\beta_{33} & \beta_{22}\beta_{33} + \beta_{23}\beta_{32} & \beta_{21}\beta_{33} + \beta_{23}\beta_{31} & \beta_{22}\beta_{31} + \beta_{21}\beta_{32} \\ \beta_{31}\beta_{11} & \beta_{32}\beta_{12} & \beta_{33}\beta_{13} & \beta_{12}\beta_{33} + \beta_{13}\beta_{32} & \beta_{11}\beta_{33} + \beta_{13}\beta_{31} & \beta_{11}\beta_{33} + \beta_{12}\beta_{31} \\ \beta_{11}\beta_{21} & \beta_{11}\beta_{22} & \beta_{13}\beta_{23} & \beta_{22}\beta_{13} + \beta_{12}\beta_{32} & \beta_{11}\beta_{23} + \beta_{13}\beta_{21} & \beta_{22}\beta_{11} + \beta_{12}\beta_{21} \end{bmatrix}$$

$$\mathbf{N} = \begin{bmatrix} \beta_{11}^2 & \beta_{12}^2 & \beta_{13}^2 & \beta_{12}\beta_{13} & \beta_{13}\beta_{11} & \beta_{11}\beta_{12} \\ \beta_{21}^2 & \beta_{22}^2 & \beta_{23}^2 & \beta_{22}\beta_{23} & \beta_{23}\beta_{21} & \beta_{21}\beta_{22} \\ \beta_{31}^2 & \beta_{32}^2 & \beta_{33}^2 & \beta_{32}\beta_{33} & \beta_{33}\beta_{31} & \beta_{31}\beta_{32} \\ 2\beta_{21}\beta_{31} & 2\beta_{22}\beta_{32} & 2\beta_{23}\beta_{33} & \beta_{22}\beta_{33} + \beta_{23}\beta_{32} & \beta_{21}\beta_{33} + \beta_{23}\beta_{31} & \beta_{22}\beta_{31} + \beta_{21}\beta_{32} \\ 2\beta_{31}\beta_{11} & 2\beta_{32}\beta_{12} & 2\beta_{33}\beta_{13} & \beta_{12}\beta_{33} + \beta_{13}\beta_{32} & \beta_{11}\beta_{33} + \beta_{13}\beta_{31} & \beta_{11}\beta_{33} + \beta_{12}\beta_{31} \\ 2\beta_{11}\beta_{21} & 2\beta_{11}\beta_{22} & 2\beta_{13}\beta_{23} & \beta_{22}\beta_{13} + \beta_{12}\beta_{32} & \beta_{11}\beta_{23} + \beta_{13}\beta_{21} & \beta_{22}\beta_{11} + \beta_{12}\beta_{21} \end{bmatrix}$$

(4-18)

The effective medium stiffness, or compliance tensors of multiple set of inclusions, can be expressed by the following equations:

$$C^{eff} = C^0 + \sum_i^n [M_i][\Delta C_i][M_i]^T$$

$$S^{eff} = S^0 + \sum_i^n [N_i][\Delta S_i^1][N_i]^T \quad (4-19)$$

Gassmann's fluid substitution equation allows one to calculate the bulk modulus of rocks when the fluid in the pores is replaced by a new fluid (Gassmann, 1951). Equation (4-20) is Gassmann's equation to link dry rock modulus with that of fluid-saturated rock. K_{sat} is the bulk modulus of the fluid-saturated rock, while K_{dry} and K_{fl} are the bulk moduli of dry rock and fluid. K_0 is the mineral bulk modulus. μ is the shear modulus.

$$\frac{K_{sat}}{K_0 - K_{sat}} = \frac{K_{dry}}{K_0 - K_{dry}} + \frac{K_{fl}}{\phi(K_0 - K_{fl})}$$

$$\mu_{sat} = \mu_{dry} \quad (4-20)$$

Brown-Korringa's equation (1975) can be used to conduct fluid substitution for an anisotropic medium. s_{ijkl}^{dry} is the effective compliance tensor component of dry rock, while the superscript "sat" means saturated. The superscript "0" indicates the mineral solid. β_{fl} and β_0 are the compressibility of the fluid and the mineral.

$$s_{ijkl}^{sat} = s_{ijkl}^{dry} - \frac{(s_{ijaa}^{dry} - s_{ijaa}^0)(s_{bbkl}^{dry} - s_{bbkl}^0)}{(s_{ccdd}^{dry} - s_{ccdd}^0) + \phi(\beta_{fl} - \beta_0)} \quad (4-21)$$

4.1.3 Comparing Hudson's and Kachanov's models with Rathore's experimental data: the importance of proper model choice with proper implementation

Each rock physics model has its own assumptions and limitations. Thus, choosing a proper model depends on several conditions, such as the lithology of the rock, the frequency of waves and assumptions about interactions among pores, and the cracks of the models. In this section, we use Rathore and colleagues' experimental data to compare Hudson's and Kachanov's models for modeling crack inclusion in a clean sandstone case. Their experiment (1995) was conducted in a way to test the accuracy of Hudson's model by adding penny-shaped human-made inclusion in Danish beach sand, where we know the actual petrophysical and elastic properties with high accuracy. They measured seismic velocity by changing the angle of seismic incidence with the orientation of artificially made cracks. shows the experiment configuration. The exact properties of the host sandstone and geometry of the artificial crack can be found in Table 4-1.

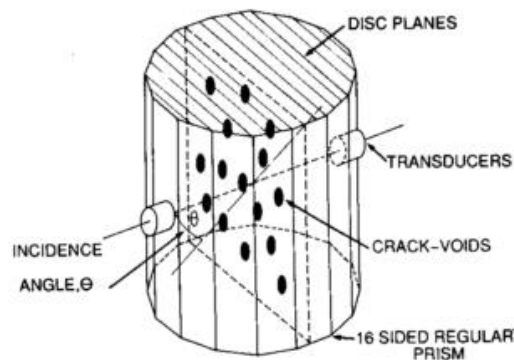


Figure 4.1: Configuration of the experiment of Rathore et al., 1994. A series of disc planes of sandstone were assembled after the crack-voids were carved out. The crack density of the artificial crack was controlled to be 0.1.

Table 4-1: Properties of the host sandstone and geometry of the artificial cracks. The velocity measurement on crack-free host sandstone for both the dry and water-filled case are in the right column.

Crack info:	Test seismic frequency: 100 kHz
Diameter: 5.5 mm	
Aperture: 0.02 mm	Velocity measurement on host medium
Crack density: 0.1	$V_p^{\text{dry}}=2.543$ km/sec
Crack porosity: 0.23 %	$V_s^{\text{dry}}=1.517$ km/sec
	$V_p^{\text{wet}}=2.715$ km/sec
Matrix info:	$V_s^{\text{wet}}=1.408$ km/sec
Porosity: 34.6 %	
Dry bulk density: 1.712 g/cc	

They repeated the measurements once for a dry case, and again for a wet case by water. Their procedures were as follows:

- For dry case: apply Hudson's model with 2nd order correction terms using equation (4-6) and equation (4-7), with dry bulk and shear moduli of sandstone, 5.82 and 3.94 GPa from dry rock velocity, and 0 GPa bulk modulus for dry air. A comparison between the measurement and the calculation from Hudson's model is shown in Figure 4.2.
- For the wet case: apply Hudson's model with 2nd order correction terms using equation (4-6) and equation (4-7), with wet bulk and shear moduli of sandstone, 9.72 and 4.07 GPa from wet rock velocity, and 2.16 GPa for water bulk modulus. Results can be seen in Figure 4.3.

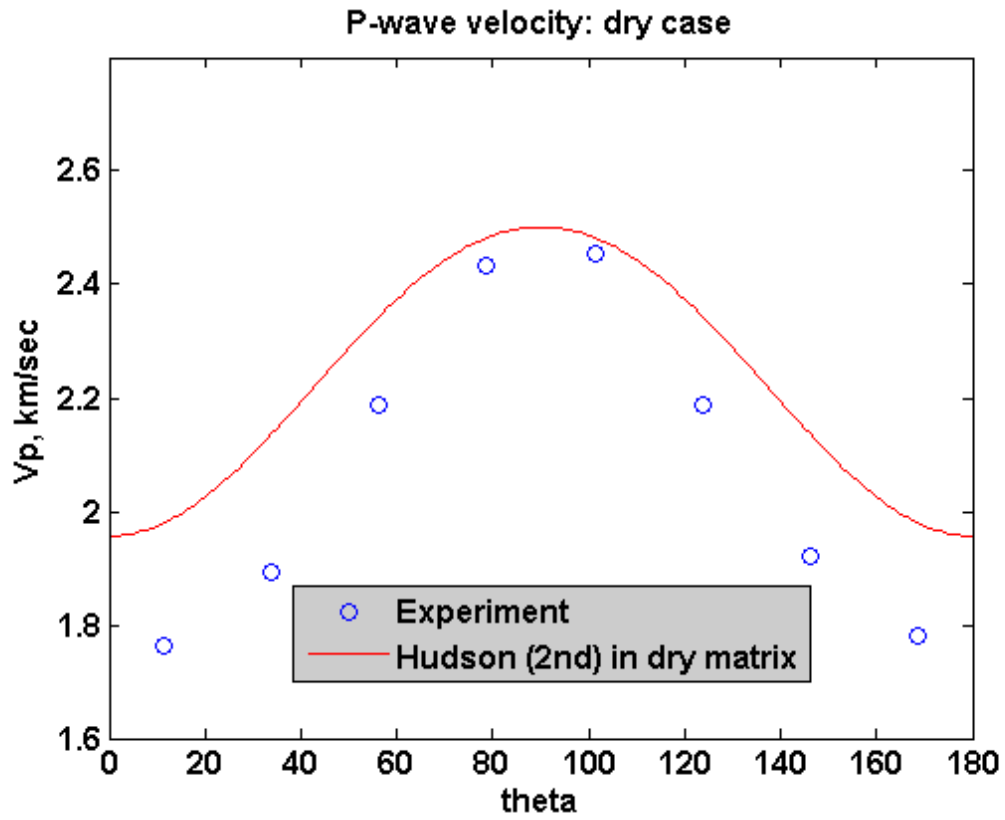


Figure 4.2: Rathore and colleagues' experiments on dry sample. The circles are the measured velocity, and the solid line is the velocity calculated from Hudson's model using 2nd order corrections, showing good agreement. Theta is the angle between the seismic wave and the orientation of the crack normal.

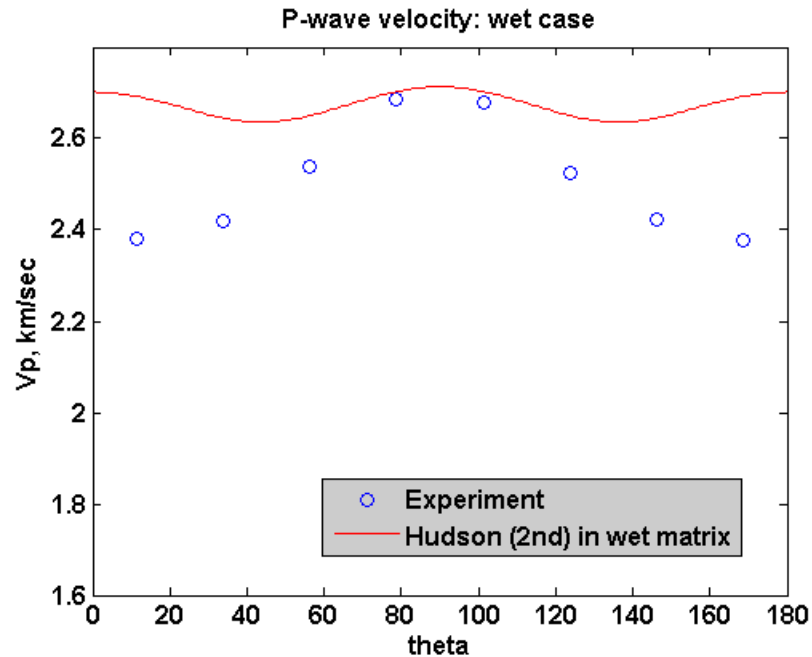


Figure 4.3: Rathore and colleagues' experiments on a wet sample. The circles are the measured velocity, and the solid line is the velocity calculated from Hudson's model using 2nd order corrections, which does not show good agreement. Theta is the angle between the seismic wave and the orientation of the crack normal.

In the original paper, the authors claimed that Hudson's model works well in reproducing the experiment data for the dry sand case, but fails to reproduce the experiment data for the wet case. But the reason why their results for the wet case deviated from the experiments is because they implicitly assumed the interactions of pores and cracks by applying the process of Hudson's model directly, using wet rock properties with fluid properties. By doing so, they assume no fluid communications among the pores and crack inclusions.

We are going to re-calculate the effective elastic properties in a way that assumes communication between pores and cracks. We call this implementation B, while the previous one is implementation A.

- Start from Hudson's model results for the dry case. Then, apply Brown-Korringa's fluid substitution, equation (4-21), to make the dry stiffness tensor a wet stiffness tensor. Compute the velocity again.

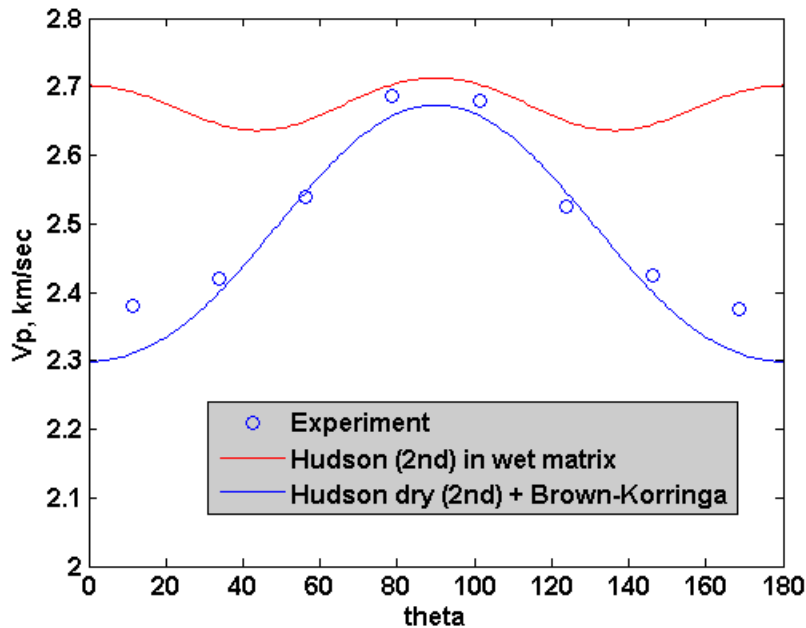


Figure 4.4: Comparison of implementation A and implementation B with the experiment data. After applying fluid substitution on the dry crack, the calculated velocity agrees with the measurements (blue solid). Red solid line is a result from implementation A. blue circles are measurements from the experiments.

Figure 4.4 shows that implementation B agrees well with the measurement. Implementation A assumes no fluid interaction among the pores and cracks when the rock is excited by the applied seismic wave. However, implementation B assumes fluid interaction among the pores and cracks by applying fluid substitution after it adds a dry crack on the dry host rock.

The reason why implementation B is more appropriate for the given experiment could be because the rock used for the experiment is a very clean and very porous sandstone. The porosity was 34.6%, and considering the given seismic frequency, 100 k Hz, and the seismic velocity, 2200 m/s, the wave length is about 2.2 cm. The penny shaped human-made crack was also relatively gentle, with a 0.0036 aspect ratio and 0.02 mm crack thickness. Even with the high frequency, the pores of the host rock and cracks could be relatively permeable to allow pressure relaxations among each other. In

short, the pores and crack could communicate with each other in those specific experiments under the applied seismic perturbation.

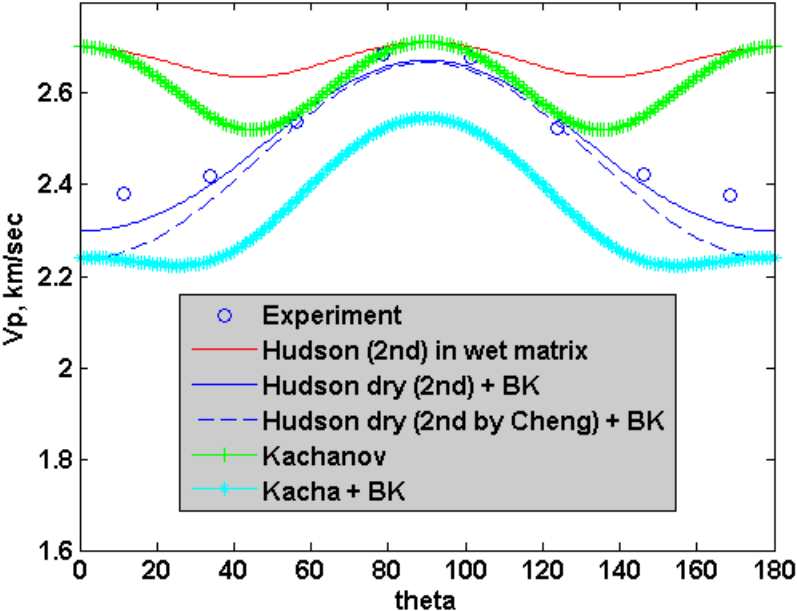
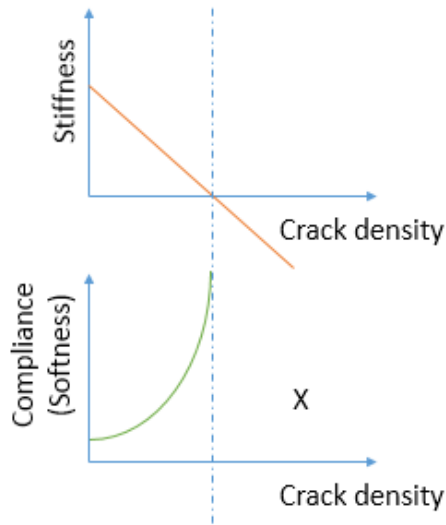


Figure 4.5: Comparisons of computation results from other options. Red solid – Hudson’s model with 2nd order correction adding wet inclusion in wet matrix; blue solid – Hudson’s model with 2nd order correction adding dry crack in dry matrix, then fluid substitution applied; Blue dash - 2nd order correction by Cheng; green cross - Kachanov model; cyan star - dry Kachanov model with fluid substitution.

We also applied Hudson’s model with Cheng’s modified 2nd order correction, and Kachanov’s model, with the same setting. Figure 4.5 shows the results. Cheng’s method give nearly the same results as the original 2nd order correction. Kachanov’s model gives the most accurate reproduction when the angle of the seismic wave is nearly parallel with the fracture, but accuracy becomes poor when the angle becomes close to the crack normal. This is slightly unfair because we know that there is communication between pores and cracks in that experiment, but Kachanov’s model assumes no interactions from the beginning. For practical applications, we can customize Kachanov’s model with Brown-Korringa’s fluid substitution to handle a case where we force communication among pores and cracks (cyan color in Figure 4.5). But by doing so, we break the underlying assumptions of Kachanov’s formulations. The results also show a poor reproduction of measurements. Comparing red solid to blue solid, or green

cross to cyan cross, there are fundamental difference in angular dependency of seismic velocity for communicating versus non-communicating assumptions among pores and inclusions.

Hudson: correction term on Stiffness tensor by linear subtraction



Kachanov: correction term on Compliance tensor by linear addition

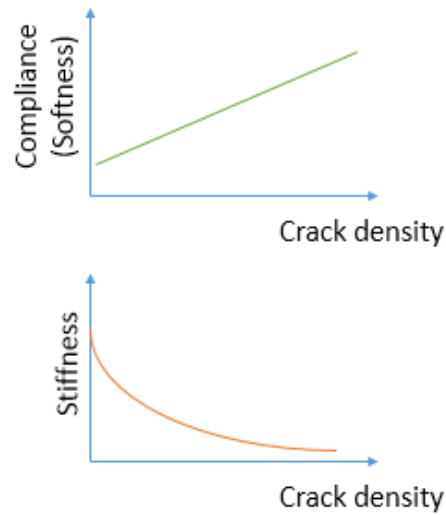


Figure 4.6: Schematic comparison between Hudson's and Kachanov's models. Both models make the adjustment linearly proportional to the crack abundance, which is expressed by crack density. In a way, Hudson's model subtracts stiffness while Kachanov's adds compliance.

Figure 4.6 shows fundamental differences between Hudson's model and Kachanov's model. Both of them start from inclusion-free properties and make adjustments proportionally as the inclusion abundance, the crack density from equation (4-4), increases. While Hudson's model reduces stiffness by subtracting stiffness constants with increased numbers of cracks, Kachanov's model increases the compliance constants with increased numbers of cracks.

The biggest drawback of Hudson's regular model is that it only can handle a limited amount of crack inclusion from mathematical formulations. Since it linearly subtracts stiffness, when crack density becomes bigger than a certain amount, the results

become physically meaningless. For a simpler explanation, stiffness becomes a negative value. The upper left plot on Figure 4.6 shows how the stiffness becomes negative as crack density increases. Normally it is recommended to use Hudson's model with crack density values of less than 0.1. For Kachanov's model, as we add more and more soft inclusion, the medium becomes softer and softer by having bigger and bigger values on its compliance tensors. Stiffness, the inverse of compliance, asymptotically goes to zero but never becomes negative.

The mathematical drawback of Hudson's model does not mean that it is inferior, and the mathematical stability of Kachanov's model does not mean that it is superior. But definitely one will outperform the other when the way it sees stiffness and/or compliance is well-matched with the actual physical characteristics. For sandstone, as we tested by applying Rathore and colleagues' experiments, Hudson's model works. Compared to shale, sandstone is stiffer, and stiff sandstone tends to break out since it cannot handle more than a certain number of inclusions. But for shale, or any material where non-interaction assumptions hold well, Kachanov's model may work better because some materials are actually more compliant than other stiffer minerals. As Gretchka and Kachanov tested (2006a), for less permeable and more compliant minerals, Kachanov's model may be a safer choice since both of them give similar results, as we saw from Figure 4.5. Actually, under the non-interaction assumption, if we compare the red solid line with Kachanov's results (the green cross), Kachanov's model outperformed Hudson's for Rathore and colleagues' experiments.

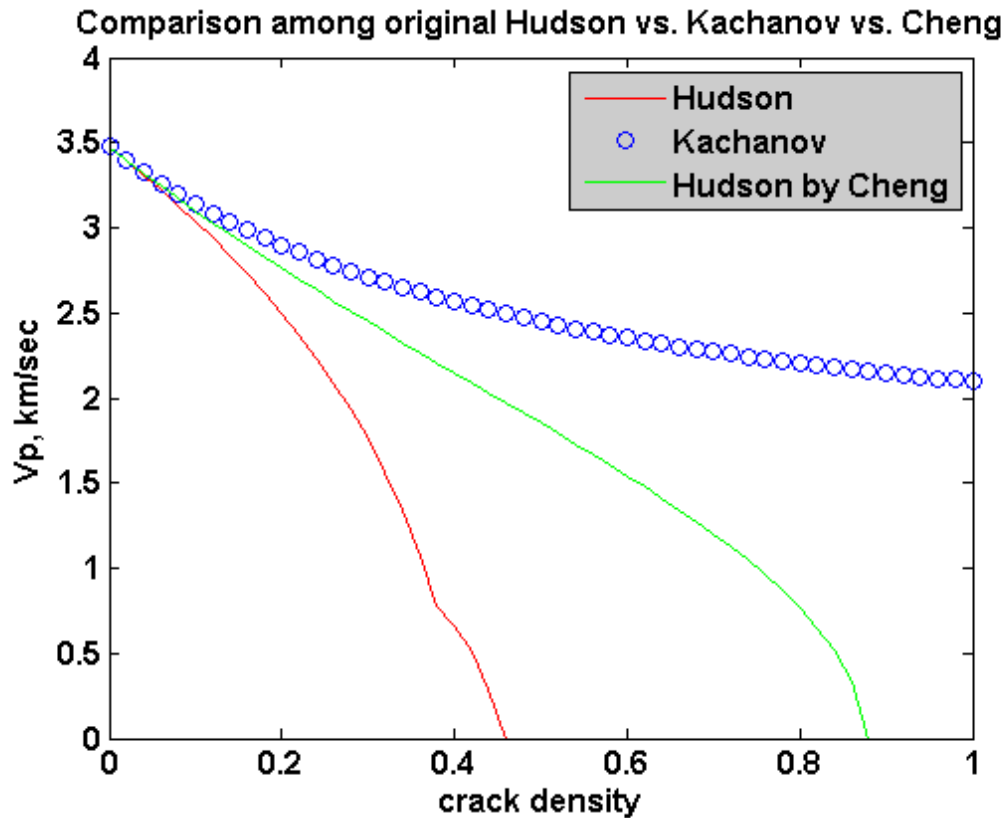


Figure 4.7: Comparison among Hudson, Kachanov, and Hudson by Cheng

If we recall equation (4-7), which uses the second order correction terms of Hudson’s model, what the second order terms do is simply reduce the 1st order subtraction by adding up the 2nd order corrections. Recall from Figure 4.6, the 2nd order correction terms try to pull the slope up to make it drop less linearly. Similarly, Cheng’s modified 2nd order correction (equation 3.8) does not subtract stiffness, but multiplies adjustment terms from basis stiffness. This actually makes Hudson’s model more similar to Kachanov’s model. Figure 4.7 shows changes in P-wave velocity as crack density increases, as computed by Hudson’s (red solid), Kachanov’s (blue circle), and Hudson’s by Cheng (green solid) model. By changing subtraction into multiplication, it acts like Hudson’s model with smaller crack density, but more like Kachanov’s when crack density is increased.

This example case does not prove that one model excels the others. What we can take from the example is that we need to choose a proper model by considering the

lithology we want to model, and the effect of seismic frequency on communications among pores and inclusions. For a relatively porous host medium with relatively low frequency, Hudson's model works well. Using Cheng's modified 2nd order correction term in Hudson's model is a safer option since it gives nearly the same results as the original, but has better numerical stability. For ductile materials where we have information that the material can endure a large portion of soft inclusions, using Kachanov's model would be more appropriate.

4.1.4 Problem statement

First problem: insufficient measurements

To reconstruct the elastic anisotropy of rock, we need to have many different measurements. For an isotropic medium, we only need the P-wave velocity and S-wave velocity. But for a transversely isotropic medium, we need at least five velocity measurements to construct the elastic properties. In many real field practices, we only measure P-wave velocity by measuring the slowness of the sonic log. S-wave velocity is usually inferred by using empirical assumptions, or from analogous well data. Cores are only retrieved from important target intervals. Not only do we have very limited data to reconstruct the medium without inclusion, but we will also have little data to infer the possible existence of cracks unless they are clearly noticeable from the well log, or from the cores. Thus, any resultant anisotropic medium properties - starting from the background medium property, adding inclusion properties, and then reaching the final properties - relies on a certain degree of idealization into available measurements, models, and analogies.

Second problem: how hard is our hard data? Representative elementary volume of well log, seismic data, and reservoir property modeling are all different.

Even if we have a perfect measurement in perfectly corrected and treated cores, we still encounter a typical scale problem. The resolution of the well log is on the centimeter to meter scale, while the resolution of seismic data is meters to tens of meters.

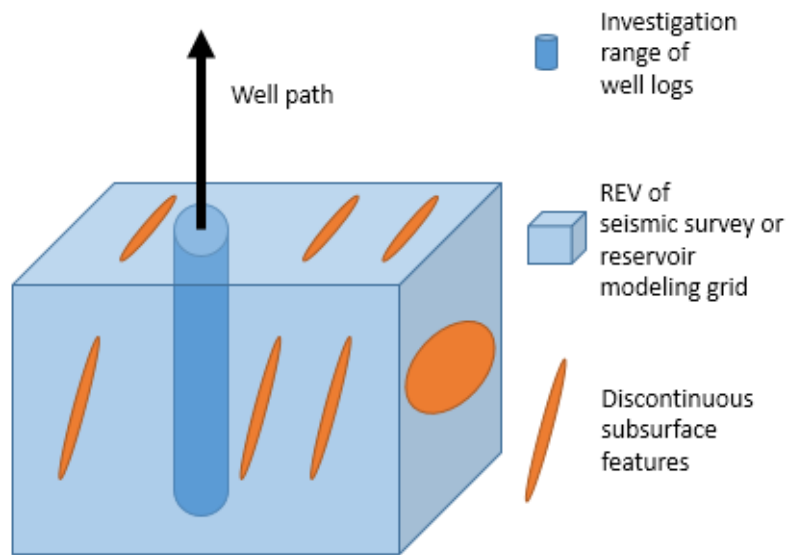


Figure 4.8: Schematic figure of an example when data from the well can miss abundant subsurface features.

It is possible to have a swarm of vertical joints one foot away from the vertical well we drilled. What we measure through the well is not necessarily representative of the bigger scale modeling. When we have measurements from a smaller REV and try to extrapolate into a bigger scale, we always have uncertainties about un-measured subsurface features. Figure 4.8 is a schematic figure to explain a possible situation when we can fail to encounter any fractures from the well, but abundant fractures actually exist. If we use the experiments in Rathore et al. (1994) as an analogy of the schematic figure, the P-wave velocity measured from the core would be 2.7 km/s. The vertical velocity from a velocity survey, such as check shot survey, would be around 2.5~2.6 km/s if we assume the fractures are tilted about 10~20°. If we do not take the possible existence of fractures into account, one of many possible wrong interpretations could overestimate the porosity of the given area. For the case of unconventional shale fields, shale is normally believed to have a higher degree of anisotropy than sandstone (Vernik and Nur, 1992; Bandyopadhyay, 2009). With that higher intrinsic anisotropy, interpretations from seismic responses can be over- or underestimated if we fail to have proper assumptions about subsurface conditions.

Third problem: if we add un-observed inclusion, we cannot honor the measured data

One of the inputs of existing rock physics models for inclusion is the elastic properties of an "inclusion-free" background medium. By knowing the inclusion-free properties, idealized shapes of inclusion, and the properties of the inclusion, existing rock physics models can calculate the effective medium properties of medium with inclusion. Well-known rock physics models for determining the effective medium with inclusions, such as Hudson's and Kachanov's, are typical examples.

We are supposed to start with the mineral first, then consider inclusion. First, we need to know the elastic properties of the host rock without cracks, which requires well retrieved cores and a clean section of the rock where we do not have any significant fractures or inclusions. If we go back to the example of Figure 4.8, we can easily calculate back and reconstruct a combination of host rock and crack effects, while preserving the bulk density and vertical velocity. But if there is a possibility of having horizontal cracks which we happened to fail to capture from the well, we cannot use the optimal combinations of host rock properties and crack information. As soon as we add horizontal cracks to our model, the vertical velocity drops significantly. By following the typical implementation process, we may develop a tendency to narrow down to a specific combination among numerous possible scenarios.

Fourth problem: there is no rock physics model for cracks with arbitrary orientations on a vertically transversely isotropic medium

The biggest difficulty of calculating scenario-dependent seismic properties of shale is the limitation of the orientation of inclusion for working shale models. Current SCA and DEM models only allow inclusions with orientations that are parallel with the symmetry axes of the background. Two reasons can account for the lack of a rock physics model for crack inclusions oriented at arbitrary directions with respect to the symmetry of the background anisotropic mediums. First, previous studies of investigating crack inclusion on shale were focused on either depth trends of crack-like pores in shale (Bandyopadhyay, 2009; Nishizawa and Yoshino, 2001), or on the dependency or aspect ratio of crack-like

pores with hydrocarbon maturation (Vernik and Nur, 1992). Rock physics models which allow us to model bedding parallel cracks were sufficient for those purposes. The second reason comes from the limitation of mathematical formulations of anisotropic SCA and DEM models, where an explicit form is only available when the axis of symmetry of the background material and the inclusion material are aligned (Mura, 1983; Nishizawa and Yoshino, 2001).

4.2 A new rock physics workflow to determine effective stiffness tensors of crack inclusions in an anisotropic medium

4.2.1 Background idea and requirements of a new model

We propose a new rock physics modeling workflow to allow one to add cracks with arbitrary orientation in an anisotropic host medium, by decomposing the background anisotropy into two parts: an effective isotropic part, and anisotropy by crack-like pores. The idea is rooted in the shared viewpoints on the shape of pores in shale, to model the crack-like pores of shale by ellipsoids (Vernik, 1993; Vernik and Nur, 1992; Bandyopadhyay, 2009; Nishizawa and Yoshino, 2001). These scholars modeled the pores of shale as crack-like inclusions which can be expressed by aspect ratios. After assuming shale as a VTI medium, Vernik (1993) and Bandyopadhyay (2009) linked the aspect ratio of pores with hydrocarbon maturation, or compaction trend with depth. Their work shows that simplifying the shape of pores in shale into cracks gives a good representation of actual elastic properties of shale.

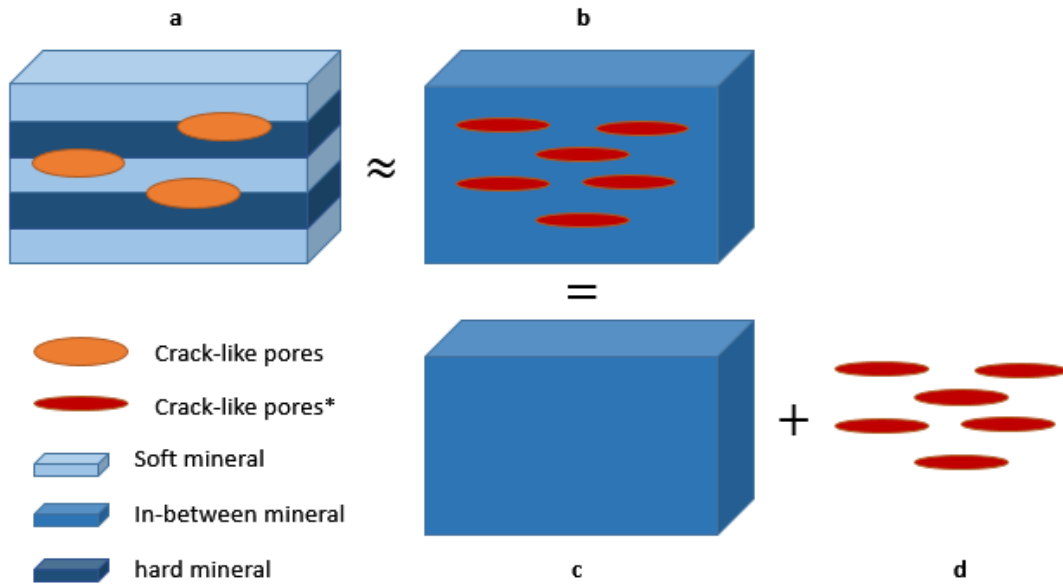


Figure 4.9: Schematic figure of the proposed model. Model **a** is a typical way of seeing shale: anisotropy by fabric, and anisotropy by crack-like pores. Model **b** is equivalent to **a**, by combining isotropic host (cartoon **c**) medium and crack-like pores (cartoon **d**). Crack-like pores* (red) have smaller crack aspect ratio than crack aspect ratio of the model **a** to make the same level of anisotropy from the isotropic background medium (cartoon **c**).

Based on these grounds, we can attempt to see the intrinsic anisotropy as caused by crack-like pores (Figure 4.9). Apparently, it is not true that the major part of the anisotropy of shale comes from the fabric and alignment of mineral components having horizontally parallel trends (model **a** in Figure 4.9). But even when seeing the shale as in model **a**, what we do mathematically is calculate an effective stiffness of VTI medium by adding inclusion having same axis of symmetry with host medium. The proposed idea also attempts to construct an effective VTI medium, but by adding inclusion with axis of symmetry in an isotropic host medium, not an VTI medium in a way the resultant effective medium acceptably reproduce the anisotropy while preserving the same axis of symmetry. We call it a “Reconstruction of Equivalent Isotropic Medium” as a name of process, or “Reconstructed Equivalent Isotropic Medium” for the extracted isotropic host medium. We will use REIM for both the process and for the host medium.

If we conduct a thought experiment, the original shale in model **A** has two interbedded minerals: one stiffer, the other softer. Since it is layered, the vertical

stiffness is less than the horizontal stiffness. With crack-like pores, this stiffness contrast becomes larger. To construct an equivalent model like **b**, the starting point is finding the isotropic elastic properties which give slightly higher stiffness than the horizontal stiffness of model **a**, because once we add cracks, the equivalent stiffness will be slightly smaller. Then, we can try to find the optimal aspect ratio of the crack-like pores of model **b** in a way that reproduces the same vertical stiffness while also keeping the same total porosity. Since the crack-like pores are horizontally elongated soft inclusions, the horizontal stiffness would be nearly the same while the vertical stiffness would drop significantly. Now we can reconstruct an equivalent effective medium model. Even if the final VTI medium has slightly different values in some other direction than vertical and horizontal, the equivalent model will honor bulk density, porosity, seismic velocity along the axis of symmetry, and horizontal velocity. The benefit of this approximation is that it allows us to add incrementally any set of fractures with any direction of orientation.

To do this simplified decomposition, we want to meet the following constraints:

- The porosity of "crack-like" pores should be same as the shale porosity
- The bulk density should remain the same
- The model should reproduce vertical P-wave and S-wave velocity
- The model should reproduce horizontal P-wave velocity
- The bulk and shear moduli of isotropic host material should fall within reasonably realistic ranges for shale, or its mineral components

4.2.2 A two-step optimization to find equivalent isotropic hosts and crack-like inclusion

To implement the proposed decomposition with the given constraints, we need to find an optimal combination of 1) the aspect ratio of crack-like pores, 2) the bulk modulus of the host medium, and 3) the shear modulus of the host medium. Now it becomes a typical optimization problem. We divided the optimization procedure into two steps:

one for finding the optimal aspect ratio of crack-like pores with a given bulk and shear moduli to preserve vertical and horizontal P-wave velocity, and the other for finding the optimal bulk and shear moduli to honor the vertical phase velocities with a given aspect ratio.

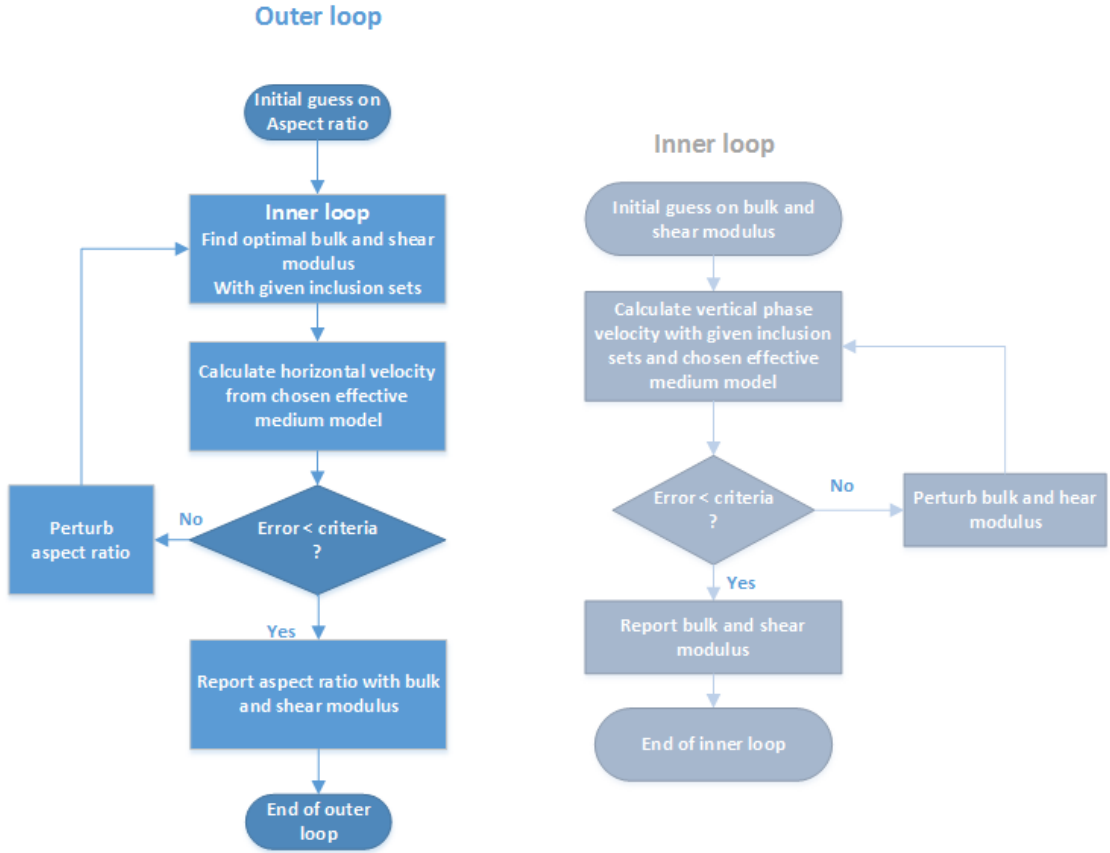


Figure 4.10: Flow charts of the inner and outer optimization loops. The inner loop aims to find the optimal isotropic host medium, while the outer loop aims to find the optimal shape of the crack-like pores.

The algorithm consists of a two-step optimization - an outer loop to find the optimal aspect ratio of crack-like pores to meet Thomsen’s epsilon, ϵ , “optARcrack,” and an inner loop to find the optimal bulk and shear moduli to meet the vertical phase velocity and bulk density with the given information on multiple inclusion sets, “optKGmdls.” The outputs of “optKGmdls” are equivalent bulk and shear moduli of the isotropic medium, to reproduce vertical phase velocities with given information on inclusions. The output of “optARcrack” is the optimal aspect ratio of the crack-like pores with the bulk and shear moduli of the equivalent isotropic medium.

Example: applying Sarout’s velocity measurement on shale cores

To test the proposed model, we compare it with actual shale data from Sarout’s experiment (Sarout and Guéguen, 2008; Sarout et al., 2008). The experiment was conducted on dried and wet shale with a similar setting to Rathore’s experiment. We are going to use the wet case experiment.

Bulk measurement:			
Porosity: 5 %	Extracted Voigt’s stiffness tensor, C =		
Saturated bulk density: 2.3775			
Water bulk modulus: 2.3 GPa	35.3	14.3	10.9
Crack porosity: 0.23 %	14.3	35.3	10.9
	10.9	10.9	22.0
Extracted Thomsen’s parameter:			7.1
ϵ : 0.3023			7.1
γ : 0.2394			10.5
δ : 0.1556			

Table 4-2: Measurements and results of Sarout’s experiment on wet shale

Table 4-2 shows key measurements from the experiment. The right column is the stiffness tensor reconstructed from Sarout’s experiments. By applying the proposed model, we can decompose the VTI stiffness tensor into two parts: an isotropic stiffness tensor from the extracted bulk and shear moduli, and the incremental anisotropy which is the difference between the VTI stiffness tensor and the isotropic stiffness tensor. The numbers of each component can be seen in Figure 4.11.

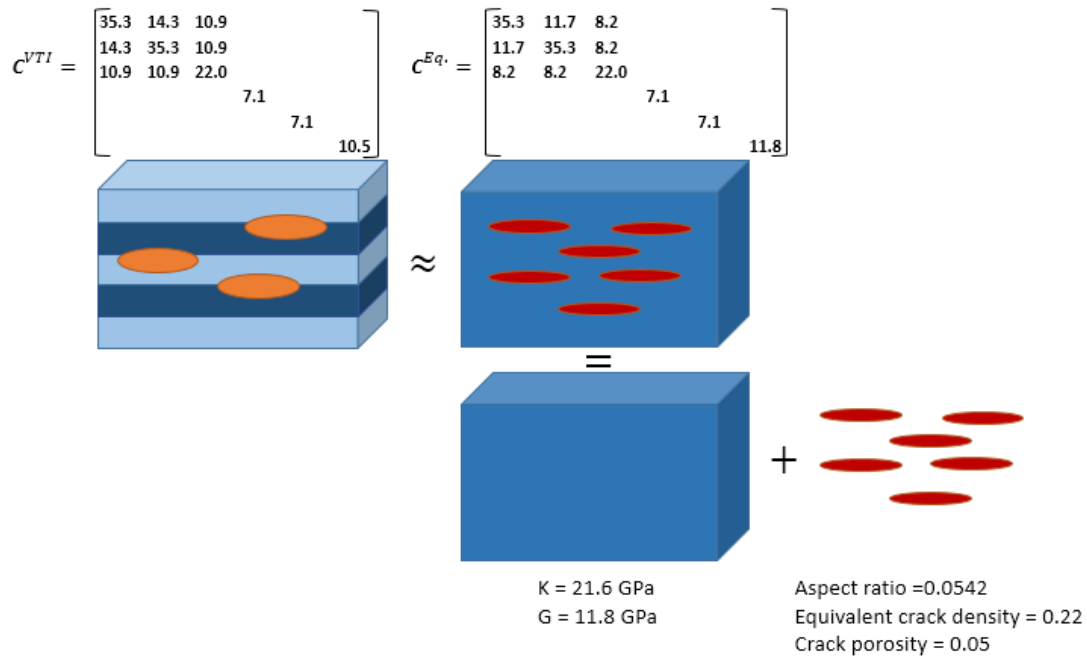


Figure 4.11: A decomposed isotropic medium and crack-like pores. Equivalent stiffness tensors are preserving the C11, C33, and C44 components.

Now, we have a combination of isotropic host medium and crack-like pores that contribute incremental adjustments for developing anisotropy. Note that Voigt average bulk modulus, K_V , which is average of upper left 9 components with 18.31 GPa for the C^{VTI} material, is smaller than the bulk modulus of equivalent isotropic host medium. This can be explained in a simple way. If we have a shale which has faster horizontal P-wave velocity V_{p1} , and slower vertical P-velocity V_{p2} , we can reconstruct this observation by starting with an isotropic medium which will give slightly faster P-wave velocity than V_{p1} (Thus, average bulk modulus must be slightly higher for the equivalent host than the true rock). Then we add an optimal set of crack-like pores, which are ellipsoid, in such a way that the porosity of inclusion is the same as the shale porosity. Since we added the cracks in a VTI manner, the vertical P-wave velocity will drop significantly, while the horizontal P-wave velocity will drop slightly. By having optimal combinations of the aspect ratio of pores and the bulk and shear moduli, we can reproduce the same phase velocities in vertical and horizontal directions.

Figure 4.12 shows a comparison of the measured velocity from the experiment (circles), the calculated velocity from the true stiffness tensor (red solid), and the calculated velocity from the equivalent stiffness tensor of the isotropic medium with crack-like pores (blue dash). Results from the proposed model show good agreement with the true data. Now the obvious merit of this approach is that we can calculate “what if” stiffness tensors while assuming any fracture sets we want to test. Another advantage is the ability to use the equivalent aspect ratio of crack-like pores with any available trends, such as aspect ratio depth trends or TOC trends, and conduct additional analysis to evaluate the formation.

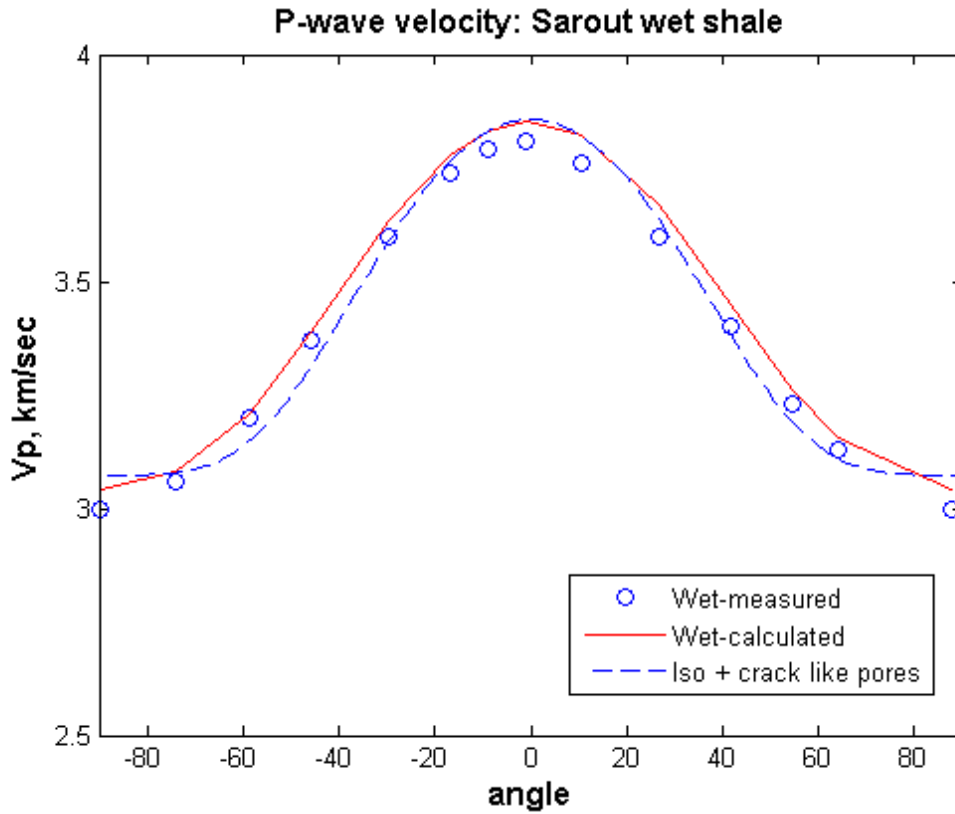


Figure 4.12: Comparison of true vs. calculated velocity using the proposed model.

Effective properties with cracks in an anisotropic medium

Now we can calculate incremental changes in fracture inclusion using an equivalent isotropic medium. For example, we will add one vertical fracture set, filled with water with a 2.3 GPa bulk modulus, its normals along axis-1, with the same crack density, 2.2 with an aspect ratio of 0.01. This aspect ratio was intentionally chosen to exaggerate the effects on effective stiffness. By using Hudson's model with Cheng's 2nd order modification, together with a Bond transformation, we can calculate the effective stiffness tensor of vertical cracks in VTI shale as in equation (4-22). $C^{VTI}-C^{ISO}$ in the equation is equivalent to the incremental anisotropy modeled by the crack-like pores.

$$\begin{aligned}
C^{eff} &= C^{VTI} + \sum_i^n [\Delta C_i^{crack}] \\
&= C^{ISO} + (C^{VTI} - C^{ISO}) + \sum_i^n [\Delta C_i^{crack}]
\end{aligned} \tag{4-22}$$

$$\begin{aligned}
&\begin{bmatrix} 30.6 & 12.6 & 9.2 & 0 & 0 & 0 \\ 12.6 & 34.7 & 10.3 & 0 & 0 & 0 \\ 9.2 & 10.3 & 21.4 & 0 & 0 & 0 \\ & 0 & 0 & 0 & 7.1 & 0 \\ & 0 & 0 & 0 & 0 & 2.4 \\ & 0 & 0 & 0 & 0 & 0 \\ & 0 & 0 & 0 & 0 & 5.8 \end{bmatrix} = \begin{bmatrix} 35.3 & 14.3 & 10.9 & 0 & 0 & 0 \\ 14.3 & 35.3 & 10.9 & 0 & 0 & 0 \\ 10.9 & 10.9 & 22 & 0 & 0 & 0 \\ & 0 & 0 & 0 & 7.1 & 0 \\ & 0 & 0 & 0 & 0 & 7.1 \\ & 0 & 0 & 0 & 0 & 0 \\ & 0 & 0 & 0 & 0 & 10.5 \end{bmatrix} \\
&+ \begin{bmatrix} -4.7 & -1.7 & -1.7 & 0 & 0 & 0 \\ -1.7 & -0.6 & -0.6 & 0 & 0 & 0 \\ -1.7 & -0.6 & -0.6 & 0 & 0 & 0 \\ & 0 & 0 & 0 & 0 & 0 \\ & 0 & 0 & 0 & 0 & -4.7 \\ & 0 & 0 & 0 & 0 & -4.7 \end{bmatrix}
\end{aligned} \tag{4-23}$$

Equation (4-23) shows Voigt's stiffness tensors of Sarout's wet shale, the incremental portion by adding vertical fractures, and the resultant stiffness tensor of the effective medium of Sarout's wet sands with vertical cracks. By adding a vertical crack

which is perpendicular with axis-1, now c_{11} , the stiffness constant for axis-1 becomes smaller than c_{22} , and it has orthorhombic symmetry

Since we have an effective stiffness model for vertical fractures on Sarout's wet shale, let's compare it with the effective medium of having a vertical fracture set in an isotropic medium. This would be the case when we model any anticipated fracture set without using the proposed model. Instead of orthorhombic symmetry, the effective tensor would have HTI (transversely isotropic with horizontal symmetry axis) symmetry. From equation (4-16) with the vertical P- and S-wave velocity of Sarout's wet shale, which are 3.04 km/s and 1.73 km/s, the bulk and shear moduli of the rock under the isotropic assumption would be 12.53 GPa and 7.1 GPa. Note that the bulk modulus of the equivalent isotropic medium from the proposed model was 21.6 GPa. Figure 4.13 shows the effective stiffness of the rock calculated by Using Cheng's 2nd order Hudson model.

$$\begin{bmatrix} 30.6 & 12.6 & 9.2 & 0 & 0 & 0 \\ 12.6 & 34.7 & 10.3 & 0 & 0 & 0 \\ 9.2 & 10.3 & 21.4 & 0 & 0 & 0 \\ 0 & 0 & 0 & 7.1 & 0 & 0 \\ 0 & 0 & 0 & 0 & 2.4 & 0 \\ 0 & 0 & 0 & 0 & 0 & 5.8 \end{bmatrix} \quad \begin{bmatrix} 20.3 & 7.2 & 7.2 & 0 & 0 & 0 \\ 7.2 & 21.8 & 7.6 & 0 & 0 & 0 \\ 7.2 & 7.6 & 21.8 & 0 & 0 & 0 \\ 0 & 0 & 0 & 7.1 & 0 & 0 \\ 0 & 0 & 0 & 0 & 4.2 & 0 \\ 0 & 0 & 0 & 0 & 0 & 4.2 \end{bmatrix}$$

Figure 4.13: Effective stiffness tensors: left - when the background medium was modeled as VTI; right - when the background medium was modeled as isotropic medium.

As we can see, c_{33} and c_{44} , which are linked with vertical P- and S-wave velocities, are almost the same while c_{11} and c_{33} , which are linked to the horizontal seismic velocity along axis-1 and axis-2, are quite different.

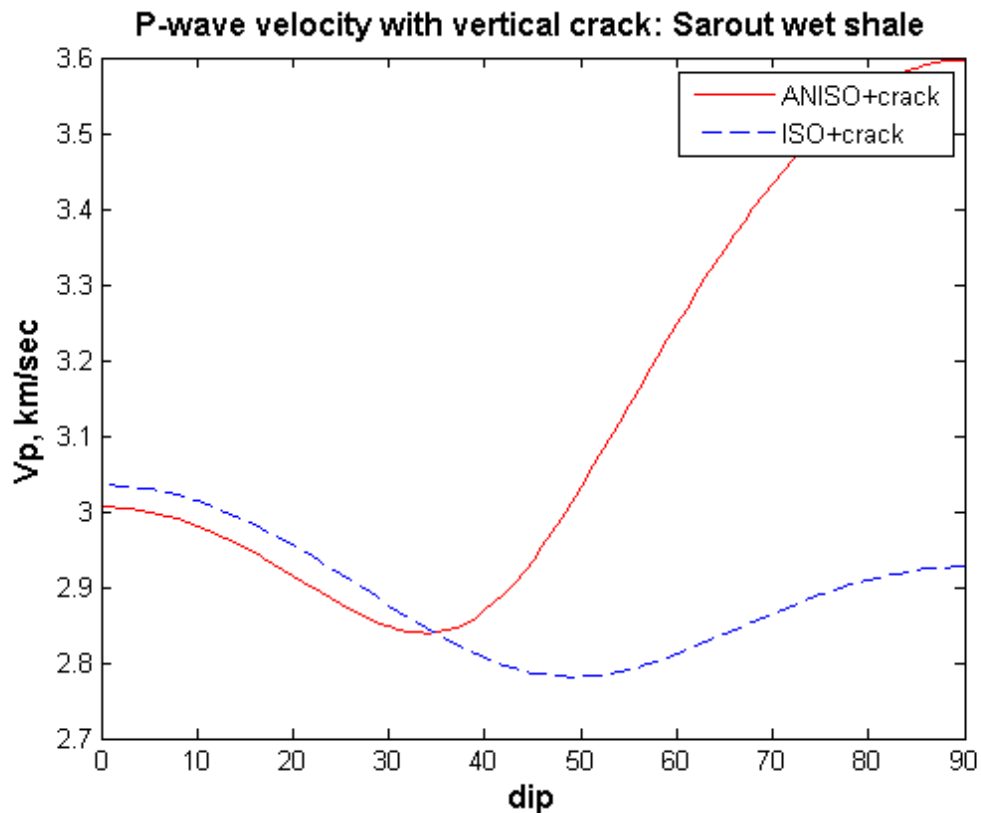


Figure 4.14: P-wave velocity with angle of incidence from vertical to dipping toward axis-1. Red solid-crack on anisotropic medium; blue dash-crack on isotropic medium.

Figure 4.14 shows the P-wave velocity calculated from Christoffel’s equation by varying the angle of incidence from axis-3 to axis-1. Notice that the stiffness constants are reduced to smaller numbers as we include cracks in Figure 4.13, and the vertical velocities for each case are not identical. With fixed bulk and shear moduli of the host medium, we cannot preserve the velocity profile we have when we add new inclusions in our considerations. We want to model different combinations of crack inclusions while preserving the velocity profile. In the next section, we cover how to use the proposed approach to model elastic properties for several scenarios that have different geological features.

4.2.3 Different host medium properties for different geological assumptions

Interpretation of reservoir properties along the wells is one of the most important tasks in subsurface modeling, because the interpreted values are used as "hard" data for reservoir property modeling. The values are starting points when we propagate any kind of property modeling in the volume of interest.

Thus, if we have alternative geological scenarios, the interpretations along the wells and the values of reservoir properties along the wells should be made consistent with the alternative scenarios.

In section 4.2.2, we proposed a two-step optimization to decompose shale anisotropy into an isotropic host medium and anisotropy caused by inclusion of crack-like pores. The inner loop optimization is used to find the optimal bulk and shear moduli of the host isotropic medium to reproduce vertical phase velocity with given sets of multiple inclusions.

I am going to reuse Sarout's wet shale scenario, to which we added a vertical crack, as an example.

Measurements	Equivalent Isotropic medium	Inclusions
Bulk density: 2.36 g/cc	K: 21.6 GPa	Set 1: crack-like pores
V_p^{vertical} : 3.0 km/s	G: 11.8 GPa	Set 2: vertical cracks
V_s^{vertical} : 1.7 km/s		
Porosity: 5.92 %		

Table 4-3: Properties and measurements of Sarout's wet shale with vertical cracks

Table 4-3 contains the bulk density, vertical phase velocity, and total porosity. Notice that the bulk density is reduced slightly from Sarout's wet shale since we added a vertical fracture set. The **K** and **G** in the center are equivalent isotropic host rocks before we added vertical fractures.

Case	assumption	K, GPa	G, GPa	Thomsen's [ϵ, γ, δ]
1	Pore (O), Fractures (O)	19.9	11.9	0.2, 0, -.006
2	Underestimate fracture abundance (50%)	19.2	11.9	0.24, 0.15, -0.043
3	Wrong assumptions on pore shape	12.1	7.1	-0.03, -0.20, -0.02
4	Assume no fracture	18.6	11.9	0.27, 0.34, -0.03
5	Assume wrong fracture orientation	24.7	12.8	0.26, 0.08, 0.12
6	Assume wrong fluid properties (softer fluid)	21.6	11.8	0.13, 0, -0.09
7	Isotropic medium w/o fracture	11.9	7.1	0, 0, 0

Table 4-4: Assumptions about subsurface and corresponding optimization results of the host rock properties, and Thomsen's parameters on a final effective medium

Let's assume that we have vertical phase velocity and bulk density measurements, but we are not sure of the intrinsic anisotropy or the existence of fracture sets. Table 4-4 contains seven scenarios with different assumptions. Case 1 is where we know the correct set of inclusions, for both crack-like pores and vertical fractures. In Case 2 we underestimate the abundance of vertical fractures. For Case 3 we assumed vertical fractures in the isotropic host rock. Case 4 assumes VTI on the shale correctly, but does not assume the existence of fractures. In Case 5, we assume the fractures are tilted 30° from vertical axis. Case 6 assumes a lighter and softer fluid, such as hydrocarbon, while Case 7 just models the rock as a pure isotropic medium. Note that all of the cases exactly reproduce the vertical P- and S-wave velocity when calculated based on the effective stiffness tensor, which is a combination of the host isotropic medium from K and G in the middle column, with assumed pore geometry with a fracture set.

If we believe the crack density of vertical fractures is less, the host rock should be slightly softer to honor the velocity profile. The bulk modulus of equivalent isotropic

host medium (EIM) in Case 2 is slightly softer than that of Case 1. If we ignore the intrinsic anisotropy, the bulk modulus of EIM becomes much smaller because we ignore the fact that the horizontal stiffness of shale is much higher than the vertical. Cases 3 and 7 show much smaller bulk moduli of EIM than the other cases, while Case 3 has slightly stiffer properties to honor the velocity when having vertical fractures. By assuming no vertical fractures, the bulk modulus EIM of Case 4 can be softer than Case 1. If we assume the fractures are actually tilted, they will reduce the vertical velocity noticeably. To compensate for this, the EIM bulk modulus of Case 6 becomes much stiffer than in Case 1. When we assume a lighter and softer inclusion material, such as oil, the rock stiffness must become stiffer as can be seen from Case 7.

Again, all the cases exactly honor and reproduce vertical velocity and bulk density, while they have different properties for host rocks and crack parameters. As we can see, Thomsen's anisotropy parameters are also different for each set of assumptions. Since geological control factors for mineral distributions and fracture abundances are different, property modeling based on incorrect assumptions will lead to wrong conclusions, even though they honor the hard data (vertical velocities and density). Any extrapolations based on that would drift further away from the more likely realizations.

One more thought experiment with simple calculations are as follows. We drill into Sarout's shale with the crack we just created after we hit the overlying sandstone, as schematized in Figure 4.15. The seismic reflectivity in this region is -0.1. The adjacent region to the left of the drilled region shows no seismic reflectivity, but we are sure that there is sandstone above. One of the easiest explanations would be lithology changes. If we have sandstone in the left region with the same seismic impedance as the overlying sandstone, we do not have seismic reflectivity in that region.

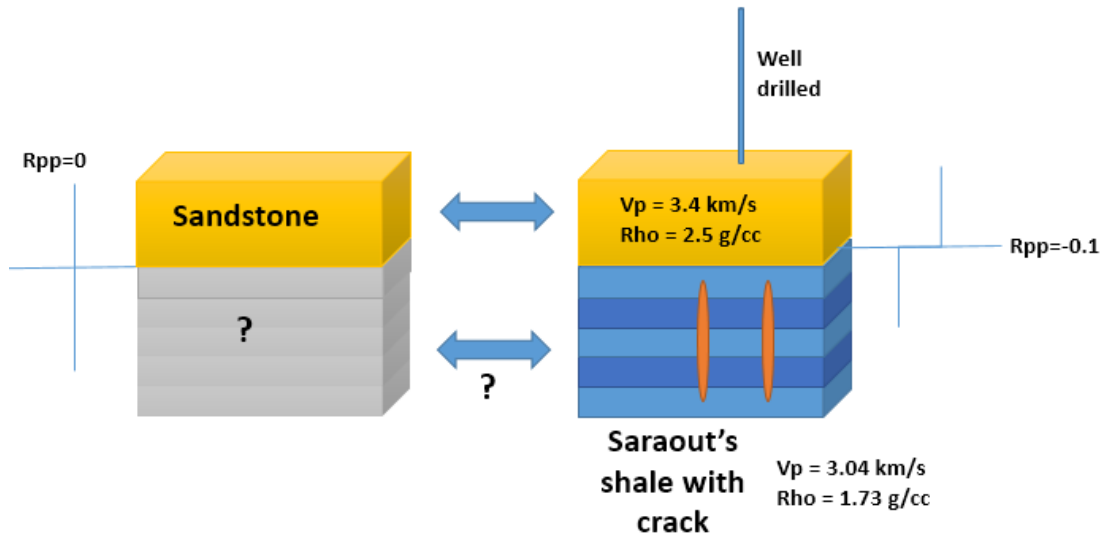


Figure 4.15: Thought experiments on extrapolation of surface properties. By having sandstone over the Saraout shale with vertical cracks, we have negative reflectivity on the right-hand region. The left-hand region has no drilling has nearly zero reflectivity.

But the reality of the un-drilled area is the exact same Saraout shale, with the same stiffness tensor and properties before we added cracks, but horizontally tilted 70° by some geological process.

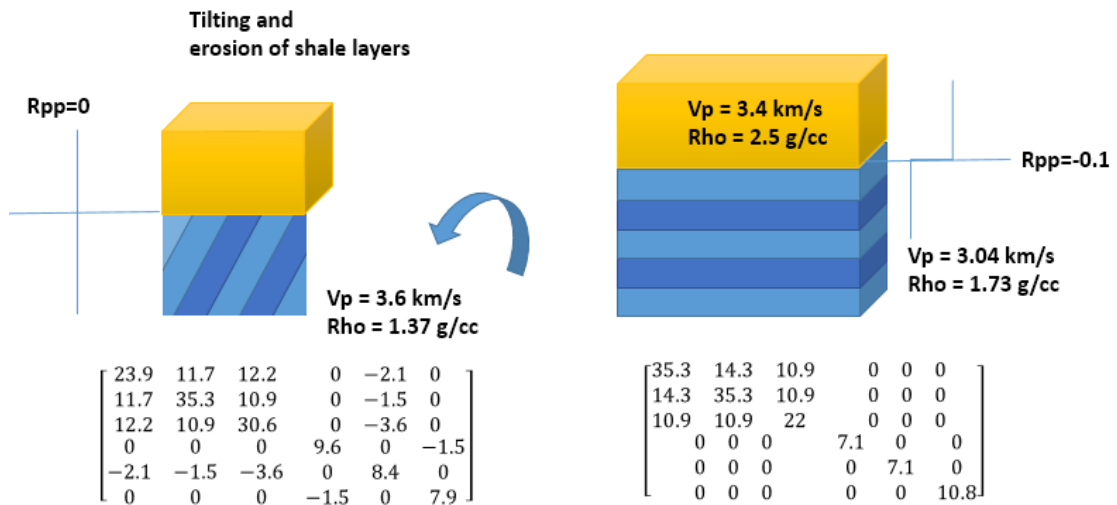


Figure 4.16: Stiffness tensor after rotation gives faster vertical velocity.

Figure 4.16 shows the schematic assumptions and Voigt's stiffness tensor after conducting the Bond transformation from equation (4-17). Unless we assume a geological scenario where we can anticipate the tilting of the formation, it would be extremely difficult to model that region as a shale formation. This is not a purely made-up example. Some horizontally compressed Marcellus formations in the Appalachian basin show rotation, tilting, and development of vertical foliation which enhance vertical stiffness. We are going to cover these cases in chapter 4.

4.2.4 Cone search method

The next challenge is how to compare the synthetic data of each realization of the different scenarios to the available field data. Within the provided data set using in Chapter 5, we have the azimuth cube of the fastest P-wave velocity and differences between the fastest and slowest velocity data as 3D cubes. Thus, if we extract the azimuth of the fastest and slowest seismic velocities, a comparison between the field seismic data and the synthetic data becomes geologically and practically meaningful. The technical challenge is that we need to calculate the orientation and the values of the fastest and slowest velocity in every simulation grid block. From the equations covered in Chapter 4, we can calculate seismic velocity at any angle of incidence when Voigt's stiffness tensors are given. However, the challenge is the number of calculations to extract an azimuthal profile of seismic velocity. It is doable to calculate seismic velocities on discrete combinations of azimuth and offset angles, but computationally heavy. On top of that, it is subject to a decision to choose the discrete steps of the azimuth and the offset of angle of incidence.

To resolve this problem, we propose a fast searching technique, a Cone searching method, to minimize the required number of velocity calculations while guaranteeing the ability to find the exact azimuth of the fastest seismic velocity. The idea is simple. If we assume the anisotropy of rock is orthotropic, we can extract three principal directions of stiffness by conducting Eigen value decomposition. The first

challenge is the fact that rocks with multiple sets of joints and fractures with different orientations may not be orthotropic. However, this condition is acceptable when considering that what we want is the azimuth of fastest seismic velocity, and that the velocity itself and an orthotropic assumption is more than enough to calculate the data we want. For analyzing other seismic attributes, such as AVO or AVAz, an orthotropic assumption on symmetry is enough to investigate the angular or azimuthal variations of seismic responses.

Second, we need to reconstruct Voigt's stiffness tensor, which is a fourth-order tensor notated into six by six matrix form, into a certain second-order tensor form from which we can extract principal orientations that correspond to fastest-intermediate-slowest seismic velocity. For this purpose, we can use a second-order Voigt tensor, or a dilatational modulus that we can construct by using Equation (4-24) and (4-25) from Voigt's stiffness tensor components (Cowin and MehRabdi, 1987; Sun, 2002).

$$\mathbf{A} = \begin{bmatrix} C_{11} + C_{12} + C_{13} & C_{16} + C_{26} + C_{36} & C_{15} + C_{25} + C_{35} \\ C_{16} + C_{26} + C_{36} & C_{12} + C_{22} + C_{23} & C_{14} + C_{24} + C_{34} \\ C_{15} + C_{25} + C_{35} & C_{14} + C_{24} + C_{34} & C_{13} + C_{23} + C_{33} \end{bmatrix} \quad (4-24)$$

$$\mathbf{B} = \begin{bmatrix} C_{11} + C_{55} + C_{66} & C_{16} + C_{26} + C_{45} & C_{15} + C_{46} + C_{35} \\ C_{16} + C_{26} + C_{45} & C_{22} + C_{44} + C_{66} & C_{24} + C_{34} + C_{56} \\ C_{15} + C_{46} + C_{35} & C_{24} + C_{34} + C_{56} & C_{33} + C_{44} + C_{55} \end{bmatrix} \quad (4-25)$$

The Eigen vectors of \mathbf{A} and \mathbf{B} are identical and correspond to the orthotropic axis of symmetry where the axis with the maximum Eigen value coincides with the orientation of fastest seismic velocity. Now, it is straightforward to calculate the fastest and slowest velocity with their azimuths, using Christoffel's equation from Chapter 4.

However, if the axis of fastest velocity were vertical, or nearly vertical, its azimuth would not correspond with the azimuth of the fastest velocity of the field seismic data. This is because the azimuth of fastest velocity in the seismic data is the fastest velocity in azimuthal variation, not of the vertical velocity when it is the fastest.

To resolve this situation, we compare the dip of the fastest axis with the offset angle of a representative searching offset of the given azimuthal data from the seismic survey. For instance, if the azimuthal variation of velocity was extracted from seismic data with azimuthal stacks with offset angles of up to 40 degrees, we may use a 20-degree offset and a corresponding “searching” cone to test azimuthal velocity from the synthetic data. Figure 4-17 is a cartoon example of the searching cone and orthotropic axis of symmetry, extracted from Eigen value decomposition of the Voigt tensor from Equation (4-24).

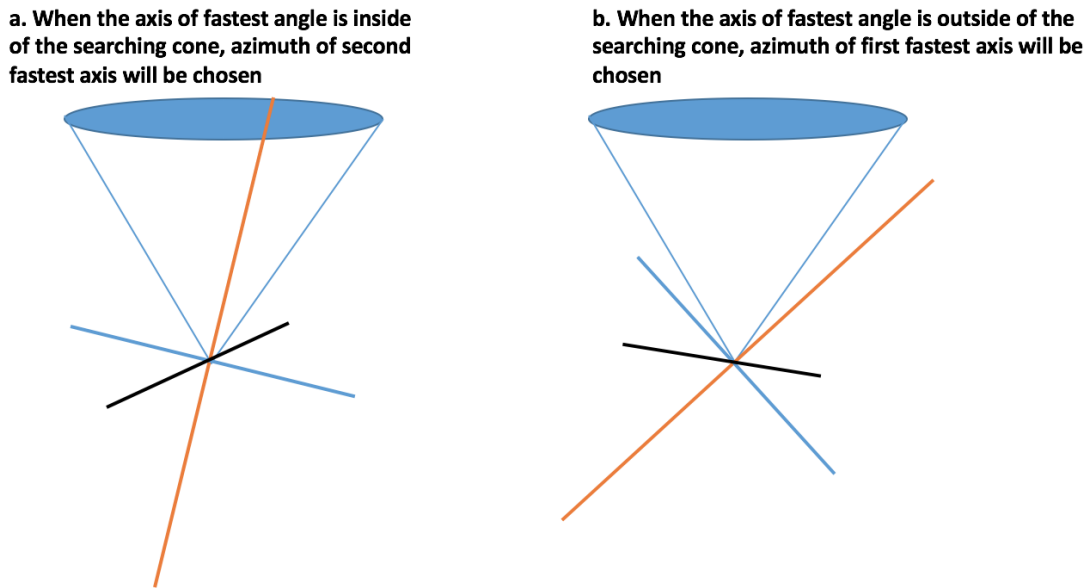


Figure 4-17: Cartoon example of a cone searching method to find the azimuth of fastest velocity. Left (a): when the axis of fastest velocity is nearly vertical (red), the azimuth of the second-fastest axis will be chosen to represent the orientation of the fastest velocity (blue). Right (b): if the axis of fastest velocity is off from vertical, its azimuth can directly represent the fastest orientation. The blue cone is a representation of the representative offset angle used to produce the azimuthal variation of velocity from seismic data (searching cone).

Now, we can calculate four velocities along the searching cone: two with the azimuth of the fastest velocity, and with 180° added, two perpendicular to the previous direction. By averaging those two sets, we have the fastest and slowest azimuthal velocity from the stiffness tensors having multiple sets of sub-seismic features along the geological scenarios.

4.3 Summary

In this research, two key ideas are modeling inclusions in an anisotropic medium by decomposing it into equivalent isotropic host mediums superimposed with anisotropy from inclusions, and modeling hard data along the wells when we have uncertainty about the existence of geological features.

If we select one or two specific cases out of the tested combinations, we are going to have slightly different vertical profiles of equivalent isotropic host media and inclusions along the well. Together with different assumptions on the distribution of orientations and the abundances of multiple sets of inclusions, the property distributions of subsurface models will be different from each other by using different REIM profiles along the wells. Application to an unconventional Marcellus shale gas field using this idea, and propagating geological assumptions to 2D and 3D models, are explored in Chapter 4.

Note that the proposed model for decomposing background shale anisotropy into an isotropic medium and crack-like pores is not a rigorous rock physics model. It is a workaround approach to model the “what-if” responses. To make a rigorous comparison, we may conduct either constructed composites of anisotropic mediums with artificial inclusions, as Rathore did, or more detailed numerical simulations in the same way as Grechka and Kachanov compared effective medium theory with FEM simulation results (Grechka and Kachanov, 2006; Rathore et al., 1995). Such comparisons with either experiment, or detailed numerical simulations, remains an important part of future work.

Chapter 5

5 Unconventional Shale Reservoir

Modeling with Multiple Geological Scenarios for Deformation of Reservoir Structure and Evolution of Rock Properties: Application on a Marcellus shale gas field

In this chapter, we apply the workflows in Chapter 3 – geomodeling that considers different geological scenarios for structural deformation and rock accommodation - and the rock physics method in Chapter 4 - decomposing measurements along the wells into equivalent isotropic mediums and sets of localized accommodational features - to an unconventional Marcellus gas field which has structural complexity and unexpected reservoir responses. Our method helps to rule out less likely geological assumptions using seismic response comparisons, and the models from the remaining scenarios allow enhanced geological and engineering understanding of a given field. For fields with structural complexity and small amounts of well data, applying the workflow may provide what-if field responses and corresponding contingency plans.

5.1 Introduction and Motivations

5.1.1 Marcellus shale with unconventional resources

The middle Devonian Marcellus Shale play in the Appalachian Basin is one of the largest unconventional hydrocarbon-producing plays in the United States. Since 2013, shale gas has become the largest natural gas provider in the United States, and Marcellus shale contributes the largest portion of natural gas with production rates of nearly 15 Bcf per day, comprising 85% of U.S. shale gas production (U.S. Energy Information Administration, Annual Energy Outlook, 2015). The reserve potential of Marcellus shale is estimated from 50 tcf to 500 tcf (Zagorski et al., 2012; Carter et al., 2011).

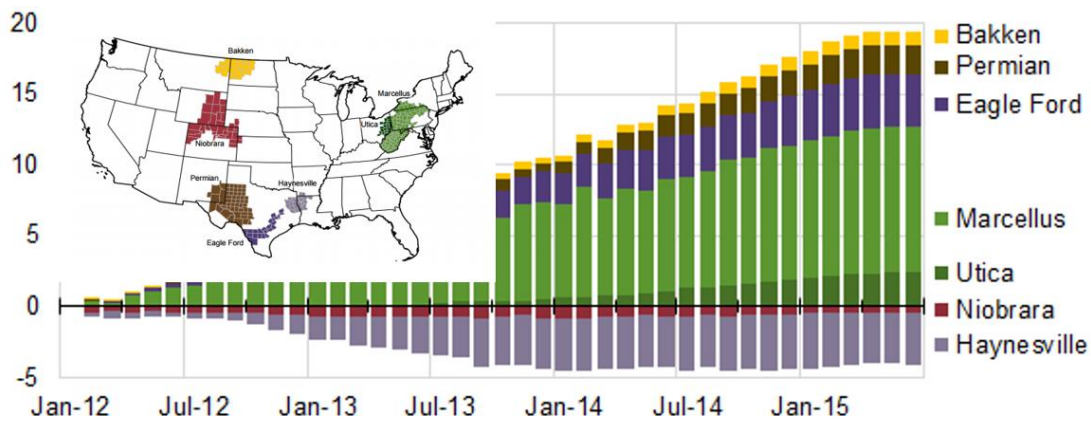


Figure 5.1: Natural gas production in the U.S. by region, from 2012 to 2015. Color-coded regions are marked on the U.S. map (Source: U.S. EIA Drilling Productivity Report, 2015).

Figure 4.1 shows cumulative changes in shale gas production in key regions in the U.S. from 2012 to the present (U.S. EIA Drilling Productivity Report, 2015). Marcellus shale outnumbered Bakken shale and Haynesville shale thanks to steady increases in production.

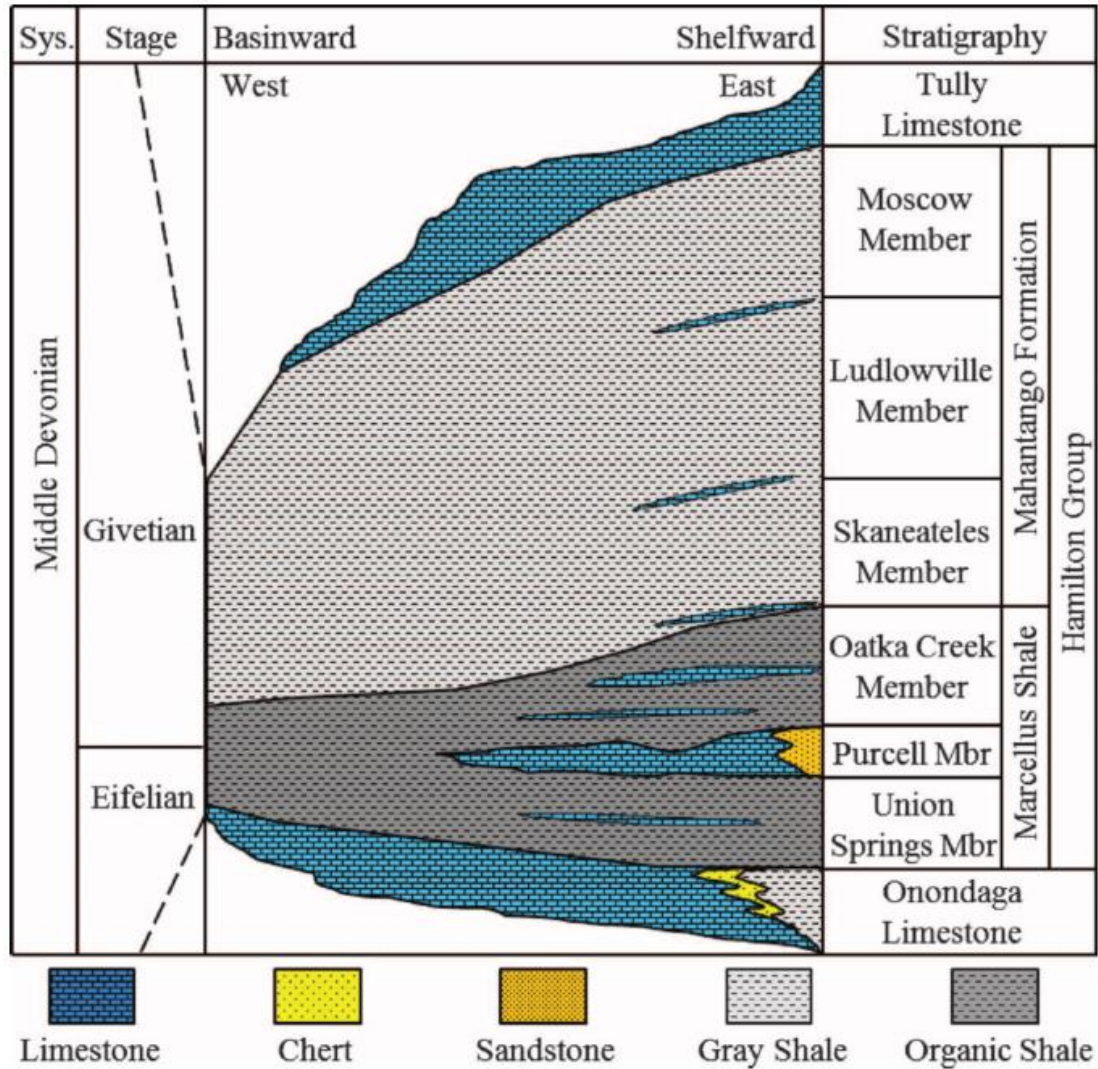


Figure 5.2: Generalized stratigraphy of Middle Devonian formations in the Appalachian Basin (Wang and Carr, 2013). Union Spring Member and Oatka Creek Member correspond to Lower and Upper Marcellus where less geological terms used. Upper Devonian Rhinestreet Shale seats over Tully Limestone. Devonian Huntersville chert and Oriskany sand formation are deposited below Onondaga formation.

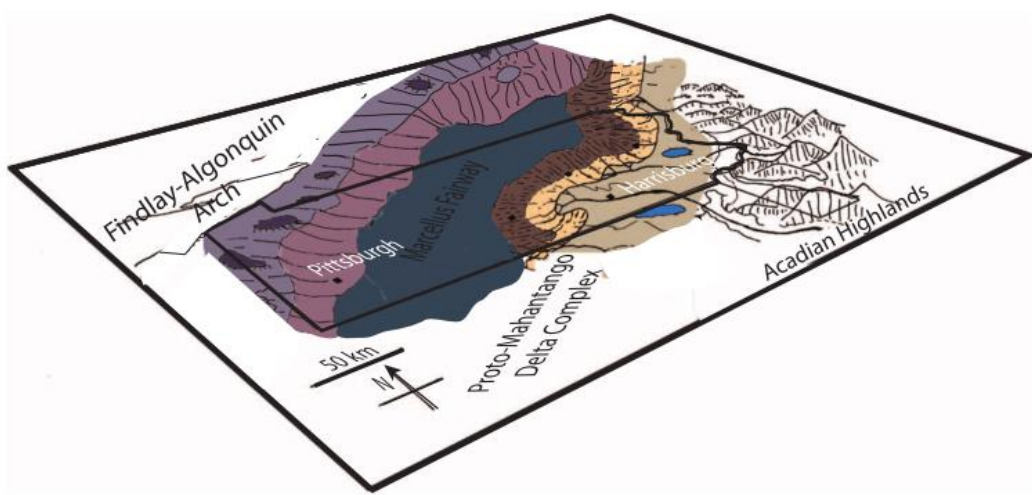


Figure 5.3: Cartoon depicting the paleogeography of the Middle Devonian Acadian foreland basin (Kohl et al., 2014). The central basin (dark blue) is the fairway of Marcellus shale. Sources of deposition are fed from the Acadian highlands. The western part of the Marcellus fairway is believed to be a persistent depocenter of carbonates.



Figure 5.4: Iron fertilization by dust storms near the Sahara desert (Wrightstone, 2010). Iron fed from storms with tropical climates created conditions for maximum algae generation.

Having organic rich black Devonian shale deposited in a marine environment, Marcellus shale is placed in an Appalachian basin which experienced a basin-wide collision, developing structural complexity with folds and faults through a series of orogenies that created the Appalachian Orogen (Zagorski et al., 2012; Engelder et al., 2009; Wang and Carr, 2013; Kohl et al., 2014). Regional depositional setting is related to the Acadian orogeny and can be subdivided into the following steps: 1) rapid subsidence leading to accumulation of marine black shale, 2) deposition of terrestrial gray and silty shale, 3) collision developing basin-wide uplift, and 4) limestone accumulation during a tectonically quiet transgressive period (Zagorski et al., 2012). The paleoclimate during the deposition is believed to be tropical with significant seasonal storm activities. Terrestrial iron components fed into the depositional center during stormy seasons are believed to be one source to increase the amount of algae and make the Marcellus shale organically rich (Wrightstone, 2011). Figure 5.2 shows generalized

stratigraphy of the Middle Devonian formations in the Appalachian Basin (Wang and Carr, 2013). Upper Devonian Rhinestreet Shale seats above Tully Limestone. Oatka Creek Member and Union Spring Member are also called as Upper and Lower Marcellus. Devonian Huntersville Chert and Oriskany Sandstone locate below Onondaga Limestone. Figure 5.3 is a cartoon of the paleogeography of the Middle Devonian foreland basin (Kohl et al., 2014). Figure 5.4 is an aerial photo of iron fed into the ocean by Saharan dust storms. Consistent supplies of fertilizers through tropical weather are believed to account for the rich organic contents of Marcellus shale (Kohl et al., 2014; Wrightstone, 2011; Zagorski et al., 2012).

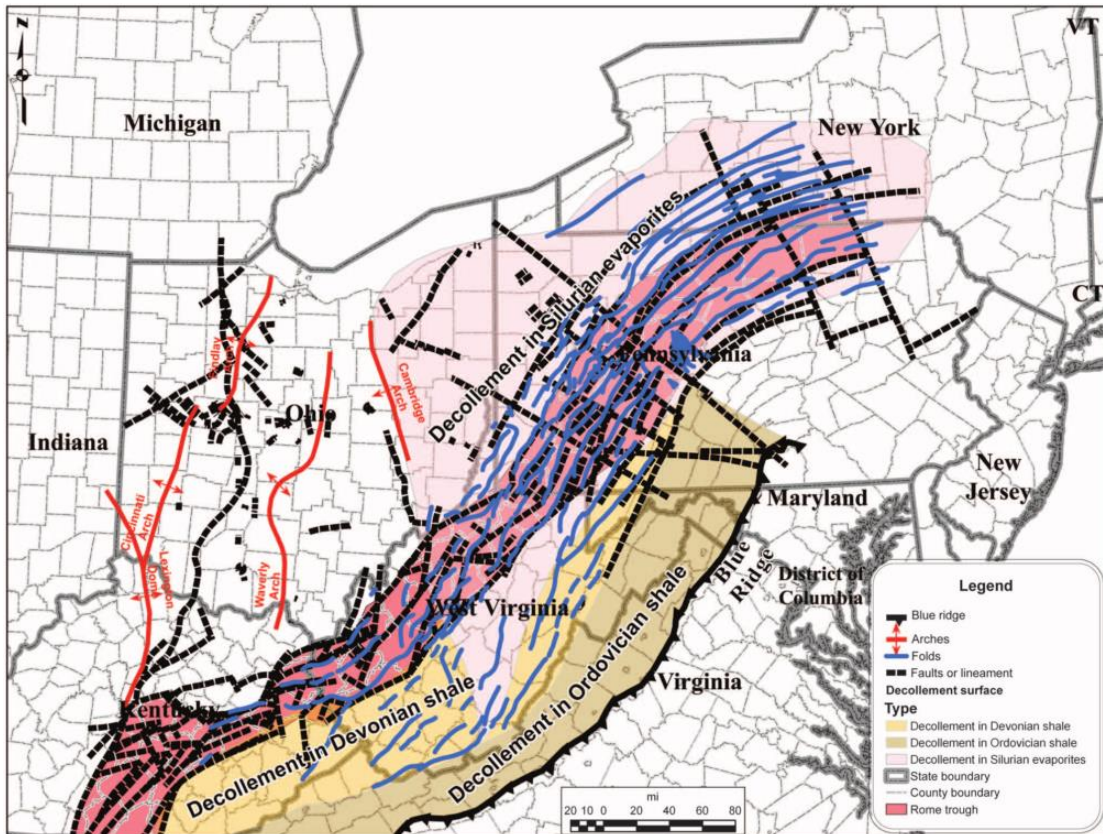


Figure 5.5: Trend map of Marcellus shale play. The blue solid lines are defined folds, with black dashes for faults. The basin-wide trends of folds and faults are striking NE-SW (figure from Zagorski et al., 2012).

Figure 5.5 shows the general trends of faults and folds in the Appalachian basin (Zagorski et al., 2012). Since the basin was compressed NW-SE during Pennsylvanian-

Permian Alleghenian orogeny, the strikes of the major faults and folds are trending NE-SW. Due to its compressional setting, the Appalachian basin has structural complexity toward the basin margin (the valley and ridge on the SE side) while it is relatively gentle toward the basin (Appalachian Plateau, NW side). Many of the observed geological features - fractures, joints, and cleavage sets - have correlations with structural trends of the Appalachian basin. All or some of the geological features are believed to be structurally originated and thought to be the main reason for the high shale gas production in the Marcellus shale play (Engelder et al., 2009; Evans et al., 2014; Wilkins et al., 2014; Zagorski et al., 2012). Due to the massive deposition, lower Marcellus shale seldom has signs of bioturbation and is less laminated. However, the upper Marcellus shale is more laminated and has heavy bioturbation. Thus, the upper Marcellus has less organic content than the lower Marcellus shale.

5.2 Field and data description

We were provided with field data, including 3D seismic data and data from a couple of wells, on a Marcellus shale play located in West Virginia. To maintain confidentiality, the data donor asked to remain anonymous. Therefore, while the analysis for this study used the area's real features and real numerical data, the numbers reported have been changed slightly.

5.2.1 Available data

3D seismic data cubes in travel time and after depth migration are available. Figure 5.6 shows the pre-stack depth migration (PSDM) seismic cube with two exploration wells in the data region. On the same wellpad with Well-A, there are four additional horizontal wells. Similarly, one other horizontal well shares a wellpad with Well-B. Only Well-A and Well-B have well log data along the vertical sections.

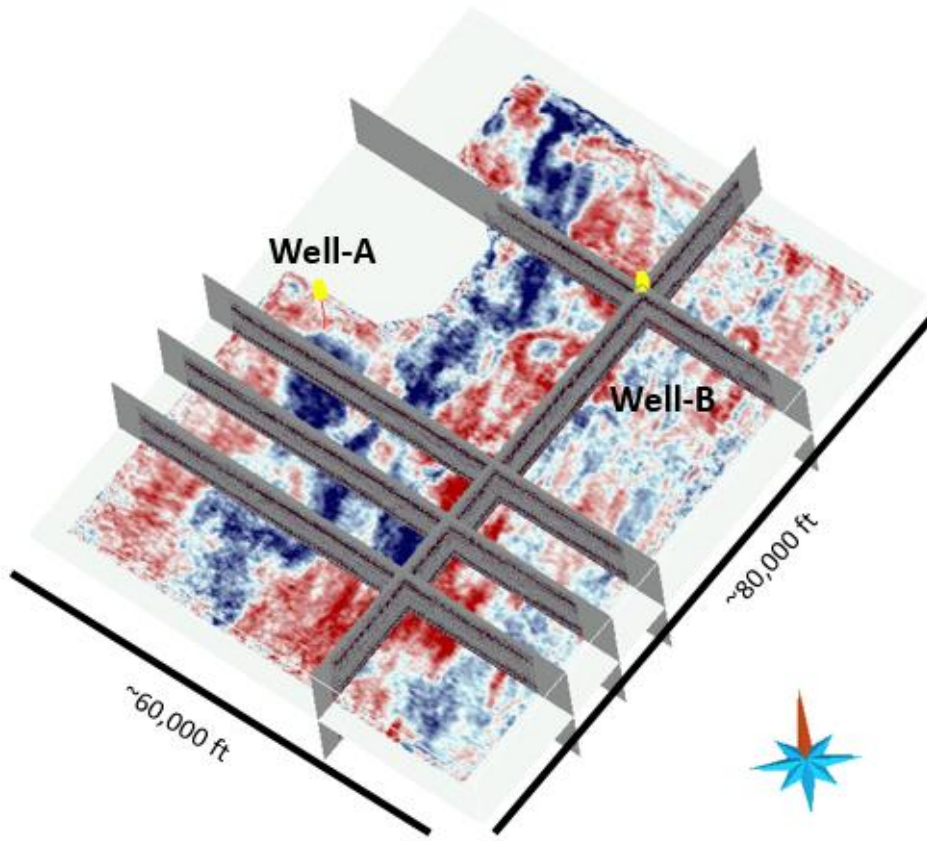


Figure 5.6: 3D PSDM seismic data and the two main exploration well locations. Well-A is located toward the basin while Well-B is located toward the Appalachian thrust belt. Thus, the Well-A region is seismically gentle, while the Well-B region has more complex seismic responses.

5.2.2 General characteristics of the data area

The area is located close to the front of an Appalachian thrust fold. Following the major structural axis of the Appalachian basin, structural features such as folds and faults are well-aligned, with a strike direction of NE-SW. Since the eastern part of the data area, where Well-B is located, is closer to the Basin thrust and the seismic horizons have more complicated geometry in this region, the operator calls this a complex area. Well-A is located in the western part (gentle area), which is closer to the basin side and does not have any structural perturbations, as seen in the seismic data.

The operators encountered productive gas columns in the target Marcellus formation for both Wells A and B. The field is under appraisal status, as the operators

conducted evaluations to define well productivities to develop optimal spacing for horizontal producers in the Well-A and B regions, and possible well locations for the next exploration wells. Due to the structural location of the field – a transition between a structurally complex overthrust and a structurally gentle depocenter – the operators have difficulties extracting field-wide general rules from Well-A and B, to extrapolate to un-drilled regions. We will cover the basin- and field-level challenges and difficulties in Sections 5.3 and 5.4.

5.3 Factors affecting gas productivity in Marcellus play

Reserve estimation and well productivities of the Marcellus shale play heavily depend on the lithofacies of shale, their thickness, and the pre-existing joint network (Wang and Carr, 2013; Wilkins et al., 2014; Zagorski et al., 2012; Thompson et al., 2011; Osholake et al., 2012). The first two are obvious factors in any natural resource evaluation process. If we have shale with higher gas contents with thicker formations, the region has a larger static amount of gas in place. The joint network is related to well productivity and the economics of the field developments. For example, if one field has thick and rich shale formation but no pre-existing fracture networks, it may require intense hydraulic fracturing operations. However, if the field has well-distributed pre-existing fracture networks, it would require less expensive development since fewer producing wells would need to be drilled and the field would have a larger per-well estimated recovery.

There are differences among these three factors. The first two factors are more global factors that become less uncertain the moment we choose fields to investigate or develop within the Appalachian Basin. However, the third factor remains uncertain even after we choose the fields to investigate, and even after getting well data from the region.

5.3.1 Basin scale factors: Lithofacies of shale and their thickness

The spatial distribution of lithofacies is one of the most important sources of uncertainty in subsurface resource evaluation, because it directly affects not only the static volumes or specific subsurface resources, but also the dynamics of how to extract them (Strebelle

and Journel, 2001; Park et al., 2013; Vo and Durlofsky, 2015; Vo and Durlofsky, 2014; Jeong, 2014; Xu, 2014).

However, the relative importance of the spatial distribution of lithofacies and their thickness is slightly different for different scales and different applications. First, the uncertainty on facies distribution depends on the scale of observation and the scale of the deposition processes. When we deal with a channelized sandstone reservoir, the geometries and locations of channel sand bodies are highly uncertain (Vo and Durlofsky, 2015; Jeong, 2014). When we deal with channel and lobe deposition patterns in a delta scale, the locations and paths of the channel and the attached lobes are uncertain (Xu, 2014). However, if a region of investigation is a bin on a several kilometers by kilometers scale in a depocenter on a hundreds of kilometers scale, if we encounter specific facies along the well, it is less likely that we will have horizontal variability in lithofacies within the bin of investigation. Thus, the importance of uncertainty on spatial distribution of lithofacies is very relevant when we are dealing with a region deposited in highly variable locations in depositional processes, and on a scale having meaningful variations of the deposition of lithofacies in paleogeography (syn-depositional condition).

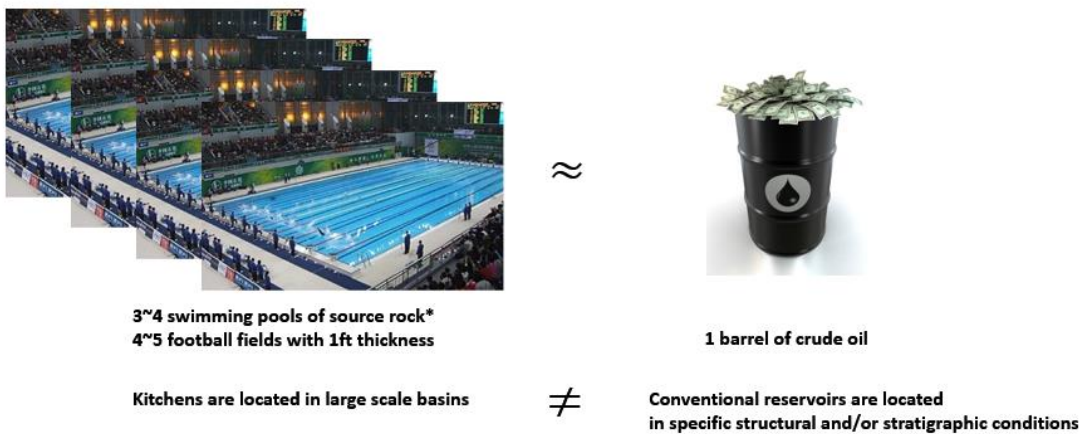


Figure 5.7: Volume comparison of the required amount of source rock to produce one barrel of oil. The volume of required source rock was calculated by Andrews (2013).

Figure 5.7 is a cartoon comparison of the required volume of source rock to produce a barrel of crude oil (volume calculation from Andrew, 2013). If we spread one

barrel of oil to a height of one foot it will be a 2.3 ft by 2.3 ft rectangle, while the required area of source rock is four to five football fields one foot thick. This depicts fundamental differences on the level of heterogeneities of the source rock and reservoir rocks. An effective source rock should be massive and have largescale deposition, while an effective reservoir rock should have certain geometrical conditions with stratigraphic settings. Accordingly, reservoirs are the results of special levels of heterogeneities while sources are the results of special levels of homogeneities. Horizontal variograms of the lithofacies in Marcellus shale across the Appalachian basin are around 400,000 ft, with the major axis orienting NE-SW (Wang and Carr, 2013). The length of the given field is 80,000 ft. The lithofacies that Wang and Carr categorized are not sand versus shale, but a subset of shale and mud distinguished by slight differences in organic contents and the compositions of silt and carbonate. When we are trying to choose a lease in an unconventional fairway, the spatial variability of lithofacies and their depth is one of the key uncertainties to be more or less economical. However, once we choose a region to evaluate, uncertainty in lithofacies and their thickness is no longer the biggest uncertainty compared with the spatial variability of well productivities.

5.3.2 Field scale factor: Joint sets and their importance in Marcellus play

Well productivities of the Marcellus shale play heavily depend on pre-existing fracture networks, because the effects of hydraulic fracturing hugely hinge on whether or not the cracking connects and/or reopens pre-existing natural fracture networks (Engelder et al., 2009; Inks et al., 2015; Osholake et al., 2012). Since many observations on fractures and joints sets are highly related with Appalachian thrust belt and major faults and folds that align with Appalachian thrust, many researchers and operators believe that pre-existing fracture and joints sets were developed during orogeny and controlled the structural geometry of the Appalachian thrust belt (Wilkins et al., 2014; Aydin, 2014).

However, there are different opinions on defining different sets of flow enhancing/preventing geological features: joints/ fractures/ veins/ cleavages/

deformations bands; origins of specific features – structural/ hydrocarbon maturation/ chemical reactions; and timing of features – pre-/ syn-/ post-orogenic. Since the existence, abundance, and orientations of those features are important factors in estimating gas productivity, having multiple theories means geological uncertainty in understanding and evaluating the fields in the Marcellus shale play.

Fractures and joints in Marcellus shale play are typically categorized into three sets: J1, J2, and J3 (Engelder et al., 2009; Aydin, 2014; Plumb et al., 1991; Plumb and Hickman, 1985; Hancock, 1985; Zoback et al., 1985). The J1 set is nearly vertical and generally parallel with the strike of the Appalachian ridge and its major faults and folds. The J2 set is also vertical in general and is either perpendicular with J1, or the mean of the conjugate sets are perpendicular when the J2 joints are placed as conjugate joints. J3 is less common and sub-vertical, generally striking parallel with J1.

Figure 5.8 shows the strike orientations of the J1 and J2 joint sets of Marcellus shale (Engelder et al., 2009). The strike of J1 coincides with the orientation of current maximum compressional stress, NE-SW, while the mean strike of J2 coincides perpendicularly with the current maximum compressional stress, NW-SE.

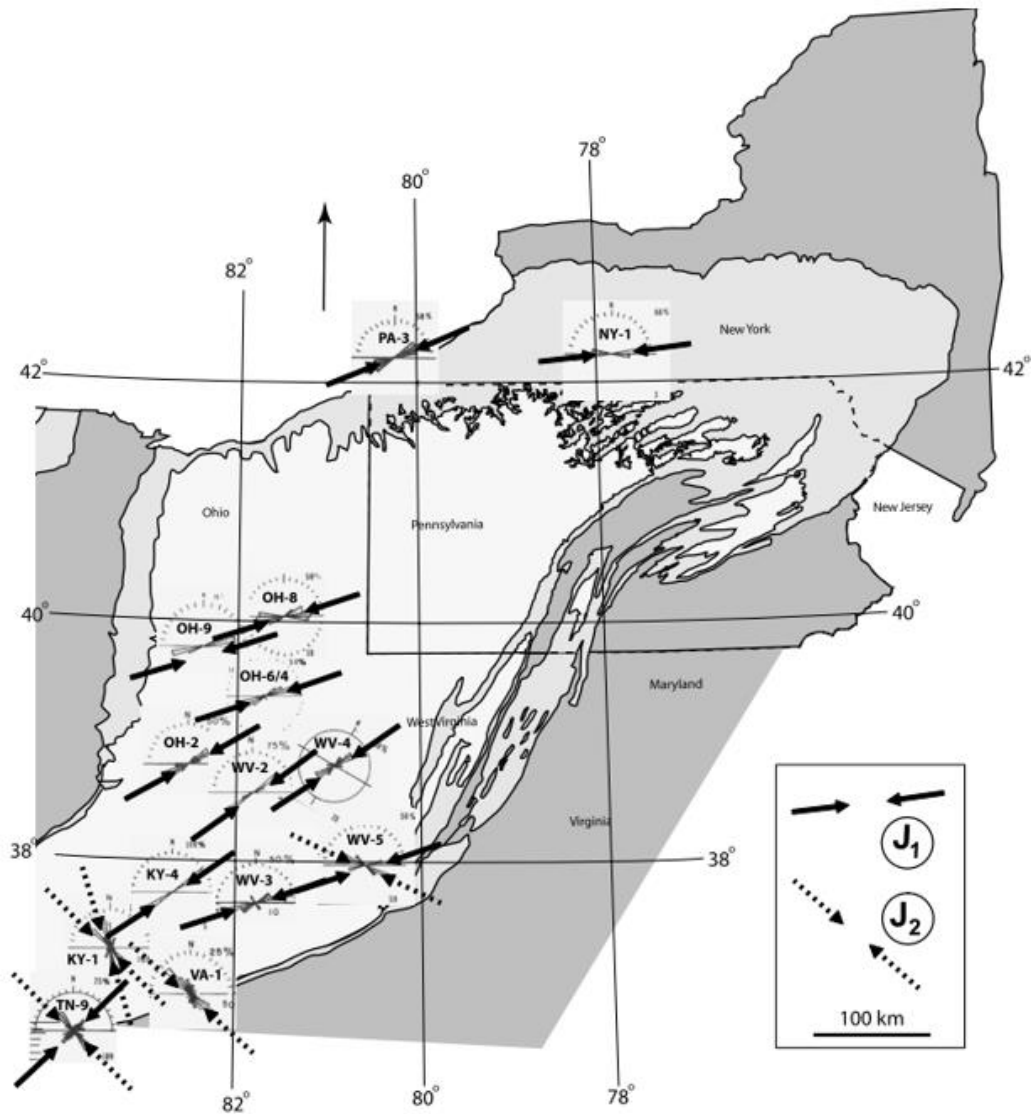


Figure 5.8: Orientations of J1 and J2 sets of joints in Marcellus shale (Engelder et al., 2009). The strike of J1 is parallel with the current maximum compressional stress, NE-SW ($S_{H_{max}}$), and the strike of J2 is perpendicular with the current maximum compressional stress.

Engelder and his colleagues (2009) addressed three conundrums on Marcellus fractures. First, the vertical joint sets, J1 and J2, have nearly perfect planarity. Either an opening joint or shear mode joints are generally curvilinear and less likely to form a perfect planarity (Figure 5.9). Second, regarding the J1 joint, open-mode joints that have persistently remained open in current conditions have strikes perpendicular to tectonic loadings from orogeny, NW-SE. Since the tectonic loading compressed NW-SE, joints

opened by striking NE-SW are hard to keep open. Third, the orientation of maximum compression has been rotated 90 degrees horizontally from the orientation of the tectonic loading, to the currently measured maximum compressional stress. The direction of tectonic loading is parallel with strike of J2, NW-SE, while the borehole stress measurements are consistently parallel with the strike of J1 in a compressional sense. The geological aspect of the third conundrum is the mechanism of the 90-degree rotation of principal stress, while the engineering aspect of the third conundrum is that estimations of orientation of hydraulic fractures from bore-hole stress measurements do not work well in Marcellus play, due to the flipping of principal stress.

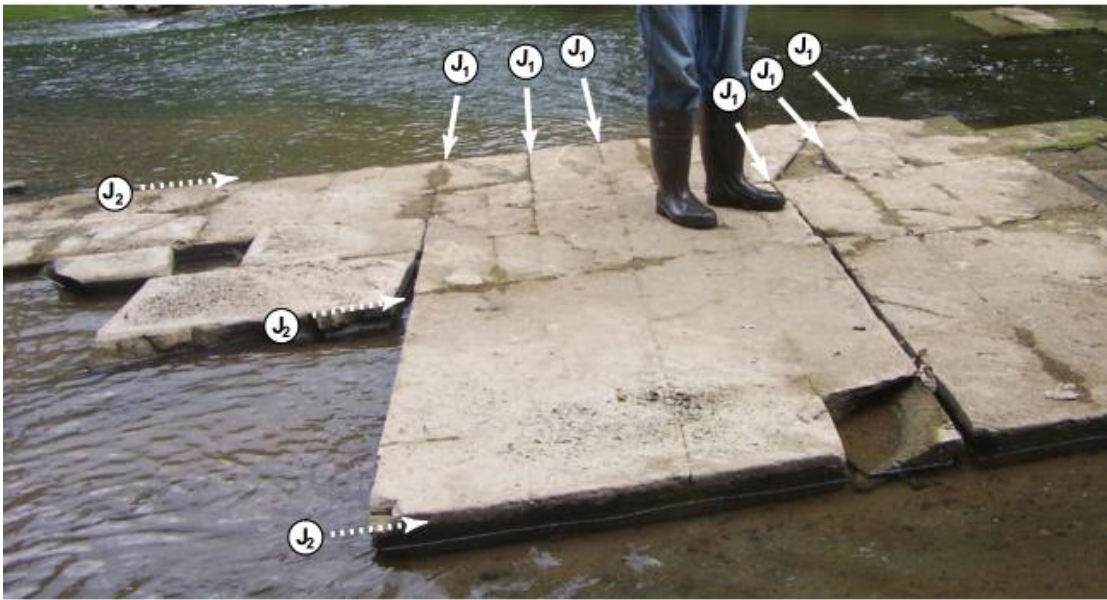


Figure 5.9: Photo of outcrop of J1 and J2 joint sets (Engelder et al., 2009). Both sets are vertical and have nearly perfect planarity.

These three conundrums, given the inconsistency with common knowledge and that we don't know the mechanism behind these problems, increase difficulties when estimating the preferential directions of higher flow connectivity and make development plans less optimal, due to discrepancies between the estimated abundance and orientations of joint sets and the actual joint sets encountered after drilling.

5.4 Problem statements of the field

As we discussed in 5.3, defining and understanding the spatial distribution of accommodational features in the target shale formation – the number of joint sets and their abundance, mean orientations, easiness to re-open, and possible connectivity – is one of the most important tasks to evaluate unconventional shale gas plays.

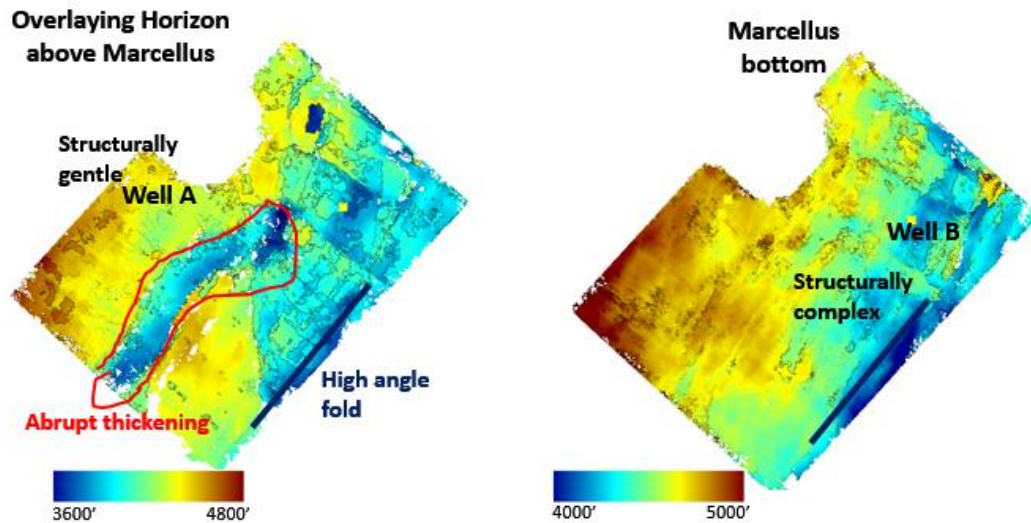


Figure 5.10: Horizon tops of a formation above Marcellus shale (left) and a formation below Marcellus shale (right). The Well-A region is seismically gentle, while the Well-B region has geometrical complexity from seismic data.

The given data field successfully encountered gas-producing shale formations from the vertical exploration of both Well-A and Well-B (Figure 5.10). Since the existence of a gas-flowing formation is verified, the remaining questions for the operators were how to test productivity and the optimal development plan, including the orientation and spacing of horizontal wells, and where to drill the next exploratory well to maximize understanding and valuation of the field.

5.4.1 Higher well connectivity on a structurally gentle area

The operators drilled a few horizontal wells to test frac job efficiency and configure the best frac job settings for the area. Since the Well-A region is expected to be structurally gentle and flat (Figure 5.10 and Figure 5.11b), they drilled the horizontal wells relatively close to one another, and the operator originally believed a large and intense frac job

might be needed. However, when the test frac job was conducted, widespread fracturing was detected in the micro-seismic observations, even with a small amount of injection (Figure 5.11).

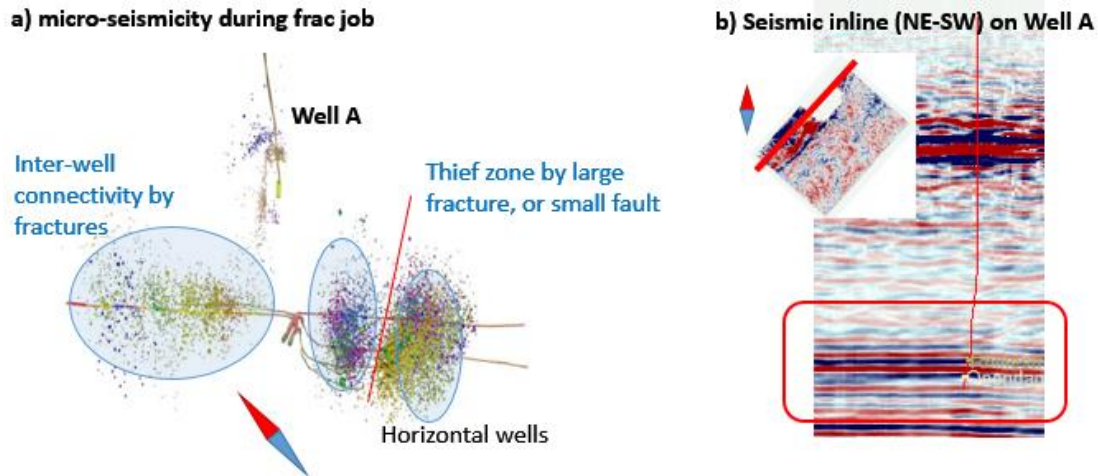


Figure 5.11: Micro-seismicity during hydraulic fracturing (left) and a vertical section of the seismic inline along Well-A.

The test revealed the possibility of having well-developed, widespread pre-existing fracture networks which were not observed in the vertical well log, with preferential connectivity along the NW-SE direction. A strong thief zone absorbing a huge amount of injecting fluid was also observed. This indicates the presence of faults, or relatively big fractures. It is hard to define any fault near the thief zone based on seismic data. More importantly, the horizontal wells were too closely spaced to be optimal due to the unexpected high connectivity.

5.4.2 Water influx without water injection

The Well- B region is located in a structurally more complex region toward the basin ridge (Figure 5.10 and Figure 5.12). In this region, a gas productivity test was suspended by an unexpected large amount of water influx without injecting any water. Because the target formation is located below thick columns of interbedded shale and carbonates and overlaid above thick Onondaga carbonate (Recall the stratigraphy from Figure 5.2),

together with nano-scale permeability of Marcellus shale, the large amount of water influx was extremely unexpected.

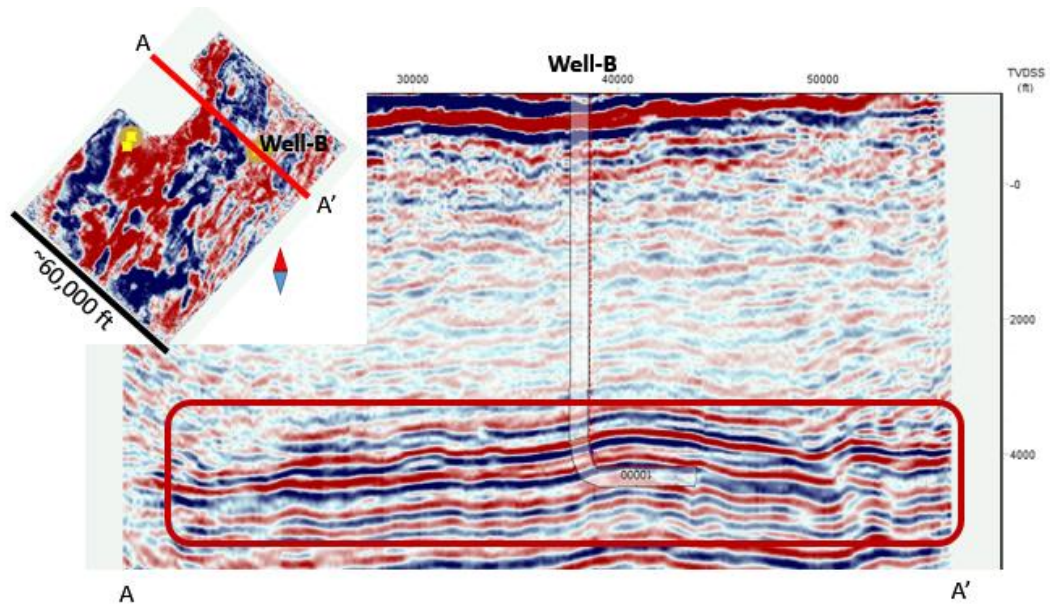


Figure 5.12: Seismic crossline along Well-B. Unlike Well-A, the Well-B region has more complex geometry around the target formation from seismic responses.

5.4.3 Existence of pre-existing sub-seismic geological features and their orientation

Unexpected observations from the Well-A and Well-B regions indicate the existence of sub-seismic geological features that enhance flow with preferential orientation. The presence of a meaningful amount of fractures in the Marcellus formation was not expected from the well log and cores from the vertical wells in the Well-A region.

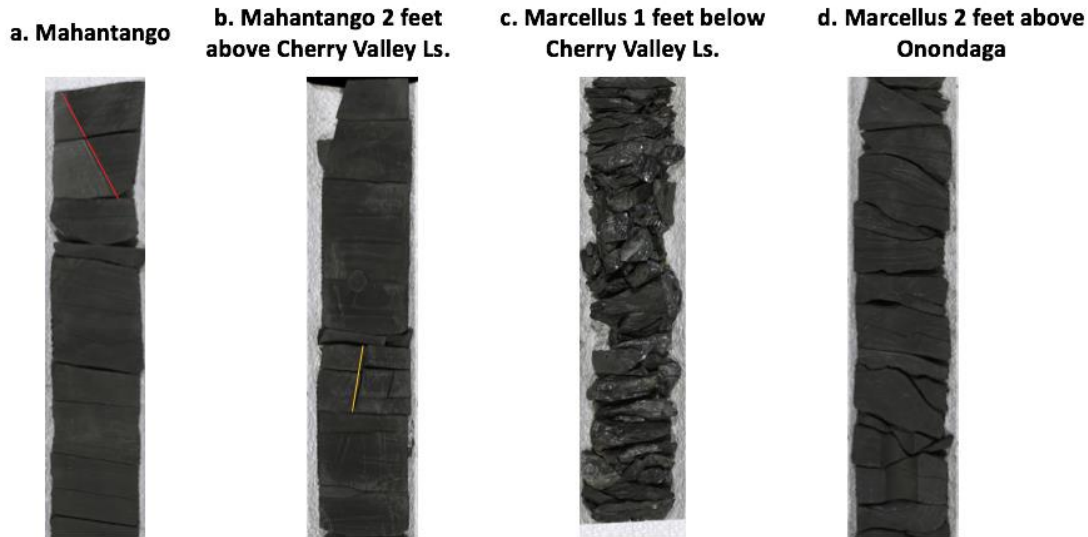
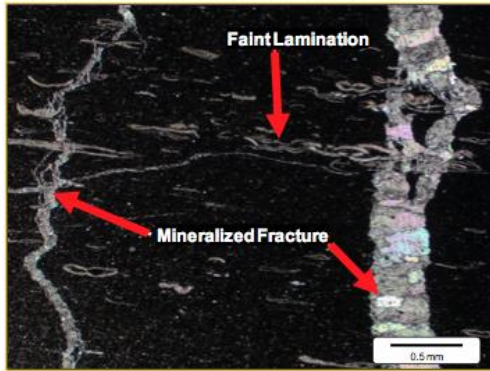


Figure 5.13: One-foot long core sections selected from cores from Well-A. a) One-foot section from Mahantango shale. Red lines represent a fracture preserved in the core. All the other horizontal cracks are post-drilling cracks from horizontal fabrics. b) One-foot core section of Mahantango located two feet above Cherry Valley limestone. The orange vertical line is a crack line, but we cannot determine whether it is a drilling-induced crack or a vertical joint. c) One-foot core section of Marcellus shale one foot below Cherry Valley limestone. They all crashed during drilling and core retrieval. Slickenside and mineralized fractures are observed in the fragmented core particles. d) One-foot core section of Marcellus shale two feet above Onondaga limestone. All cracks are drilling-induced, or post-drilling cracks along foliation and fabric. Unlike the core from Mahantango, there are many tilted and curvilinear surfaces.

Figure 5.13 shows four one-foot core section images from cores retrieved from Well-A. In 5-12a, the red line indicates a natural fracture indicated in the Mahantango formation. All the nearly horizontal cracks are drilling induced, or post-drilling cracks along fabrics. 5-12b is a one-foot section of Mahantango. The orange line is a vertical crack but we cannot determine whether it is a drilling-induced crack or a natural fracture. 5-12c is a one-foot section of Lower Marcellus shale located one foot below Cherry Valley limestone. The section was fragmented during coring. Slickenside and mineralized fractures are observed in the section. Finally, 5-12d is a one-foot core section of Lower Marcellus located two feet above an Onondaga formation. Here, the surfaces of drilling/coring induced cracks are not horizontal but tilted and curvilinear, and look like a feet-level thrust system.

a. Section image of mineralized fracture in Mahantango



b. Section image of organic rich Lower Marcellus

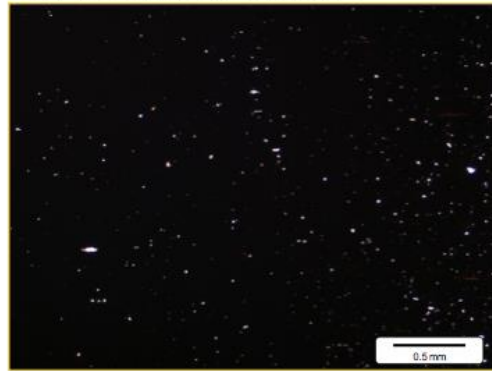
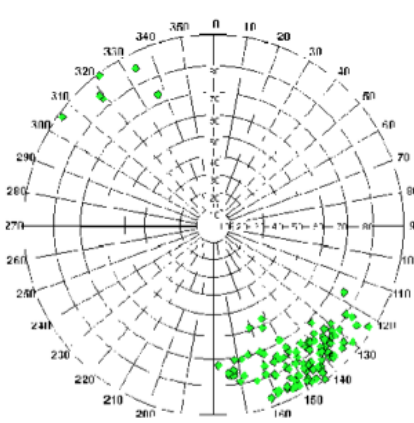


Figure 5.14: Section slides of cores from Mahantango and Lower Marcellus. a) Mineralized fractures in Mahantango formation. b) This organic-rich Marcellus shale section does not have noticeable fabrics at inch-level resolution.

Figure 5.14 shows core section images of (a) Mahantango shale with veins in it and (b) organic rich Lower Marcellus shale. From the cores, we can definitely see that the formation is brittle enough to be broken down easily based on the horizontal and sub-horizontal drilling-induced cracks.

a. Stereonet of drilling induced cracks



b. Rosette plot of strike of drilling induced cracks

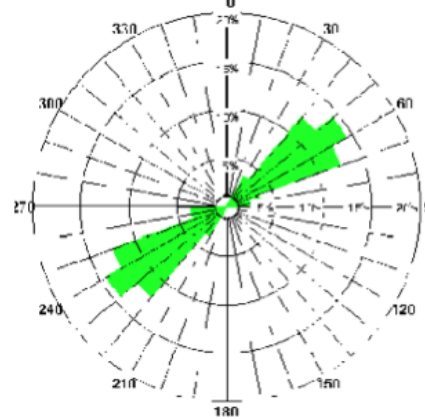


Figure 5.15: Stereonet (a) and Rosette plot of the strikes of drilling-induced cracks. Note that the nearly horizontal foliations from Figure 5.13 (the red line) are not included and only the crack surface lines (orange lines) are counted. The orientations of drilling-induced cracks show a high level of consistency.

Figure 5.15 shows the orientations of drilling-induced cracks. Though the formation shows a relatively high level of brittleness during drilling and core retrieval, the abundance of natural fractures and joints or faults are not significant, based on observation along Well-A. However, given the indicated microseismic activity during hydraulic fracturing in the Well-A region and the water influx in the Well-B region during well testing, a pre-existing fracture network or a series of sub-seismic faults, flow-enhancing features, is expected. Since the fractures are not well-defined from the vertical well, we do not have a good understanding of the intensity and directions of the flow-enhancing features. As mentioned earlier, the major compressional direction of the Marcellus basin is NW-SE. If the Marcellus shale has shear mode natural fractures, the mean of the directional normal of conjugate fractures would orient in a NE-SW direction. If it has open mode joints, the joints would orient with the strike of joints parallel with NW-SE. However, the preferential directions of the connectivity of microseismicity, which the origin can be interpreted by a linkage of fracture networks or faults from the Well-A region, are persistently NE-SW, parallel to the current maximum compressional stress while perpendicular to tectonic compressions from a series of orogeny.

5.4.4 Uncertainty on geometrical interpretation

In the 3D seismic data for the given field, we have interesting features that increase the complexity of geometrical interpretations of the subsurface structure. Along the NE-SW strike direction in the central area of the survey boundary, there are persistent repeated horizons near the Marcellus formation. Figure 5.16 is a crossline of the PSDM seismic cube with Well-A in the line. In the central part, there is triangular geometry that has a segmented horizon. In Figure 5.10, while the left figure – a horizon above Marcellus shale – has a localized “bump” that looks like a band of anticline, the right figure – a horizon below Marcellus shale – remains flat. This localized “bump” or abrupt thickening corresponds with the repeated section in Figure 5.16.

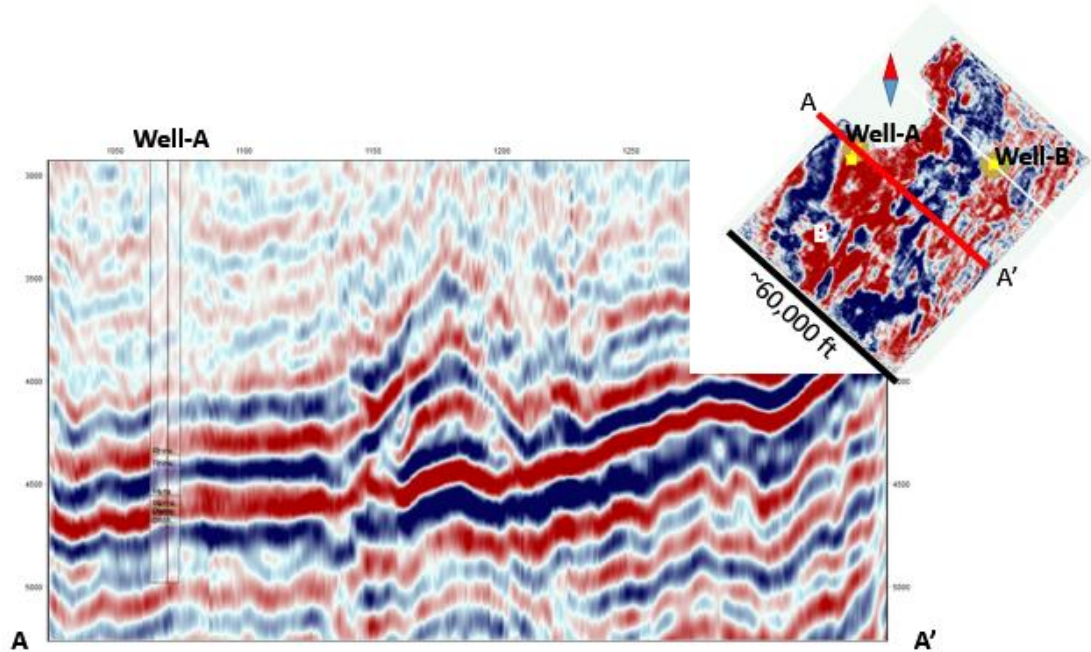


Figure 5.16: Repeated sections near the target horizons along a seismic crossline including Well-A. The type and origin of the feature is unclear and it leads to uncertainty in structural interpretation.

5.4.5 Consequences for further appraisal and developments

From the basin-wide joint observation, the persistent direction of a major joint, J1, on the Marcellus shale is a NE-SW strike, with directional normals toward NW-SE. The directional normals of the second major joint set, J2 a younger joint set than J1 (this is controversial among geologists; it will be covered in 5.5), are parallel with the strike of the Appalachian thrust. Both of them are nearly vertical, and the angle between the two sets varies around the basin from around 50 degrees to nearly perpendicular (Engelder et al., 2009). Figure 5.9 shows the orientations of the J1 and J2 joint sets. Note that these observations are a general description of fractures on Marcellus shale, not a field-specific description. Thus, we are not even sure whether the flow-enhancing geological features are related to J1 and J2 or not. As Engelder et al. (2009) mentioned, the observed persistent directions of main joints cannot be explained by conventional geomechanical models following Mohr-Coulomb failure criteria. In the given field, we failed to link the structural geometry directly to the joint abundances (from the Well-A region). Current stress conditions, magnitudes, and orientations do not give mechanical

explanations of joint networks in basin-wide observations. Thus, we have difficulties estimating the spatial distribution of the abundance of flow-enhancing features, one of the most critical factors in developing unconventional shale gas developments.

Let's assume that we have a reliable rule: that subsurface structure indicates the existence and abundance of flow-enhancing features. Even in that case, from the uncertainty of the repeated section in the seismic data, we can determine neither the current structural geometry nor the deformational history of the subsurface. On top of that, we are not sure whether the flow-enhancing features are linked with present stress, or with paleo-deformational stress.

5.5 Defining sources of geological uncertainty

As we discussed in 5.3 and 5.4, we have not only field-specific but also basin-wide geological uncertainties about how to interpret structural geometry, and about what sub-seismic geological features enhance or hinder flow, and their origin. These two uncertainties correspond to geological uncertainties in the structural deformation and rock accommodation, covered in Chapter 2. As we discussed in Chapter 2, classification and separation of these two sources of uncertainty are scale-dependent and involve model-related uncertainty. A group of relatively small faults can be understood and modeled as a set of shear fractures when the size of the modeling grid block is relatively bigger than the size of the faults. A certain mode of rock accommodation can be a consequence of a certain type of mode of structural accommodation, and vice versa.

In the following sections, we first define the sources of geological uncertainty in modes of structural deformation and in modes of rock accommodation, separately. In addition, we review and propose geological models of how the deformation mode and accommodation mode are linked, to explain the larger- and smaller-scale phenomena together.

5.5.1 Defining sources of structural deformation uncertainty

For the repeated section in Figure 5.16 the operators use the term “duplex,” which is a branch of a thrust system different from imbricate fans on the structural closure of accommodating horizontal displacement (Boyer and Elliott, 1982). Since thrust is a very common feature in compressional tectonic loading conditions, and duplexes become more likely where there is rigidity contrast and vertical heterogeneity, the presence of duplexes in the Appalachian thrust belt is highly likely. Figure 5.17a shows the difference between imbricate fans and duplexes as subsets of thrust systems (Boyer and Elliott, 1982). Figure 5.17b and c are conceptual model of duplexes and fault-bend folds (Thomas, 2001). However, it is not certain whether this is actually a duplex feature and if so, which horizon is repeated, or which side is the overlying part and which is the underlying.

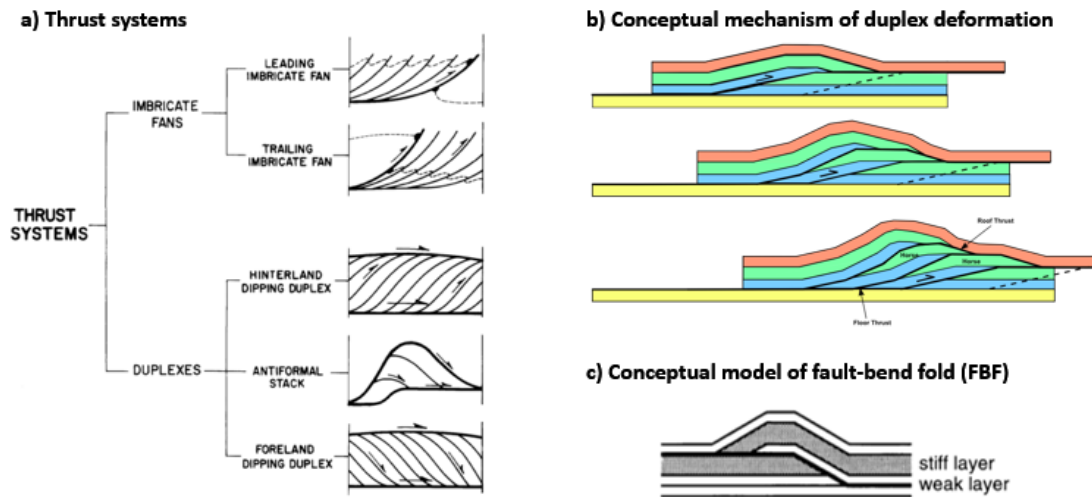
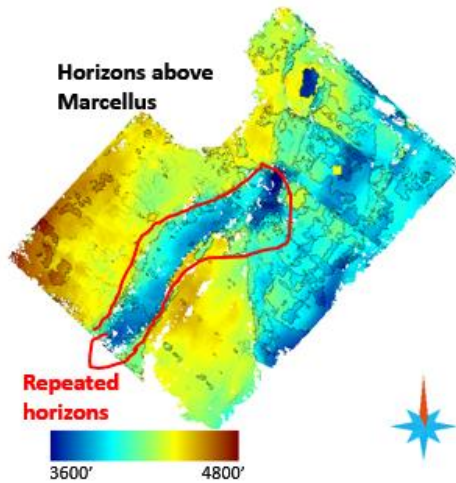


Figure 5.17: Duplex models as a branch of the thrust system. a) Imbricate fans and duplexes (Boyer and Elliott, 1982). b) Conceptual cartoon of duplex system (from data donor). c) Cartoon of fault-bend fold (FBF) (2001, Thomas). An FBF can be understood as the smallest component to compose a duplex that may have a series of FBFs inside.

a) Localized thickening from seismic data



b) Satellite photo of coral reef in Miami beach

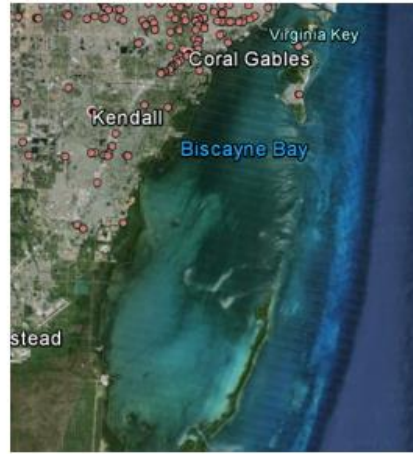
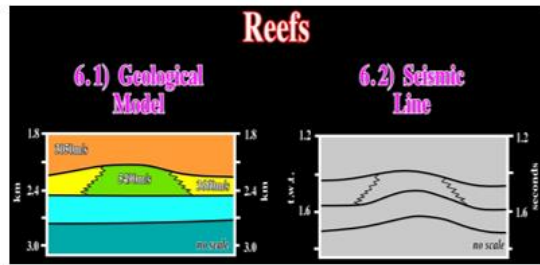


Figure 5.18: Alternative interpretation of abrupt thickening by a band of reef carbonate. On the left is the horizon of a formation above Marcellus shale. On the right is a contemporary photo image of a band of coral reef in Miami Beach.

Another possible interpretation of the repeated section is a long band of carbonate reef. The left part of Figure 5.18 is an overhead view of the horizon of a formation above Marcellus shale which has a long band of locally elevated horizon tops. The right part of Figure 5.18 shows a present-day carbonate reef near Miami Beach that can be an analogy to interpret the localized thickening or repeated section. Since the area is expected to be located in a marine environment with interbedded shale and limestone, either the Onondaga carbonate below or the overlaying Tully limestone could have developed a massive local reef complex.

a) Seismic pull-up by carbonate



b) Localized thickening and seismic responses in deeper horizons

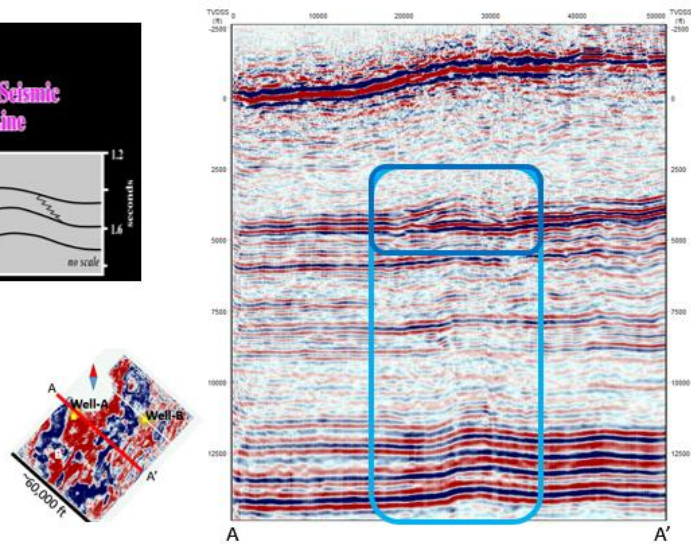


Figure 5.19: Seismic pull-up below reef platform. The left image is a cartoon example of seismic pull-up in seismic response by faster travel time in denser carbonate (a) (from the website of Universidade Fernando Pessoa). The right image is a crossline along Well-A. The dark blue box identifies the region having uncertainty in structural interpretation. The light blue box covers all the horizons below the Marcellus shale formation.

Figure 5.19a depicts a typical seismic pull up in the presence of a carbonate reef. Due to the denser and stiffer property of carbonate, waves travel faster and have shorter travel times. Thus, the two-way-travel time of lower horizons becomes shorter. Figure 5.19b depicts the vertical crossline that has Well-A in it. The localized thickened area around Marcellus, in the dark blue box, is the uncertain feature. All the horizons below the Marcellus shale formation have well-aligned anticlines (the lighter blue box). This could be a well-aligned anticline from the compression. Alternatively, it can be a seismic pull-up from the presence of a localized stiffer or thicker carbonate formation. The problem here is that both the duplex and reef interpretation can explain the seismic pull-up. If the duplexed structure involves repeated sections of a carbonate formation, it produces the same effect as a localized thick reef platform in seismic travel time for the lower horizons.

We can use the analogy of a localized thickness anomaly observed in the Appalachian basin to qualitatively review the two interpretations we just proposed.

Since Marcellus and its adjacent formations have been exposed in the same basin-level depositional environment and tectonic loading, the thickness anomaly observed in the given field should be observed in different regions. Wang and Carr (2013) conducted lithofacies analysis of 3880 public well data of Marcellus shale formation on the Appalachian basin. Among those wells, a couple of wells with distinctive thickness anomalies were recognized.

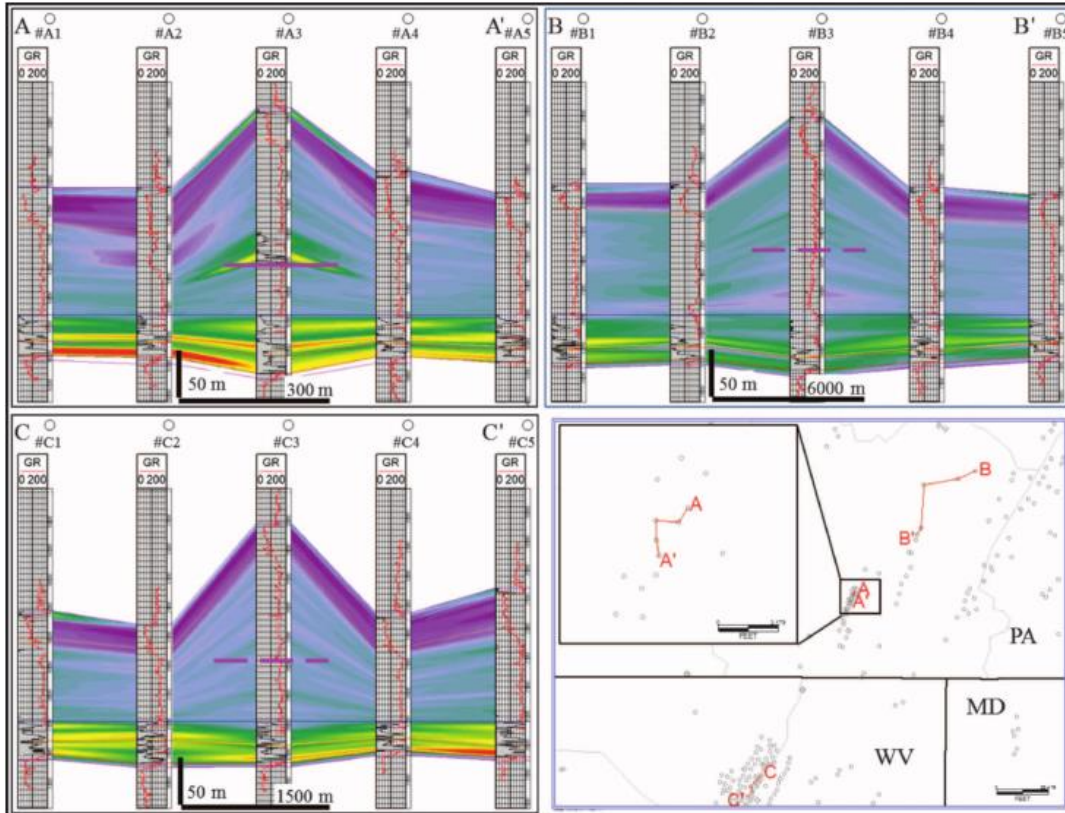


Figure 5.20: Wells with localized thickness anomalies. Section AA' and BB' are wells from Philadelphia and CC' is from West Virginia (Wang and Carr, 2013).



Figure 5.21: Satellite image of well sections with thickness anomalies (image from **Google Earth**). The three red lines correspond with AA', BB', and CC' from Figure 5.20.

Figure 5.20 shows three well sections with thickness anomalies in formation above the Lower Marcellus shale (Wang and Carr, 2013). Figure 5.21 is a satellite image of the well sections from Figure 5.20. They are all located along the Appalachian ridge. Since all three wells are located along the basin ridge, this suggests a possible relation between structural deformations and localized thickening. In Figure 5.20, well section AA' has a fault interpretation along the well with a distinguishable repeated section of the Lower Marcellus formation. However, well sections BB' and CC' have fault interpretations from the wells, but without noticeable repeated sections. Though well section AA' is an obvious example of repeated sections from duplexes, fault-bend folds, or any combination of a sub-system of thrusts, observations from BB' and CC' do not decisively indicate that the thickenings are from duplexes or fault-bend folds. This is because any minor reverse fault in these regions is one of the most frequent features in the Appalachian basin, while the thick formation can still be originated from other geological processes such as the deposition and erosion process, or from forming anticlines.

Though we have limited data on localized thickening, or the repeated section, we can use observations of deeper or shallower formations in the same basin, which

have experienced relatively similar tectonic loadings over geological time. Figure 5.22 shows a duplex in Silurian-Ordovician formations observed from an outcrop in West Virginia (Ferrill and Dunne, 1989). Although these are deeper formations than the formations around Marcellus shale, the observed duplexes were generated from the Pennsylvanian-Permian Alleghenian orogeny that also applied as tectonic loadings on the Marcellus shale. Observations of duplexes in deeper horizons do not indicate the same geological processes in different formations. However, they surely indicate that duplexes are working deformational mechanisms in the Appalachian basin, absorbing tectonic loadings.

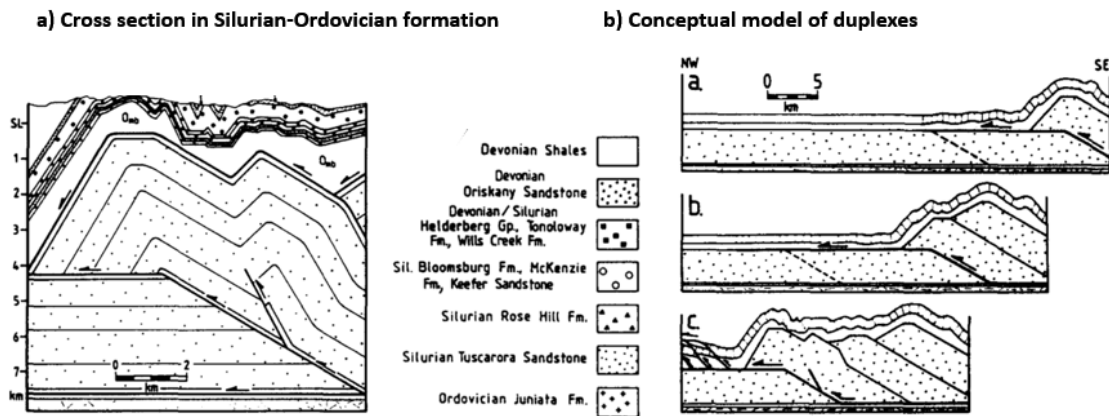


Figure 5.22: Duplex of Silurian-Ordovician formation observed from an outcrop section in West Virginia (Ferrill and Dunne, 1987). On the left is a sketch of part of a duplex (a fault-bend fold) of Silurian-Ordovician formations observed in West Virginia. On the right is a conceptual model of observed duplexes by Ferrill and Dunne (1987).

Note that these interpretations are not collectively inclusive of all possible modes of structural deformation, nor are they perfectly mutually exclusive to some degree. Fault-bend folds and duplexes are nucleated from basement faults. Bands of carbonate platforms, or faulted carbonate platforms can nucleate basement faults by acting as a stiffer boundary (Thomas, 2001; Bigi and Costa Pisani, 2005). There are always possibilities that a set of different structural deformation mechanisms worked together to make the larger-scale deformation work. The adequate number of modes to cover the geological uncertainty depends on the complexity of the structural geometry, the level of understanding of the geological history of the region, the resolution of the

data, the availability of adequate geological models to explain the situation, the types of decisions to be made from the study, and the subject decisions of geo-scientists.

5.5.2 Defining sources of rock accommodation uncertainty

As we discussed in Section 5.4, the given field is under appraisal with a limited number of wells. Thus, we need to rely on published studies to develop rock accommodation scenarios. In Marcellus shale gas plays, the existence and abundance of pre-existing or possible fluid conduits constitute one of the most important geological factors to decide the productivity and commerciality of fields, by affecting the results of hydraulic fracturing (Osholake et al., 2012; Zagorski et al., 2012; Sahai et al., 2012; Thompson et al., 2011). Researchers who are more focused on engineering aspects – optimal well spacing, length of horizontal drilling, and distance among hydraulic stimulation – attempt to estimate the so-called SRV, simulated reservoir volume, and use the brittleness of the rock to estimate the productivities of the region (Sahai et al., 2012; Osholake et al., 2012; Zagorski et al., 2012).

Defining and testing possible modes of rock accommodation is important because the existence and abundance of sub-seismic geological features directly act as, or are closely linked with, flow-enhancing or flow-hindering features. For instance, a joint set remaining open makes fluid easier to flow and makes SRV bigger. However, if the same joint set in a different lease lots is healed or cemented, and becomes a set of veins, it acts as a flow barrier. The rocks that experienced fracturing in a past geological time may respond differently when stimulation jobs are applied, because of hysteresis from previous accommodational events (Nygård et al., 2006).

In Section 5.3, we discussed the field-wide and basin-wide geological uncertainty on the spatial distribution of sub-seismic geological features. Due to the limited data in the given data set, we should start developing possible modes of rock accommodation from basin-wide observations. Sources of the uncertainty on rock accommodation style can be sorted into two groups: (1) uncertainty on defining and categorizing sub-seismic features affecting seismic and flow responses, and (2) uncertainty on the origins of the sub-seismic features.

We briefly discussed the first group in Section 5.3. Researchers have different interpretations and opinions on how to categorize the number of different accommodational features. The origins and timing of each feature are also arguable. Indeed, these uncertainties are linked because if we assume a joint set originated from structural folding, we will anticipate a joint set near a ridge of the field. However, if we believe that high pore pressure from hydrocarbon maturation was the origin of the joint set, our estimation of joint abundance should rely more on the spatial distribution of organic-rich shale.

The following are the geological features from different modes of rock accommodation defined in Marcellus shale and adjacent carbonate formations.

- J1 joints, nearly vertical and orienting parallel with Appalachian ridge
- J2 joints, nearly vertical and orienting perpendicular with Appalachian ridge
- J2 as conjugate shear fractures, not as joints
- J3 joints, sub-vertical and having the same strike orientation as J1
- Veins that used to be J1 or J2 joints
- Lateral Parallel Shortening (LPS) and cleavages - vertical or sub-vertical planar potential joint surfaces – during LPS
- Vertical stylolites in carbonates orienting parallel with Appalachian ridge
- Vertical veins in carbonates orienting perpendicular with Appalachian ridge

When we dealt with a synthetic reservoir in Chapter 3, we could clearly divide one mode of rock accommodation from alternative modes of accommodation, because the history of geological events in the synthetic reservoir was simply chosen among one of combinations that we created. However, in the real field application on the Marcellus case, the modes of accommodation style mentioned above cannot be clearly divided, or considered fully independent from each other.

On this issue, there are no unanimous classifications on different types of Marcellus fracture/joint sets and their origins among geologists. The discordance on classifications and interpretations might originate from; 1) different survey locations having different geological conditions within Marcellus play, 2) natural complexity of geological processes that we cannot fully resolve. Though there are minor differences on defining different joint sets themselves, grouping them into three major sets (J1 to J3) is common among researchers. However, some researchers contend that these sets were generated in a relatively short period, while others argue that the generations of joints happened in distinctively different geological times. We will call the first argument the mechanical approach and the second one the episodic approach.

The first group of thought – the mechanical approach – focuses more on mechanical explanations of joint development. Researchers in this group try to explain the joints by tectonic loading, fold geometry, or present stress orientation (Aydin, 2014; Wilkins et al., 2014; Engelder, 1985). Researchers in the episodic group focus more on the sequence of geological episodes, especially on fabric developments in the shale and on hydrocarbon maturations (Evans, 1994; Plumb et al., 1991; Engelder et al., 2009; Inks et al., 2015). It is noteworthy that this discordance do not necessary mean that one interpretation is wrong or right because different interpretations are based on different fields and data within Appalachian Basin having different geographical and geological conditions. Because the field we have has limited data, we are not sure what types of joint/fracture sets do we have and how they formed. Thus, we are not sure which interpretations and analogies are the most appropriate for this field.

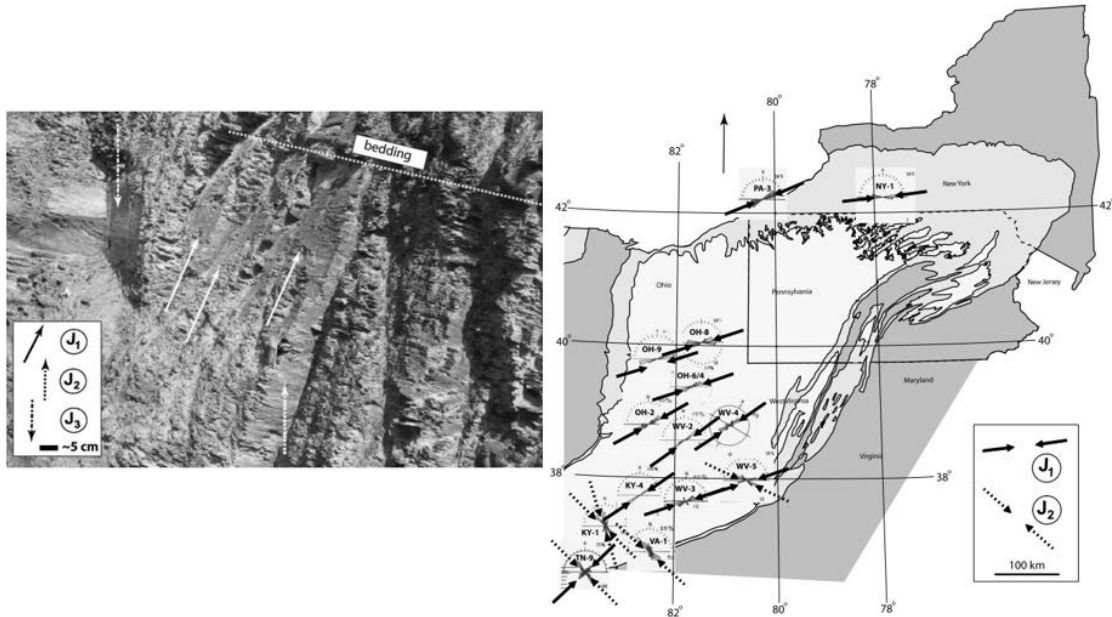
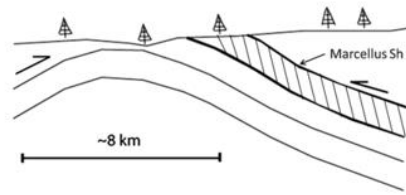


Figure 5.23: Joint sets in Marcellus shale and trends of their orientation (Engelder et al., 2009).

Among the different interpretations, the most critical differences in field evaluation and engineering applications are in the sequence and origin of J1 and J2 sets. We will refer to these models as “Aydin’s”, “Engelder’s”, or “Wilkin’s” models, using the name of the first or sole author of the related publications (Aydin, 2014; Wilkins et al., 2014; Engelder, 1985; Engelder et al., 2009). Aydin’s model tries to explain joint sets as consequences of rock accommodation on tectonic loadings (Figure 5.24). He explains that J2, parallel in this paper with the left picture in Figure 5.23 and perpendicular with the Appalachian structural front (ASF), is slightly older than J1 and J3, and was generated when the basin was compressed in a NW-SE direction but before any complex structural geometry such as faults, folds, and thrust systems developed. Thus, the orientation of J2 is strike-parallel with the maximum tectonic compression. The J1 set is shear fractures from folding and thrusting, with J3 as a splay of J1. Thus, both J1 and J3 are strike-parallel with ASF. Cleavage development during compressional loading is the reason of having nearly perfectly planar joint surfaces for J1.

a) Cartoon of a fold during tectonic loadings



2nd-b (J3) is a splay of 2nd-a (J1)
In Marcellus,
J2 is the first, and J1 and J3
together

b) Outcrop of Marcellus Shale

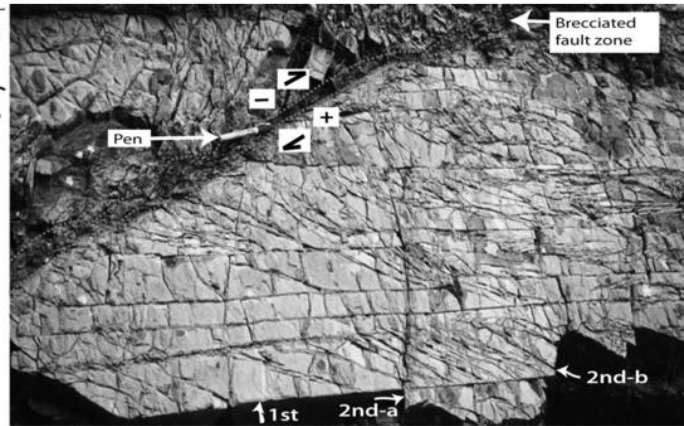


Figure 5.24: Aydin's (2014) model to explain J1 to J3 as consequences of tectonic loadings. Tectonic loading is parallel to these vertical sections. J2 was generated from compressional loading by having joint surfaces with surface normals perpendicular to the loading. J1 (2nd-a) was generated when structural deformation occurred, with J3 (2nd-b) as a splay set.

Engelder's model has a different order of episodes (Engelder et al., 2009). In this model, the J1 sets are pre-folding, the J2 sets are syn-tectonic, and the J3 sets are post-folding. Thus, all three joint sets formed at different geological times. As with Aydin's (2014) interpretation, the orientation of J1 is influenced by cleavages developed during layer-parallel-shortening (LPS) – NW-SE direction tectonic compression. The difference is that in Aydin's model, the pre-fold cleavages opened to be J1 joints as syn-folding events, while Engelder's model interprets the time of the J1 joint as pre-folding from excessive pore pressure resulting from hydro-carbon generation. In this model, the J2 joints are syn-tectonic and opened or sheared to the minimum compressional tectonic stress. J3 is believed to have formed after J2 by the reactivation of J1 joints. Thus, it can easily be misinterpreted as a splay of J1. For both Aydin's and Engelder's models, the role of cleavage is critical. We will address that element in more detail after we cover Wilkins' model.

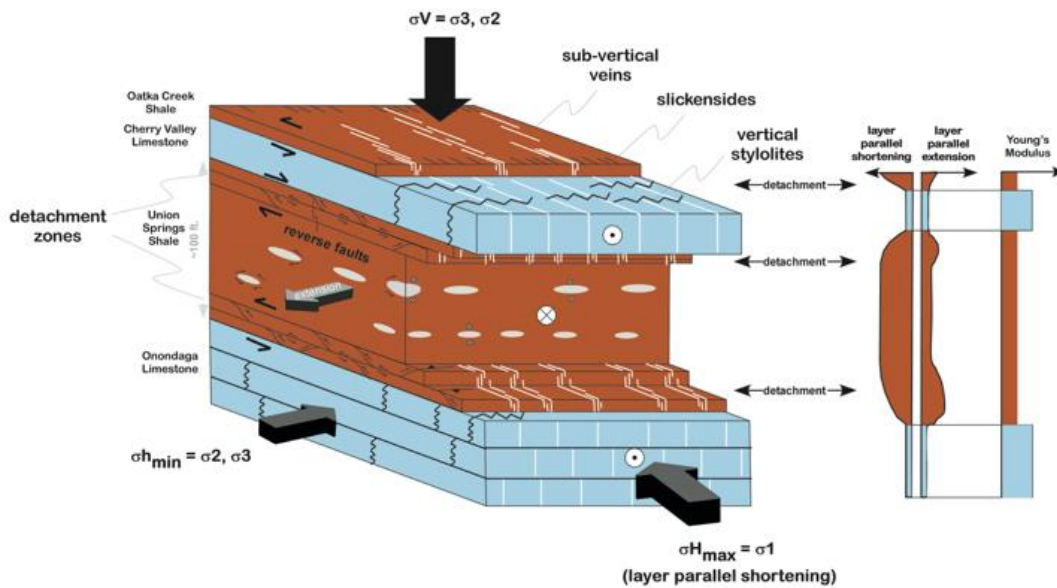


Figure 5.25: A kinematic model of the sub-seismic features of the Marcellus shale play in Wilkins et al. (2014). The model focuses on detachment faults near stiffer carbonate formations as the main drivers of forming joints and stylolite.

Wilkins' model is one of the mechanical approaches that attempts to explain sub-seismic features with tectonic loadings and structural deformation. The difference between Aydin and Wilkins is that Wilkins' model attempts to explain all the features being generated together in the geological time scale – they are not necessary instantaneous, but not in distinctively different geological times either. Figure 5.25 shows the kinematic model of Wilkins' model. This interpretation attempts to explain joint/fracture/vein sets by considering the deformation and accommodation of carbonate formations around Marcellus shale formations. This model disagrees with the other two on joint set J1. In this model, instead of J1, there are a series of sub-seismic reverse faults that can be understood as a counterpart to J1 in Engelder's and Aydin's models. The veins in Figure 5.25 are a counterpart of J2 by extending to the minimum stress orientation during tectonic loading. In this model, all the discontinuous features in the shale formations are only located close to adjacent carbonate formations. Likewise, the central part of the Marcellus shale in terms of depth does not have joints and veins. Joints and fractures in the Marcellus shale in this model only happen near the carbonate formations, where the shale experiences large displacements that cannot be resolved by

plastic and ductile deformation. The model is based on observations from a field with a relatively thick Marcellus shale formation.

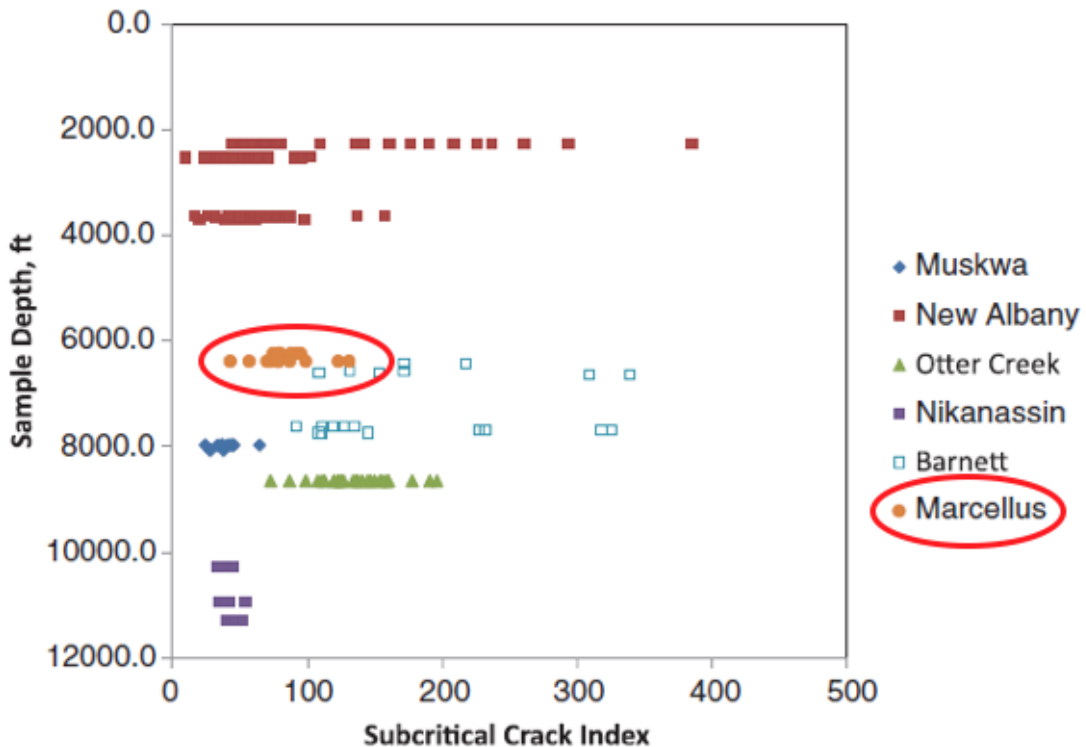


Figure 5.26: Subcritical crack index of U.S. onshore unconventional shale play (Gale et al., 2014).

Figure 5.26 shows the subcritical crack index (SCI) of unconventional shale plays in the U.S. (Gale et al., 2014). SCI is an exponent having mode I stress intensity as a base to compute crack propagation velocity (Holder et al., 2001). Since mode I stress intensity is the magnitude of the stress components in the near-tip field of crack tip when it propagate under linear elasticity, having a small SCI value means crack tips propagate even with smaller stress concentration applied. With a small SCI, propagation of crack tips of new or small cracks happens more often than the propagation of bigger crack tips. The SCI values of the Marcellus shale play are relatively small compared with other shale plays. The variance of SCI is also relatively small given the similar values. The consequence is more widespread cracks with better crack connectivity. The spatial distribution of crack flaws is more important with small SCI with contrast to the

case of high SCI, where the distribution of flaws are less impactful than the stress distributions on crack propagations. Since cleavages – vertical foliation from lateral compaction – are easy to break out, if a given field has also experienced LPS or developed cleavages, the field may have relatively small SCI and significant horizontal connectivity. Faint horizontal fabric and foliations from core sections in Figure 5.14 can also offer support for this scenario.

All three of these models are considering LPS (layer parallel shortening) as one of the most important drivers in generating sub-seismic features. However, because of different assumptions and interpretations, estimations based on different models can be quite different. For instance, under Wilkins' model, if the Marcellus formation is relatively thicker, we may not expect to have joints sets from the major portion of the target Marcellus formation. Under Aydin's model, the joint sets will be densely located near the higher curvature along the folds, because the kinematic model of fold parallel joints are syn-tectonic. However, under Engelder's model, the J1 joints are less sensitive to the curvature of geometry because they are created by pre-folding from hydrocarbon generation.

5.5.3 Effects of hydrocarbon generation

The above interpretations attempt to link tectonic loadings and the corresponding structural deformation to link joints, veins, and fractures. However, as Engelder's model assumes a weak correlation between structure and the J1 joint, some researchers argue that open-mode fractures in shale are not closely linked with structural aspect.

In this section, we will cover observations of the characteristics of open-mode fractures in shale made by different researchers. Gales et al. (2014) conducted a meta-analysis of fractures in shale and argued that the existence of an open-mode fracture in shale does not show a strong correlation with structural features such as folds and faults. Hydrocarbon generation is believed to be a potential driver of fractures in shale (Swarbick et al., 2002). High correlations among fracture abundance with TOC on shale support these arguments (Rodrigues et al., 2009). A basin-wide study on joints in the Appalachian basin showed that joints in shale are more systematic and vertical than

joints in sandstone (Nickelsen, 1986). In this study, the orientations of the joints in the shale do not change with the changes of the fold axis.

On top of different interpretations linking structural aspects with the abundance and orientations of joints sets in shale, these studies argue that correlations between obvious structural geometry (such as folds and faults) and joints in the shale are thin. We cannot be definitive on which interpretation is right. One possible explanation is the different viewpoints and focus of the researchers when conducting their respective studies. The studies in Section 5.5.2 were focused on kinematic models explaining fractures and joints in tectonic loadings. They happened to be joints and fractures in shale. Studies in this section focus more on shale and hydrocarbon maturations in shale. Open-mode fractures are one of the hydrocarbon expulsion vehicles, and if the maturation of hydrocarbon happens before major geometrical deformation, studies focusing on shale and hydrocarbon maturations in it would not find any meaningful correlations among joints and structural shapes of the subsurface. The former emphasizes “fracturing” in rocks while the latter emphasizes “shale” that has fractures.

5.5.4 Non-deformational factors affecting the accommodation style of shale: saturation and burial history

In a previous section, we showed a group of studies arguing that joints in shale are not following structural trends that other rocks, such as sandstone and carbonate, do. Those studies are arguing that shale accommodates deformational loading in a shale-like way – with ductile and plastic deformation. This conflicts with other studies that claim correlations among joint sets and structural deformations. We need some vehicles to reconcile these discrepancies.

Different behaviors of shale under different saturation conditions and different loading histories may provide some useful explanations (Valès et al., 2004; Nygård et al., 2006). Valès et al. (2004) conducted repeated mechanical failure tests on shale with different water saturations. When shale was fully saturated by water, the failure surfaces followed shale fabric, not the typical failure angles of sandstone cores. However, when

water saturation was reduced by including air-filled pores in it, failure surfaces were generated in angles typical of sandstone experiments. Using this finding, if a shale formation develops a set of joints from hydrocarbon generation that is in a liquid phase, the formation will still react as shale-like when deformation is applied. If a gas phase is produced from maturation, the formation becomes partially gas saturated and starts to behave like typical sandstone when deformation is applied.

Nygård and colleagues' (2006) experiments were conducted in saturated conditions but with different loading histories to test the hysteresis of shale failure. When shale cores are normally consolidated – meaning that the current stress is the maximum stress applied – shale cores behave ductilely. When the cores are overconsolidated – meaning that the cores have been pre-loaded and relaxed – they easily break down. If this finding can be generalized, when shale formations are monotonically buried deeper and deeper by newer sediments, any joint sets in the shale may have little correlation with structural deformation. However, if there was uplifting or erosion on overlaying formations that reduced overburden stress on the shale formations before structural deformation, joint sets in the shale may have a noticeable correlation with the structural geometry of folds and faults. Thus, burial history can be a critical factor in estimating a proper combination of structural deformation and rock accommodation.

5.6 The effect of interaction among different formations

One of the obvious geological events that the Marcellus shale play experienced was compressional tectonic loadings involving Appalachian orogeny. LPS (lateral parallel shortening) from the tectonic loading and rock accommodations to LPS are two of the main sources of geological uncertainty we defined from previous sections. If we recall Wilkins' model, the abundance of accommodation features in shale is denser near the adjacent stiffer carbonate formations (Wilkins et al., 2014). Developments of vertical cleavage are closely related with the deformation of adjacent stiffer layers (Nickelsen, 1986; Ferrill and Dunne, 1989). From the previous studies, we can infer that structural deformation of adjacent formations interfere with each other and affect rock accommodations.

Thus, we propose to expand our interest to the adjacent stiffer layers for a better evaluation of Marcellus shale formation. On top of the fact that the adjacent formations were deformed together with the Marcellus formation, there are a couple of reasons for this expansion. First, the thickness of the Marcellus shale formation in the given field is relatively too thin to be fully defined separately. It is inevitable to define shale formations from seismic data by defining adjacent carbonate or sandstone formations. Second, we anticipate that the field-specific problems – the water influx and strong connectivity along the ASF strike discussed in Section 5.4 – are closely linked with structural deformation and rock accommodation of the adjacent formations. In an unconventional reservoir, the underlying carbonate or sandstone, which are the main targets for conventional reservoirs, are normally ignored for flow simulations by only considering the dynamic modeling within the shale boundary (Osholake et al., 2012). If the Onondaga carbonate formation below the Marcellus shale has fractures and faults in the formation, wells on the overlaying Marcellus shale may have a huge influx of water. In this case, modeling flow simulations around the well bore on the shale formation becomes less meaningful if we consider the order of differences in the hydraulic conductivity of sandstone, or fractured limestone versus shale.

The third reason to expand our focus is the fact that adjacent non-shale formations are typical targets of “conventional” reservoirs while a shale gas play is an “unconventional” reservoir. Researchers and practitioners in industry have more experience and expertise in defining and understanding non-shale formation. We want to use geological knowledge and data from adjacent conventional formations to investigate the unconventional Marcellus formation. For instance, giving more attention to the underlying Onondaga carbonate may give useful inferences on possible areas of caution regarding water influx issues. To do that, we need geological models to link geological processes in multiple adjacent formations.

5.6.1 Structural deformation and rock accommodation for adjacent formations: the necessity of expanding the boundary of investigation

Though there are many uncertainties in details on the timing and amount of, it is certain that formations near the Marcellus shale experienced a series of compressional tectonic loadings over geological time. The Appalachian Mountains and the fold and fault belts that we can see from the surface are evidence of compressional tectonic loadings. In terms of applied lateral shortening, some regions and formations accommodate shortening via structural deformation. All other formations that have gentle structures in a macroscopic sense must have some sub-scale deformation and accommodation to absorb the basin-level shortening. If we assume the localized thickening in Figure 5.16 indicates duplexes, it is an intriguingly obvious question to ask what would happened to un-duplexed adjacent formations, or structurally gentle areas. If one of the adjacent stiffer carbonate formations was duplexed, we want to have explanations of deformations on the other stiff layers below and above the duplexed one. Among those formations, there are softer shale formations. We also want to know how the shale formation accommodated the compressional loading with neighboring stiffer formations.

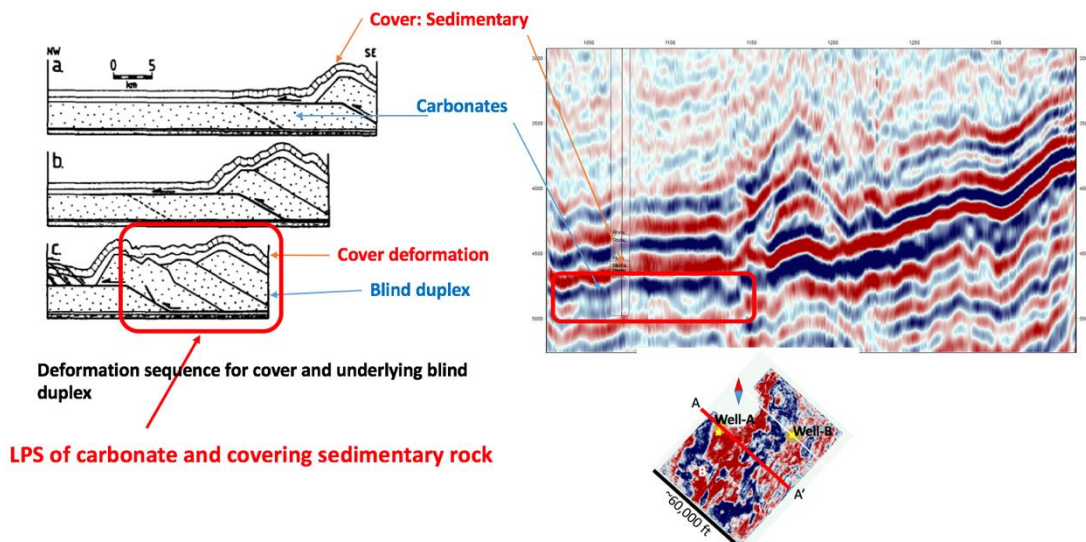


Figure 5.27: Blind duplex and cover deformation observed in an Ordovician formation in the Appalachian Basin (Ferrill and Dunne, 1989), with a seismic section of cross line along Well-A of the given data set. The red rectangular box in the seismic vertical section corresponds to the Marcellus shale and Onondaga carbonate formations.

For the stiffer formations with apparent gentle structure but exhibiting complex structural deformation in adjacent stiff formations, a “blind duplex” model can give a plausible explanation (Ferrill and Dunne, 1989). This is a proven concept in West Virginia from field observations of Ordovician formations, including outcrops. It explains that by having a series of fault-bend folds – a duplex – on lateral stacking, a stiff carbonate or sandstone formation can go through LPS while remaining perfectly horizontal and flat in a macroscopic sense. It also gives an explanation for the overlying shale formation. Ferrill and Dunne also observe that the cover deformation of the overlying shale formation is accommodated by developing vertical cleavages. Figure 5.27 shows a conceptual model of Ferrill and Dunne’s blind duplex with cover deformation, with a vertical seismic section of the crossline along Well-A where it was considered structurally gentle. If we assume a stiff formation above Marcellus shale is duplexed, it is possible to have a blind duplex on the Onondaga carbonate formation with cover deformation on the Marcellus by forming vertical cleavages.

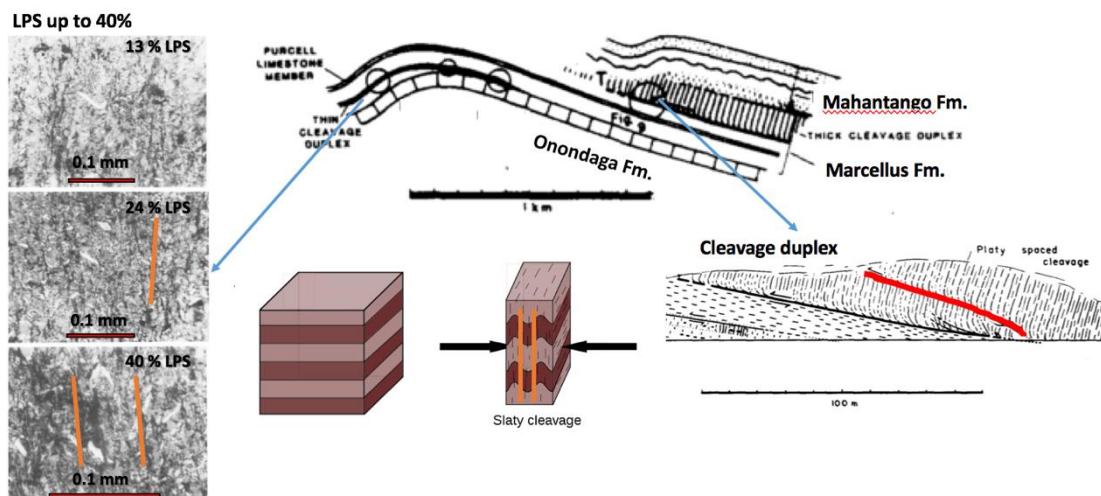


Figure 5.28: Cleavage duplexes accommodate up to 40% of LPS by forming vertical cleavage and inter-layer cleavage (figure modified from Nickelsen, 1986). Vertical lines with orange colors represent vertical cleavage development during LPS. The red tilted line is a reverse fault component of interlayer cleavage.

For the LPS of the Marcellus shale formation, we have cleavage duplex as another type of “blind” duplex that is observed in outcrops of Marcellus shale

(Nickelsen, 1986; Ferrill and Dunne, 1989). Figure 5.28 shows the cleavage duplex with an image of the outcrop and a schematic cartoon (Nickelsen, 1986). On top of LPS accommodation by forming vertical cleavages, Nickelsen observed a series of reverse faults forming an interlayer duplex, which made the regional thickness of the Marcellus shale evenly thicker. The beauty of Nickelsen's model is that it allows an explanation that can resolve discrepancies among the interpretations of different researchers. For instance, Aydin and Engelder disagreed on the timing of J1 and J3: Aydin interpreted J3 as a splay of J1 while Engelder believed J3 is a consequence of re-activation in a different geological time (Engelder et al., 2009; Aydin, 2014). Both agree that cleavage development was a critical vehicle of LPS accommodation. In Nickelsen's model, J1 can be a joint set opened from a vertical cleavage and J3 can be mapped to a series of reverse faults that consists of a cleavage duplex. Figure 5.29 shows schematic models of the developments of vertical cleavage and a cleavage duplex (Nickelsen, 1986).

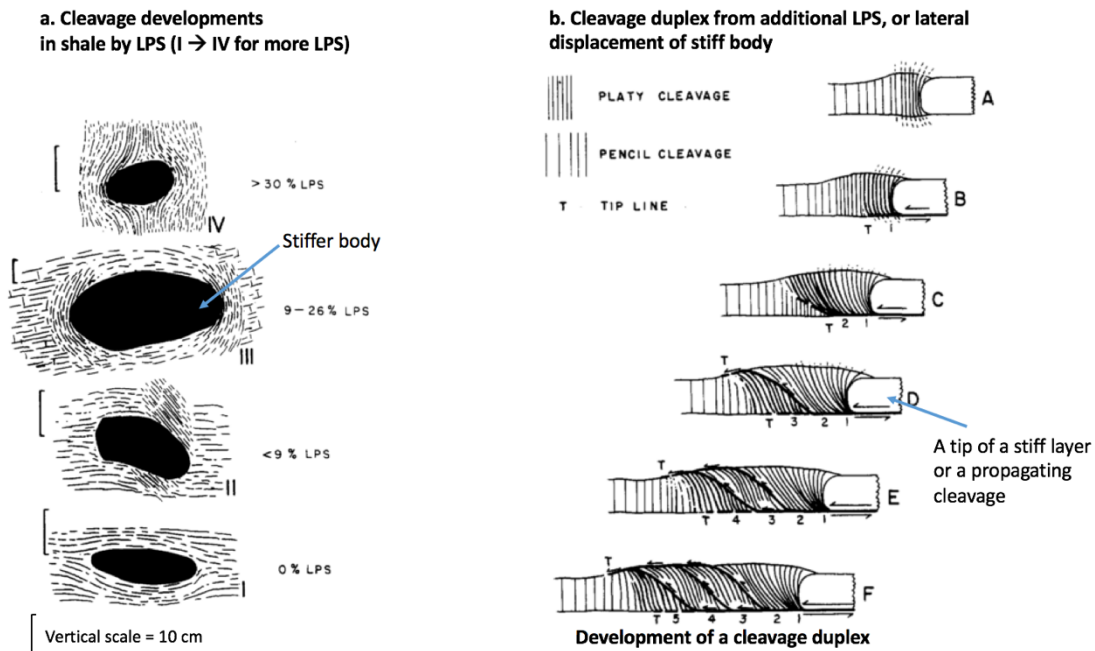


Figure 5.29: Sketches of cleavage and cleavage duplex development under LPS (Nickelsen, 1986). Left (a): vertical cleavage development from LPS. Horizontal foliation prior to LPS is masked out, as cleavage is development during LPS. Right (b): Excessive LPS on top of pre-developed cleavage deformation ignites to develop thrusting by forming an interlayer blind duplex.

Nickelsen’s model does not reject any of Aydin’s and Engelder’s models since not all vertically cleavaged shale formations have duplexes in them. It also can reconcile the observation of Wilkins and his colleagues (2014), who did not see vertical joints but rather many high angled fractures or interlayered reverse faults, by using reverse fault in the cleavage duplexes in Figure 5.28. Since not all cleavage surfaces become joints or fractures but duplexed shale surely contains a series of reverse faults, Nickelsen’s model can also explain the high angle fracture, or faults only focused near stiff layers. The existence of a cleavage duplex system in a Marcellus shale formation is a good example of the scale dependency of geological description mentioned in Chapter 2. The same category of thrust systems – duplex – can make noticeable structural geometry from seismic resolution, and it can also process smaller scales to accommodate deformational loadings.

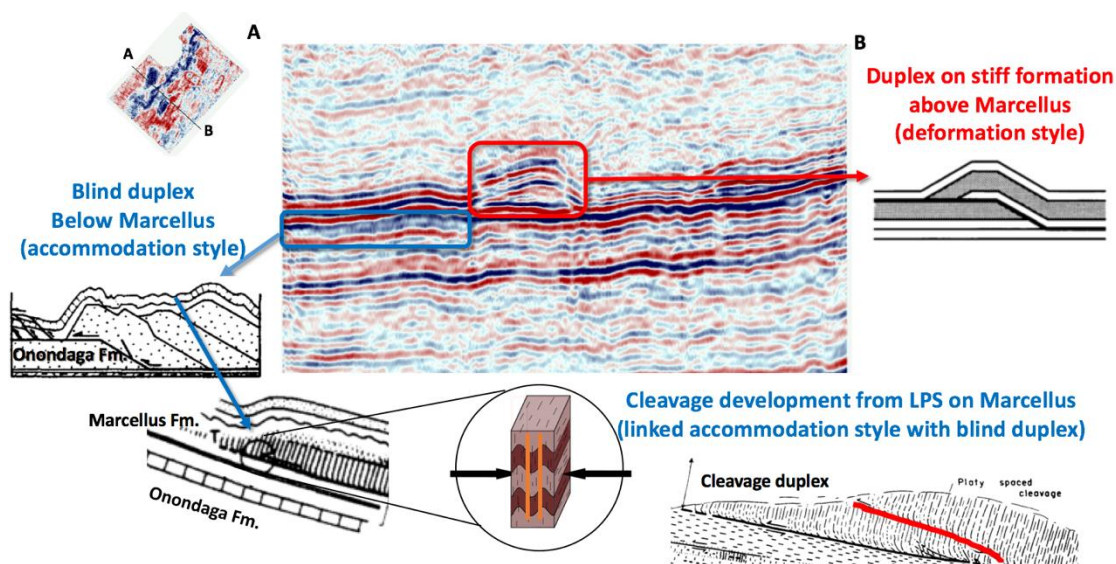


Figure 5.30: A combination of structural deformations and rock accommodations considering adjacent formations to Marcellus shale. In these specific combinations, a duplex of stiff formation above the Marcellus formation in the central part absorbs LPS. The Onondaga formation accommodates LPS by a blind duplex. Marcellus shale on top of a blind duplexed Onondaga accommodates LPS by forming vertical cleavage and a cleavage duplex.

Figure 5.30 shows a combination of duplexes on the formation above the Marcellus, a blind duplex on the Marcellus, and vertical cleavage and a cleavage duplex

in the Marcellus formation. This combination can explain both what we observed from other researchers on joint set characteristics and field-specific observations: high horizontal connectivity in a structurally gentle area. It is noteworthy that we are not attempting to explain everything with one model, but rather demonstrate possible benefits of expanding our focus to adjacent formations to supplement the multiple scenario approach to link structural deformation and rock accommodation.

5.6.2 Contrasting flexural rigidity among adjacent stiff formations

A duplex system, as a subset of a thrust system, exists when a layer parallel slip is promoted by a vertical contrast of layered formations. If the condition does not promote a layer parallel slip, either by having a more massive and mixed deposition with lack of horizontal layering, or by a lighter overburden when tectonic loading is applied, the earth may deform by imbricate fan systems rather than duplex or fault-bend folds (Boyer and Elliott, 1982; Ferrill and Dunne, 1989; Thomas, 2001).

Flexural rigidity, resistance offered by formation when bending is applied, can be a useful way to estimate the relative tendency of bending when stiff layers are exposed to deformation (Pollard and Johnson, 1973). In Equation (3-3)), E is Young's modulus, h is the thickness of the layer, and μ is Poisson's ratio of the formation rock. On top of Young's modulus that can be understood as the stiffness index, the thickness of the formation affects the overall rigidity in cubic law.

$$R = \frac{Eh^3}{12(1 - \nu^2)} \quad (5-1)$$

Figure 5.31 is the well log along Well-A, with Young's modulus and the interpreted lithofacies marked, and part of a vertical section of seismic amplitude along the cross-line with Well-A. The Onondaga formation is at least twice as stiff as the Tully limestone formation, and thicker than the Tully formation. On top of that, Tully limestone is bounded by softer overlaying Rhinestreet and underlying Mahantango and Marcellus shale formations. This flexural rigidity contrast – stiffness and layer thickness

– can be used as input parameters for structural geologists to evaluate candidate scenarios of structural deformation across Marcellus and adjacent formations.

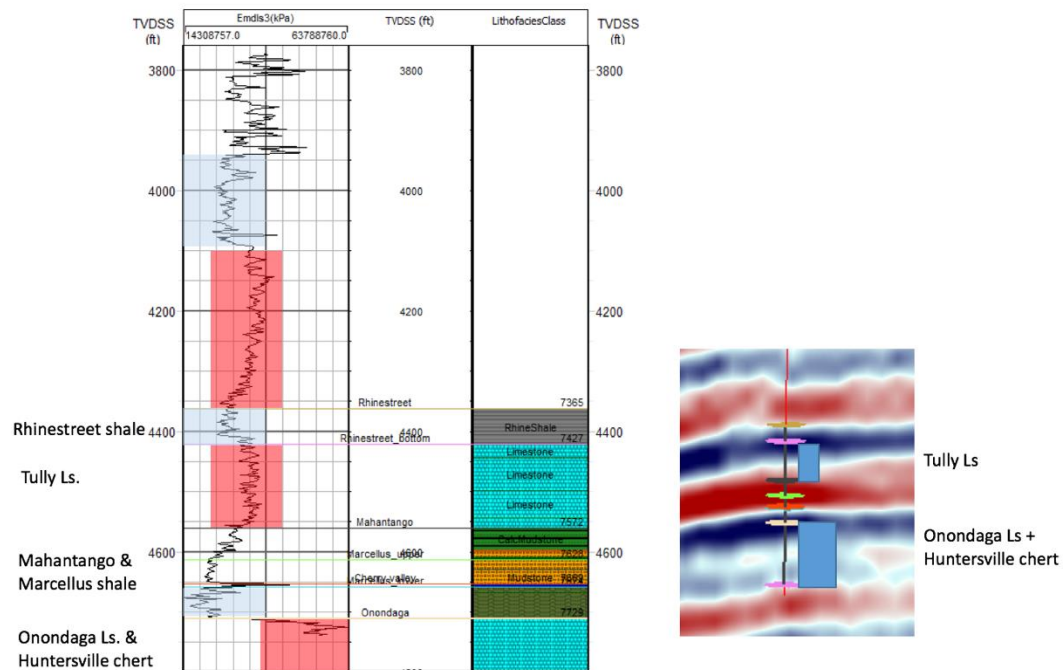


Figure 5.31: Young's modulus along Well-A. Red boxes are carbonate formations and blue boxes are shale formations. The figure on the right side shows the relative thickness and Young's modulus of the Onondaga and Tully carbonate formations.

5.6.3 Differences between interactions among adjacent formations: joints from shale vs. joints from non-shale formations

Another type of interaction that we can consider is the initiation formation of joint generation in the case of open-mode joints. Spencer's study, based on the Rocky Mountains, showed that joints in sandstone formations are usually contained in the sandstone formations, while joints in shale formations always indicate joints in adjacent stiffer formations (Spencer, 1987). Spencer used contrasts of the fracture gradients to explain these observations. Though sandstone is stiffer than shale with a higher elastic modulus, the tensile strength of shale is much stronger than sandstone. Thus, hydraulic fractures in sandstone remained within the sandstone formation, while hydraulic formation in shale also creates fractures in adjacent sandstone formations.

Spencer's model has two practical usages for explaining observations in a Marcellus shale play, in both field-specific and basin-wide terms. First, it gives very straightforward explanations of engineering difficulties found in the given field for both the Well-A and Well-B regions. As we discussed, the Well-A region had too high horizontal connectivity when hydraulic fracturing was conducted, and the Well-B region had an unexpectedly large amount of water influx during well tests. Since the given field is located near the structural front of the Appalachian Ridge, the shale formations are relatively thinner than in the northeastern part of the basin. Hydraulic fracturing in the Marcellus formation would definitely initiate fractures in adjacent stiffer formations. Relatively thin shale formations surrounded by fractured carbonate formations can have relatively high horizontal connectivity and water influx from adjacent fractured formations.

Second, Spencer's model allows us to anticipate vertical connectivity between the Marcellus and overlaying Mahantango shale formations. Vertical inter-formation connectivity is a critical question to estimate per-well productivity. If open-mode fractures from hydrocarbon maturations of Marcellus shale formation were confined within the formation, the thickness of the pay zone will be limited in the Marcellus shale only. However, if hydrocarbon expulsion created vertical fractures up to the Mahantango shale formation, the region becomes more profitable by having a thicker pay zone and more efficient hydraulic fracturing, since both of the shale formations have been fractured.

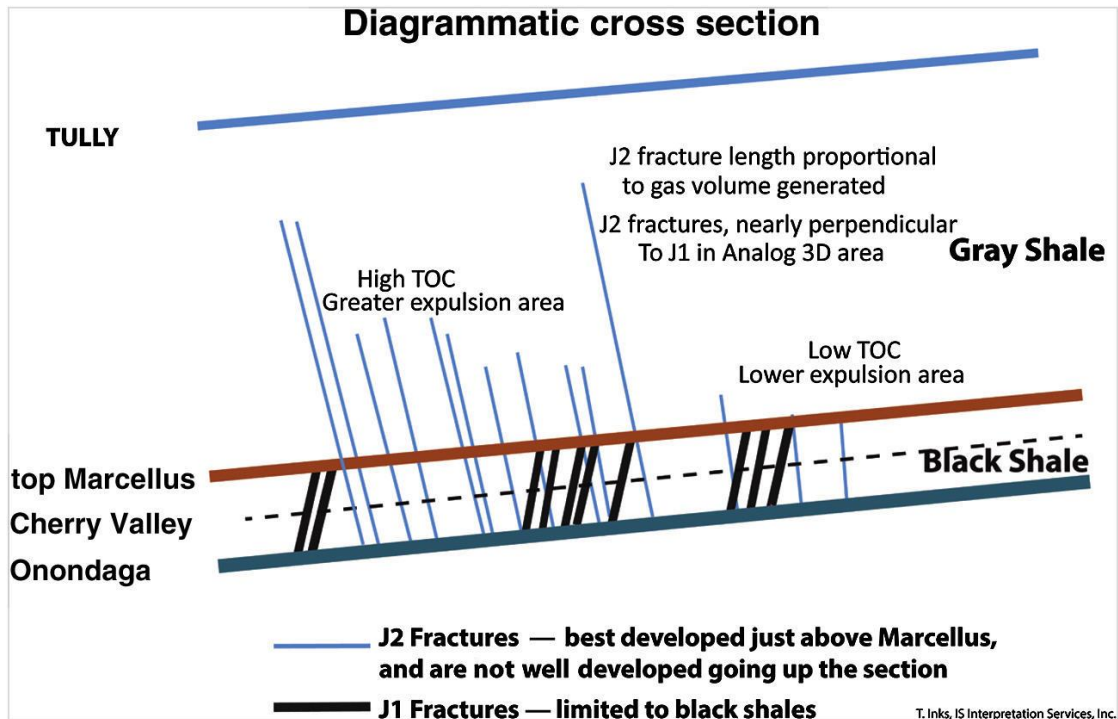


Figure 5.32: Vertical fracture connectivity to overlaying shale formations (Ink et al., 2015).

Figure 5.32 is a schematic diagram of the vertical connectivity of natural fracture sets – J1 and J2 (Inks et al., 2015). In this figure, the J1 fracture sets remain in the Marcellus shale formations while the J2 fractures run up into the overlaying Mahantango shale formation. This interpretation assumes that the J2 fractures were generated when the Marcellus shale expelled gas, while J1 was formed earlier, prior to the maximum maturation, by generating liquid phase hydrocarbon. If we follow Spencer’s (1987) and Inks and colleagues’ (2015) interpretations, defining the location of thicker and organically richer black shale lithofacies out of all the other variations of shale lithofacies would be the most important factor, to guarantee both a larger gas reserve amount and less-expensive production costs from vertical connectivity from the J2 fracture.

5.7 Applying the proposed framework to the Marcellus data

In the previous sections, we investigated basin-wide and field-wide sources of geological uncertainties and their impacts on the field evaluation. In the present chapter,

we test the proposed framework. First, we define a discrete number of structural deformation scenarios and rock accommodation scenarios. We then apply the proposed workflow in a 2.5D vertical region along the seismic crossline having well-A within it. Once the overall best structure model is selected from the comparison generated by the 2.5D model, we will create 3D models having both of Well-A and Well-B using the best structural deformation scenario.

5.7.1 Facies and rock property interpretation along well-A

Before populating the properties following each deformational scenario, we must extract the petrophysical properties and their relations to the seismic properties. In Well-A, we have core analysis data, well log data, and a velocity profile along the well from the VSP survey. Since the main target formations are shale and contain a large portion of water in the shale minerals and hydrocarbon contents, porosity derived from the neutron porosity log tends to be high compared to the porosity measured in core analysis. While porosity measurement and mineral density from cores are well aligned with porosity ranges and mineral density range from the Marcellus core analysis (around 5-8 percent), neutron porosity is detected up to 40 percent with excessively low bulk density values. Washout from the drilling activities, drilling induced fractures, and poor attachments of tools on the wellbore can be the reason. Thus, the neutron porosity and density from the well log cannot be taken as hard data for petrophysical modeling. We derive porosity and density from the P-velocity profile along the well, using a rock physics model. The process is as follows:

- Define lithofacies along the well
- Develop Density-Vp relations for each facies
- Take the mineral density of each facies from core analysis
- Derive fluid properties for sub-surface conditions
- Derive porosity along the well

First, we defined the lithofacies along the Well-A by comparing interpretations from core analysis, mud log reports, and well logging to published typical log-facies relations (Zagorski et al., 2012; Wang and Carr, 2013; Carter et al., 2011). The resolution of the property modeling grid is approximately 100ft by 100ft horizontally and 3ft vertically, and the right column of Figure 5.33 shows the up-scaled lithofacies. The target formations are relatively thin (tens of feet) and available core analysis is based on the formations themselves instead of each lithofacies. Table 4-1 shows the comingled lithofacies of each formation.

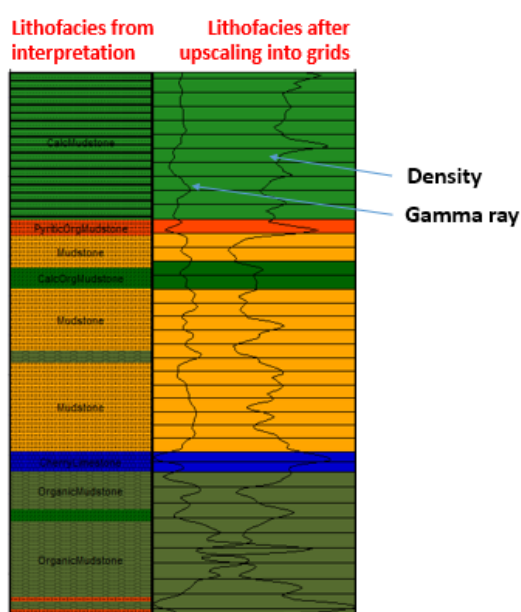


Figure 5.33: Defined lithofacies along the well from well log interpretation, core analysis, and mud log interpretation (left), up-scaled lithofacies in property grids (right).

Table 5-1: Lithofacies and average properties of each formation (CMS – calcareous mudstone, POM – pyritic organic mudstone, MS – mudstone, COM – calcareous organic mudstone).

	Lithofacies	f_coeff.	d_coeff.	ρ_{bulk}	ρ_{fluid}	K_{fluid}
				g/cc		GPa
Rhinestreet	Shale	0.288	1.8385	2.67	1.0084	2.6984
Tully	Limestone	0.3740	1.5828	2.72	1.0084	2.6948
Mahantango	CMS/POM/M S/COM	0.2820	1.8000	2.64	0.5939	0.1240
Upper Marcellus	MS	0.2680	1.8450	2.58	0.6278	0.1345

Cherry Valley	Limestone	0.2800	1.7500	2.64	0.6278	0.1345
Lower Marcellus	Organic mudstone	0.2620	1.8290	2.53	0.6870	0.1578
Onondaga	Limestone	0.2300	2.6892	2.62	0.6532	0.1436

Second, we derived the empirical density-velocity relations from each formation. Since the main formations are shale, we use Gardner’s power law (Mavko et al., 2003) relation in Equation (4-9).

$$\rho = d \cdot V_p^f \quad (5-2)$$

By comparing the P-wave velocity along the well to the density log, we derive Gardner’s d and f coefficients for each layer so that the mean bulk density from the empirical relations fall into the Marcellus core analysis results. Coefficients for each formation are in Table 4-1 along with the mean bulk density of each formation.

Next, we derive the fluid properties for each formation. Data on fluid content and the saturation of each fluid are available from the core analysis. We use Batzle-Wang equations (Wang, 2001) to calculate the density and bulk modulus of mixed fluid in each formation (Table 4-1). Finally, we get a porosity profile along the well that reflects core data and the velocity profile.

For property grid cells without fractures, we use the average mineral and fluid density in each formation to calculate cell by cell bulk densities. After adding random errors, Gardner’s equations with different derived coefficients are used to calculate P-wave velocity. After adding random errors on P-wave velocity, S-wave velocity was calculated by using the following empirical relations from Marcellus core analysis data according to Equation (5-3):

$$V_{S_{transit\ time}} = 1.511 \times V_{P_{transit\ time}} + 16.56, \text{ } \mu\text{Sec}/\text{ft} \quad (5-3)$$

Note that the above procedure calculates isotropic and un-fractured bulk density and P-wave velocity. In the conventional approach, we either use bulk density or P-wave velocity with adding artificial errors to reproduce natural variability (Castro et al., 2005; Lee and Mukerji, 2012). Since we assume several different inclusion sets that

comprise rock anisotropy, relations between P-wave velocity and bulk density of isotropic rocks for each formation form the starting point for reconstructing the rock properties along the well under different scenarios using methodologies proposed in Chapter 4.

5.7.2 Variogram modeling for property generation

Since only Well-A and Well-B are available in the given field, we performed vertical variogram analysis using the well log and horizontal variogram analysis using the amplitude of the seismic data. Though we populate properties on each formation, not on each lithofacies, we conducted facies modeling by using variogram ranges from Wang and Carr (Wang and Carr, 2013). Table 5-2 shows the variogram ranges of lithofacies and properties.

Table 5-2: Variogram ranges for lithofacies and properties

	Max range	Medium	Vertical	Main direction
Lithofacies	300,000 ft	15,000 ft	10 ft	NE-SW
Properties	18,000 ft	9000 ft	10 ft	NE-SW

Figure 5.34 shows the results of lithofacies modeling (left) and color-coded boundary of each formations. As Figure 5.34 demonstrates, the longer range compared to the size of the modeling boundary renders changes in the lithofacies not significant in the modeling area. The longest horizontal length of the field is about 80,000 feet, or approximately one quarter of the maximum range from Wang and Carr’s study. Additionally, the variability of the lithofacies within each formation reflects minor differences such as organic mudstone versus pyritic organic mudstone; these become less meaningful given the high degree of uncertainty in the scale of the given field for the lithofacies. Thus, we model lithofacies by each formation such as Upper Marcellus shale and Lower Marcellus shale, not by organic mudstone versus carboniferous organic mudstone.

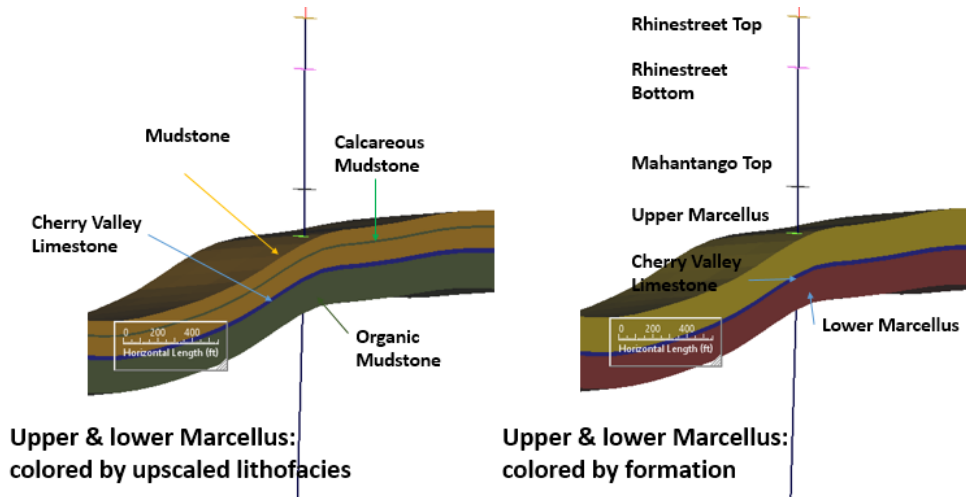


Figure 5.34: Modeling grids color coded by populated lithofacies (left) and formation (right). Only the Marcellus formations are shown.

5.7.3 Modeling alternative structural models with different structural deformation modes

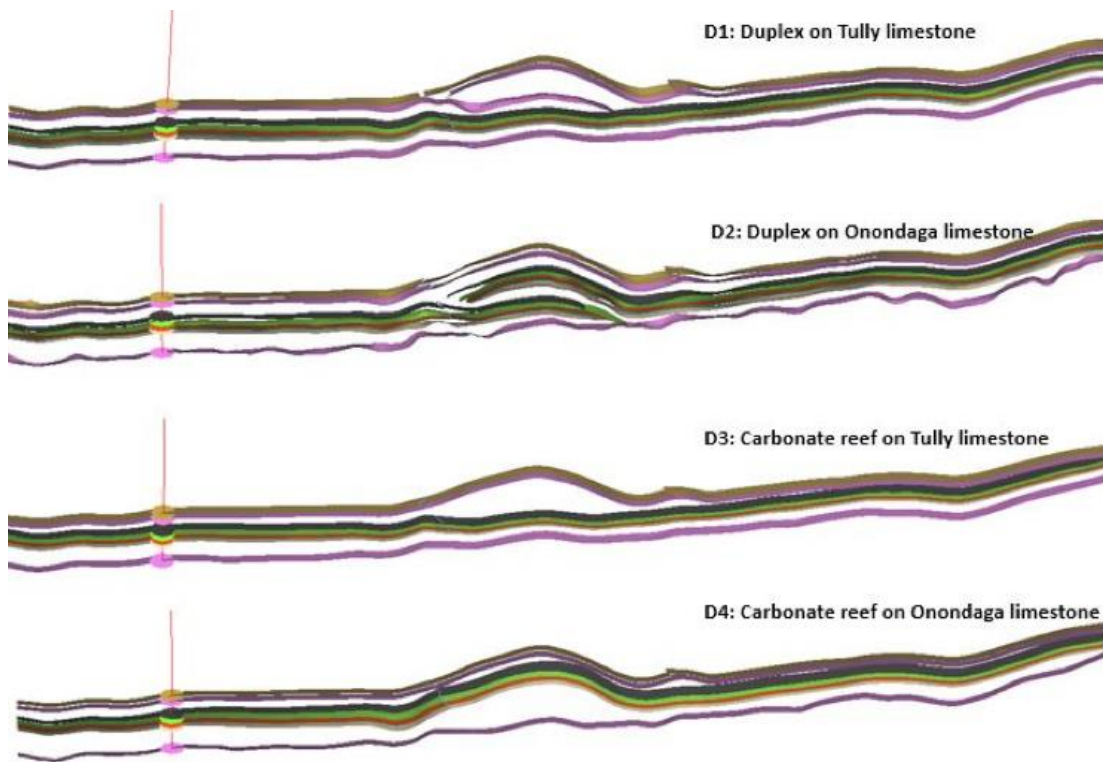


Figure 5.35: Structural models of four different scenarios on modes of structural deformation.

Based on the observations from seismic data and reviews on literatures from Section 5.5 and Section 5.6, we defined four different modes of structural deformations from D1 to D4. The structural model of D1 has a duplex of Tully limestone on stiffer layers above the Marcellus formation. For D2, Onondaga limestone is duplexed in a structural model. The structural model of D3 has locally thickened horizons in the center of the section to model localized reef structure, while the model of D4 has a localized thickened section on the Onondaga formation. Structural models are generated using the Paradigm SKUA® platform, as can be seen from Figure 5.35. Petrophysical properties inside each formation are populated by following each accommodation style.

5.7.4 Defining rock accommodation styles

Based on field specific observations and geological interpretations of different researchers in section 5.5 and 5.6, we assume seven different accommodation scenarios with two possible assumptions on how to model background anisotropy in shale formations. Thus, we have a total of 14 different combinations of accommodation modes. For simple notation, “A1a” corresponds to accommodation mode one with modeling background shale anisotropy. “A2i” corresponds to accommodation mode two with modeling shale as an isotropic medium.

The conventional approach makes no explicit considerations of structural deformation and rock accommodation in property modeling process; it corresponds with “A1.” In this case, well interpretation along Well-A in section 5.7.1 is directly used for reservoir modeling and all formations are modeled without the existence of any crack or fracture. Mode “A2” and Mode “A3” are ductile accommodation and shear fractures following the accommodation amount and fracture orientation assigned from dilatation and Eigen strains from deformation analysis. From A1 to A3 exactly correspond to the scenario used for the synthetic example in Chapter 2.

Mode “A4” follows “Aydin’s” interpretation covered in Section 5.4 (Aydin, 2014). Three different joint sets, J1, J2, and J3, are all assigned from geometrical analysis. Mean curvature is used to indicate abundance of joints, while geometrical dip

and azimuth guide orientations of joint sets. Under “Aydin’s” mode, all joint sets are modeled only in main shale formations – Mahantango, Upper Marcellus, and Lower Marcellus.

Mode “A5” is following “Engelder’s” interpretation in Section 5.4. The difference between “A4” and “A5” is the abundance and orientation of the “J1” joint set. In Engelder’s case, the orientation of J1 joints do not follow current geometry. Instead, it strikes perpendicular with the paleo-tectonic loading orientation, NW-SE. The abundance is guided by the LPS indicator which is a normalized indication of the relative amount of lateral parallel shortening by multiplying compressional dilation from restoration strain and normalized thickness variation of Onondaga formation by following the assumption of Nickelsen of blind duplex (Nickelsen, 1986). Furthermore, it also considers the existence and abundance of cracks or fractures in the main shale formations. However, the previous four modes differ precisely in how they consider deformation in adjacent formations, by distinguishing variations in thickness in Onondaga formation resulting from the deformation process.

The interpretation of “Wilkin’s” in Section 5.4 is assigned into Mode “A6”. Onondaga formation is not only used as a LPS indication, but also a formation having nearly horizontal fractures representing series of sub-seismic reverse faults originating from the LPS. In this mode, orientations of joint sets are identical with “A3” – Aydin’s – while the abundance of the joint set corresponding to J1 is guided by the distance from the Onondaga formation. If the formation is close to the Onondaga, the crack abundance is larger.

The “A7” mode of accommodation is a new interpretation proposed by combining ideas of A5 and A6 and using Nickelsen’s model and Ferrill and Dunne’s model to link the LPS of adjacent formations (Nickelsen, 1986; Ferrill and Dunne, 1989); it combines blind duplex on the stiff layer and cover deformation on the soft formation by developing vertical cleavage. The relationship between adjacent horizons was depicted in Figure 5.30. We call it as “NFD” by following the first characters of the three authors.

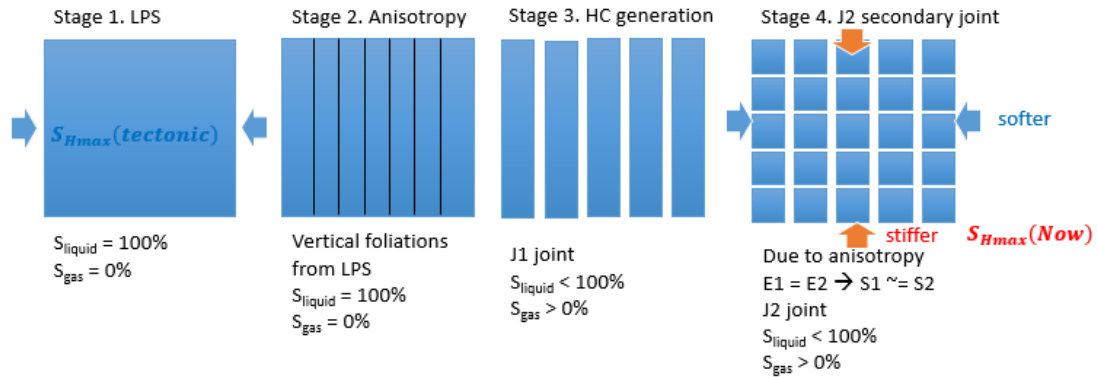


Figure 5.36: Vertical cleavage development during the LPS resulting in both a perpendicular and stiffer orientation. The opening of vertical cleavage resulting from the generation of hydrocarbons made the rock stiffer. It provides a coherent explanation on the discrepancy between the orientation of current maximum stress and paleo maximum compressional stress.

Figure 5.36 depicts how vertical cleavage and J1 joints accommodated the LPS in mode “A7”. The abundance of J1 joints are guided by the LPS of the Onondaga formation. Thus, it shares the same orientation and abundance with “A4” – “Engelder’s” mode for J1 joint sets. It differs from “A4” in the explicit modeling of fractures in the Onondaga formation. “A7” can be understood as a hybrid of “A4” and “A6” using Nickelsen’s idea of blind duplex with cover deformation (Nickelsen, 1986).

These 14 different combinations – seven modes with two assumptions on background anisotropy of shale – will be combined with the four different structural interpretations covered in Section 5.7.3. In each of the 56 combinations, the existence of space and abundances of crack/joint/fracture sets are modeled by following the different assumptions of each combination.

5.7.5 Modeling background shale anisotropy

In the present section, we populate the background anisotropy of Marcellus shale under VTI symmetry assumptions. By applying REIM (Reconstruction of Equivalent Isotropic Medium) along Well-A, we can extract equivalent solid isotropic medium by having equivalent bulk modulus and equivalent shear modulus, K_{eq} and G_{eq} respectively, and the aspect ratio of crack-like pores discussed in Chapter 4. When the axis of

symmetry is tilted, we can easily compute stiffness tensors using Bond's transformation. Although constructing the anisotropic stiffness tensors of Marcellus shale by itself is not our main goal, the anisotropic tensors reveal the background anisotropy of rock and divide it into equivalent isotropic solid phases and crack-like pores. This process closely and acceptably approximates the stiffness anisotropy when the crack-like pores are added back to the isotropic solid phase. Having the isotropic background media allows us to construct and compute the anisotropy of the elastic responses of shale having multiple sets of inclusions such as joints, fractures, or veins.

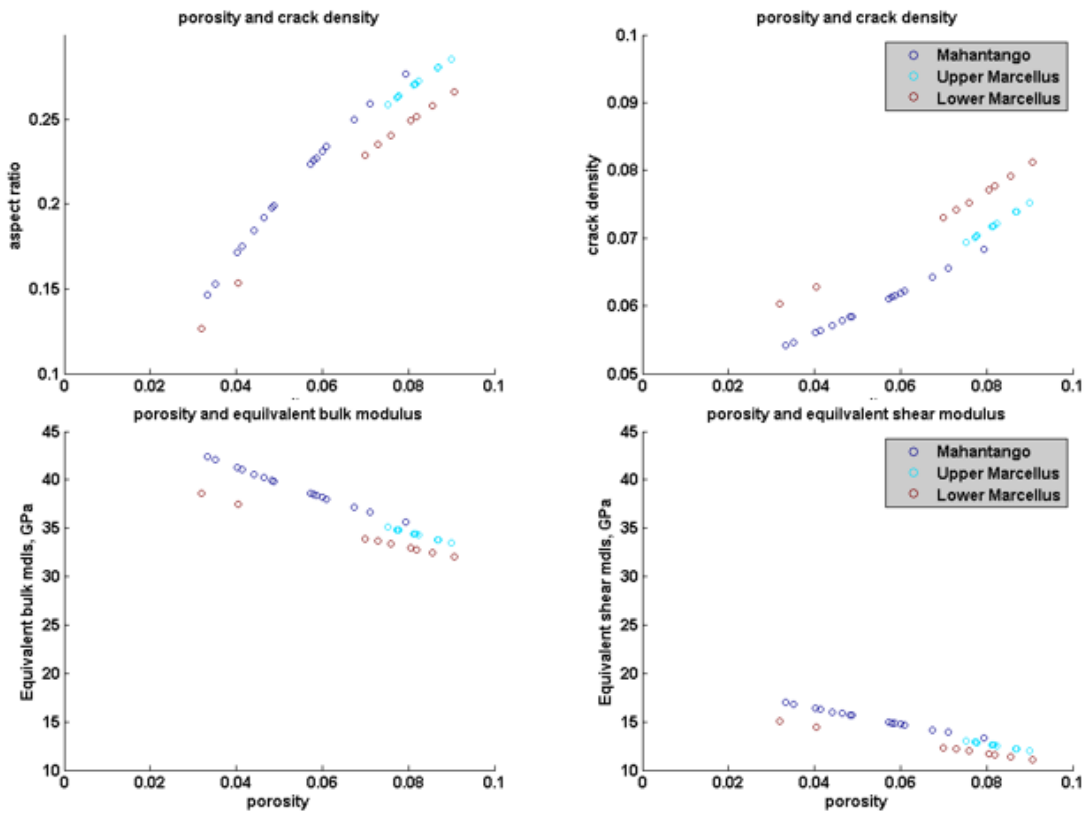


Figure 5.37: Relations among equivalent bulk and shear modulus, and the aspect ratio, crack density to porosity of crack-like pores color-coded by formations.

Figure 5.37 shows the relationship between porosity and aspect ratio of crack-like pores and elastic moduli of equivalent isotropic solid phase. Each color-coded formation follows the same pattern of having a higher aspect ratio and softer equivalent

isotropic media. Thus, less dense rock with slower seismic velocity will be modeled to have a higher level of anisotropy. When the pores are added back into the isotropic solid media with aspect ratio, the resultant stiffness tensors reproduce both the expected vertical velocity and the desired amount of stiffness anisotropy (Figure 5.38).

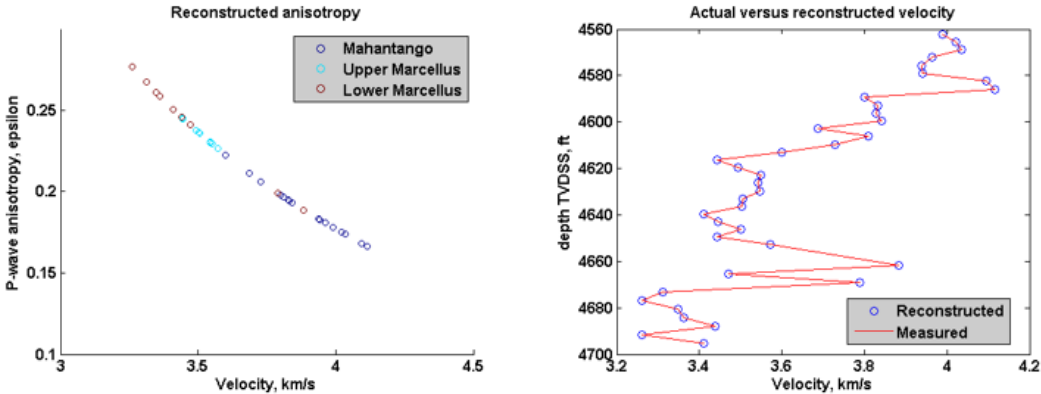


Figure 5.38: Reproduction of velocity and P-wave anisotropy (Thomsen’s epsilon). Left figure shows calculated P-wave anisotropy by combining crack-like pores with the equivalent isotropic solid phase using Hudson’s model and Cheng’s second order correction terms. The reconstructed effective medium exactly reproduces the measured velocity (right figure) and stiffness anisotropy.

The trend curves of both porosity to the aspect ratio of crack-like pores and porosity to elastic moduli for each formation can be used to model background anisotropy on rocks in the regions away from the well locations. When fitted into 2nd order polynomials, the coefficients for each formation are contained in Table 5-3. When a porosity value is given for a specific formation, we can retrieve the bulk and shear modulus of isotropic solid phase and the aspect ratio of pores. This approach makes it easier to populate the background elastic properties under TI (transversely isotropic) assumption.

Table 5-3: coefficient of 2nd order polynomial linking porosity to aspect ratio, crack-like pores, and the elastic moduli of equivalent isotropic media. Three numbers correspond to a,b, and c of $ax^2 + bx + c$.

	Mahantango	Upper Marcellus	Lower Marcellus
Porosity to aspect ratio	-17.98, 4.84, 0.006	-14.23, 4.17, 0.026	-14.86, 4.19, 0.0079

Porosity to bulk modulus	620.46, -217.7, 48.99	657.80, -217.91, 47.76	592.33, -184.12, 43.93
Porosity to shear modulus	189.70, -100.99, 20.13	175.11, -98.83, 19.48	164.09, -89.06, 17.78

The relationship indicated here assumes that the shale with higher porosity has higher anisotropy. Vernik and Liu explained this trend by arguing that micro-cracks increased when pore pressure induced greater porosity. (Vernik and Liu, 1997). However, if the porosity of shale kept increasing from pore pressure (e.g. from hydrocarbon generation) the higher porosity and lower density may perhaps lead lower aspect ratio of crack-like pores and a lower level of stiffness anisotropy (Vernik and Nur, 1992; Bandyopadhyay, 2009). Recalling from Figure 5.14, core sections from Mahantango, which is denser than Marcellus, has more visible horizontal foliation while the core section from lower Marcellus has faint lamination than Mahantango. Thus, some geological conditions may produce exactly the opposite relationship between porosity, or bulk density, and the aspect ratio of crack-like pores.

One other possible way of constructing relations among petrophysical parameters is to change the portion of crack-like pores out of total porosity while fixing aspect ratio of crack-like pores into a single number. Neither approach produces significantly different results. A smaller aspect ratio alongside a higher crack porosity increases the stiffness anisotropy by making the crack density value larger. Additionally, the reconstruction of crack-like pores and the equivalent isotropic solid phase can be modeled to acquire the isotropic medium. The goal of this analysis is not to produce a realistic shale model, but to capture how it develops anisotropy with different geological conditions and processes.

5.7.6 Reconstruction of equivalent isotropic medium along the well under different rock accommodation scenario

In Section 5.7.4, we defined seven different types of accommodation scenario. Together with the assumptions on background anisotropy of shale, we have 14 different

accommodation styles. If we assume the existence of certain geological features along the well region, we need to adjust the petrophysical properties accordingly. For instance, if we anticipate the existence of vertical joints filled with light fluid near the wellbore, a stiffer and denser un-fractured bulk material is necessary to preserve bulk density and effective stiffness

One may challenge this idea of having different sets of shear and bulk moduli by noting that we have some of the most reliable data along the wells. Yet interpreting this data involves many geological assumptions themselves, which may lead to widely disparate and conflicting interpretations. Recall that porosity from the Neutron density log along Well-A contains many porosity values larger than 40 percent. One possibility interpretation is to attribute these values to the washout from drilling or bad attachments from the logging device to the borehole surfaces. But pre-existing fractures might also cause this as well. In fact, distinguishing natural fractures from those induced by drilling was practically impossible in Figure 5.13.

By using the internal optimization loop on the REIM process to extract optimal bulk and shear modulus (see Chapter 4), we can recalculate different bulk and shear modulus along Well-A according to 14 different accommodation scenarios. Note that if we assume background anisotropy, the number of inclusion sets are increased by one by having pores act as one extra set of crack inclusion.

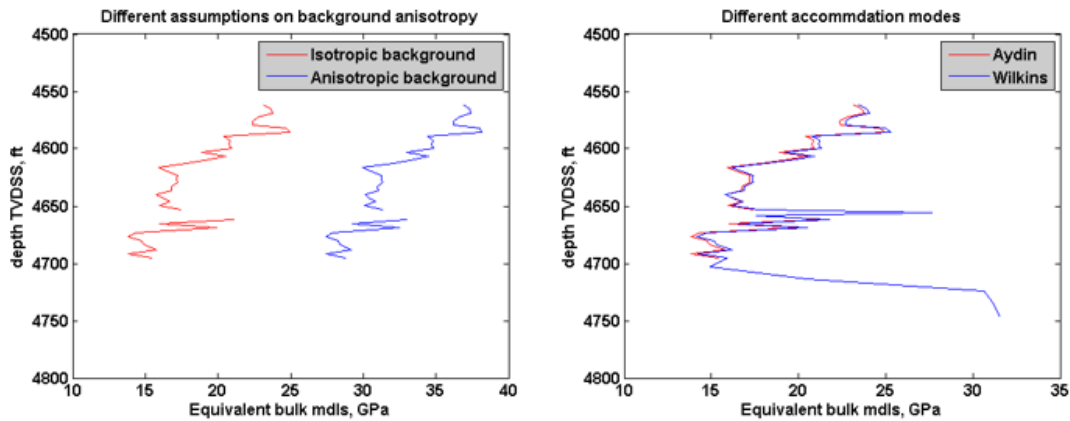
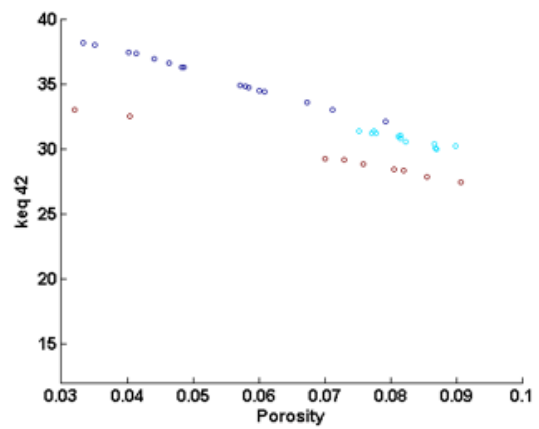
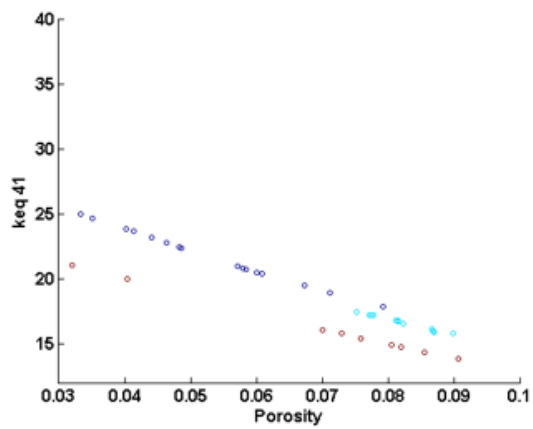
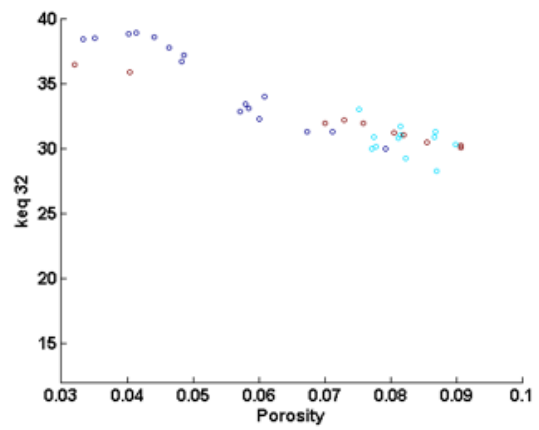
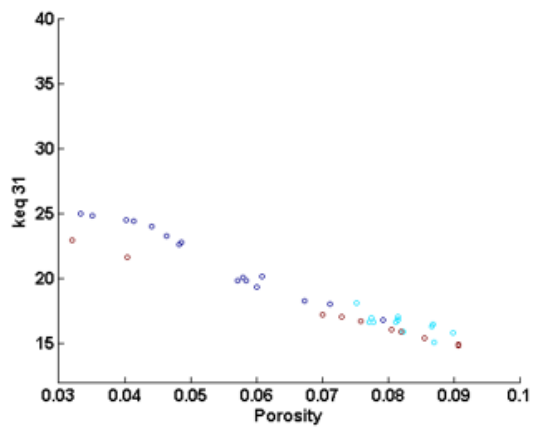
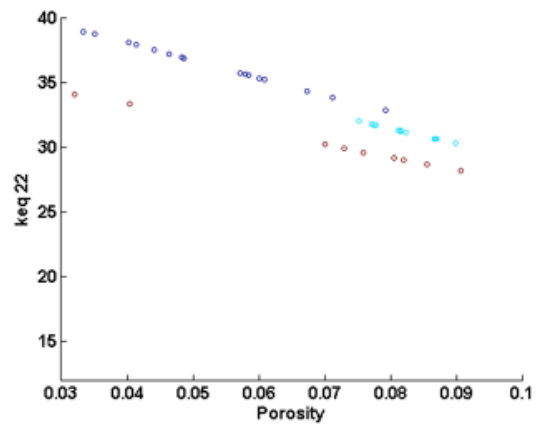
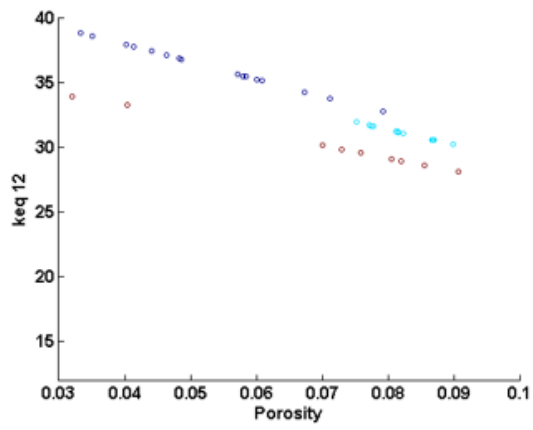


Figure 5.39: Left – comparison of assumptions on background shale. By having stiffer solid isotropic media, resultant vertical stiffness will be preserved with one more crack inclusion – crack-like pores. Right – different accommodation styles yield different bulk modulus profiles.

Figure 5.39 compares the effect of different assumptions on background anisotropy (left) and different accommodation scenarios involving different sets of crack inclusions (right). The left figure contains a distinctively larger bulk moduli profile based on the difference in background isotropic medium. When background anisotropy is assumed, the blue curve, we extract isotropic solid phase without pores. When we assume isotropic background, we extract isotropic bulk rock with pores in it. While two curves in the left figure have discontinuous sections, the blue curve on the right figure does not have discontinuous sections. A6, accommodation style based on Wilkins et al., assumes crack and vein existence on Cherry Valley and Onondaga formations. Thus, REIM under A6 produces equivalent bulk and shear modulus on carbonate formations while Accommodation style from A1 to A5 do not produce equivalent background medium on Cherry Valley and Onondaga formations.



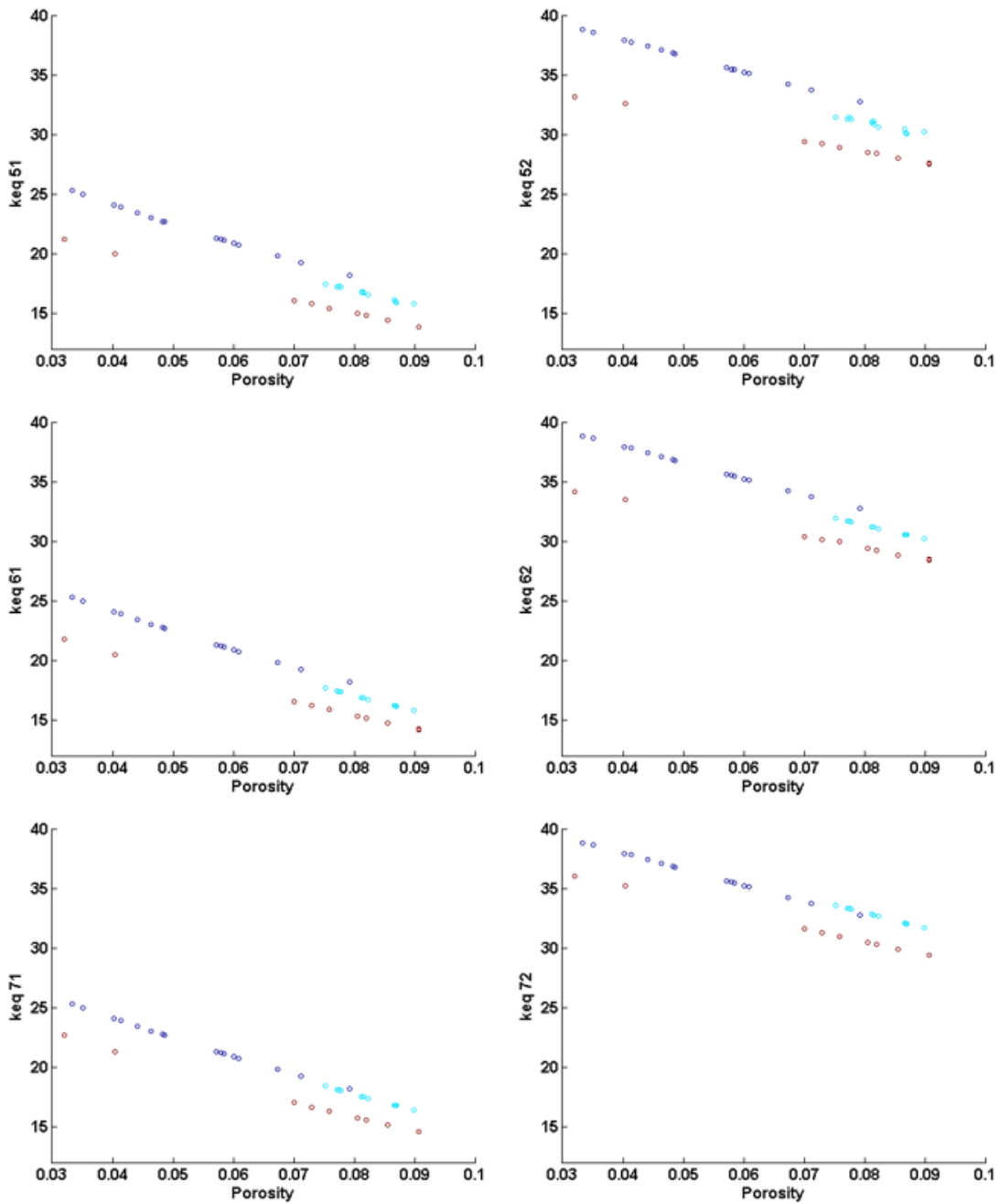


Figure 5.40: Trend among porosity and equivalent bulk and shear moduli of isotropic background media. Upper rows assume isotropic shale while the lower rows assume anisotropic shale. First number corresponds to accommodation scenario and second number corresponds one for assuming isotropic background matrix and two for anisotropic background medium. “Keq42” is for the equivalent bulk modulus assuming background shale anisotropy with Accommodation scenario A4.

Figure 5.40 shows a reconstructed bulk modulus plot with porosity, color-coded by formations. Under anisotropic assumptions, bulk modulus is shifted to larger values because it assumes the extraction of pores from the rock. Direct comparison of the bulk modulus from this process with actual bulk modulus of consisting minerals may be a good quality check on the process. We can extract empirical relations to extrapolate background isotropic properties for regions away from the well locations.

In this analysis, we focused on modeling inclusions into shale rocks. However, shale is ductile material compared to carbonate and many sandstones. We less stressed the ductile accommodation simply because it is straightforward to model and already covered it in Chapter 2. Furthermore, Marcellus shale has multiple joint/fracture sets spreading across Appalachian basin.

5.7.7 Petrophysical property modeling for each scenario

We have four different structural models having different grid cells, 14 different models of the petrophysical properties along the wells. By using empirical relations between porosity to bulk and shear modulus, and the aspect ratio of crack-like pores for cases assuming background anisotropy, the properties of background media are decided by the formation and porosity values. Spatial distributions of orientation, abundance, and the existence of each inclusion set is decided by deformational strain, structural geometry, or combinations of them as defined from Section 5.7.4. When all the information of background medium and crack inclusions are determined for a specific simulation node, we can use any effective model of crack inclusion. To make the process consistent, the same effective model (Hudson's model with Cheng's 2nd order correction terms) used on extraction of isotropic background media is used (Cheng, 1993).

Once all the cell nodes are calculated, we can compute seismic responses for the different orientation thanks to having Voigt's stiffness tensors considering multiple crack inclusions without constraints on their orientations. Using the cone searching method covered in Chapter 4, we can easily extract the azimuth of the fastest seismic velocity and variations of seismic velocity. We also can calculate the seismic anisotropy of resultant rock media assuming different combinations of inclusion sets.

5.7.8 Comparisons and discussion

We compare the volume-weighted sum of squared errors (SSE) between seismic attributes from survey and synthetic attributes computed for each structural model and accommodation model (Equation (5-4)). 25 models for each combinations are populated and the total number of models are 1400. In here, the main purpose is to find the overall best structural deformation model out of four alternatives to expand a 3D model in a following section.

$$SSE_{Volume\ weighted} = 1/\sum_{i=1}^{Cell\ \#} CellVolume_i \times \sum_{i=1}^{Cell\ \#} CellVolume_i \cdot (Attrbt_i^{synthetic} - Attrbt_i^{survey})^2 \quad (5-4)$$

Seismic reflectivity in 0-degree angle (Rpp0), azimuth of fastest P-wave velocity (AzimVfast), and difference between fastest and slowest azimuthally varying P-wave velocity (dVfVs) are used to compute volume weighted SSE.

Table 5-4: Comparison by Rpp0.

\Deformation Accommodation	D1: Tully Duplex	D2: Tully Reef	D3: Onondaga Duplex	D4: Onondaga Reef
A1: Conventional	1.58	1.82	1.95	2.31
A2: Ductile	1	1.24	1.65	1.67
A3: Brittle	2.04	2.32	2.43	4.27
A4: Aydin's	1.27	1.57	1.94	2.25
A5: Engelder's	1.13	1.33	1.74	1.76
A6: Wilkin's	1.14	1.36	1.70	1.72
A7: NFD	1.09	1.35	1.73	1.72

Table 5-5: Comparison by dVfVs.

\Deformation Accommodation	D1: Tully Duplex	D2: Tully Reef	D3: Onondaga Duplex	D4: Onondaga Reef
A1: Conventional	1.43	1.45	1.37	1.33
A2: Ductile	1	1.30	1.17	1.15
A3: Brittle	1.25	1.39	1.25	1.28
A4: Aydin's	1.50	4.40	1.59	3.20
A5: Engelder's	2.37	2.84	1.91	2.70
A6: Wilkin's	1.51	1.49	1.32	1.39

A7: NFD	1.35	1.40	1.31	1.28
---------	------	------	------	------

Table 5-6: Comparison by AzimVfast.

\Deformation Accommodation	D1: Tully Duplex	D2: Tully Reef	D3: Onondaga Duplex	D4: Onondaga Reef
A1: Conventional	1.99	2.68	2.59	2.70
A2: Ductile	1.05	2.33	2.23	2.36
A3: Brittle	1.19	2.34	2.17	2.38
A4: Aydin's	1.12	2.37	2.23	2.42
A5: Engelder's	1.16	2.36	2.27	2.36
A6: Wilkin's	1.13	1.20	1.13	1.24
A7: NFD	1.20	1.06	1	1.02

Table 5-7: Comparison by multiple of Rpp0 – dVfVs - AzimVfast.

\Deformation Accommodation	D1: Tully Duplex	D2: Tully Reef	D3: Onondaga Duplex	D4: Onondaga Reef
A1: Conventional	4.23	6.77	6.62	7.93
A2: Ductile	1	3.58	4.15	4.33
A3: Brittle	2.92	7.18	6.30	12.38
A4: Aydin's	2.03	15.61	6.60	16.59
A5: Engelder's	2.96	8.55	7.21	10.77
A6: Wilkin's	1.85	2.33	2.42	2.82
A7: NFD	1.70	1.91	2.16	2.16

We also compute volume-weighted SSE only along the well where we know the measured seismic velocity and density from the well log. Because this value is comparison between the true Rpp0 from seismic data and the closest Rpp0 when we have detailed measurements, if any volume-weighted SSE is smaller than this value, we cannot reject that scenario. In the same way, we can convert the SSE into likelihood probability by using Equation (5-5). Table 5-8 shows likelihood normalized by the maximum values.

$$p(d|m) \cong \exp\left(-\frac{SSE}{SSE_{Data@well}}\right) \quad (5-5)$$

Table 5-8: Comparison by multiple of Rpp0 – dVfVs – AzimVfast (likelihood).

\Deformation Accommodation	D1: Tully Duplex	D2: Tully Reef	D3: Onondaga Duplex	D4: Onondaga Reef
----------------------------	------------------	----------------	---------------------	-------------------

A1: Conventional	0.06	0.02	0.02	0.01
A2: Ductile	1.00	0.09	0.06	0.06
A3: Brittle	0.09	0.01	0.02	0.00
A4: Aydin's	0.25	0.00	0.02	0.00
A5: Engelder's	0.07	0.01	0.02	0.00
A6: Wilkin's	0.31	0.20	0.16	0.12
A7: NFD	0.40	0.28	0.18	0.19

Average of volume-weighted SSE of 50 models for each scenario combinations normalized by the minimum mean SSE. Table 5-4, Table 5-5, and Table 5-6 are for normalized SSE tables of Rpp0, dVfVs, and AzimVfast respectively. In each table, combinations of structural deformation scenarios and rock accommodation scenarios having smaller values close to one are the combinations showing better similarity among synthetic and actual seismic responses. From Rpp0 table, D1-A2 and D1-A7 combinations show the lowest errors. In overall, D1- Tully duplex yields the smallest errors with any combinations of rock accommodation scenarios. However, Rpp0 comparison does not distinguish among accommodation scenarios. dVfVs comparison shows smaller differences among combinations except A4 and A5 yield relatively larger errors. When compared by AzimVfast, D1 – Tully duplex – gives the least amount of SSE as we seen from Rpp0 comparison. However, when focusing on A7 – accommodation scenario based on Nickelsen-Ferrill-Dunne, results from all deformational scenarios gives relatively same level of errors. Table 5-7 shows multiplications of all three normalized SSE of Rpp0 – dVfVs – AzimVfast. Though the values in the tables are not representing likelihood of the scenarios, the multiplied values can be understood as proxy of likelihood. In overall, D1-A2, Tully Duplex with having ductile deformation yields the smallest errors. The second and third combinations having smallest errors are D1-A6 and D1-A7. In overall, D1 yields the smallest errors.

Table 5-9 and Table 5-11 shows the sum of SSE of each comparison summed into same structural models and accommodation models respectively. Table 5-10 and Table 5-12 show the likelihood probability normalized by the maximum values.

Table 5-9: Comparison volume-weighted SSE by structural deformation scenarios. SSEs from 14 accommodation scenarios sharing the same structural deformation scenario are averaged and normalized by the minimum value among four deformational scenarios.

Scenario\Attributes	Rpp0	dVfVs	AzimVfast
D1: Tully Duplex	1	1.05	1
D2: Tully Reef	1.18	1.44	1.62
D3: Onondaga Duplex	1.42	1	1.54
D4: Onondaga Reef	1.70	1.24	1.64

Table 5-10: Comparison of likelihood by structural deformation scenarios. Likelihood probabilities from 14 accommodation scenarios sharing the same structural deformation scenario are averaged and normalized by the minimum value among four deformational scenarios.

Scenario\Attributes	Rpp0	dVfVs	AzimVfast	Combined
D1: Tully Duplex	1.00	0.98	1.00	0.98
D2: Tully Reef	0.66	0.70	0.50	0.23
D3: Onondaga Duplex	0.37	1.00	0.56	0.20
D4: Onondaga Reef	0.31	0.87	0.50	0.13

Table 5-11: Comparison of volume-weighted SSE by accommodation scenarios. Results from different assumptions on shale anisotropy are combined for comparison focusing on the effects of accommodational style only.

Scenario\Attributes	Rpp0	dVfVs	AzimVfast
A1: Conventional	1.38	1.21	2.33
A2: Ductile	1	1	2.33
A3: Brittle	1.99	1.12	1.86
A4: Aydin's	1.27	2.31	1.90
A5: Engelder's	1.07	2.13	1.90
A6: Wilkin's	1.06	1.24	1.06
A7: NFD	1.06	1.16	1

Table 5-12: Comparison of likelihood probability by accommodation scenarios. Results from different assumptions on shale anisotropy are combined for comparison focusing on the effects of accommodational style only. Likelihood probability is normalized by the maximum value.

Scenario\Attributes	Rpp0	dVfVs	AzimVfast
A1: Conventional	0.40	0.66	0.21
A2: Ductile	1.00	1.00	0.44
A3: Brittle	0.16	0.79	0.40
A4: Aydin's	0.56	0.27	0.41
A5: Engelder's	0.83	0.14	0.41
A6: Wilkin's	0.83	0.63	0.89

A7: NFD	0.86	0.73	1.00
---------	------	------	------

Differences in near offset seismic reflectivity (Rpp0) among models are not noticeably significant for both comparisons by structural deformation modes and rock accommodation modes. Since the attributes capture the vertical seismic responses, the results make sense because we modeled petrophysical properties so as to reproduce the vertical velocity profiles observed along the well. Scenarios having structural features on Tully formation, D1 and D2, shows slightly smaller SSE than D3 and D4. When we compare the differences between fastest and slowest seismic velocity (dVfVs) among structural deformation modes, duplex scenarios, D1 and D3, show smaller SSE than reef scenarios, D2 and D4. dVfVs captures geological features introducing offset dependency on seismic responses such as pore fluid, or existence of fractures. D1 scenario yields the smallest SSE on comparisons of azimuth of fastest P-wave velocity (AzimVfast). D1 gives the best match with seismic attributes when compared independently, or compared sequentially from Rpp0, dVfVs, and AzimVfast in order of seismic attributes of no angular dependency, of offset dependency, and of azimuthal dependency.

When compared by accommodation scenarios, the accommodation scenarios of A6 and A7 show smaller SSEs than other cases. All two models assume LPS accommodation as one of the most important guiding factors on inclusion features. A6 and A7 have inclusion sets in Onondaga limestone. A2 – ductile accommodation – yields the smallest SSE for Rpp0 and dVfVs comparisons. Since all four structural deformation scenarios are under assumptions of compressional condition and fracture sets are also for the compressional environments, spatial regions having large dilatation correspond to regions with high fracture abundance. It can be interpreted as a coincidence or an indication of noticeable correlations between structural attributes and petrophysical properties.

Tully duplex showed overall smaller SSEs among different structural deformation scenarios. Actually, the accommodation models having best matches with seismic attributes, A6 to A7, are only meaningful when the Onondaga formation has been

exposed to accommodations related to LPS. For the case of Onondaga duplex, or Anticline of Onondaga formation, the Onondaga formation accommodates the tectonic loading by having noticeable structural deformation. Thus, A6 to A7 become meaningful only when the Onondaga formation accommodated by LPS does not involve major structural changes. Tully Duplex, D1, is more likely scenario not only from the direct comparisons to seismic attributes but also the structural deformation scenario to justify the observations of having A6 and A7 as accommodation modes with smallest SSEs. Thus, we choose the Tully duplex model for further investigation in a full 3D model.

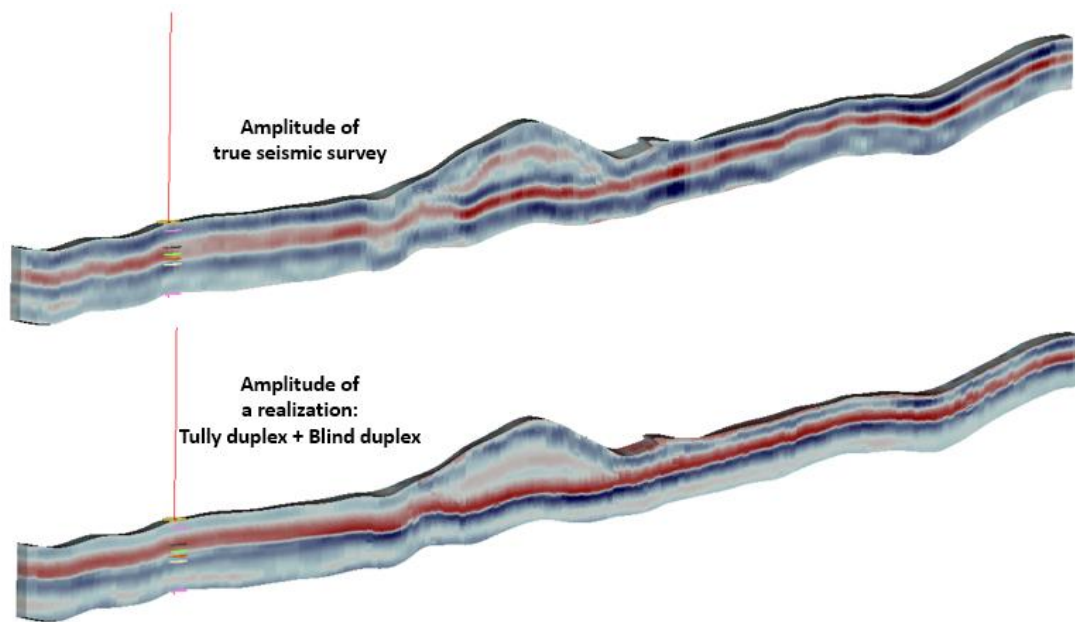


Figure 5.41: Seismic amplitude from true seismic survey (top). Synthesized amplitude in field scale from a realization on the scenario of Tully duplex with blind duplex (bottom).

Figure 5.41 compares seismic amplitude with actual seismic data and synthetic seismic amplitude with the combination of Tully duplex as structural deformation model and A7 as accommodation model. From the combination of Tully duplex and any of A5 to A7, we can extract information from Onondaga formation to estimate abundance of fractures in the adjacent Marcellus formation.

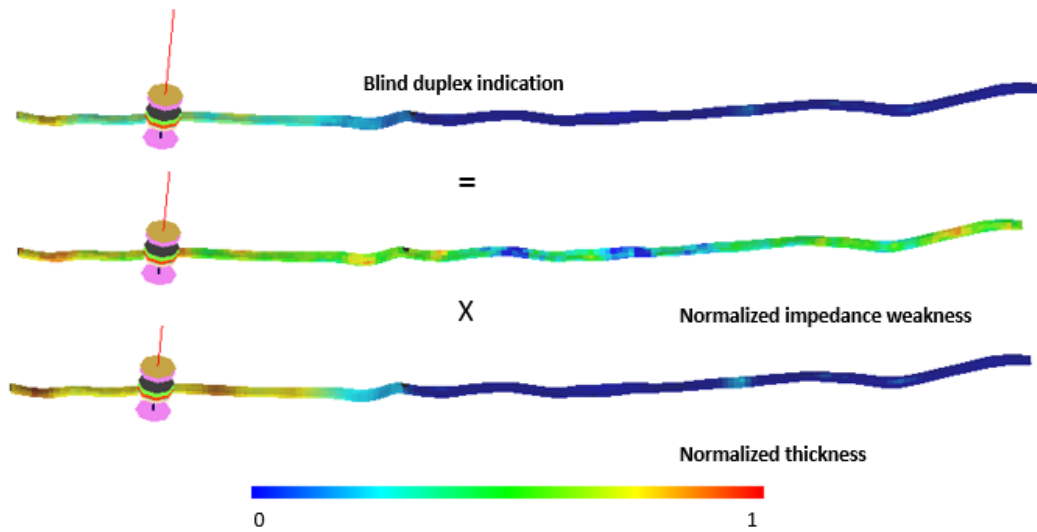


Figure 5.42: Indication of blind duplex from thickness variation and weakness of seismic responses on Onondaga formation. Well-A region has higher indication values than other regions. When blind duplex is assumed as accommodation model in Onondaga, thickness variation and weaker amplitude in blindly duplexed area can be anticipated.

Figure 5.42 is a 2.5D section of Lower Marcellus shale colored by blind duplex indication. Blind duplex indication is derived from Normalized Onondaga thickness and vertical summation of normalized seismic amplitudes on Onondaga formation. Blind duplex creates elongated thickening without having noticeable geometrical perturbations from seismically driven structural geometry. If the formation is blindly duplexed, it may contain a series of nearly horizontal faults. Thus, the seismic amplitude becomes weaker. The blind duplex indication has higher values around the Well-A region. Thus, the Well-A region does not have fracture or fault networks, yet the orientation of the fractures/fault NE-SW correspond with reverse fault on Onondaga formation and vertical cleavage of Marcellus.

5.8 Expansion to 3D model

We selected the Tully duplex structural model for 3D expansion. Within the 3D model, we apply 14 different accommodation styles on property modeling.

5.8.1 3D structural model of Tully duplex scenario

In the 3D structural modeling, we want to capture repeating section of Tully duplex and thus reproduce the localized thickening we see from the seismic survey (Figure 5.43). By applying different accommodation modes within the 3D model, we investigate whether models from certain accommodational assumptions more closely reproduce seismic observations. Finally, we aim to see whether the combination of the structural model and accommodation models can explain the field specific problems discussed earlier.

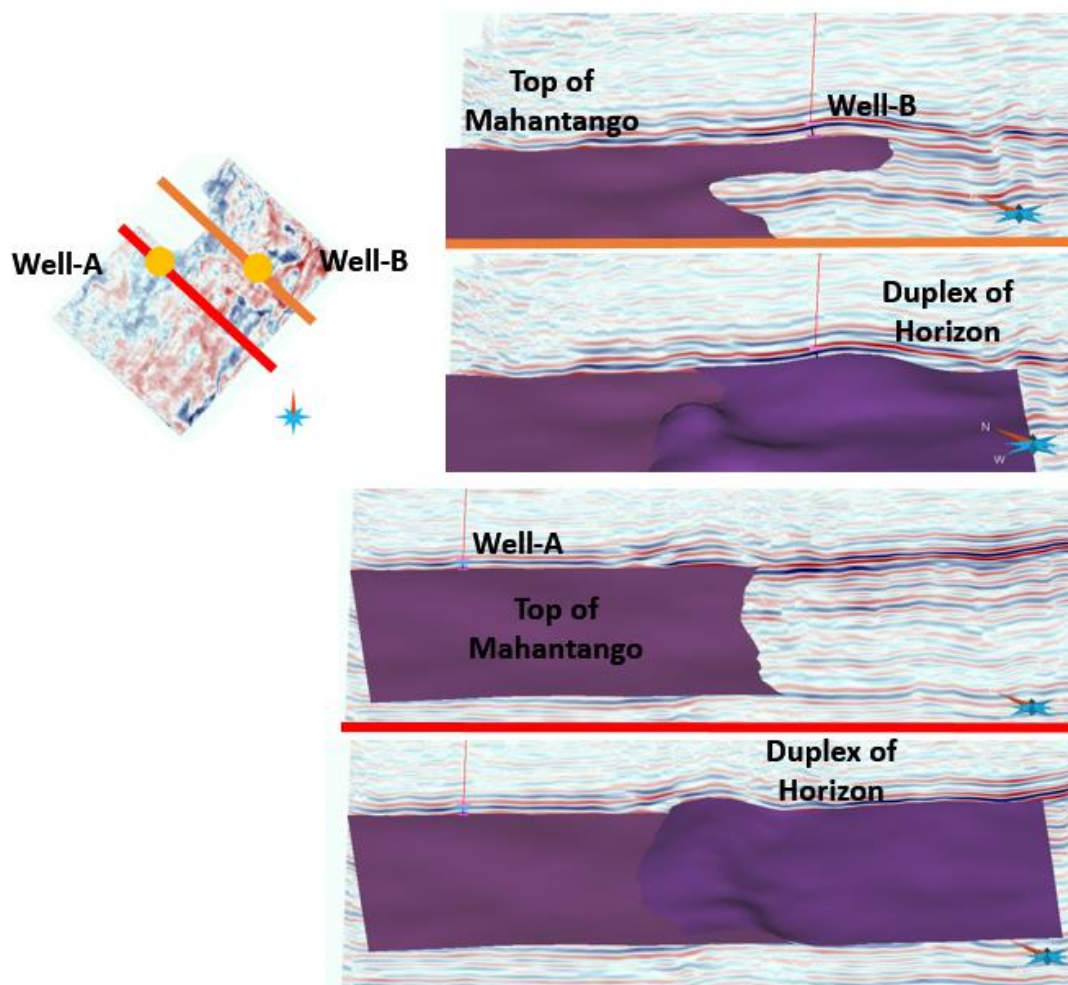


Figure 5.43: Seismic section with Mahantango horizon of localized thickening. Orange color – crossline along Well-B region. Red color- crossline along Well-A region. Under the Tully duplex scenario, localized thickening region in the seismic cube are modeled as repeated sections of Tully and Mahantango formation from duplex deformation.

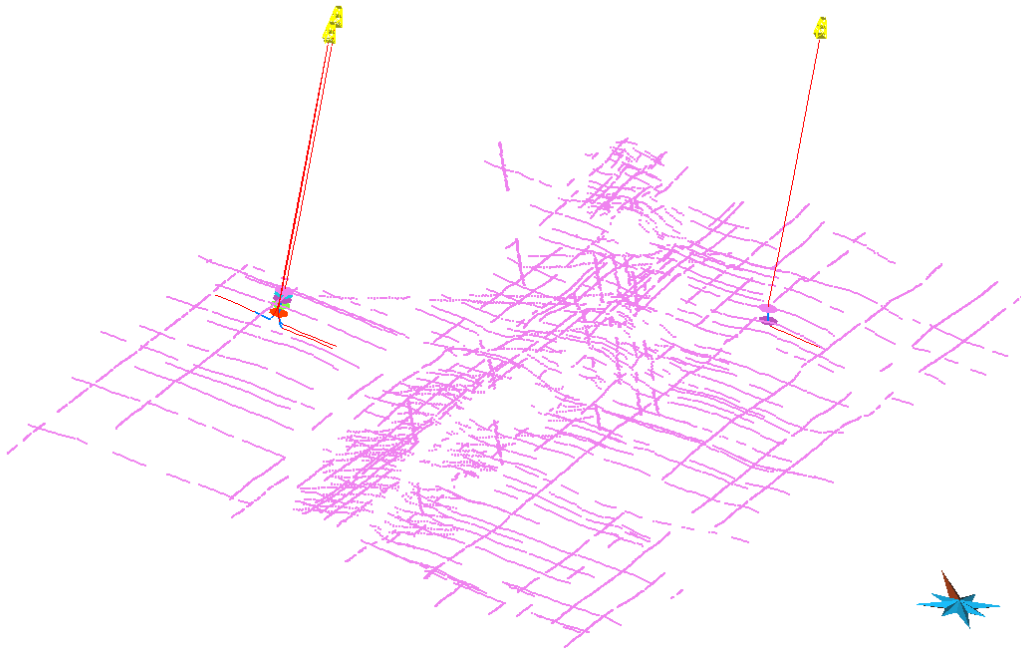


Figure 5.44: Horizon picks of Rhinestreet shale formation

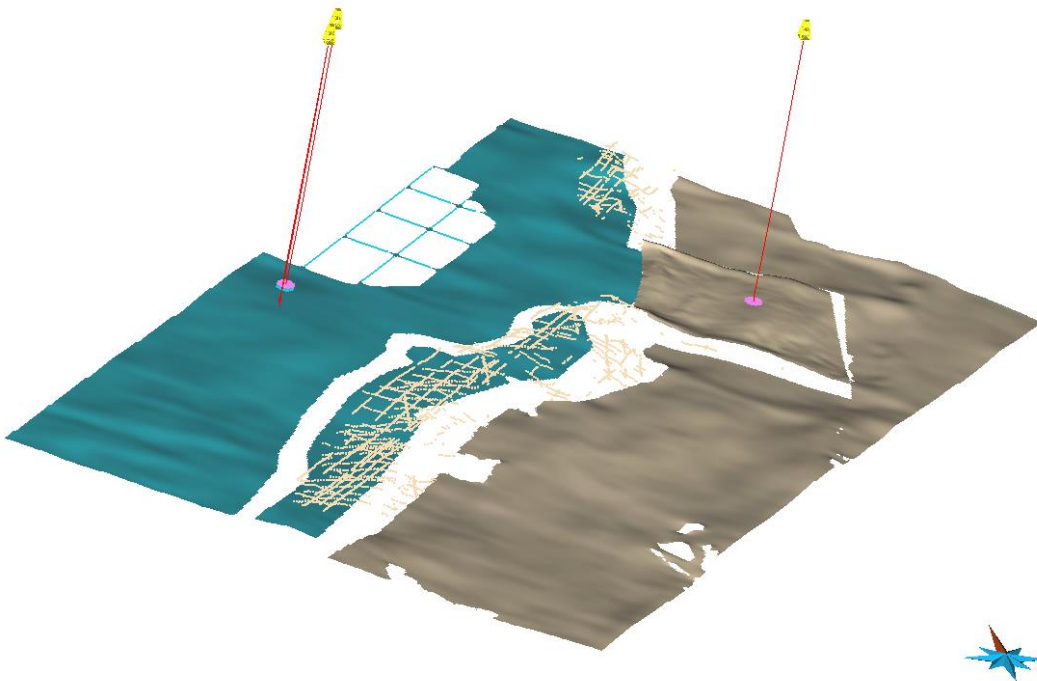


Figure 5.45: Optimized surfaces and partial manual picks for Tully limestone horizons.

First, horizon picks for each formations from seismic survey are conducted. Figure 5.44 shows horizon picks of Rhinestreet shale formation. The second step involves creating optimized surfaces from manual picks. Figure 5.45 shows the optimized surfaces of the top of Tully limestone formation. Parts with light blue are for the Tully limestone with the repeating section under the other repeating section above (light gray).

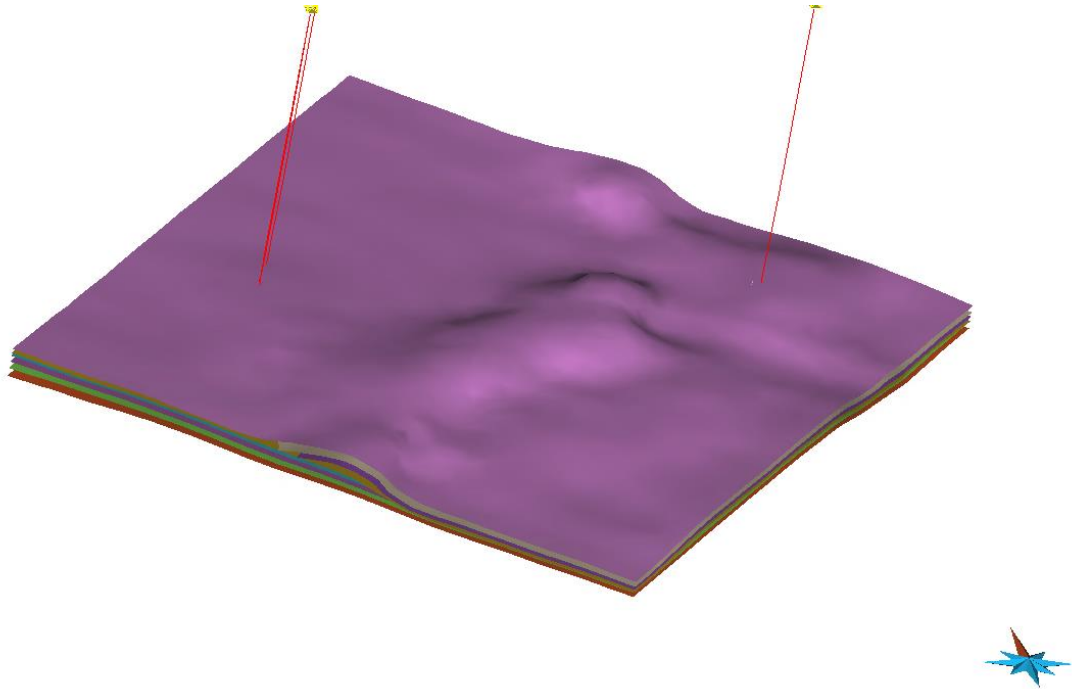


Figure 5.46: Structural model of Tully duplex model with surface horizons.

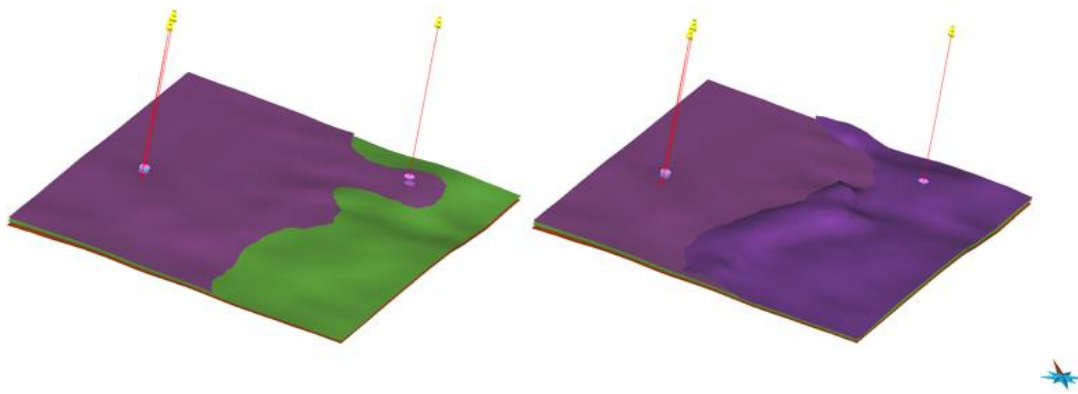


Figure 5.47: Duplex features captured in the structural model. The left figure is the surface top of a Mahantango formation and the right figure is the repeating horizon by duplex.

Figure 5.46 shows a structural model of a Tully duplex scenario. Figure 5.47 depicts the repeating section on the Mahantango formation by removing the Rhinestreet shale and Tully limestone formations on top of the Mahantango formation.

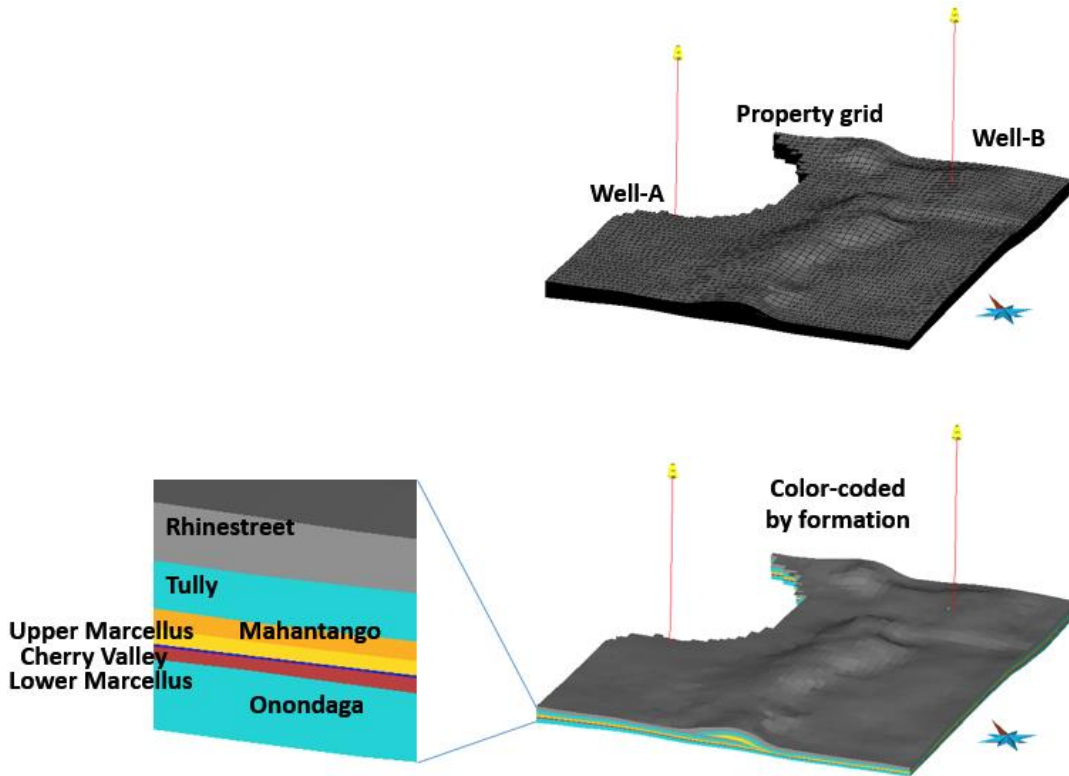


Figure 5.48: Property grid colored by formation index.

Figure 5.48 is a geological grid for property modeling colored by formation index. Using the same procedure we followed for 2.5D vertical section modeling, we can populate and calculate petrophysical properties according to each accommodation scenario.

5.8.2 Discussion

From the same type of comparisons among seismic responses of from field data and synthetic responses from each model, we compare the SSE and the likelihood of the models from each accommodation scenario (Table 5-13 and Table 5-14). Models from the accommodation scenarios assuming the blind duplex on Onondaga carbonate formation give a lower level of SSEs. From the comparison of chosen attributes, A6 and A7 are more likely scenarios than other accommodation scenarios.

Table 5-13: comparison of SSE of near-offset seismic reflectivity (Rpp0), differences between fastest and slowest P-wave velocity (dVfVs), and azimuth of fastest P-wave velocity (AzimVfast) by different accommodation scenarios.

Scenario\Attributes	Rpp0	dVfVs	AzimVfast
A1: Conventional	3.02	1.18	2.89
A2: Ductile	1.74	1	2.46
A3: Brittle	2.15	1.12	2.56
A4: Aydin's	3.20	2.07	2.61
A5: Engelder's	1.50	2.46	2.59
A6: Wilkin's	1.37	1.23	1
A7: NFD	1	1.14	1.05

Table 5-14: comparison of likelihood probability of near-offset seismic reflectivity (Rpp0), differences between fastest and slowest P-wave velocity (dVfVs), and azimuth of fastest P-wave velocity (AzimVfast) by different accommodation scenarios.

Scenario\Attributes	Rpp0	dVfVs	AzimVfast
A1: Conventional	0.45	0.58	0.07
A2: Ductile	0.75	1.00	0.31
A3: Brittle	0.64	0.70	0.17
A4: Aydin's	0.42	0.01	0.00
A5: Engelder's	0.82	0.02	0.01
A6: Wilkin's	0.86	0.58	0.49
A7: NFD	1.00	0.66	0.66

The results align with 2.5D comparisons. One minor differences from 3D over 2.5D results are the Ppp0 comparisons. Compared to 2.5D, differences of SSE on Rpp0 among scenarios become larger. When the modeling volumes are small and close to the hard data (Well-A), all models can reproduce relatively similar reproductions on seismic responses. However, results from A1 to A5 are deviated away from the obtained seismic responses when 2.5D is expanded to 3D. It depicts possible caveat when the scenarios or models are selected from the comparisons of one or two parameters. Comparisons by offset dependent and azimuthal dependent attributes remain nearly unchanged.

Results of A6 and A7 are negligible in terms of SSE of all three attributes. If we recall the accommodational scenario of A6 and A7, both are nearly identical except how they call the features – reverse fault vs J1 joints on Lower Marcellus, assumptions on reverse faults making blind duplex in Onondaga for only A7. However, the effect of reverse faults in Onondaga under A7 scenario on azimuthal variation is less likely detectable from AzimVfast because the normals of fault surfaces are 30 degree from vertical axis. With having vertical veins striking NW-SE, AzimVfast would not vary by the existence of Onondaga blind duplex. However, Modeling Onondaga blind duplex as reverse faults can be the reason of smaller SSE on Rpp0 of A7 over A6.

Having larger errors do not mean that those accommodation scenarios are inferior, or more likely to be wrong. It just means that the realizations under those scenarios yields less similar synthetic seismic responses compared to the seismic data of the field. If we interpret the smaller SSE as an indication of being a more appropriate scenario for the field, the interpretation would only hold good for this field, or fields having similar geological settings – especially structural setting.

From the comparisons, we choose A7 – a new interpretation proposed by combining interpretations of Nickelsen (1986) and Ferrill and Dunne (1989) – as the most likely accommodation model. Now, we test whether the combination of structural deformation model and rock accommodation model – Tully Duplex and Ay – allow us to anticipate anomalies on Well-B region. Well-B region had difficulties during well test analysis by having strong water influx from unknown sources.

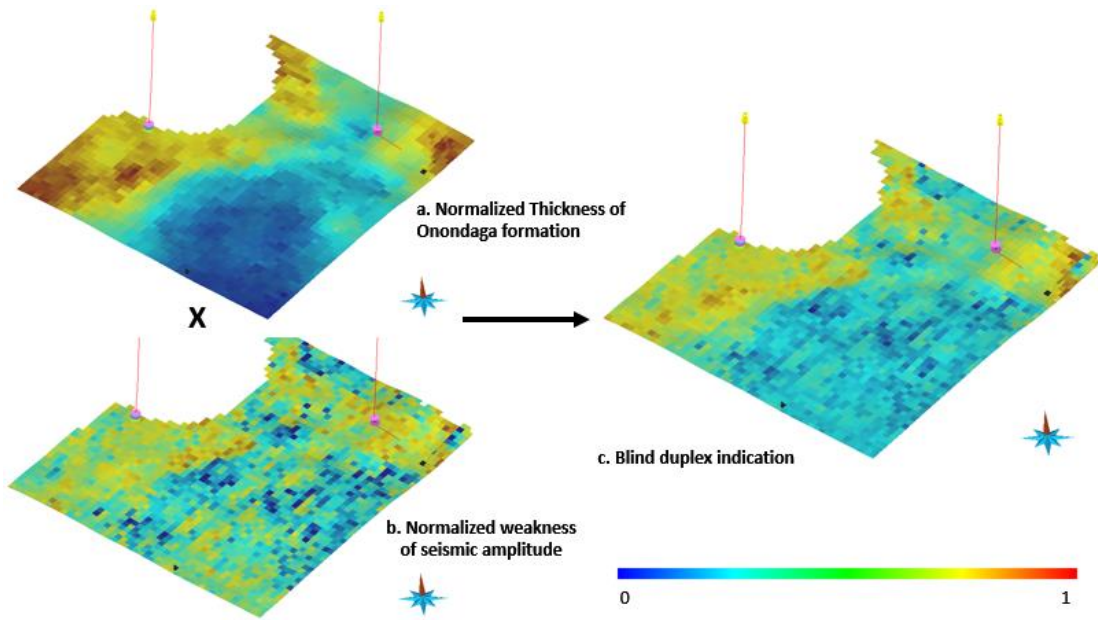


Figure 5.49: Blind duplex indication from normalized Onondaga thickness and normalized weakness of seismic amplitude. All of them are scaled from zero to one.

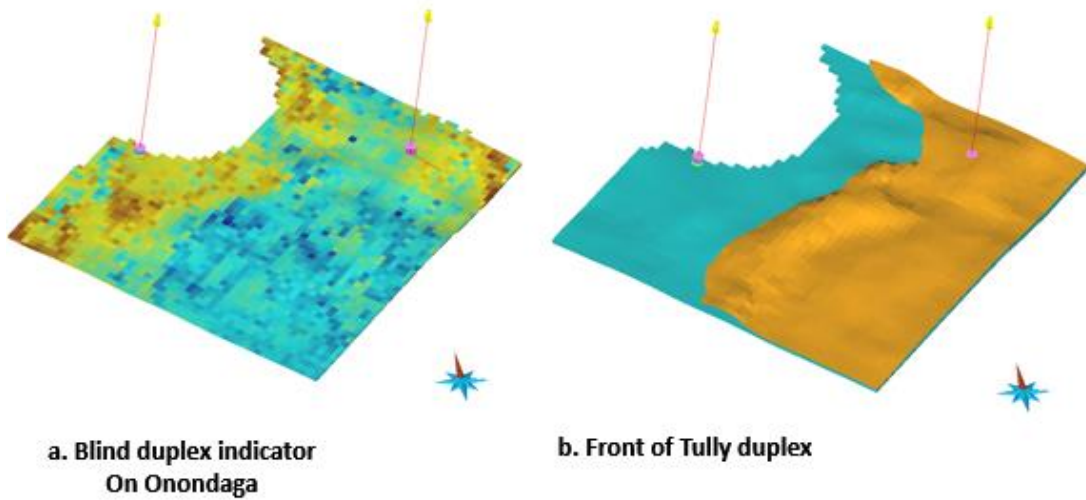


Figure 5.50: Blind duplex indicator on Onondaga (a) and structural front of Tully duplex. Regions with higher blind duplex indicator corresponds the foreland of Tully duplex.

Figure 5.49 shows the blind duplex indication used in Figure 5.42. As can be seen from Figure 5.49c, both the Well-A region and the Well-B region have higher blind duplex indication. Under the scenario of accommodation modes from A6 and A7, having blind duplex in the Onondaga formation yields cleavage/joint/fracture

developments on Marcellus shale because of LPS. Figure 5.50 shows the regions having higher blind duplex indicator are coincide with the foreland of Tully duplex.

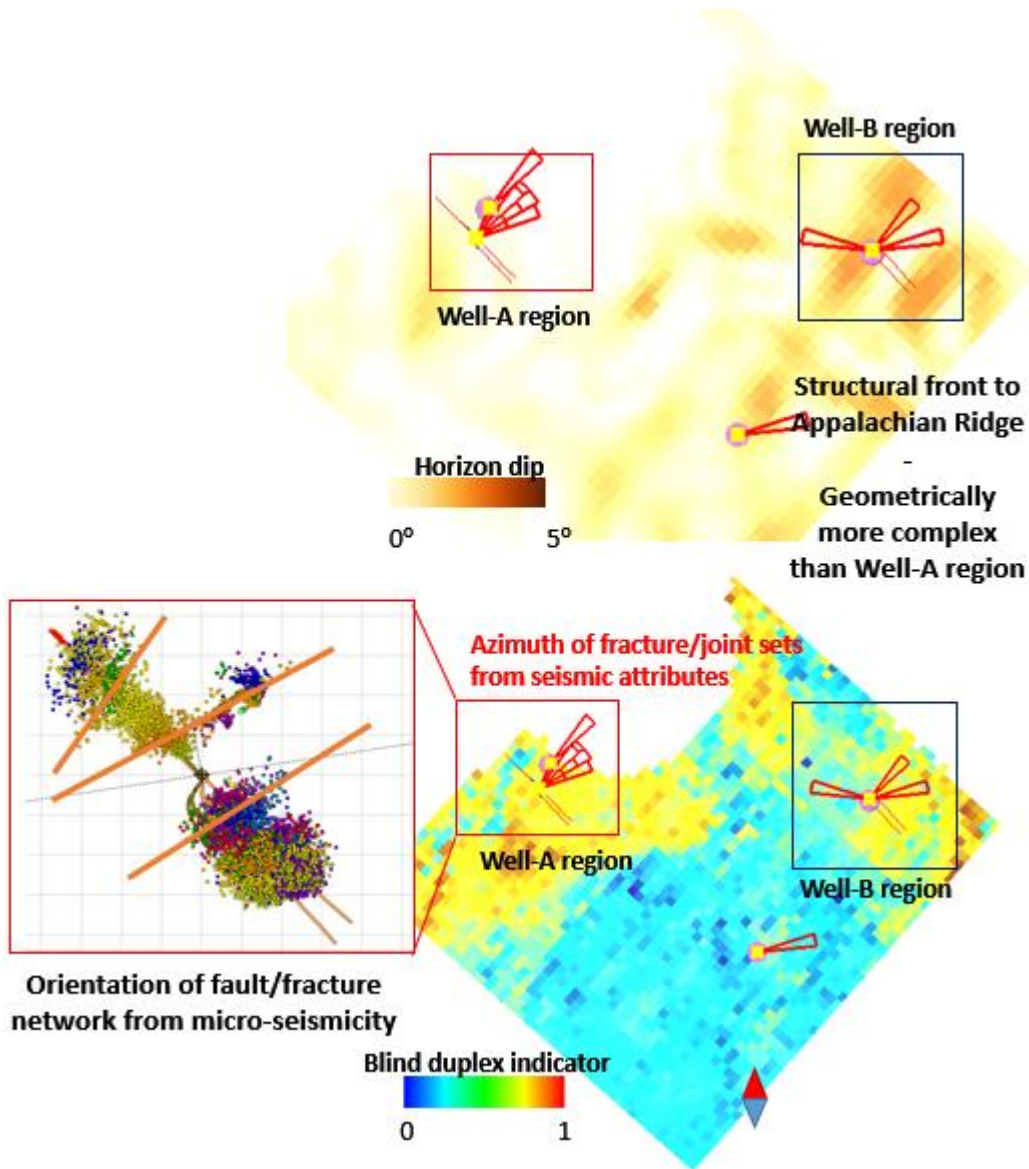


Figure 5.51: Comparison of blind duplex indication, horizon dip, and azimuth of fastest P-wave velocity in the Well-A and Well-B regions.

Figure 5.51 superimposes the Well-A and Well-B regions on top of the blind duplex indication map (bottom) and horizon dip (top) with azimuth of fastest P-wave velocity near the Well-A and Well-B region after flipping 90 degree. In the Well-A region, the azimuth of fastest P-wave velocity corresponds perpendicular to the

orientation of possible fracture swarms or fault networks. In accommodation modes of A6 and A7, Onondaga formation forms vertical joints/vein perpendicular to shortening orientation to compensate LPS and make the azimuth of fastest seismic velocity perpendicular to preferential flow orientation (Inks et al., 2015).

The Well-B region also has a higher value on blind duplex indication. The difference between the Well-A region and Well-B is the variability of the azimuth of fastest P-wave velocity and geometrical complexity on Well-B region. The Well-B region is closer to the present structural front of the Appalachian ridge. Thus, the Well-B region may have not only the blind duplex on Onondaga formation and cover deformation with developing cleavages on Marcellus shale as Well-A region might have experienced, the region may contain a series of faults or fractures. Having a series of reverse faults in Onondaga carbonates with a series of joint/fracture/cleavages – named differently under different accommodation scenario – can explain the possible conduits of water influx from the formation below Marcellus shale. This water could stem from the Onondaga formation or Oriskany sandstone formation beneath the Onondaga carbonate. Due to densely existing reverse faults from blind duplex – if this is the correct accommodation – the Onondaga formation can act as a highway for water influx toward the Marcellus formation. The southern region in Figure 5.51 shows relatively low blind duplex indicator for being a hinterland of Tully duplex. It also shows relatively flat surface horizons. We may anticipate relatively less dense fracture, or fault abundance in the region. In retro-perspective, the southern region may be a good candidate for closer distance on horizontal drilling than the Well-A region.

5.9 Summary

In this chapter, we applied the proposed geomodeling workflow on an unconventional shale gas field on Marcellus play. We investigated the uncertainty of geological understanding for both structural deformation and rock accommodation on Marcellus play by comparing explanations proposed by different groups of geologists.

Applying the new rock physics methods from Chapter 4 allow us to conduct petrophysical modeling under any number of inclusion sets with arbitrary orientation for each inclusion set. Comparing angle-dependent seismic responses with synthetic responses created from a new rock physics method allows us to evaluate the likelihood of combinations of structural deformation scenarios and rock accommodation scenarios.

By expanding 3D modeling from the Well-A region to the Well-B from combinations of scenarios selected from 2.5D comparison, we generated models that allow us to give coherent explanations on the field specific problems; unexpected horizontal connectivity on the Well-A region and water influx during well-testing operation on the Well-B region. Expanding the focus on modeling to adjacent formations provided geologically coherent interaction among formations on how they may have accommodated LPS. Investigating adjacent formations also help to mitigate problems from limited amount of data on the target formation.

The field application in this chapter depicts the benefits of considering alternative geological interpretations on structural deformation and rock accommodation in the geomodeling process. We assume the geological interpretations as a fixed input on quantitative analysis using geomodeling. However, the geological interpretations are one of the most uncertain parts of the subsurface evaluation process. Applying the proposed workflow on structurally complex geological subsurface problems may provide a better understanding of geological settings and possible engineering problems.

Acknowledgments

We thank the data donor, who want to be remained anonymous, for providing the data, meetings, and many inputs for this investigation. We also appreciate Paradigm® for donating the GOCAD-SKUA geomodeling software.

Chapter 6

6 Conclusions and Future Works

This work has endeavored to integrate two geological uncertainties – modes of structural deformation and rock accommodation – in the geomodeling and evaluation process. These two geological uncertainties are not only closely linked to each other, but also to petrophysical properties and subsurface flow and seismic responses. Previous works attempting to link structural attributes with reservoir evaluations could lead to underestimation of the effects of structural uncertainty on reservoir responses by relying on one interpretation or a combination of sub-resolution features such as faults and joints. We claimed that we have to vary interpretations and assumptions on structural deformation and their effects on sub-resolution features to conduct subsurface evaluations rigorously when we have complex structure and uncertainties on sub-resolution geologic features. We proposed a new geomodeling workflow that propagates geological assumptions on structural deformation of subsurface and accommodation of rock to reservoir properties. Alternative structural deformation scenarios introduce different structural attributes such as deformational strain and stress on top of geometrical attributes such as curvature and thickness variations. Different rock accommodation scenarios relate the structural deformation attributes to realizations of spatial distributions of geological features and rock properties differently. Realizations under different sets of scenarios for structural deformation and rock accommodation have different spatial distributions of geological features and rock properties yet honor conditioning data.

Because these two geological uncertainties have not been studied in the context of geomodeling, we first examined the sources of geological uncertainty that affect the subsurface evaluation (Chapter 2). These uncertainties include not merely cases where the geometry is different, but also cases where the geometry is identical, as multiple deformation scenarios can result in either instance. Even for identical geometries, the

resulting rock properties may be different because of differences in rock accommodation modes. Because our knowledge of the exact geometry and deformation mechanism of it is limited, multiple geological models for the structural deformations are necessary resulting in additional interpretational uncertainties. Additionally, we discussed different modes of rock accommodations as an additional layer of geological uncertainty by having either discrete or continuous accommodation styles such as creating fractures or pore rearrangement as accommodational vehicles to the structural deformation.

We proposed a new geomodeling and evaluation workflow to propagate multiple geological scenarios of structural deformation and rock accommodation (Chapter 3). Using a structurally complex synthetic reservoir case, we demonstrated that even with the same present subsurface geometry and well data, realizations and their seismic and flow responses are dramatically different when different geological scenarios are applied. The results depict possible underestimation of the uncertainty of reservoir responses when we use only a single geological interpretation. We also depict the usefulness of using a rock physics model to compute what-if seismic attributes when assuming different modes of rock accommodation and their sub-resolution deformation processes.

In Chapter 4, we proposed a new rock physics method to compute seismic attributes with multiple sets of inclusions having different orientations in anisotropic media such as shale. By extracting the intrinsic anisotropy of the background medium into both an equivalent isotropic medium with equivalent crack-like pores, we overcame limitations and computational costs of previously available rock physics models where constraints on the orientations of inclusions with respect to the symmetry of a symmetry the effective medium exists to have explicit forms of computation. Our proposed model expands upon earlier studies by allowing us to understand more of the possible types of cracks the formations may have under situations when we lack clear knowledge of the orientation of inclusion and the level of background anisotropy of shale formation. To reflect the velocity and density profile along the wells under different scenarios of rock accommodation, such as different sets of joints, cleavages, and porosity, we

reconstructed the rock along the wells as combinations of equivalent background media and multiple sets of inclusion under each geological scenario.

In Chapter 5, we applied the new geomodeling workflow and rock physics models to an unconventional Marcellus Shale gas field. The field has not only structural complexity leading to multiple interpretations on structural deformation but also uncertainty on rock accommodation. By considering the multiple scenarios of structural deformation and rock accommodation, we created noticeably different realizations for each scenario yet each honoring the well data. The new rock physics model proposed in Chapter 4 compares what-if seismic attributes with real seismic data. Realizations from a scenario selected according to seismic attribute comparison better explains previously difficult to understand field observations.

The key findings from this study are as follows:

- Uncertainty about the structural deformation of subsurface geometry and the uncertainty of the rock accommodation correlate with uncertainty on affecting the abundances and distributions of key geological features acting as flow barriers or flow enhancers.
- Thus, we should not be bounded by a single structure model with a single assumption on sub-seismic geological features such as fracture sets.
- Comparisons between synthetic seismic responses according to different geological scenarios and actual seismic responses are effective tools for choosing a more likely geological scenario.
- By expanding investigations from target formations to adjacent formations, we can better understand the subsurface geological conditions of the target formations. When the existence of geological features in target formations are correlated with the structural deformation and rock accommodation of adjacent formations, we can utilize adjacent formations where having more data and knowledge helps to mitigate difficulties from sparseness and resolution of data on the target formation.

Our method helps rule out less likely geological assumptions. By using seismic response comparisons and the models from the remaining scenarios, we understand better the previously misunderstood subsurface responses. For the fields with structural complexity and small amounts of the well data, applying the workflow may provide "what-if" field responses and corresponding contingency plans.

This work is the first attempt to investigate and capture multiple scenario uncertainties of structural deformation and rock accommodation in geomodeling process; thus, many areas require additional research:

- In this work, the geological models used for structural deformation were limited to restoration methods under linear elasticity. Conducting deformational analysis using nonlinear constitutive laws is more challenging due to the paucity of data. Comparing geomodeling results from linear versus nonlinear deformation analysis in the workflow may provide a better understanding of the relationship between structural deformation, the spatial distribution of petrophysical properties, and corresponding subsurface responses from measurements.
- Synthetic and field applications of the proposed workflow are conducted for particular situations when spatial variability of lithofacies are negligible. We can apply this process to more conventional reservoirs where higher level of heterogeneity occurs in the facies distribution. Improving our understanding of the relative effects of facies upon structural uncertainty can advance our understanding of the reservoir evaluation process. Furthermore, by contrasting the modes of accommodation across distinctive boundaries of facies, such as channel sands and floodplain, we can discover both geological and engineering applications such as uncertainties on shale formations on top of target sandstone reservoir to be a sealing layer or to be a leaking conduit.
- Development of a fast but reliable proxy for seismic responses is also beneficial. Though we can extract many different seismic attributes from real

seismic data, comparing the real data with synthetic seismic data is challenging because of the difficulties in finding the optimal level of accuracy and complexity of seismic forward modeling for synthetic responses. Comparing multiple tailored proxy seismic simulators on realizations under different geological scenarios with flow responses represents an additional thorough investigation for maximizing the usefulness of models of rock physics and the actual seismic data for real field applications.

- Linking the proposed workflow and rock physics model with basin and petroleum system modeling (BPSM) will make the subsurface evaluation process more consistent from the study of geology to the application through engineering. In this work, we ignored the possible effects of vertical movements of target formations that may be applied on basin-scale, such as lifting and subsidence, and the uncertainty of erosions. Both are important factors on both the developments and the abundances of geological features. Relatively sparse data limits our ability to fully construct a 3D BPSM. Thus, it probably would not be meaningful for the scale of conventional reservoirs. However, since evaluations of unconventional fields are conducted in basin scale, linking the workflow with BPSM may enhance our quantitative and qualitative understanding of the spatial distribution of geological features and their effects on subsurface responses.

Bibliography

- Al-Dossary, S., and Marfurt, K.J., 2006, 3D volumetric multispectral estimates of reflector curvature and rotation: *Geophysics*, v. 71, no. 5, p. P41, doi: 10.1190/1.2242449.
- Antonellini, M. a., and Pollard, D.D., 1995, Distinct element modeling of deformation bands in sandstone: *Journal of Structural Geology*, v. 17, no. 8, p. 1165–1182, doi: 10.1016/0191-8141(95)00001-T.
- Atkinson, B.K., 1984, Subcritical crack growth in geological materials: *Journal of Geophysical Research*, v. 89, no. B6, p. 4077, doi: 10.1029/JB089iB06p04077.
- Auld, B.A., 1990, *Acoustic fields and waves in solids*: RE Krieger.
- Avseth, P., Dvorkin, J., and Mavko, G., 2000, Rock physics diagnostic of north sea sands: Link between microstructure and seismic properties: v. 27, no. 17, p. 2761–2764.
- Avseth, P., Mukerji, T., Jørstad, a., Mavko, G., and Veggeland, T., 2001, Seismic reservoir mapping from 3-D AVO in a North Sea turbidite system: *Geophysics*, v. 66, no. 4, p. 1157–1176, doi: 10.1190/1.1487063.
- Aydin, A., 2014, Failure modes of shales and their implications for natural and man-made fracture assemblages: *AAPG Bulletin*, v. 98, no. 11, p. 2391–2409, doi: 10.1306/07311413112.
- Aydin, A., Borja, R.I., and Eichhubl, P., 2006, Geological and mathematical framework for failure modes in granular rock: *Journal of Structural Geology*, v. 28, no. 1, p. 83–98, doi: 10.1016/j.jsg.2005.07.008.
- Aydin, O., and Caers, J., 2015, Determining model complexity using image transforms in a top-down and bottom-up approach: , p. 1–35.
- Aziz, K., and Settari, A., 1979, *Petroleum reservoir simulation*: Chapman & Hall.
- Bandyopadhyay, K., 2009, *Seismic anisotropy: Geological causes and its implications*

- to reservoir geophysics: Stanford University.
- Bergbauer, S., Mukerji, T., and Hennings, P., 2003, Improving curvature analyses of deformed horizons using scale- dependent filtering techniques: v. 8, no. 8, p. 1255–1272, doi: 10.1306/0319032001101.
- Berryman, J.G., 1980, Long-wavelength propagation in composite elastic media II. Ellipsoidal inclusions: *The Journal of the Acoustical Society of America*, v. 68, no. 6, p. 1820, doi: 10.1121/1.385172.
- Bigi, S., and Costa Pisani, P., 2005, From a deformed Peri-Tethyan carbonate platform to a fold-and-thrust-belt: an example from the Central Apennines (Italy): *Journal of Structural Geology*, v. 27, no. 3, p. 523–539, doi: 10.1016/j.jsg.2004.10.005.
- Borg, I., and Groenen, P., 2003, Modern Multidimensional Scaling: Theory and Applications: *Journal of Educational Measurement*, v. 40, no. 3, p. 277–280, doi: 10.1111/j.1745-3984.2003.tb01108.x.
- Borja, R.I., and Aydin, A., 2004, Computational modeling of deformation bands in granular media. I. Geological and mathematical framework: *Computer Methods in Applied Mechanics and Engineering*, v. 193, no. 27-29, p. 2699–2718, doi: 10.1016/j.cma.2003.09.018.
- Borja, R.I., Regueiro, R.A., and Lai, T.Y., 2000, FE Modeling of Strain Localization in Soft Rock: *Journal of Geotechnical and Geoenvironmental Engineering*, v. 126, no. 4, p. 335–343, doi: 10.1061/(ASCE)1090-0241(2000)126:4(335).
- Boyer, S.E., and Elliott, D., 1982, Thrust Systems: *AAPG Bulletin*, v. 66, no. 9, p. 1196–1230, doi: 10.1306/03B5A77D-16D1-11D7-8645000102C1865D.
- Brandes, C., and Tanner, D.C., 2014, Fault-related folding: A review of kinematic models and their application: *Earth-Science Reviews*, v. 138, p. 352–370, doi: 10.1016/j.earscirev.2014.06.008.
- Bristow, J.R., 1960, Microcracks, and the static and dynamic elastic constants of annealed and heavily cold-worked metals: *British Journal of Applied Physics*, v. 11, no. 2, p. 81–85, doi: 10.1088/0508-3443/11/2/309.
- Bruno, M.S., 1994, Micromechanics of stress-induced permeability anisotropy and damage in sedimentary rock: *Mechanics of Materials*, v. 18, no. 1, p. 31–48, doi:

- 10.1016/0167-6636(94)90004-3.
- Budiansky, B., 1965, On the elastic moduli of some heterogeneous materials: *Journal of the Mechanics and Physics of Solids*, v. 13, no. 4, p. 223–227, doi: 10.1016/0022-5096(65)90011-6.
- Bürgmann, R., and Pollard, D.D., 1994, Strain accommodation about strike-slip fault discontinuities in granitic rock under brittle-to-ductile conditions: *Journal of Structural Geology*, v. 16, no. 12, p. 1655–1674, doi: 10.1016/0191-8141(94)90133-3.
- Burgreen, B., and Graham, S., 2014, Evolution of a deep-water lobe system in the Neogene trench-slope setting of the East Coast Basin, New Zealand: Lobe stratigraphy and architecture in a weakly confined basin configuration: *Marine and Petroleum Geology*, v. 54, p. 1–22, doi: 10.1016/j.marpetgeo.2014.02.011.
- Buseti, S., Mish, K., Hennings, P., and Reches, Z., 2012a, Damage and plastic deformation of reservoir rocks: Part 2. Propagation of a hydraulic fracture: *AAPG Bulletin*, v. 96, no. 9, p. 1711–1732, doi: 10.1306/02011211011.
- Buseti, S., Mish, K., and Reches, Z., 2012b, Damage and plastic deformation of reservoir rocks : Part 1 . Damage fracturing: v. 9, no. 9, p. 1687–1709, doi: 10.1306/02011211010.
- Caers, J., 2011, *Modeling Uncertainty in the Earth Sciences*: John Wiley & Sons, Ltd, Chichester, UK.
- Caers, J., 2005, *Petroleum geostatistics*: Society of Petroleum Engineers, Richardson, TX.
- Caers, J., Park, K., and Scheidt, C., 2010, Modeling uncertainty of complex Earth systems in metric space: *Handbook of Geomathematics*. Springer Berlin Heidelberg, p. 865–889, , doi: 10.1007/978-3-642-01546-5_29.
- Carter, K.M., Harper, J. a., Schmid, K.W., and Kostelnik, J., 2011, Unconventional natural gas resources in Pennsylvania: The backstory of the modern Marcellus Shale play: *Environmental Geosciences*, v. 18, no. 4, p. 217–257, doi: 10.1306/eg.09281111008.
- Cartwright, J., and Huuse, M., 2005, 3D seismic technology: the geological “Hubble”:

- Basin Research, v. 17, no. 1, p. 1–20, doi: 10.1111/j.1365-2117.2005.00252.x.
- Castro, S.S.A., 2007, A probabilistic approach to jointly integrate 3D/4D seismic, production data and geological information for building reservoir models: Stanford University.
- Castro, S., Caers, J., and Mukerji, T., 2005, The Stanford VI reservoir, *in* SCRF Annual Meeting, Stanford, 1–73.
- Cheng, C.H., 1993, Crack models for a transversely isotropic medium: *Journal of Geophysical Research*, v. 98, no. B1, p. 675, doi: 10.1029/92JB02118.
- Chopra, S., and Marfurt, K.J.K., 2007, Seismic Attributes for Prospect Identification and Reservoir Characterization: Society of Exploration Geophysicists and European Association of Geoscientists and Engineers.
- Cleary, M., Lee, S., and Chen, I., 1980, Self-consistent techniques for heterogeneous media: *Journal of the Engineering Mechanics Division*, v. 106, no. 5, p. 861–887.
- Cloos, H., 1953, *Conversation with the Earth*: Alfred A Knopf.
- Cloos, E., 1968, Experimental Analysis of Gulf Coast Fracture Patterns: *AAPG Bulletin*, v. 52, no. 3, p. 420–444.
- Coats, K.H., 1969, Use and Misuse of Reservoir Simulation Models: *Journal of Petroleum Technology*, v. 21, no. 11, p. 1391–1398, doi: 10.2118/2367-PA.
- Cowin, S.C., and MehRrabdi, M.M., 1987, On the identification of material symmetry for anisotropic elastic materials: *The Quarterly Journal of Mechanics and Applied Mathematics*, v. 40, no. 4, p. 451–476, doi: 10.1093/qjmam/40.4.451.
- Dahlstrom, C.D. a., 1969, Balanced cross sections: *Canadian Journal of Earth Sciences*, v. 6, no. 4, p. 743–757, doi: 10.1139/e69-069.
- Demyttenaere, R.R.A., Sluijk, A.H., and Bentley, M.R., 1993, A fundamental reappraisal of the structure of the Cormorant Field and its impact on field development strategy, *in* *Petroleum Geology of Northwest Europe: Proceedings of the 4th Conference*, Geological Society of London, 1151–1157.
- Dewhurst, D.N.N., Brown, K.M.M., Clennell, M.B.B., and Westbrook, G.K.K., 1996, A comparison of the fabric and permeability anisotropy of consolidated and sheared silty clay: *Engineering Geology*, v. 42, no. 4, p. 253–267, doi:

10.1016/0013-7952(95)00089-5.

- Dorn, G.A., 1998, Modern 3-D seismic interpretation: The Leading Edge, v. 17, no. 9, p. 1262–1262, doi: 10.1190/1.1438121.
- Engelder, T., 1985, Loading paths to joint propagation during a tectonic cycle: an example from the Appalachian Plateau, U.S.A.: *Journal of Structural Geology*, v. 7, no. 3-4, p. 459–476, doi: 10.1016/0191-8141(85)90049-5.
- Engelder, T., Lash, G.G., and Uzcátegui, R.S., 2009, Joint sets that enhance production from Middle and Upper Devonian gas shales of the Appalachian Basin: *AAPG Bulletin*, v. 93, no. 7, p. 857–889, doi: 10.1306/03230908032.
- Evans, M. a., 1994, Joints and decollement zones in Middle Devonian shales. Evidence for multiple deformation events in the central Appalachian Plateau: *Bulletin of the Geological Society of America*, v. 106, no. 4, p. 447–460, doi: 10.1130/0016-7606(1994)106<0447:JADCZI>2.3.CO;2.
- Evans, M. a., DeLisle, A., Leo, J., and Lafonte, C.J., 2014, Deformation conditions for fracturing in the Middle Devonian sequence of the central Appalachians during the Late Paleozoic Alleghenian orogeny: *AAPG Bulletin*, v. 98, no. 11, p. 2263–2299, doi: 10.1306/07221413135.
- Ferrill, D. a., and Dunne, W.M., 1989, Cover deformation above a blind duplex: An example from West Virginia, U.S.A.: *Journal of Structural Geology*, v. 11, no. 4, p. 421–431, doi: 10.1016/0191-8141(89)90019-9.
- Gale, J.F.W., Laubach, S.E., Olson, J.E., Eichhülle, P., and Fall, A., 2014, Natural Fractures in shale: A review and new observations: *AAPG Bulletin*, v. 98, no. 11, p. 2165–2216, doi: 10.1306/08121413151.
- Gelfand, a E., Zhu, L., and Carlin, B.P., 2001, On the change of support problem for spatio-temporal data: *Biostatistics*, v. 2, no. 1, p. 31–45, doi: 10.1093/biostatistics/2.1.31.
- González, E.F., Mukerji, T., and Mavko, G., 2008, Seismic inversion combining rock physics and multiple-point geostatistics: *Geophysics*, v. 73, no. 1, p. R11–R21, doi: 10.1190/1.2803748.
- Grechka, V., and Kachanov, M., 2006, Seismic characterization of multiple fracture

- sets: Does orthotropy suffice? *Geophysics*, v. 71, no. 3, p. D93–D105, doi: 10.1190/1.2196872.
- Grechka, V., Kachanov, M., Rechka, V.L.G., and Shell, E., 2006, Effective elasticity of fractured rocks: The Leading Edge, p. 152–155.
- Grechka, V., and Tsvankin, I., 2004, Characterization of dipping fractures in a transversely isotropic background: *Geophysical Prospecting*, v. 52, no. 1, p. 1–10, doi: 10.1046/j.1365-2478.2004.00396.x.
- Gringarten, E., Arpat, B., Haouesse, A., Dutranois, A., Deny, L., Jayr, S., Tertois, A.L., Mallet, J.L., Bernal, A., and Nghiem, L., 2008, 3D Reservoir Grids – State Of The Art *in* SPE Annual Technical Conference and Exhibition: Proceedings of the Conference, Society of Petroleum Engineers, doi: 10.2118/116649-MS.
- Hakami, A.M., Marfurt, K.J., and Al-dossary, S., 2004, Curvature Attribute and seismic interpretation : Case study from Fort Worth Basin , Texas , USA, *in* SEG International Exposition and 74th Annual Meeting: Expanded Abstract, p. 544–547, doi: 10.1190/1.1851292.
- Hamiel, Y., Lyakhovsky, V., and Agnon, A., 2004, Coupled evolution of damage and porosity in poroelastic media: theory and applications to deformation of porous rocks: *Geophysical Journal International*, v. 156, no. 3, p. 701–713, doi: 10.1111/j.1365-246X.2004.02172.x.
- Hancock, P.L., 1985, Brittle microtectonics: principles and practice: *Journal of Structural Geology*, v. 7, no. 3-4, p. 437–457, doi: 10.1016/0191-8141(85)90048-3.
- Hanks, C.C.L., and Wallace, W., 2004, Character, relative age and implications of fractures and other mesoscopic structures associated with detachment folds: an example from the Lisburne Group of the: *Bulletin of canadian petroleum geology*, v. 52, no. 2, p. 121–138, doi: 10.2113/52.2.121.
- Hennings, P., Allwardt, P., Paul, P., Zahm, C., Jr, R.R., Alley, H., Kirschner, R., Lee, B., Hough, E., Subsur-, P.H.C., Technology, S., and Reid, R., 2012, Relationship between fractures, fault zones, stress, and reservoir productivity in the Suban gas field, Sumatra, Indonesia: *AAPG Bulletin*, v. 96, no. 4, p. 753–772, doi:

10.1306/08161109084.

- Hennings, P.H., Olson, J.E., and Thompson, L.B., 2000, Combining outcrop data and three-dimensional structural models to characterize fractured reservoirs: An example from Wyoming: *AAPG Bulletin*, v. 84, no. 6, p. 830–849, doi: 10.1306/A967340A-1738-11D7-8645000102C1865D.
- Hill, R., 1965, A self-consistent mechanics of composite materials: *Journal of the Mechanics and Physics of Solids*, v. 13, no. 4, p. 213–222, doi: 10.1016/0022-5096(65)90010-4.
- Holder, J., Olson, J.E., and Philip, Z., 2001, Experimental determination of subcritical crack growth parameters in sedimentary rock: *Geophysical Research Letters*, v. 28, no. 4, p. 599–602, doi: 10.1029/2000GL011918.
- Hubbert, M.K., 1951, Mechanical basis for certain familiar geologic structures: *Bulletin of the Geological Society of America*, v. 62, no. 4, p. 355–372, doi: 10.1130/0016-7606(1951)62[355:MBFCFG]2.0.CO;2.
- Hubbert, M.K., 1937, Theory of scale models as applied to the study of geologic structures: *Geological Society of America Bulletin*, v. 48, no. 10, p. 1459–1520, doi: 10.1130/GSAB-48-1459.
- Hudson, J.A., 1990, Overall elastic properties of isotropic materials with arbitrary distribution of circular cracks: *Geophysical Journal International*, v. 102, no. 2, p. 465–469, doi: 10.1111/j.1365-246X.1990.tb04478.x.
- Inks, T.L., Engelder, T., Jenner, E., Golob, B., Hocum, J.S., and O'Brien, D.G., 2015, Marcellus fracture characterization using P-wave azimuthal velocity attributes: Comparison with production and outcrop data: *Interpretation*, v. 3, no. 3, p. SU1–SU15, doi: 10.1190/INT-2014-0215.1.
- Isaaks, E., and Srivastava, R., 1989, *Applied geostatistics*: Oxford University Press.
- Jahns, H.O., 1966, A Rapid Method for Obtaining a Two-Dimensional Reservoir Description From Well Pressure Response Data: *Society of Petroleum Engineers Journal*, v. 6, no. 04, p. 315–327, doi: 10.2118/1473-PA.
- Jeong, C., 2014, *Quantitative Reservoir Characterization Integrating Seismic Data and Geological Scenario Uncertainty*: Stanford University.

- Jeong, C., Mukerji, T., and Mariethoz, G., 2014, Adaptive spatial resampling as a Markov chain Monte Carlo method for uncertainty quantification in seismic reservoir characterization, *in* SCRF Annual Meeting, Stanford, 1–18.
- Jolley, S.J., Barr, D., Walsh, J.J., and Knipe, R.J., 2007, Structurally complex reservoirs: an introduction: Geological Society, London, Special Publications, v. 292, no. 1, p. 1–24, doi: 10.1144/SP292.1.
- Kachanov, M., 1980, Continuum model of medium with cracks: *Journal of the engineering mechanics division*, v. 106, no. 5, p. 1039–1051.
- Kohl, D., Slingerland, R., Arthur, M., Bracht, R., and Engelder, T., 2014, Sequence striating and depositional environments of the Shamokin (Union Springs) Member, Marcellus Formation, and associated strata in the middle Appalachian Basin: *AAPG Bulletin*, v. 98, no. 3, p. 483–513, doi: 10.1306/08231312124.
- Laurent, G., Caumon, G., and Jessell, M., 2015, Interactive editing of 3D geological structures and tectonic history sketching via a rigid element method: *Computers & Geosciences*, v. 74, p. 71–86, doi: 10.1016/j.cageo.2014.10.011.
- Lee, J., and Mukerji, T., 2012, The Stanford VI-E Reservoir : A Synthetic Data Set for Joint Seismic-EM Time-lapse Monitoring Algorithms, *in* SCRF Annual Meeting, Stanford, 1–53.
- Lewis, H., Hall, S. a., Guest, J., and Couples, G.D., 2007, Kinematically-equivalent but geomechanically-different simulations of fault evolution: the role of loading configurations: Geological Society, London, Special Publications, v. 292, no. 1, p. 159–172, doi: 10.1144/SP292.9.
- Lewis, H., Hall, S.A., Guest, J., and Couples, G.D., 2013, simulations of fault evolution : the role of loading configurations Kinematically-equivalent but geomechanically-different simulations of fault evolution : the role of loading configurations: , doi: 10.1144/SP292.9.
- Li, L., Caers, J., and Sava, P., 2015, Assessing seismic uncertainty via geostatistical velocity-model perturbation and image registration: An application to subsalt imaging: *The Leading Edge*, v. 34, no. 9, p. 1064–1070, doi: 10.1190/tle34091064.1.

- Lohr, T., Krawczyk, C.M., Tanner, D.C., Samiee, R., Endres, H., Thierer, P.O., Oncken, O., Trappe, H., Bachmann, R., and Kukla, P. a., 2008, Prediction of subseismic faults and fractures: Integration of three-dimensional seismic data, three-dimensional retrodeformation, and well data on an example of deformation around an inverted fault: *AAPG Bulletin*, v. 92, no. 4, p. 473–485, doi: 10.1306/11260707046.
- Lovely, P., 2011, *Fault-related Deformation Over Geologic Time: Integrating Field Observations, High Resolution Geospatial Data and Numerical Modeling to Investigate 3D*: Stanford University.
- Lovely, P., Flodin, E., Guzowski, C., Maerten, F., and Pollard, D.D., 2012, Pitfalls among the promises of mechanics-based restoration: Addressing implications of unphysical boundary conditions: *Journal of Structural Geology*, v. 41, p. 47–63, doi: 10.1016/j.jsg.2012.02.020.
- Maerten, L., Gillespie, P., and Pollard, D.D., 2002, Effects of local stress perturbation on secondary fault development: *Journal of Structural Geology*, v. 24, no. 1, p. 145–153, doi: 10.1016/S0191-8141(01)00054-2.
- Maerten, L., Maerten, F., Point, R., Franklin, B., and Cedex, M., 2006, Chronologic modeling of faulted and fractured reservoirs using geomechanically based restoration: *Technique and industry applications: AAPG Bulletin*, v. 90, no. 8, p. 1201–1226, doi: 10.1306/02240605116.
- Maerten, F., Maerten, L., and Pollard, D.D., 2014, iBem3D, a three-dimensional iterative boundary element method using angular dislocations for modeling geologic structures: *Computers & Geosciences*, v. 72, p. 1–17, doi: 10.1016/j.cageo.2014.06.007.
- Maerten, L., Pollard, D.D., and Maerten, F., 2001, Digital mapping of three-dimensional structures of the Chimney Rock fault system, central Utah: *Journal of Structural Geology*, v. 23, no. 4, p. 585–592, doi: 10.1016/S0191-8141(00)00142-5.
- Mallet, J., 2004, *Space – Time Mathematical Framework for Sedimentary Geology: Mathematical Geology*, v. 36, no. 1, p. 1–32, doi:

10.1023/B:MATG.0000016228.75495.7c.

- Marder, M., and Fineberg, J., 1996, How things break: *Phys. Today*, v. 49, no. 9, p. 24–29.
- Mavko, G., Mukerji, T., and Dvorkin, J., 2003, *The rock physics handbook: Tools for seismic analysis of porous media*: Cambridge University Press, New York.
- Mogi, K., and Publishing, E., 1972, Fracture and flow of rocks: *Tectonophysics*, v. 13, no. 1-4, p. 541–568, doi: 10.1016/0040-1951(72)90037-6.
- Mukerji, T., Avseth, P., and Mavko, G., 2001, Statistical rock physics: Combining rock physics, information theory, and geostatistics to reduce uncertainty in seismic reservoir characterization: *The Leading Edge*, v. 20, no. 3, p. 313–319.
- Mukerji, T., and Mavko, G., 1994, Pore fluid effects on seismic velocity in anisotropic rocks: *Geophysics*, v. 59, no. 2, p. 233, doi: 10.1190/1.1443585.
- Mukerji, T., Mavko, G., Mujica, D., and Lucet, N., 1995, Scale-dependent seismic velocity in heterogeneous media: *GEOPHYSICS*, v. 60, no. 4, p. 1222–1233, doi: 10.1190/1.1443851.
- Mura, T., 1983, *Micromechanics of Defects in Solids*: Springer Science & Business Media.
- Nenna, F., and Aydin, A., 2011, The formation and growth of pressure solution seams in clastic rocks: A field and analytical study: *Journal of Structural Geology*, v. 33, no. 4, p. 633–643, doi: 10.1016/j.jsg.2011.01.014.
- Nevitt, J.M., Pollard, D.D., and Warren, J.M., 2014, Evaluation of transtension and transpression within contractional fault steps: Comparing kinematic and mechanical models to field data: *Journal of Structural Geology*, v. 60, p. 55–69, doi: 10.1016/j.jsg.2013.12.011.
- Nickelsen, R.P., 1986, Cleavage duplexes in the Marcellus Shale of the Appalachian foreland: *Journal of Structural Geology*, v. 8, no. 3-4, p. 361–371, doi: 10.1016/0191-8141(86)90055-6.
- Nishizawa, O., 1982, Seismic velocity anisotropy in a medium containing oriented cracks. Transversely isotropic case.: *Journal of Physics of the Earth*, v. 30, no. 4, p. 331–347, doi: 10.4294/jpe1952.30.331.

- Nishizawa, O., and Yoshino, T., 2001, Seismic velocity anisotropy in mica-rich rocks: an inclusion model: *Geophysical Journal International*, v. 145, no. 1, p. 19–32, doi: 10.1046/j.1365-246x.2001.00331.x.
- Norris, A.N., 1985, A differential scheme for the effective moduli of composites: *Mechanics of Materials*, v. 4, no. 1, p. 1–16, doi: 10.1016/0167-6636(85)90002-X.
- Novoa, E., Suppe, J., and Shaw, J.H., 2000, Inclined-shear restoration of growth folds: *AAPG Bulletin*, v. 84, no. 6, p. 787–804, doi: 10.1306/A96733F6-1738-11D7-8645000102C1865D.
- Nur, A., and Simmons, G., 1969, The effect of saturation on velocity in low porosity rocks: *Earth and Planetary Science Letters*, v. 7, no. 2, p. 183–193, doi: 10.1016/0012-821X(69)90035-1.
- Nygård, R., Gutierrez, M., Bratli, R.K., and Høeg, K., 2006, Brittle-ductile transition, shear failure and leakage in shales and mudrocks: *Marine and Petroleum Geology*, v. 23, no. 2, p. 201–212, doi: 10.1016/j.marpetgeo.2005.10.001.
- Olson, J.E., 2004, Predicting fracture swarms - the influence of subcritical crack growth and the crack-tip process zone on joint spacing in rock: *Geological Society, London, Special Publications*, v. 231, no. 1, p. 73–88, doi: 10.1144/GSL.SP.2004.231.01.05.
- Olson, J., and Pollard, D.D., 1989, Inferring paleostresses from natural fracture patterns: A new method: *Geology*, v. 17, no. 4, p. 345, doi: 10.1130/0091-7613(1989)017<0345:IPFNFP>2.3.CO;2.
- Osholake, T., Yilin Wang, J., and Ertekin, T., 2012, Factors Affecting Hydraulically Fractured Well Performance in the Marcellus Shale Gas Reservoirs: *Journal of Energy Resources Technology*, v. 135, no. 1, p. 013402, doi: 10.1115/1.4007766.
- Owen, G., 1987, Deformation processes in unconsolidated sands: *Geological Society, London, Special Publications*, v. 29, no. 1, p. 11–24, doi: 10.1144/GSL.SP.1987.029.01.02.
- Park, H., Scheidt, C., Fenwick, D., Boucher, A., and Caers, J., 2013, History matching and uncertainty quantification of facies models with multiple geological

- interpretations: *Computational Geosciences*, v. 17, no. 4, p. 609–621, doi: 10.1007/s10596-013-9343-5.
- Paterson, M., and Wong, T., 2005, *Experimental rock deformation: the brittle field*: Springer Berlin Heidelberg, Berlin.
- Paul, P.K., Zoback, M.D., and Hennings, P.H., 2009, Fluid Flow in a Fractured Reservoir Using a Geomechanically Constrained Fault-Zone-Damage Model for Reservoir Simulation: *SPE Reservoir Evaluation & Engineering*, v. 12, no. 04, p. 562–575, doi: 10.2118/110542-PA.
- Picou, C., and Utzmann, R., 1962, La “coupe sismique vectorielle”: *Geophysical Prospecting*, v. 10, no. 4, p. 497–516, doi: 10.1111/j.1365-2478.1962.tb00004.x.
- Plumb, R.A., Evans, K.F., and Engelder, T., 1991, Geophysical log responses and their correlation with bed-to-bed stress contrasts in Paleozoic rocks, Appalachian Plateau, New York: *Journal of Geophysical Research*, v. 96, no. B9, p. 14509, doi: 10.1029/91JB00896.
- Plumb, R. a., and Hickman, S.H., 1985, Stress-induced borehole elongation: A comparison between the four-arm dipmeter and the borehole televiewer in the Auburn Geothermal Well: *Journal of Geophysical Research*, v. 90, no. B7, p. 5513, doi: 10.1029/JB090iB07p05513.
- Pollard, D., and Fletcher, R., 2005, *Fundamentals of structural geology*: Cambridge University Press, New York.
- Pollard, D.D., and Johnson, A.M., 1973, Mechanics of growth of some laccolithic intrusions in the Henry mountains, Utah, II: Bending and failure of overburden layers and sill formation: *Tectonophysics*, v. 18, no. 3–4, p. 311–354, doi: [http://dx.doi.org/10.1016/0040-1951\(73\)90051-6](http://dx.doi.org/10.1016/0040-1951(73)90051-6).
- Powell, C.M., 1979, A morphological classification of rock cleavage: *Tectonophysics*, v. 58, p. 21–34, doi: 10.1016/0040-1951(79)90320-2.
- Rathore, J.S., Fjaer, E., Holt, R.M., and Renlie, L., 1995, P- and S-wave anisotropy of a synthetic sandstone with controlled crack geometry1: *Geophysical Prospecting*, v. 43, no. 6, p. 711–728, doi: 10.1111/j.1365-2478.1995.tb00276.x.
- Remy, N., Boucher, A., and Wu, J., 2009, *Applied geostatistics with SGeMS: a user’s*

guide: Cambridge University Press.

- Renshaw, C.E., and Pollard, D.D., 1994, Numerical simulation of fracture set formation: A fracture mechanics model consistent with experimental observations: *Journal of Geophysical Research*, v. 99, no. B5, p. 9359–9372, doi: 10.1029/94JB00139.
- Rodrigues, N., Cobbold, P.R., Loseth, H., and Ruffet, G., 2009, Widespread bedding-parallel veins of fibrous calcite ('beef') in a mature source rock (Vaca Muerta Fm, Neuquen Basin, Argentina): evidence for overpressure and horizontal compression: *Journal of the Geological Society*, v. 166, no. 4, p. 695–709, doi: 10.1144/0016-76492008-111.
- Rutter, E.H., 1986, On the nomenclature of mode of failure transitions in rocks: *Tectonophysics*, v. 122, no. 3-4, p. 381–387, doi: 10.1016/0040-1951(86)90153-8.
- Sahai, V., Jackson, G., Rai, R., and Coble, L., 2012, Optimal Well Spacing Configurations for Unconventional Gas Reservoirs, *in Proceedings of SPE Americas Unconventional Resources Conference*, 20.
- Sarout, J., and Guéguen, Y., 2008, Anisotropy of elastic wave velocities in deformed shales: Part 1 — Experimental results: *Geophysics*, v. 73, no. 5, p. D75–D89, doi: 10.1190/1.2952744.
- Sarout, J.J., Guéguen, Y., and Guéguen, Y., 2008, Anisotropy of elastic wave velocities in deformed shales: Part 2 — Modeling results: *Geophysics*, v. 73, no. 5, p. D91, doi: 10.1190/1.2952745.
- Sava, D., 2004, QUANTITATIVE DATA INTEGRATION FOR FRACTURE CHARACTERIZATION: Stanford University.
- Sava, D., and Mukerji, T., 2001, Rock Physics Analysis And Fracture Modeling of the San Andres Reservoir, Yates Field: 2001 SEG Annual Meeting.
- Schilthuis, R.J., and Hurst, W., 1935, Variations in Reservoir Pressure in the East Texas Field: *Transactions of the AIME*, v. 114, no. 01, p. 164–176, doi: 10.2118/935164-G.
- Sevostianov, I., and Kachanov, M., 2007, Effect of interphase layers on the overall

- elastic and conductive properties of matrix composites. Applications to nanosize inclusion: *International Journal of Solids and Structures*, v. 44, no. 3-4, p. 1304–1315, doi: 10.1016/j.ijsolstr.2006.06.020.
- Sevostianov, I., Yilmaz, N., Kushch, V., and Levin, V., 2005, Effective elastic properties of matrix composites with transversely-isotropic phases: *International Journal of Solids and Structures*, v. 42, p. 455–476, doi: 10.1016/j.ijsolstr.2004.06.047.
- Smiser, J.S., and Wintermann., D., 1935, Character and possible origin of producing rock in hilbig oil field, bastrop county, texas: *AAPG Bulletin*, v. 19, no. 2, p. 206–220.
- Spencer, C.W., 1987, Hydrocarbon Generation as a Mechanism for Overpressuring in Rocky Mountain Region: *AAPG Bulletin*, v. 71, no. 4, p. 368–388, doi: 10.1306/94886EB6-1704-11D7-8645000102C1865D.
- Sternlof, K.R., Rudnicki, J.W., and Pollard, D.D., 2005, Anticrack inclusion model for compaction bands in sandstone: *Journal of Geophysical Research*, v. 110, no. B11, p. B11403, doi: 10.1029/2005JB003764.
- Strebelle, S., and Journel, A., 2001, Reservoir modeling using multiple-point statistics, *in* SPE Annual Technical Conference and Exhibition: Proceeding of the conference, Society of Petroleum Engineers, doi: 10.2118/71324-MS.
- Sun, M., 2002, Optimal Recovery of Elastic Properties for Anisotropic Materials through Ultrasonic Measurements: The University of Maine.
- Suppe, J., 1983, Geometry and kinematics of fault-bend folding: *American Journal of Science*, v. 283, no. 7, p. 684–721, doi: 10.2475/ajs.283.7.684.
- Suzuki, S., Stanford, U., Daly, C., Caers, J., and Mueller, D., 2005, SPE 95498 History Matching of Naturally Fractured Reservoirs Using Elastic Stress Simulation and Probability Perturbation Method:.
- Tai Te Wu, 1966, The effect of inclusion shape on the elastic moduli of a two-phase material: *International Journal of Solids and Structures*, v. 2, no. 1, p. 1–8, doi: 10.1016/0020-7683(66)90002-3.
- Teng, L., 1998, Seismic and rock-physics characterization of fractured reservoirs:

Stanford University.

- Thomas, W.W. a W., 2001, Mushwad: Ductile duplex in the Appalachian thrust belt in Alabama: AAPG Bulletin, v. 10, no. 10, p. 1847–1869.
- Thompson, J.M., Angha, V.O.M., Energy, S.C., and Anderson, D.M., 2011, Advancements in Shale Gas Production Forecasting – A Marcellus Case Study: , no. June, p. 14–16.
- Valès, F., Nguyen Minh, D., Gharbi, H., and Rejeb, a, 2004, Experimental study of the influence of the degree of saturation on physical and mechanical properties in Tournemire shale (France): Applied Clay Science, v. 26, no. 1-4, p. 197–207, doi: 10.1016/j.clay.2003.12.032.
- Vernik, L., 1993, Microcrack-induced versus intrinsic elastic anisotropy in mature HC-source shales: Geophysics, v. 58, no. 11, p. 1703, doi: 10.1190/1.1443385.
- Vernik, L., and Landis, C., 1996, Elastic anisotropy of source rocks: Implications for hydrocarbon generation and primary migration: AAPG Bulletin, v. 80, no. 4, p. 531–544, doi: 10.1306/64ED8836-1724-11D7-8645000102C1865D.
- Vernik, L., and Liu, X., 1997, Velocity anisotropy in shales: A petrophysical study: Geophysics, v. 62, no. 2, p. 521, doi: 10.1190/1.1444162.
- Vernik, L., and Nur, A., 1992, Ultrasonic velocity and anisotropy of hydrocarbon source rocks: GEOPHYSICS, v. 57, no. 5, p. 727–735, doi: 10.1190/1.1443286.
- Vo, H.X., and Durlofsky, L.J., 2014, A New Differentiable Parameterization Based on Principal Component Analysis for the Low-Dimensional Representation of Complex Geological Models: Mathematical Geosciences, p. 775–813, doi: 10.1007/s11004-014-9541-2.
- Vo, H.X., and Durlofsky, L.J., 2015, Data assimilation and uncertainty assessment for complex geological models using a new PCA-based parameterization: Computational Geosciences, p. 747–767, doi: 10.1007/s10596-015-9483-x.
- Wang, Z.Z., 2001, Fundamentals of seismic rock physics: Geophysics, v. 66, no. 2, p. 398–412.
- Wang, G., and Carr, T.R., 2013, Organic-rich Marcellus Shale lithofacies modeling and distribution pattern analysis in the Appalachian Basin: AAPG Bulletin, v. 97,

- no. 12, p. 2173–2205, doi: 10.1306/05141312135.
- Wheeler, H.E., 1958, Time-stratigraphy: AAPG Bulletin, v. 42, no. 5, p. 1047–1063.
- Wilkins, S., Mount, V., Mahon, K., Perry, A., and Koenig, J., 2014, Characterization and development of subsurface fractures observed in the Marcellus Formation, Appalachian Plateau, north-central Pennsylvania: AAPG Bulletin, v. 98, no. 11, p. 2301–2345, doi: 10.1306/08191414024.
- Wrightstone, G., 2010, Bloomin' Algae! How paleogeography and algal blooms may have significantly impacted deposition and preservation of the Marcellus Shale.
- Xu, S., 2014, Integration of Geomorphic Experiment Data in Surface-based Modeling: From Characterization to Simulation: Stanford University.
- Zagorski, W., Wrightstone, G., and Bowman, D., 2012, The Appalachian Basin Marcellus Gas Play: Its History of Development, Geologic Controls on Production, and Future Potential as a World-class Reservoir, *in* Breyer, J. ed., Shale Reservoirs: Giant Resources for the 21st Century, AAPG Memoir 97, AAPG, 172–200.
- Zoback, M.D., Moos, D., Mastin, L., and Anderson, R.N., 1985, Well bore breakouts and in situ stress: Journal of Geophysical Research, v. 90, no. B7, p. 5523, doi: 10.1029/JB090iB07p05523.